INVESTIGATION OF FUNDAMENTAL GROWTH MECHANISMS IN PULSED LASER DEPOSITION SYNTHESIS OF NANOSTRUCTURED MATERIALS

By

WILLIAM THOMAS MOZET

A dissertation submitted to the

Graduate School-New Brunswick

Rutgers, The State University of New Jersey

In partial fulfillment of the requirements

For the degree of

Doctor of Philosophy

Graduate Program in Mechanical and Aerospace Engineering

Written under the direction of

Stephen D. Tse

And approved by

_____

_____

_____

_____

New Brunswick, New Jersey

October, 2016

ABSTRACT OF THE DISSERTATION

Investigation of the Fundamental Growth Mechanisms in Pulsed Laser Deposition Synthesis of Nanostructured Materials

By WILLIAM THOMAS MOZET

Dissertation Director:

Stephen D. Tse

Studies are conducted to better understand growth mechanisms in pulsed laser deposition (PLD) synthesis of nanostructured materials, namely graphene and bismuth telluride (Bi_2Te_3). For graphene, as the substrate temperature increases, the order of the film increases, from an amorphous carbon film to nanocrystalline graphite and few-layer graphene (FLG). By using a high energy laser, the size and type of ablated species can be controlled to create films with smaller nanocrystalline domains. PLD allows the thickness of the films to be directly controlled by the deposition duration. Films can be grown on arbitrary substrates, unlike other methods which utilize surface chemistry. Substrate morphology also affects the samples, with higher surface roughness leading to larger D/G and 2D/G ratios. Polishing substrates prior to deposition can decrease these ratios by up to 15%. Here, the type of carbon source has little impact on sample growth, except in atmospheric growth of graphene, which may not be an optimal condition

because of energy loss of the carbon species. In-situ plasma plume analysis is conducted to analyze the species being ablated from the target. Ablated species consist primarily of C+ ions, with some neutral C and C_2 species. Ablated C+ ions are at temperatures as high as 12,000 K in vacuum and 10,000 K in 0.1 torr argon. For bismuth telluride, optimal growth conditions are found for the stoichiometric transfer of Bi_2Te_3, which can vary from system to system. In general, a deposition temperature of 200°C and a deposition pressure of 0.1 to 1.0 torr argon are required for stoichiometric transfer. Using a high energy laser for ablation leads to smaller grain sizes in the nanostructured films. In addition, using a nitrogen atmosphere instead of argon leads to increased gas-phase condensation prior to deposition, resulting in a highly featured surface. When outside of the ideal pressure range, the substrate material can significantly affect the surface morphology of the sample, ranging from smooth films to nanoparticles and nanorods. These morphologies affect the electrical properties of the material. In general, the lowest electrical resistance came from films grown using 532 nm laser irradiation, which leads to larger grain sizes and more featured surfaces. Films grown at slightly reduced pressure, which leads to more featured surfaces, are also low in electrical resistance. These films also have large Seebeck coefficients, both of which lead to a higher thermoelectric figure of merit.

Acknowledgements and Dedication

This material is based upon work mainly supported by National Science Foundation Grant No. 0903661 “Nanotechnology for Clean Energy IGERT”

This research was conducted with Government support under and awarded by DoD, Air Force Office of Scientific Research, National Defense Science and Engineering Graduate (NDSEG) Fellowship, 32 CFR 168a

This research had partial support from Rutgers University in the form of a teaching assistant scholarship, as well as from the Army and Navy

This work is dedicated to my wife, Danielle DeNigris, without whom I would not be who I am today, and to my family for their continued support, both emotionally and financially.

Table of Contents

List of Tables

List of Illustrations

1 Introduction

Since its discovery in 2004 [1], graphene has been extensively studied because of its exceptional properties [1] [2] [3] [4] and the current and projected applications [3] [4] [5]. However, producing large quantities of high quality graphene is still a challenge today because of manufacturing limitations and to the constantly evolving aggregate of information in regard to graphene-based systems and low dimensional carbon materials. As a result, different methods are being explored in an attempt to find a way to scale up production and produce large volumes of high quality graphene. However, in order to successfully create a method of producing graphene in such quantities, the fundamental processes and growth mechanisms must be fully explored and understood.

Bismuth telluride is one of the most prominent thermoelectric materials and has been widely studied because of its high efficiency compared to that of other bulk thermoelectric materials at room temperature. It has been theorized that low dimensional thermoelectric materials could perform much better than do bulk samples because of quantum confinement effects and to increased scattering at the grain boundaries of nanostructured materials. Such research has led to several improvements in thermoelectric efficiency and a resurgence of research in the field of thermoelectricity [6]. To achieve the breakthrough necessary for thermoelectric devices to compete on an economic scale, these nanostructures must be fully understood. By controlling the growth conditions to obtain specific nanostructures, a correlation between material properties and features at the nanoscale can be made. This understanding would allow thermoelectric structures to be grown with tailored properties for specific applications.

1.1 Motivation and Objectives

This research aims to establish a better understanding of the fundamental growth mechanisms in pulsed laser deposition (PLD) synthesis of nanostructured materials. This bottom-up approach to nanoscale fabrication is a valuable research tool for parametric studies and fundamental analyses of complex mechanisms. PLD has the unique ability to independently test experimental parameters and observe their effects on the resulting thin films. These experimental parameters include, but are not limited to, laser ablation energy, substrate temperature, deposition pressure, and background gas. There is an almost infinite variability between these parameters and the flexibility in ablation target and growth substrate. As a result, PLD is an exceptional method for conducting proof-of-concept experiments and parametric studies on a variety of materials.

Here, particular attention is paid to graphene systems and bismuth telluride (Bi_2Te_3) systems. By studying exactly how few-layer graphene (FLG) grows from the atomic level, and what conditions exist for high-quality, controlled growth, this research aims to enhance the general knowledge of graphene, starting from the smallest scale and eventually moving up towards large volume manufacturing. This understanding would enable the widespread application of graphene-based devices.

On the other hand, examining the growth mechanisms of nanostructured bismuth telluride thin films can help improve understanding in how grains at the nanoscale affect bulk material properties, as well as improve the functionality of modern thermoelectric devices. Thermoelectric materials may then be better understood and more widespread in every-day applications. This result is especially relevant over climate concerns, since thermoelectric materials have the potential to salvage waste heat for usable energy, which

can increase the overall efficiency of many industrial applications involving energy generation and manufacturing.

1.2 Research Innovation and Strategies

Previous research in the field of graphene production is mainly focused on achieving large scale, high-quality graphene. While this research is paramount to the integration of graphene-based devices, one major drawback is the limitations in the substrate used to grow the graphene. Using PLD, the substrate material is much more flexible than other common methods, such as CVD and flame synthesis. This research focuses on developing a model for PLD graphene growth conditions by examining how several experimental parameters affect the growth of graphene on various substrates. The potential applications of graphene are nearly limitless if a suitable production method could create large graphene sheets with good electrical properties on arbitrary substrates.

For the growth of thermoelectric materials, previous research has focused on improving the thermoelectric figure of merit through chemistry or materials science, i.e. finding new materials and complex structures that have large intrinsic properties that are beneficial for thermoelectricity. However, this research focuses on improving the existing benefits of a specific material, bismuth telluride. By exploring how nanoscale features affect bulk properties, materials can be tailored to have enhanced thermoelectric properties specific to a particular application. As a result, the necessary increase in efficiency for thermoelectric materials to become viable in normal applications can be achieved. These “enhanced” thermoelectric materials could then

compete with the traditional methods of, for example, refrigeration, by negating the need for dangerous chemicals and reducing the overall environmental impact.

As such, the primary components of this research are to:

a) Construct a new pulsed laser deposition experimental setup tailored to the particular needs and aims of this research. Once constructed, the apparatus is tested to ensure its capability of performing the required experiments.

b) Conduct experiments on FLG growth via PLD. Starting by replicating previous results, work then moves on to study parametrically several different experimental parameters that are critical to graphene growth.

c) Characterize FLG samples using Raman spectroscopy and scanning electron microscopy. This investigation attempts to correlate specific properties of FLG to growth parameters to develop a better understanding of how and why graphene grows the way it does, and why certain conditions are necessary for specific outcomes.

d) Conduct experiments on bismuth telluride films grown via PLD. This research aims to study parametrically the growth conditions of nanostructured bismuth telluride in an attempt to increase the thermoelectric properties of the material.

e) Characterize bismuth telluride samples using scanning electron microscopy, energy dispersive spectroscopy, and X-ray diffraction. By relating certain growth parameters and conditions to specific material properties, specially tailored bismuth telluride films can be grown for

various applications. Directly linking growth conditions to electrical properties of a film would allow for highly customizable materials to be manufactured.

f) Explore advanced heterostructures via collaborations with colleagues. The first collaboration involves creating a Bi_2Te_3/graphene heterojunction. The second collaboration involves laminating a good thermoelectric material with good conductors. This results in a sandwich structure of a thin layer of Bi_2Te_3 between thick copper layers. This structure is theorized to have a large power factor in the direction perpendicular to the layered material.

1.3 Overview

Figure 1–1 illustrates a flowchart of the investigative strategy employed in this work. The ultimate goal of this work is to develop the foundation for eventually producing tailored nanostructured materials for various applications.

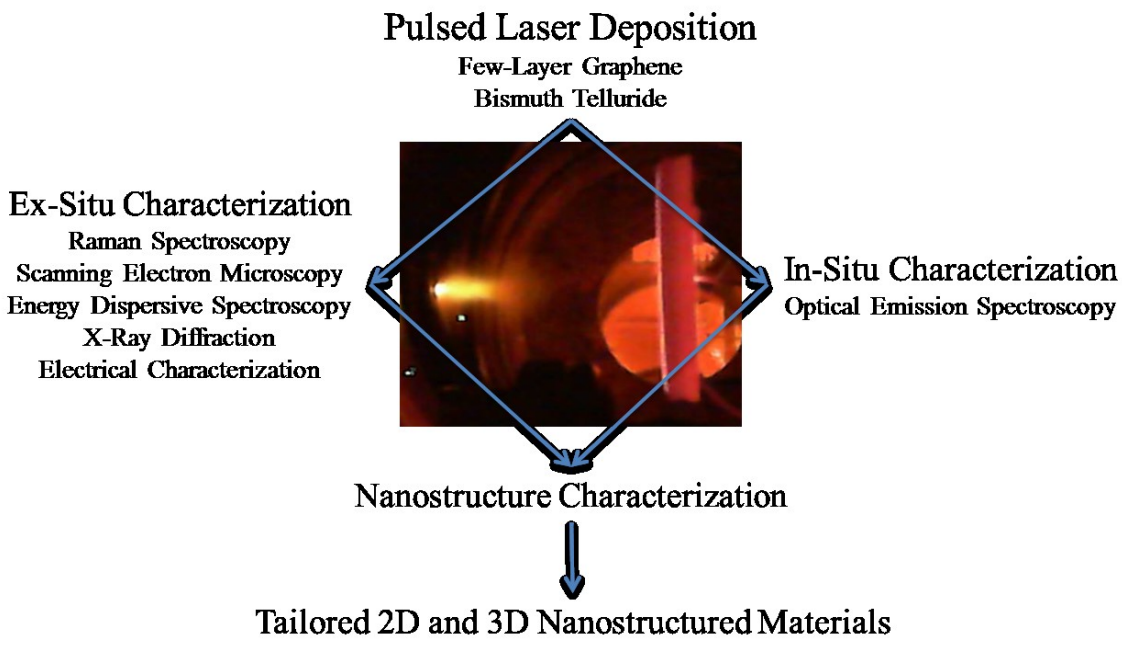

Figure 1–1: Flowchart for this dissertation

Pulsed laser deposition synthesis is utilized in graphene and bismuth telluride systems. In-situ and ex-situ characterization is used to examine and classify these materials. Using scanning electron microscopy, the surface morphology and nanostructure is observed. Using energy dispersive spectroscopy, the chemical composition is determined. X-ray diffraction probes the crystalline structure of the samples, and electrical characterization is used to find the electrical resistivity and Seebeck coefficient. From all of this data, the general structure of the nanomaterial is explored. These investigations will hopefully lead to a better understanding of how nanostructured features affect material properties at the macro-scale. Once this is achieved, nanostructured materials can be specifically tailored to various applications with increased efficiency and improved properties.

1.4 Outline of Dissertation

This dissertation begins with an overview of the pulsed laser deposition process, describing a brief history of laser ablation and going into the details of specifically how PLD works. The history of carbon and the emergence of graphene is described next, going into detail of what exactly constitutes graphene and why it is so unique. The basics of graphene production is reviewed, and a summary of graphene growth via PLD is established. Moving on, this same format is used to introduce the field of thermoelectrics, with a particular focus on bismuth telluride. A summary of bismuth telluride growth via PLD is also established. A description of the experimental setup used for this dissertation is outlined next, followed by in-depth sections on graphene growth and bismuth telluride growth using PLD. These two sections describe the growth process, experimental parameters explored, and characterization methods, while reporting any significant findings or potential avenues for further study. The next section describes some more complex hetereostructures and collaborative efforts for future research and analysis. The final chapter gives any concluding remarks and outlines the future work that can be pursued in this field.

2 Background

2.1 Pulsed Laser Deposition

2.1.1 History of Laser Ablation

Since the invention of the laser in 1960, scientists have used laser beams to ablate materials and study the interaction of the energetic source with solid surfaces. Using the high energy laser beam has introduced the field of physical vapor deposition to a new technique. This technique, now known as pulsed laser deposition, was immediately found to be unique and advantageous in many regards for depositing thin films. In the 1960s, research on PLD was mostly exploratory in nature and in the early stages of development. The very first documented PLD experiment was by Smith and Turner in 1965 [7] using a ruby laser to deposit thin films of different materials in an attempt to mimic flash evaporation. These early experiments utilized both continuous wave and pulsed lasers. It was also demonstrated that the stoichiometry of the target could be transferred to a substrate in the form of a thin film, which sparked controversy and helped bring about increased interest in the developing field of laser ablation [8]. The 1970s brought the reliable implementation of the Q-switched laser, which drastically increased the available power density of a laser pulse, opening a range of new materials for exploration and making pulsed lasers the preferred choice for laser ablation. The interaction between the laser beam and the target material was examined further, revealing dielectric breakdown and the formation of a plasma plume. Second harmonic generators were improved, allowing for shorter wavelengths to be used, resulting in smaller absorption depth and reduced splashing of the target surface. Both of these factors led to a more congruent evaporation and further improvements in film quality. It

was also realized that because of the lack of active heating or electrical elements, deposition could occur in reactive or oxidizing atmospheres, as well as in a vacuum [8]. From 1980 to 1987, more film improvements were made and epitaxial semiconductor films, heterostructures and superlattices were grown by PLD that were comparable to pristine films grown by other proven techniques, such as molecular beam epitaxy (MBE). As commercial lasers improved in quality and became more affordable, many new research groups were able to enter the field and make contributions of their own [8]. Then in 1987, researchers at Bell Labs and Rutgers University demonstrated for the first time the deposition of high temperature superconducting Y-Ba-Cu-O (YBCO) thin films via pulsed laser deposition [9]. This sparked massive interest from many researchers across a variety of fields, both because of the superconducting material and the deposition technique. PLD has many unique characteristics that make it extremely competitive for depositing complex oxide thin-films, including stoichiometric transfer, energetic species, ability to deposit in oxidizing atmospheres, and relatively cheap and simple experimental setups. This allowed for parametric studies of almost any oxide compound, which at the time was nearly impossible. As a result, the field of PLD expanded exponentially and received more and more attention, as highlighted in Figure 2–1. The highlighted publication in Figure 2–1 is the publication of the first superconducting thin film deposited by PLD [9]. Recent developments in the field of PLD include the deposition of carbon structures in the form of diamond-like carbon and graphene, multiferroics, semiconductors, insulators, metals, polymers, various oxides, and biological materials [8] [10] [11]. PLD has also contributed significantly to the rapidly expanding field of nanotechnology due to the inherently small scale of the thin film growth process.

Nanostructured films are readily grown using PLD and subsequently examined to see how the nanostructure of a material affects its bulk properties as well as its properties at the nanoscale.

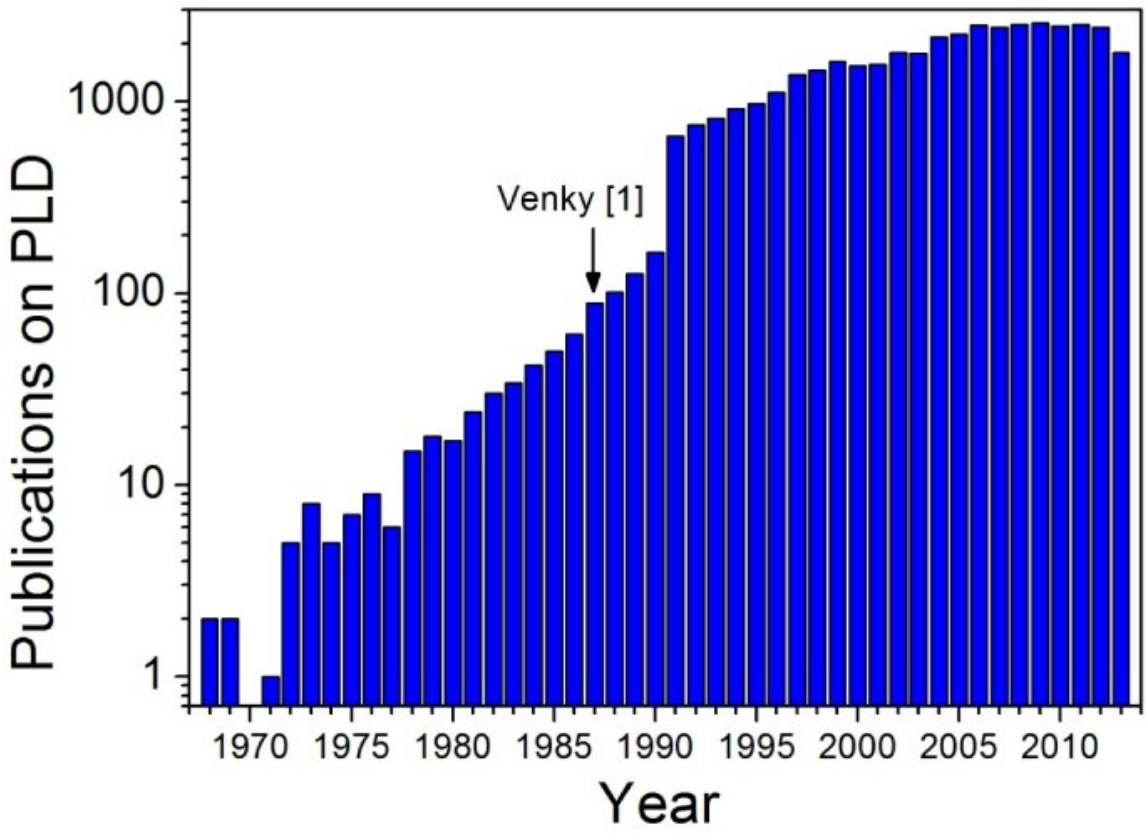

Figure 2–1: Items published by year with PLD as the title or topic – data from Thomson Reuters Web of Knowledge in September 2013 (reproduced with caption from [12])

2.1.2 Basic PLD Process

Pulsed laser deposition is a physical vapor deposition technique that uses a high powered laser as an energy source to vaporize a solid target and to deposit the material as a thin film within a vacuum chamber. PLD can be described as a three-step process, which includes (i) vaporization or ablation of a target material, (ii) transport of the ablated species, (iii) and film growth on a particular substrate material. PLD uses single

and multi-element target materials to deposit high quality thin films and heterostructures, from simple multilayered materials to more complex superlattices. This technique is able to preserve the stoichiometry of the target when depositing thin films, which makes PLD very useful for depositing thin films of complex stoichiometry materials and is one of the defining advantages of PLD. In addition, since there are no active electrical components inside of the vacuum chamber, deposition can occur in any type of reactive or nonreactive ambient atmosphere. In particular, creating oxide thin films by depositing materials in an oxygen atmosphere led to huge breakthroughs in high-temperature superconducting oxide materials during the 1980s and through today [9]. Other advantages include high instantaneous growth rates, huge flexibility in the range of possible target and substrate materials, and the ability to deposit a variety of structures, from amorphous to polycrystalline and even epitaxial, in the micro- and nano- scale [8]. PLD has the ability to deposit films with a higher degree of crystallinity at lower temperatures (even as low as room temperature) compared to other deposition techniques [13]. This thin film deposition technique is conceptually and experimentally simple, which makes it attractive for many different types of research groups. A schematic of the PLD process is outlined below in Figure 2–2.

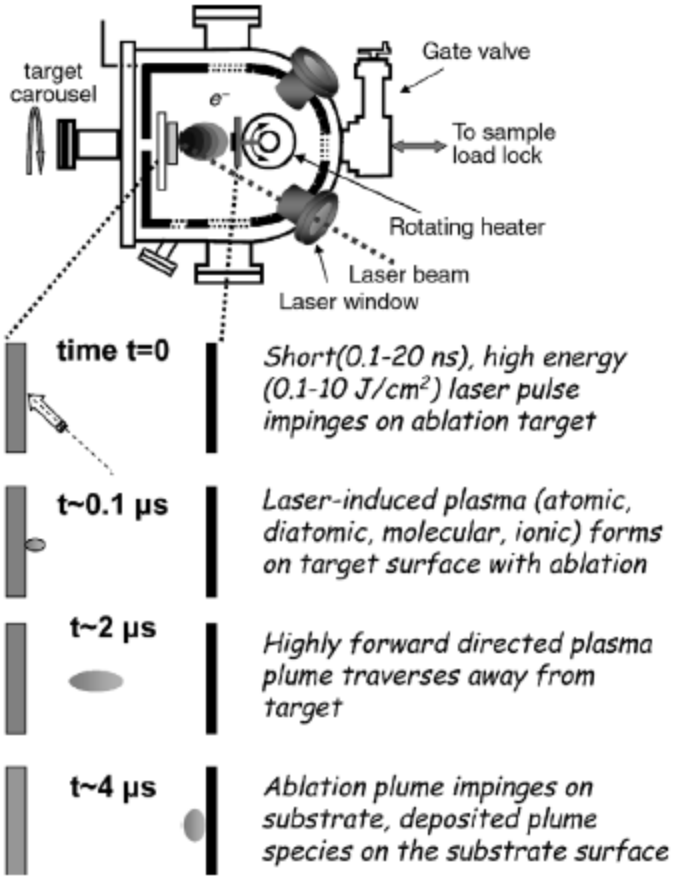

Figure 2–2: Schematic of the PLD process (reproduced with caption from [11])

2.1.3 Laser-Target Interaction and Formation of Plasma Plume

Despite the relative simplicity of the PLD process, the laser-target interaction is a very complex physical phenomenon that involves several mechanisms. Formulating a complete model to accurately describe the effects of laser ablation of a solid material has been sought after since the very first laser ablation experiment, and it has since resulted in many theories and models. For example, for low laser fluence and/or low absorption of the laser wavelength by the target material, the laser pulses simply heat the target and the ejected material is due to thermal evaporation. In this regime, a multicomponent target would eject species as determined by the vapor pressure of the constituents, and

deposition would follow a simple thermal process [11]. However, for a sufficiently high laser energy density, the ablation threshold is met and a plasma plume is formed at the target surface. The ablated material is ejected from the target surface in a highly forward directed plasma plume with energy well above thermal energy ($kT >> 1$ eV) [14]. The deposition of the ejected material onto the substrate is symmetric with respect to the target surface normal, and can be described by a $cos^n(\theta)$ distribution, where n can vary from as low as $n = 4$ up to $n = 30$. This uneven distribution can be improved by rotating the target and/or substrate, or by rastering the laser beam over the target [11].

During laser ablation, the temperature of the plasma rises extremely rapidly, on the scale of 10^{11} Kelvin per second [15]. This can result in non-equilibrium laser-induced ablation that is not dependent on the individual vapor pressures of the target constituents [11]. The outcome is a stoichiometric transfer of material from the target to the substrate. The ablation conditions are typically chosen to optimize the type of film that is desired. For example, for epitaxial films, the ablation plume should consist primarily of single atoms or ions, as well as other small species with low mass. This is done using an ultraviolet (UV) laser with a nanosecond scale pulse width. Shorter wavelengths (higher photon energy) typically have lower optical penetration depths, which are strongly absorbed by a small volume of the target material. This high level of energy absorbed per unit of the target volume leads to higher energy species in the ablated plasma plume [16]. In addition, when the plume species start to absorb laser radiation, the plasma temperature is elevated, leading to more energetic evaporants. For the deposition of non-film structures, such as nanoparticles or polymer chains, laser absorption is typically over a larger area on the target with little absorption by the plasma plume in order to preserve

the larger species being ablated from the target surface [11]. This can be done with visible or infrared (IR) lasers due to the lower photon energy.

As the laser beam hits the target, a molten layer is formed at the surface from absorbed photons. This high density gas layer is known as the Knudsen layer (KL). A schematic of the gas-kinetic and flow velocities of ablated species in the KL is shown in Figure 2–3. The particles enter free flight after leaving the KL, during which the velocities persist unchanged via unsteady adiabatic expansion (UAE). Once the Knudsen layer is formed, subsequent laser beam pulses exert a recoil pressure on the liquid layer due to the short time scale and large mass transport. This leads to the expulsion of molten droplets [8]. Particulates may also be formed as a result of surface roughening of the target from continuous laser irradiation. Microscopic irregularities that are formed at the surface can dislodge due to laser-induced thermal and mechanical shock waves. These particulates are ejected from the target surface as molten globules, typically up to several micrometers in size, which deposit on the substrate [13].

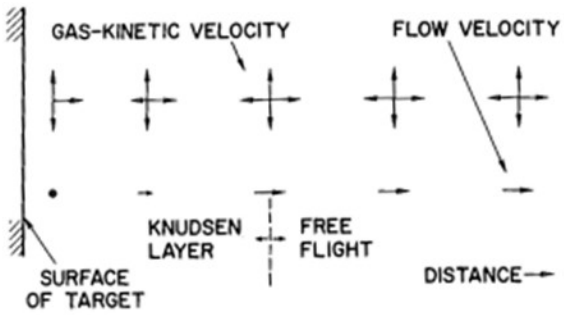

Figure 2–3: Schematic representation of KL followed by free flight (reproduced with caption from [8])

The ablation aspect of the PLD process typically consists of both primary and secondary mechanisms. The primary mechanisms, which are generally well-known processes, include thermal sputtering, electronic sputtering, exfoliational sputtering, and

hydrodynamic sputtering. Collisional sputtering, which is the principle mechanism in ion sputtering techniques, does not occur with laser ablation due to the negligible energy transfer of photons. However, indirect collisional effects do occur from complex laser-plasma interactions [8]. Thermal sputtering is simply vaporization of target material due to transient heating. Electronic sputtering arises from dense electron excitation, which occurs for large laser-pulse energies. This increases the total energy of each atom, leading to a large increase in the vapor pressure and possibly even rendering the lattice unbound. This "rapid energy deposition" model concludes that the system transitions from a tightly bound solid to a densely-packed repulsive gas that expels particles energetically. Exfoliational sputtering is when flakes from the target are detached as a result of repeated thermal shocks caused from the laser beam. These flakes can range in size from a few nanometers to several microns large. This is most common in materials with high linear thermal expansions, high melting points and high Young's modulus. The successive thermal shocks lead to cracking if not relieved by melting of the surface and subsurface. Hydrodynamic sputtering is when droplets of material form from transient melting and are expelled from the target. This type of sputtering is most common in metals, but also appears on other materials such as certain polymers [8].

The secondary mechanisms of laser ablation are based on unsteady adiabatic expansion (UAE) of the plume particles and include various types of pulsed flow processes. These mechanisms are modeled based on how the plume particles interact with the target surface and with each other. Figure 2–4 shows the different types of unsteady adiabatic expansion. The first possibility is known as "outflow," which is the same UAE that occurs when firing a gun (Figure 2–4a). This is based on a removable

wall containing a finite reservoir and a semi-infinite tube for expansion. In physical terms, this occurs when a laser pulse causes a rapid vaporization of the target into a gas-like condition. There are two types of outflow, stemming from particles that can be reflected or absorbed by the target surface when backscattered. The second possibility is known as "effusion," where gas in a semi-infinite reservoir effuses into a vacuum through a porous wall that is resealable. This describes a Knudsen layer coupled to an UAE. This possibility also has two types, reflected (Figure 2–4b) or absorbed (Figure 2–4c), depending on the behavior of the backscattered particles. These mechanisms have been solved graphically and numerically.

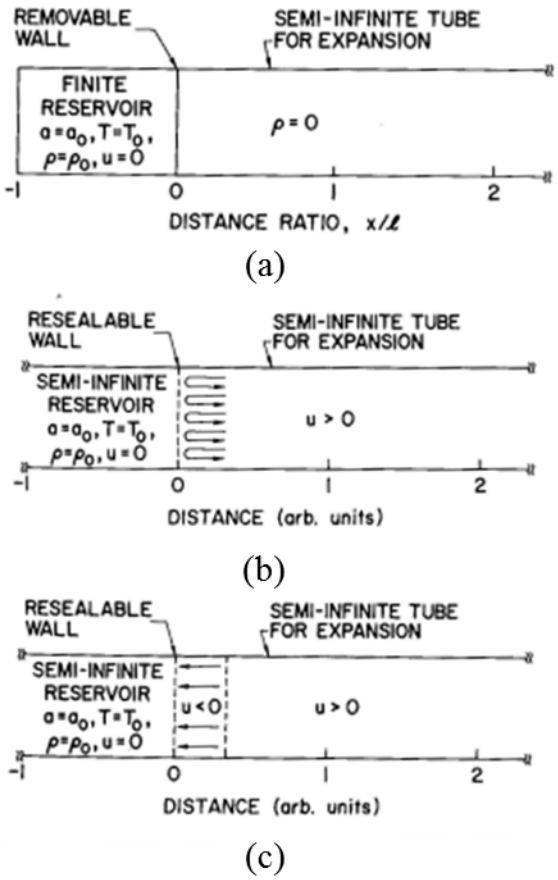

Figure 2–4: The different types of UAE (reproduced with caption from [8])

From the different models of laser ablation, it was determined that up to three types of absorptions must be taken into account during the laser-target interaction. These include the volume absorption by the electrons and phonons in the lattice, the free carrier absorption at the surface, and the absorption by the plasma plume [8]. The type of absorption that occurs depends on the material properties of the target as well as the laser beam characteristics. For example, metals absorb almost entirely at the surface from free carriers, while dielectric absorption takes place in the lattice and semiconductors exhibit a mixed type of absorption. Furthermore, the wavelength of the laser affects the type of absorption that takes place during the laser-target interaction. Infrared and visible lasers tend to involve the conversion of photon energy into thermal energy. For ultraviolet lasers, photoelectric excitation becomes significant, and both thermal and photoelectric effects contribute to the laser ablation phenomenon [17]. To have efficient ablation of a given target material, nonequilibrium excitation of the laser-irradiated target surface must occur, and temperatures much higher than those required for evaporation must be attained [11]. In addition, the laser-plasma interaction can influence the overall growth process. When using longer wavelength lasers, the laser-plasma interaction tends to be more severe, leading to a reduction in the growth rate of the films due to higher plasma coefficients at longer wavelengths [18]. Furthermore, the kinetic energy of the ablated particles can be increased when there is a larger laser-plume interaction [14].

The three step process that defines PLD is contingent upon the fact that each successive laser pulse hits a smooth surface on the target. However, in practice each laser pulse removes material, and rarely in a clean, orderly fashion. As a result, the surface modification of a solid target via repeated laser irradiation must be examined.

Target surface morphology can take the form of periodic structures such as ripples, ridges and cones. These patterns are known as laser-induced periodic surface structures (LIPSS). The composition of compound materials is also affected by laser pulses, often leading to a surface that is different than the bulk target composition. The process of material removal via laser irradiation has been studied extensively, and the resulting points are important for the analysis of surface modification: as the laser fluence increases, the temperature and melt depth of the target also increase; thermal pulses penetrate deeper into solids with high thermal conductivities and low absorption coefficients; shorter pulse lengths produce higher melting and solidification velocities. The basic thermal cycle that occurs for each laser pulse is shown in Figure 2–5.

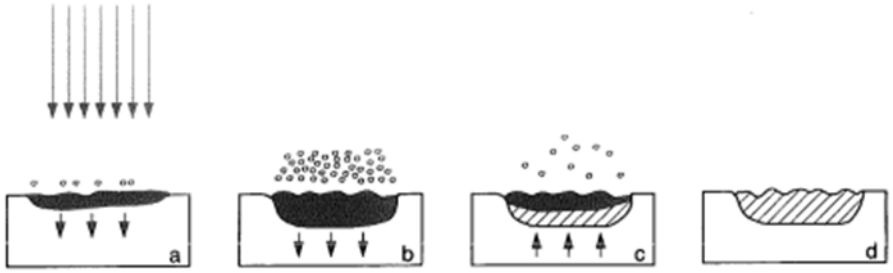

Figure 2–5: Schematic of the basic thermal cycle induced by a laser pulse. (a) Laser pulse is absorbed and the shaded area denotes melted material, (b) melt front propagates into the solid and vaporization occurs, (c) melt front recedes, leaving behind re-solidified material, and (d) solidification is completed (reproduced with caption from [8])

Laser cones are an interesting surface feature in which the cause is still up for debate. Laser cones grow in length as the laser exposure increases, and they always point in the direction of the incoming laser beam. This type of surface modification is theorized to be a result of vaporization resistant materials, either from impurities or from redeposited ablation debris. As a laser hits the target surface, cones can begin to form

from these areas that are resistant to laser vaporization. Laser irradiated surfaces of multi-component target materials typically have cones with tips that consist of a modified composition that is more resistant to vaporization, while further from the tip, the normal stoichiometry is preserved. Target material in the shadow of the impurity is protected, while surrounding material is ablated away. This can lead to a case in which laser vaporization is enhanced in the voids between cones due to light channeling of the laser beam via multiple grazing-incidence reflections from cone walls, where virgin target material can be ablated and stoichiometry can be preserved. However, this mechanism of cone formation is not the only explanation of laser-cone formation. Another theory claims hydrodynamical sputtering to be the cause of cone formation, while there also appears to be exceptions to the formation of cone growth at a laser irradiated surface. No comprehensive model of cone formation currently exists that fully describes the complex process [8]. Figure 2–6 shows a schematic of laser cone formation on a target surface.

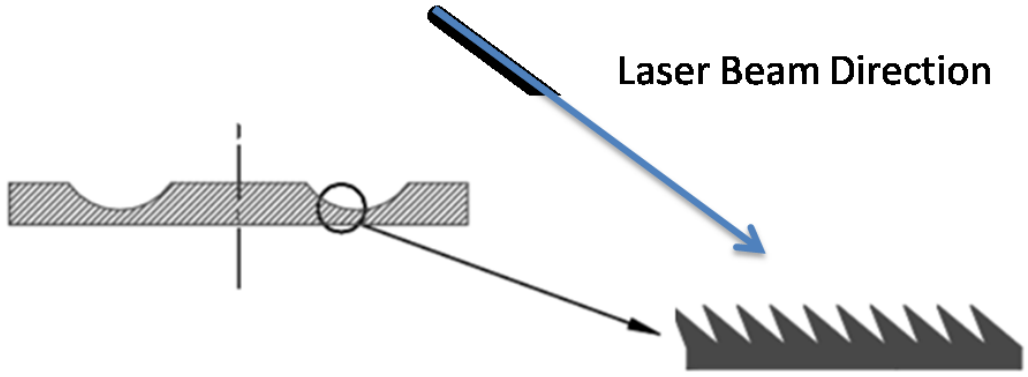

Figure 2–6: Figure of laser cone formation on a target surface without proper laser or mechanical rastering (reproduced from [11])

There are higher order phenomena in PLD that complicate the simple "three-step process" described previously. Surface segregation, for example, is the preferential

enrichment of one or more components of a complex material at surface or grain boundaries. This is one explanation for cone formation in multi-component targets, but can also occur even when cone formation is not observed. This phenomenon, along with others such as incongruent redeposition and angular variation of plume stoichiometry, complicates the simple three step process that describes PLD. The melting and resolidification of target materials determines the amount of surface segregation in a given material. Over the course of thousands of thermal cycles of laser impingement on a target surface, the constituents can migrate based on differing melting temperatures. For instance, when a material, which has been melted as a result of laser irradiation, starts to resolidify, higher melting temperature components of the liquid will freeze first, forcing the other materials towards the surface. Over the course of many cycles, these lower melting temperature components will segregate towards the surface and either resist laser vaporization and create cones, or be ablated away, leaving behind a surface that is a different stoichiometry than the original target stoichiometry. Despite these surface modifications, plume expansion remains perpendicular to the target normal surface, even though the exact motion of the vapor through the modified surface may not be obvious [8].

Laser induced surface modification and the presence of LIPSS increases the area of the exposed surface, leading to a decrease in the average laser fluence on the target. The coupling of the laser beam to the target is only negligibly affected due to surface modification, generally increasing slightly with the formation of cones on the surface, most likely due to light trapping as discussed previously [8]. Furthermore, the laser beam can be attenuated by window deposits of the ablated material on the laser entrance

window, which can reduce the total energy impingent on the target surface and thus, reduce the ablation effectiveness.

The ability to use a background gas during PLD is another key advantage of the technique. It helped lead to the resurgence of PLD in the late 1980s when high temperature superconducting YBCO was grown in an oxygen ambient gas. Using background gases during PLD causes collisional scattering and a reduction of energy of the ablated species. The background gas can reduce the kinetic energy of the ablated species to much less than one electron volt, which is several orders of magnitude lower than what these energies can achieve without the use of a background gas. It also scatters, attenuates and thermalizes the vapor plume [11]. In general, when increasing the ambient pressure, several outcomes can be expected. These include an increase in fluorescence, a sharpening of the boundary of the plume, a decrease in the speed of the plume and spatial confinement of the plume. The increase in fluorescence of the species is due to increased collisions that occur within the plume and at the expansion front. The sharpening of the plasma plume boundary indicates the formation of a contact front at the leading edge of plume expansion, which can be modeled as a shock front.

2.1.4 Characterization of Laser Produced Plasmas

Many techniques have been explored to characterize laser-induced plasmas that are formed during PLD. These techniques include mass spectroscopy, ion probes, optical spectroscopy, and laser-induced fluorescence. From these different methods, a better understanding of what typically occurs in the fast flowing laser plasma has been developed. Using time-resolved spectroscopy of the ablation plume expansion, it was shown that the kinetic energies of the species can be on the order of several hundred

electron volts [19]. Mass spectroscopy studies [8] identify several features of the laser plasma, including non-Maxwellian velocity distribution of ejected species, ions traveling faster than neutrals [14], threshold fluence where ablation does not occur below, nonlinear dependence of ablation yield on laser fluence, and variations between yields of different species with laser wavelength. From time-of-flight mass spectroscopy (TOFMS), it has been shown that the kinetic energy distribution of ablated species lack a low-velocity (thermal) component, which indicates a non-thermal mechanism for material ablation [8]. Laser-induced fluorescence is useful for determining the local rotational and vibrational temperatures of molecules in the plasma plume [20]. From the different temperatures that can be measured (translational, rotational, vibrational), information about the ablation mechanism can be inferred. For example, molecules with lower rotational and vibrational temperatures, but higher translational temperatures, do not follow a thermal sputtering mechanism. Instead, this implies an electronic mechanism of material removal.

Various diagnostic techniques have been used to analyze the plasma plume in the presence of a background gas. It was determined that the plume interacts hydrodynamically with the background gas, forming a fast moving shock front and a slower moving bulk of the plume [8]. In normal PLD under vacuum, the leading edge of the plasma remains at a constant velocity on the order of centimeters per microsecond. However, in a background gas, the ablation plume expansion slows progressively after about the first microsecond. There are two different models to characterize this slowing of the plume: the shock model and the drag model. The shock model was developed to describe the propagation of a shock wave caused by the sudden release of energy (i.e. an

explosion) through a background gas. This model tends to overestimate the plume front at lower pressures and earlier times. But as the time from the initial laser pulse increases, the model becomes more accurate. Furthermore, this model becomes increasingly accurate as the background pressure increases. The drag model is a classic drag-force model that shows better agreement with experimental values at low background pressure and early times. This model takes into account a viscous force between the ensemble of particles in the plume and the background gas that is proportional to the velocity of the particles. The drag model predicts that the plume will eventually come to rest as a result of the collisions with the background gas. On the other hand, the shock model, which neglects viscosity, predicts a continued propagation of the plume into the background gas. The experimental PLD plumes that have been observed display characteristics of both of these models. Thus, the plume is best described as a combination of these models, with the drag model dominating initially after the laser pulse, and then transitioning into the shock model once the viscous forces become negligible and a stable shock structure forms [8]. The plasma plume comparison is shown in Figure 2–7.

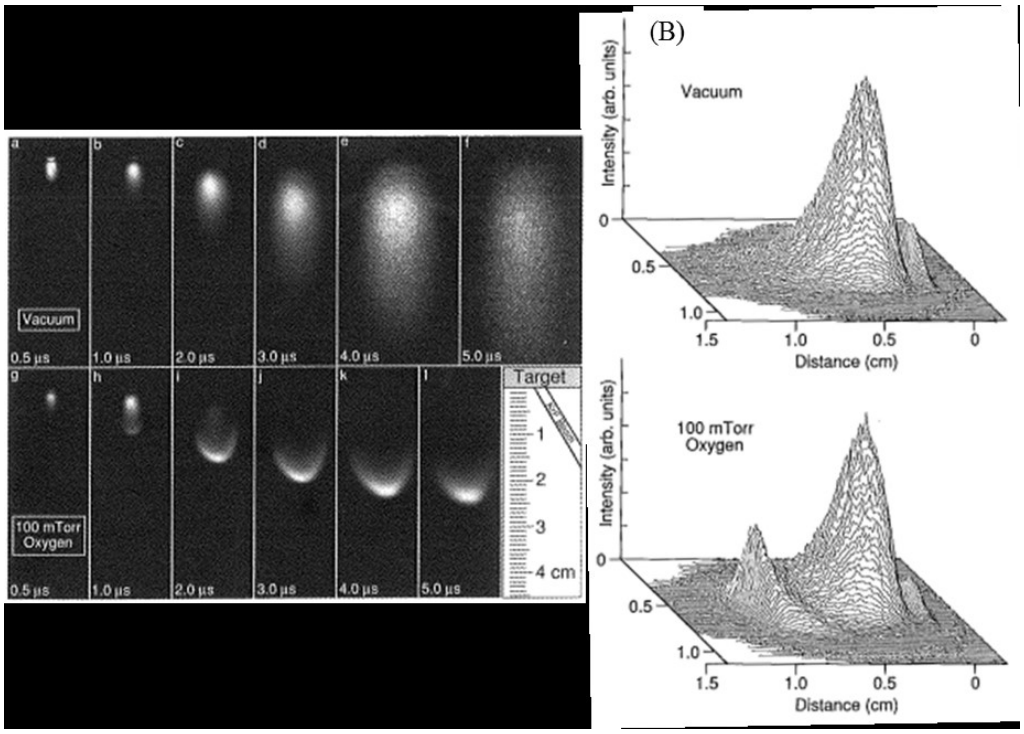

Figure 2–7: Comparison of plasma plume generated in vacuum and background gas; (A) ICCD photographs of the visible plasma emission, and (B) visible plasma emission intensity illustrating the formation of an expansion front due to background gas collisions (reproduced with caption from [8])

2.1.5 Film Growth Processes

For very high plasma temperatures, the ejected material is expected to be highly energetic. This can have a significant impact on the film deposition, both positively and negatively. The downside to this is the possibility of further penetration depth of the evaporants into the substrate material. While there are some applications where this is beneficial, it is mostly detrimental to film growth. On the other hand, if the evaporants have more energy, this means the adatom surface mobility will also be enhanced, leading to more order in the film growth and higher crystallization [8]. Figure 2–8 shows how energetic species can be detrimental to film growth due to plume-induced stress in the PLD films.

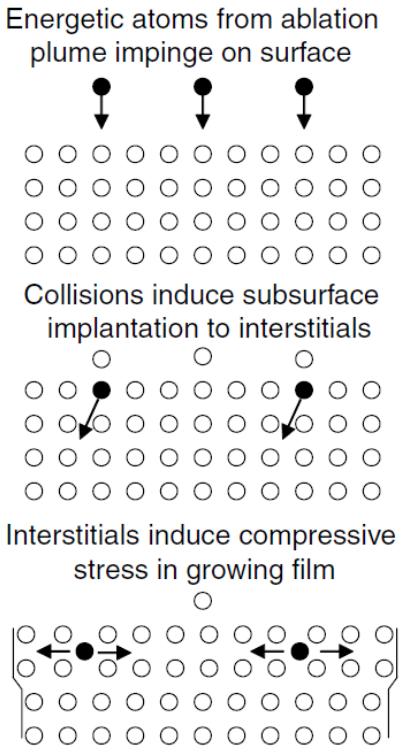

Figure 2–8: Schematic of plume-induced stress in PLD-deposited films (reproduced with caption from [11])

Once the ablation threshold of a material is reached, it is generally best to stay near this threshold. By increasing the laser fluence much higher than the ablation threshold, many issues arise that are detrimental to film growth. Higher laser fluence values generally lead to more particulates in the deposited film. For example, splashing is an effect caused when molten droplets, typically in the micron size range, are expelled from the target. These droplets deposit on the film, leaving large discontinuities and defects in the film. In general, keeping the laser fluence to a minimum reduces the number of particulates being ejected from the target surface. However, if the laser is below the ablation threshold of a material, no measurable etch pit is produced, even with repeated laser irradiation. Only very small quantities of neutral and ionized species are detected in this case, and film deposition is minimal or completely suppressed.

When using a background gas during PLD, certain parameters are affected that can be crucial to film growth, such as the spatial distribution and kinetic energy of the ablated material, as well as the overall deposition rate. The presence of a background gas can also cause reactive scattering, which results in the formation of molecules or clusters during transfer to the substrate via gas-phase condensation. This is a crucial feature for incorporating the ambient gas into the growing film (such as oxides), but it can also be detrimental to growth due to larger clusters interfering with uniform film growth, similar to the problems posed by particulates [11].

Laser induced surface modification and the presence of LIPSS can lead to several detrimental factors for film growth. For example, surface segregation, as previously discussed, is a surface modification that can lead to non-stoichiometric film deposition. Furthermore, film deposition rates are affected by surface modification of the target. As the number of shots for any given site increases, the film deposition rate and plume size typically decrease. This is due to a reduction in the amount of material being ablated by each laser pulse. This trend continues until cones have been completely formed on the target surface, at which time the deposition rate reaches a minimum [8]. Overall, the major effect of laser induced surface modification in PLD is cratering of the target surface and reduction of the deposition rate, which is not generally a huge problem for lab scale work, but can be a potential bottleneck for industrial scale-up of PLD.

2.1.6 The Future of PLD

Since the invention of PLD, it was always viewed as more of a research tool than a large-scale industrial method for mass production of thin films. Typical samples grown via PLD are on the scale of square centimeters, not square meters. However, there has

been extensive research and development geared towards making PLD a scalable technique. After the resurgence of PLD in 1987 by the deposition of a high-temperature superconductor, the growth process was analyzed to determine if large-scale production was possible. There were many obstacles that had to be overcome to realize this possibility, resulting in innovations that pushed the commercialization of PLD forward. These included laser beam scanning on the target, larger-diameter targets, substrate heaters with rotation capabilities, smart windows for keeping the laser beam path clean, in situ diagnostics, and many others [21]. Despite the lack of interest in commercial PLD systems early on, the first large-area PLD system was built in 1988 at the Research Division of Raytheon. While most researchers were focused on making very high quality small samples, on the order of 1 cm^2, the chamber built by Raytheon was growing films as large as 200 mm in diameter. This began a niche group of researchers who firmly believed that PLD was a scalable process regardless of what the majority of the PLD community believed. To date, PLD systems have been designed and built by several different companies that are capable of multi-layer and epitaxial film growth of very high quality films at wafer sizes ranging up to 300 mm diameters and deposition rates of several microns per hour. Most recently, a roll-to-roll process has been developed that has an effective surface area of 10 square meters in one run, which is typically 5-10 hours, as shown in Figure 2–9. The market for PLD products is continually expanding and demand is rising for these systems as applications expand into areas such as flexible substrates, solar cells, batteries, and so on [21].

Figure 2–9: Commercial reel-to-reel PLD tool capable of depositing films over 1 cm wide by 1 km long with a total effective area of 10 m^2 (reproduced with caption from [21])

2.2 Graphene

2.2.1 Carbon and the Emergence of Graphene

Carbon has been an important part of the world since long before humans came into existence. The capability of carbon atoms to form complicated networks and chains is fundamental to organic chemistry and is the basis for life as we know it. Throughout the universe, carbon plays a crucial role in creating the heavy elements via fusion in stars. Carbon was first known by the earliest of human civilizations in the form of soot and charcoal, and much later in the form of diamonds. This basic building block has several different forms, with widely varying properties and applications. The most recent discovery in carbon materials is the two-dimensional form, graphene, which was thought to be physically unstable, until recently [22].

Graphene is a two-dimensional honeycomb array of sp^2 bonded carbon atoms. It consists of a single layer of graphite, making it the first two-dimensional material created. Graphene is the building block of several of the allotropes of carbon, as shown in Figure

2–10. The fullerene, first discovered by Smalley et al. in 1985 [23], is a sheet of graphene consisting of 60 or more carbon atoms that are curled up into a ball, known as a "zero-dimensional" structure. Carbon nanotubes (CNTs), first discovered by Iijima et al. in 1991 [24], are sheets of graphene rolled up into a one-dimensional cylinder, with properties that depend on how the graphene sheet is rolled up, known as the chirality. Bulk graphite consists of graphene layers stacked on top of one another, either in a specific stacking order, or randomly stacked together. Each carbon atom within the planar hexagonal structure is covalently bonded to its surrounding three carbon atoms, while the bonding between layers consists of weaker van der Waals bonds. This atomically thin material is a zero band gap semiconductor with many unique properties. For example, the electrical properties of graphene include an exceptional mobility [1], massless Dirac fermions, room temperature quantum hall effect [2], unique band structure and ambi-polar electric field effect [3]. In addition, graphene also displays interesting chemical, mechanical, thermal, and optical properties [4] [22]. Extraordinarily high in-plane thermal conductivity and relatively low out-of-plane thermal conductivity highlights the versatility in the material properties of graphene. The extraordinary properties of graphene have ushered in a new age of materials research in low-dimensional nanomaterials, paving the way for countless functionalities and applications of graphene and graphene-based devices.

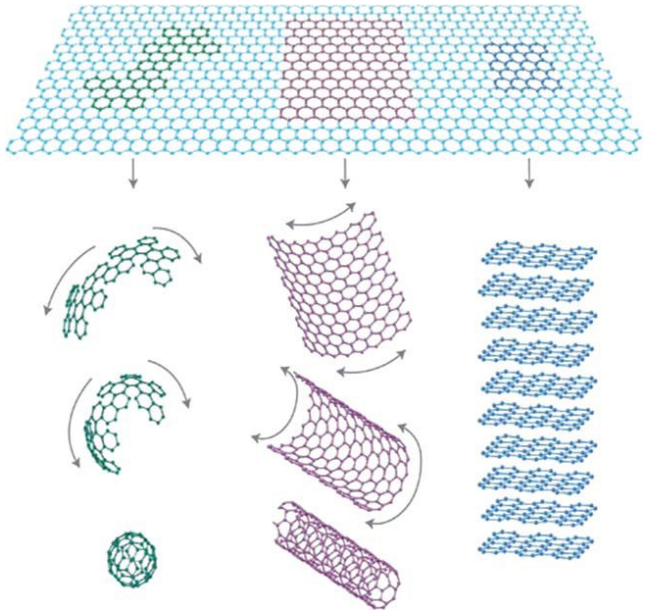

Figure 2–10: Graphene and corresponding allotropes of carbon(reproduced with caption from [3])

2.2.2 Graphene Applications

Graphene has emerged as one of the most functional materials of this time, with potential applications spanning a wide variety of fields. For example, the intrinsic carrier mobility of graphene (upwards of 200,000 cm^2/Vs [25]) is much larger than any other material, leading to potential micro- and nano-electronics applications such as high speed transistors, field-effect transistors (FETs) [26], superconductors and integrated circuits [22] [27]. The robustness of graphene allows the potential for patterning with atomic precision down to the molecular level, using standard lithographic or chemical methods. This could lead to graphene-based electronics on a smaller size scale than silicon-based electronics [28]. The long spin diffusion length of graphene (in the 100 micron range [27]) shows potential for spintronics applications. There are also many energy applications for graphene, including energy conversion (fuel cells and solar cells) and

energy storage (batteries and supercapacitors). The unique thermal properties of graphene are thought to be highly tunable, which raises interesting prospects of using graphene in both heat sink applications and thermoelectric applications. In addition, graphene exhibits novel nonlinear optical properties with high laser damage threshold energy and broad absorption bands from the ultraviolet to the near-infrared, making it desirable for several optical components. Graphene is also a biocompatible material that could interface with organic material for different applications involving bio-sensing and bio-imaging. Gas sensing can be achieved using graphene by monitoring the absorption of different gases present in the environment and the resulting changes in the resistivity of graphene [22]. Different applications of graphene often require different specifications for the materials. For example, applications in electronics require extremely high quality graphene with minimal defects and large sizes, yet optical applications require the highest purity and crystallization to reduce scattering [27]. These properties depend heavily on the morphology and atomic structure of graphene films, which has led to several methods for graphene fabrication, each with its own strengths and weaknesses.

2.2.3 Fabrication Techniques of Graphene

There are several methods that can be used to fabricate graphene. Mechanical exfoliation was the method used to first isolate graphene in 2004 by Novoselov and Geim [1]. Also known as the “scotch tape” method, this top-down technique can yield micron-sized lateral dimensions of graphene with high electrical and structural quality. However, this method is labor intensive, limited to laboratory scale production, and not a feasible technique to scale up to wafer size [2]. In addition, the samples can be contaminated by residues from the tape, which require high temperature processing to remove, leading to

higher production costs [4]. These disadvantages have led to the development of new techniques for producing high quality, high quantity graphene for both research and commercial uses. One such technique is the epitaxial growth of graphene on silicon carbide (SiC). Thermal treatment of single crystal 6H-SiC wafers is used to sublimate the silicon atoms while the remaining carbon atoms undergo graphitization and form aromatic bonds on the surface of the wafer. This surface decomposition method utilizes high operating temperatures (1000-1600°C) and ultra high vacuum conditions (10^{-9} Torr), but offers the potential for large scale graphene production [26] [29] [30]. However, there is a large lattice mismatch between the underlying SiC substrate and the epitaxial graphene, as well as significant difficulty in removing the graphene from the chemically stable SiC, increasing the cost and requiring the transfer of the graphene film onto an appropriate substrate.

Catalytic growth of graphene on metals is another approach to graphene growth, where carbon sources are directed onto metals such as ruthenium [31], platinum [32], and nickel [33] [34] to form very uniform layers of graphene. The growth of graphene layers on metal surfaces can be divided into two different methods. The first method involves segregation of bulk-dissolved carbon to a metal surface. The carbon is present via impurities, or the samples are doped with carbon. High temperature annealing then causes segregation of the carbon atoms to the surface of the metal. On the other hand, the second method involves surface decomposition of carbon-containing molecules. This occurs when carbon-containing molecules (i.e. ethylene, propene, methane, etc.) are adsorbed onto a metal surface, then annealing decomposes the molecules to desorb the

hydrogen [30]. These two methods of graphene growth on metal substrates are achieved using various methods.

Chemical vapor deposition (CVD) is one technique that utilizes surface decomposition to make high quality graphene on nickel [33] [34] and copper [35], but is restricted by the substrate material and the number of layers that can be grown. CVD typically uses high operating temperatures (e.g. 1000°C) and a precursor gas such as methane to supply the carbon species. Graphene is grown on copper via a surface catalysis process, while on nickel substrates, it grows via a precipitation process. As a result, when using CVD to grow graphene on copper, the process is self-limiting, since the chemical reaction is suppressed once the surface of the copper is covered by carbon. This process gives good control of the number of layers being grown on copper, typically with more than 95% of the surface being a monolayer of graphene. The very low carbon solubility in copper and the poor carbon saturation prevents the precipitation process, leading to the self-limiting nature of graphene growth on copper via CVD [35]. The precipitation growth process of graphene on nickel involves carbon atoms dissolving into the nickel bulk. Upon cooling, the carbon atoms precipitate out and segregate on the surface to form multiple layers of graphene. When using a single crystal nickel surface, CVD preferentially grows thinner, more uniform few-layer graphene. When using a polycrystalline nickel surface, the grain boundaries serve as graphene nucleation sites, leading to multilayer graphene growth [36].

Graphene can also be produced by a solution-based process [37]. This method starts with graphite that is oxidized to create graphite oxide (GO). The GO is exfoliated to create a stable aqueous dispersion of individual sheets. These sheets of GO can then

be reduced to graphene chemically or by thermal annealing [37]. In addition, graphene-based composite materials are produced via chemical exfoliation of GO sheets, which are created through the oxidation of graphite powders in a solution, followed by several post processing steps [38]. Solution-based processing of GO is a low cost, high throughput technique that is scalable and has sufficient chemical versatility. However, the quality of the graphene produced from GO and CVD is typically not as good as the mechanically exfoliated graphene [27]. In addition, these techniques do not offer much variability in their growth of graphene. This makes PLD a unique growth method for exploring exactly how graphene is made from the nanoscale and how we can tailor its properties based on different growth parameters.

2.2.4 Review of Graphene Growth via PLD

Using PLD to grow graphene has several advantages and disadvantages, and has been performed since graphene was discovered in 2004. One of the first instances of graphene growth via PLD was by Cappelli et al. in 2004 [39]. The paper describes a structural evolution of the carbon films based on the growth temperature of the silicon substrate. At room temperature, the films consist of smooth, amorphous carbon. At 900°C, the films consist of granular, graphitic nanoparticles [39]. Additional work further describes the different parameters that affect the growth of graphene via PLD. Several studies confirm the transition from amorphous carbon to a more ordered, aromatic film of nanostructured graphite and graphene domains as the temperature of the substrate increases. This can be attributed to the increase in mobility of the carbon species on the substrate, allowing for the more stable sp^2 bonds to form [40] [41] [42] [43] [44] [45]. Increasing the temperature beyond 900°C causes a solid state reaction between

the carbon atoms and the silicon substrate at the interface. This formation of SiC prevents any growth of graphene on silicon at higher temperatures [45].

The type of atmosphere present during deposition is also critical to film growth. Typically, PLD of graphene is done in high vacuum ($< 10^{-5}$ torr), with increasing vacuum reducing the amount of impurities in the system. However, using a helium atmosphere during deposition has been studied and shown to cause gas phase condensation of the plume particles. As a result, the grown films include macroscopic particulates and show higher surface roughness [40]. The use of any background gas is known to affect both the shape and the velocity of the ablation plume, ionizing the gas via charge transfer collisions with fast ions in the ablation plume. This slows down the plume propagation and reduces the energy of the plume particles, which in turn affects the film growth [46]. While the particulates produced in an ambient gas are sp^2 hybridized [46], they can be detrimental to the films and will greatly increase the surface roughness.

The laser parameters used for ablation has also been studied extensively to determine how it affects film growth. When using an excimer laser (193-248 nm), the ablation of graphite is known to produce activated carbon monomers and dimers (C_1^+, C_1^*, C_2^+, C_3) due to the high energy of the incident photons (5-6.4 eV) [44]. This high energy ablation causes photoelectric excitation [45]. For a 532 nm laser (photon energy of 2.33 eV), the carbon species being ejected from a graphite target are typically smaller excited carbon molecules (C_3, C_5, and C_7). For longer wavelengths approaching the infrared range, the laser energy is lower (1064 nm = 1.17 eV). The resulting carbon species ejected from the target consist mainly of long, single ionized chains, typically C_n^+ (where $n \geq$ 3-24), and neutral C_2 and C_3 molecules with low kinetic energy and low

fragmentation of the plasma plume. This lower energy ablation typically involves the conversion of multiphoton energy into thermal energy, with no photoelectric excitation [45]. This leads to films with large voids and large inter-planar spacing. As the laser energy increases, the size of the carbon fragments decreases due to enhanced photo-fragmentation effects [43]. The orientation of the graphene clusters in this early work is normal to the substrate surface [40] [41] [42] [43] [44] [45].

The energy fluence of the laser on the target surface used for ablation has also been studied. It was found that there is an optimal range of fluence for the ablation of carbon. The minimum laser fluence threshold for ablation to occur for a carbon target is around 0.8 J/cm^2 [47]. For fluence values near this threshold, films typically have a better ratio of sp^2 to sp^3 bonds, consistent with graphene-based materials [41]. When the fluence is much higher than the ablation threshold, the laser pulse is disruptive to the carbon and produces sub-optimal films with micron-size particulates. This higher threshold was found to be around 650 mJ/pulse [44]. These threshold values are dependent on the type of laser used, and unless otherwise specified, it is assumed that the laser used during ablation is a nanosecond laser. However, when using a femptosecond laser, which has a higher energy than a standard nanosecond laser, two different characteristic ablation thresholds are present. The first is a non-thermal ablation threshold, which is found to be 250 mJ/cm^2. The second is the thermal ablation threshold, which is at 450 mJ/cm^2 [48]. At this higher fluence threshold, amorphous carbon and small clusters and fragments of carbon are ablated from the target, and the films have broadened D and G bands and an absent 2D band, due to disorder in the film [48].

The substrate used to collect the ejected carbon particles is also important for the growth of carbon nanostructures. Typically, copper is used due to the small mismatch in lattice constant between copper and graphene, but PLD is able to grow graphene on several different substrates (see Table 2-1). However, other substrates can be used for various reasons. For instance, nickel substrates are used for a different type of graphene growth that involves precipitation of carbon atoms through the nickel substrate. Laser ablation is used to create and embed carbon atoms into the nickel bulk, which is typically at high temperatures, upwards of 1300°C [49]. The laser energy affects the penetration depth of carbon atoms onto the substrate, which affects the overall precipitation process. As the laser energy increases, the carbon atoms that are ablated are more energetic, leading to deeper penetration of the carbon species into the nickel bulk. At lower laser energies, the carbon species are deposited closer to the surface of the nickel. As the carbon-saturated nickel material cools, the carbon atoms precipitate as graphene layers onto the surface of the nickel [50].

Table 2-1: Lattice constants of various materials, including graphene

Material	Lattice Constant (nm)
Graphite	0.335
Graphene	0.357
Nickel	0.352
Copper	0.361
Cobalt	0.251
Iron	0.287
Silicon	0.5431
Quartz	0.49138
Mica	0.5199

Graphene has also been grown on nickel substrates at lower temperatures using PLD. One group has grown graphene films on nickel substrates at 750°C, with the

cooling rate being a key factor for the resulting graphene films [50] [51]. If the cooling rate is too fast, the carbon that precipitates to the surface of the nickel does not have the mobility to fully crystallize, and the resulting film is more amorphous in nature. At lower substrate temperatures, the carbon atoms are still able to form graphene layers on the surface due to the intrinsic energy provided to the ablated species by the PLD process. Graphene films have been grown on nickel films by Wang *et al.* at temperatures as low as 650°C [52]. This group studied how the thickness of the nickel substrate affects the resulting graphene films. This was done by first growing a nickel film on a SiO_2 wafer, and then performing the graphene growth. It was found that the carbon embedded in the nickel can over-saturate, leading to the formation of multi-layer graphene on the nickel surface. In order to achieve a single layer of graphene, the deposition time was reduced, which led to incomplete coverage of carbon on the nickel surface. Alternatively, by varying the thickness of the nickel film, the number of layers of graphene could be controlled. Thus, the number of graphene layers relies on the thickness ratio of carbon to nickel [52].

2.3 Thermoelectric Materials

2.3.1 A History of Thermoelectricity

The thermoelectric effect describes the conversion of thermal energy into electrical energy, and conversely, using electricity for heat pumping or refrigeration. This term actually encompasses three different effects consisting of the Seebeck effect, the Peltier effect, and the Thomson effect. The Seebeck effect, which was discovered in 1821 by German physicist Thomas Seebeck, describes the conversion of temperature gradients directly into an electrical current. This is done through the formation of an

electric potential (ΔV) when a circuit is made of two different electrically conducting materials that is exposed to a temperature gradient (ΔT), and can be expressed as:

$$\Delta V = -\alpha \Delta T$$

where α is a proportionality constant known as the Seebeck coefficient [53]. The Seebeck effect is defined as the ratio of the potential drop to the temperature gradient applied, and it is responsible for how a modern thermocouple works. It is the basis for thermoelectric power generation, which has been used as a clean energy source. The Peltier effect, discovered in 1834, describes the heat absorption or heat release in a junction when an electrical current (I) is applied to a circuit [54]. This can be used to extract heat from different sources, such as micro-electronic components [55]. The Thomson effect, discovered in 1851, is observed when a temperature gradient and an electrical current are simultaneously present in an electrical circuit [54]. When a current passes through a material with a temperature gradient, the material exchanges heat with the environment. On the other hand, a current is generated when a heat flux passes through a material with a temperature gradient [55]. These three effects are used to fully describe how thermoelectric materials work.

The most important parameter for characterization of thermoelectric materials is the dimensionless figure of merit, ZT, expressed by:

$$ZT = \frac{\alpha^2 \sigma T}{K}$$

where α is the Seebeck coefficient, σ is the electrical conductivity, T is the absolute temperature, and K is the thermal conductivity. The thermal conductivity consists of the electron conductivity (K_e), related to the flow of charge carries, and the phonon conductivity (K_{ph}), related to the lattice contribution via phonons, and is expressed as:

$(K = K_e + K_{ph})$. The figure of merit is important because it determines the fraction of the Carnot efficiency that can be theoretically attained by a thermoelectric material [56]. As *ZT* approaches infinity, the efficiency of a heat engine will approach the Carnot limit [57]. The term $\alpha^2\sigma$ in the figure of merit equation is known as the power factor, and involves only electronic properties of a thermoelectric material. The power factor is useful for the characterization of thermoelectric materials [58], and is the key to achieving high performance in these materials. A large power factor indicates a large voltage and a high current are produced during power generation [56].

Early research in the field of thermoelectrics was little more than a novelty, and the thermoelectric figure of merit had only incremental gains, mostly due to the fact that the parameters in the equation are coupled. For example, increasing the electrical conductivity generally leads to a comparable increase in the thermal conductivity, resulting in insignificant improvements in ZT [59]. To maximize the figure of merit, a material must have an enhanced flow of electrons, such as in a metal, but a reduced flow of phonons, such as in a glass [57].

Since nearly 60% of the generated energy in the United States is lost as waste heat [60] [61], thermoelectric materials can have a huge capacity for reducing waste and increasing overall efficiencies of power generation systems. It wasn't until the 1950s that thermoelectric materials were considered for practical applications. At this time, the basic science of thermoelectrics became well established, thermoelectric generation became reasonably efficient, and thermoelectric refrigeration became viable. Abram Ioffe found that doped semiconductors had significantly better thermoelectric properties than any other material previously tested [62]. This discovery, in addition to the known

detrimental effects of chloro-flouro-carbons (CFCs) to the environment, began a research revolution in the field of thermoelectrics in an attempt to achieve thermoelectric refrigeration. This led to a variety of applications due to the advantages that thermoelectric systems could offer. These advantages include the absence of any harmful gases or byproducts, a compact design, the lack of any moving parts, low maintenance and quiet operation. However, from 1960 through the 1990s, the most efficient devices only had a figure of merit of about one. For the proposed solid-state refrigeration, a ZT value of at least three would have to be achieved to compete economically with compressor-based refrigerators [62]. As a result, thermoelectrics were only able to penetrate niche markets due to their high cost and low efficiencies. For example, thermoelectric power supplies were used by NASA for the Voyager missions in the 1970s, and radioisotope thermoelectric generators (RTGs) are the power supplies for all deep-space missions beyond Mars [53]. Smaller, self-powered systems, especially in remote environments, often use thermoelectric generation as power sources. More recently, climate controlled seats in luxury cars are beginning to use thermoelectric generators for heating and cooling car seats. Thermoelectrics can also use temperature differences within and around the body to power biological implants such as pacemakers, and for wearables like wrist watches [53]. Typically, thermoelectrics are used when reliability or convenience are more important than cost. Thermoelectric devices have applications as temperature sensors [58] [63], detectors [58], power generators [58] [63], electric power salvaging, refrigerators [62] [63] and Peltier-cooling microdevices [64] [65] [66]. Figure 2–11 shows the basic schematic for different thermoelectric devices. These modules are required to be connected electrically in series and thermally in parallel.

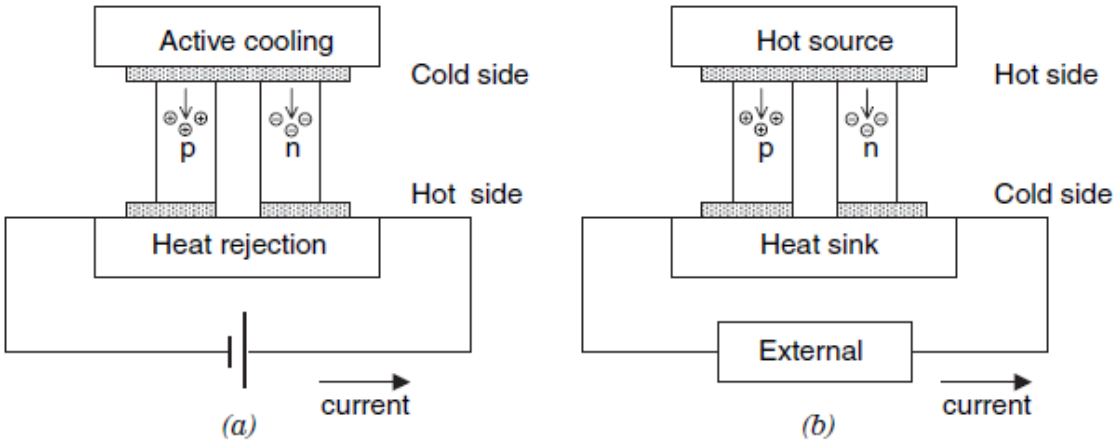

Figure 2–11: Schematic diagram of a single thermocouple device arranged for (a) refrigeration or (b) power generation (reproduced with caption from [11])

2.3.2 Next Generation Thermoelectric Materials

Recently, it has been shown that low dimensional thermoelectric materials can perform much better than bulk samples due to quantum confinement effects and increased phonon scattering at the grain boundaries in nanostructured materials. Nanostructured thermoelectric thin films have a lower thermal conductivity than bulk thermoelectric materials due to increased phonon scattering at grain boundaries and interfaces, which results in an increase in the figure of merit to values larger than those previously reported [67]. In addition, electrons are confined to two-dimensional structures, while phonons are not restricted, allowing for more phonon scattering and a lower phonon conductivity, which results in an increase of the figure of merit [59]. This has led to several improvements in thermoelectric efficiency and a resurgence of research in the field of thermoelectrics [6]. Environmental concerns have led to a particular emphasis on waste heat recovery for thermoelectric device applications. Due to the large amount of heat that is discarded in the generation of energy around the world,

thermoelectrics have been suggested to reclaim a significant portion of this energy and greatly improve the efficiency and output of energy generation plants. In addition, this principle can be applied to any system, large or small, that produces waste heat. This is becoming a much larger issue with the threat of global climate change and the greenhouse effect, as well as the need to develop and utilize alternative energy sources.

It is very difficult to find materials that satisfy the constraint of simultaneously possessing a high electrical conductivity (characteristic of metals) and a low thermal conductivity (characteristic of insulators) [55]. A high electrical conductivity is required for an enhanced flow of electrons, while a low thermal conductivity is required to impede the flow of phonons. While metals typically have high electrical conductivity, they also have a low Seebeck coefficient and a large electronic contribution to the thermal conductivity, making them a poor choice for thermoelectric. Insulators, on the other hand, have a large Seebeck coefficient and a small electronic contribution to the thermal conductivity, but have a large electrical resistivity due to a low number of carriers, leading to a poor thermoelectric effect [62]. This naturally led to the exploration of semiconductors as the new class of efficient thermoelectric materials.

2.3.3 Bismuth Telluride

Bismuth telluride (Bi_2Te_3) is one of the most popular thermoelectric materials and has been widely studied due to its large figure of merit compared to other bulk materials at room temperature. It is a narrow gap V-VI semiconductor material with unique and exceptional thermoelectric properties. Bismuth telluride has an energy gap of 150 meV; it has highly anisotropic electronic properties, and it is a part of the $D_{3d}^5 - R\bar{3}m$ space group. It has a layered hexagonal structure, which is made up of a hexagonal quintuple

unit cell (rhombohedral) and layered structure in the c_H axis, with a = 0.4383 nm and c_H = 3.0487 nm. The layers occur in the following order, with the unit cell in parenthesis:

$$– Bi – Te^1 – (Te^1 – Bi – Te^2 – Bi – Te^1) – Te^1 – Bi –$$

The bond between Te^1 and Te^1 is a weak van der Waals bond, which allow for easy cleavage of the crystal and contributes to the anisotropy of transport properties of the material [65]. Due to the covalent bonding of atoms in the planes of the layered structure of Bi_2Te_3, electrical currents are favored. However, the gaps between the planes hinder the transport of phonons, giving rise to the intrinsic benefits of bismuth telluride as a thermoelectric material [57]. The structure is shown below in Figure 2–12.

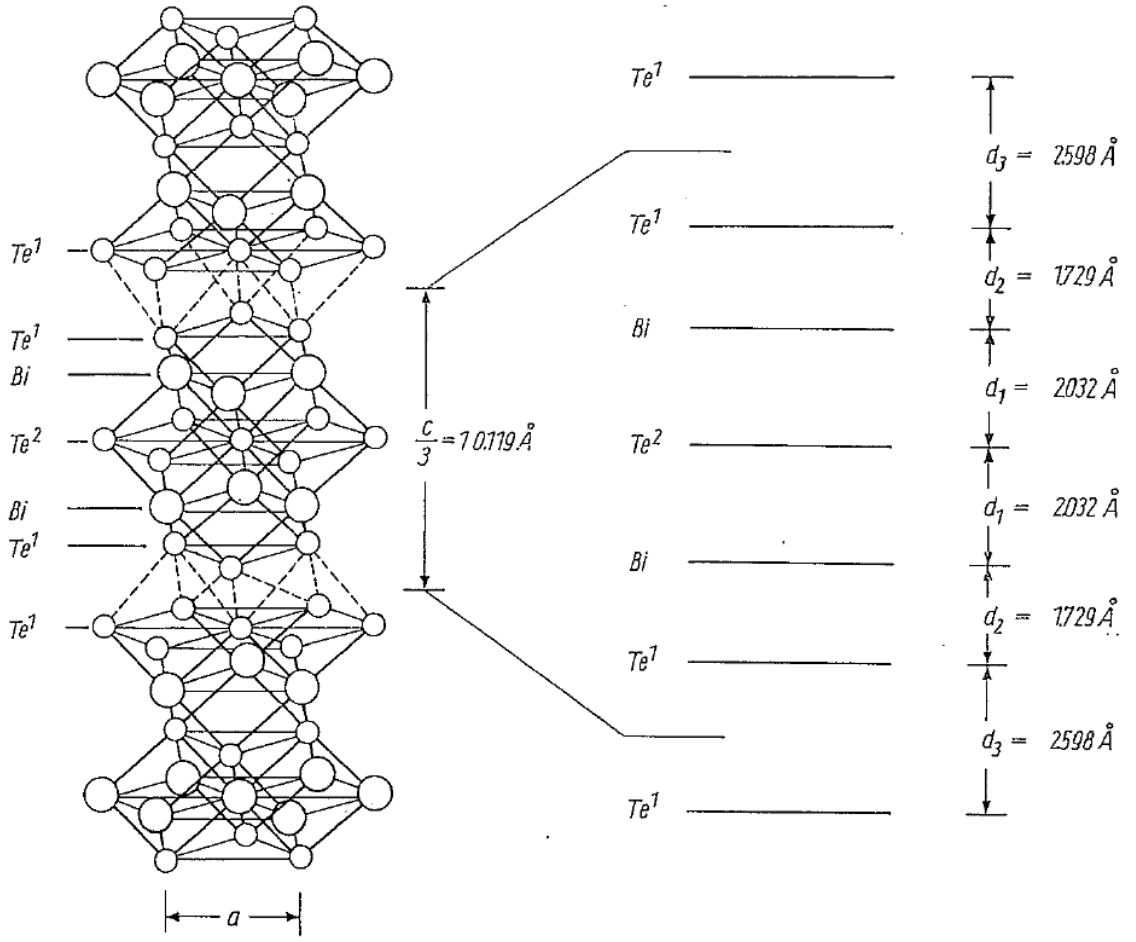

Figure 2–12: Layered structure of Bi2Te3, showing hexagonal unit cell and spacing of the layers (reproduced with caption from [68])

2.3.4 Review of Bismuth Telluride Growth via PLD

Due to the complex structure of bismuth telluride, only certain methods can be used for thin film growth. These methods include flash evaporation, co-sputtering, metal organic chemical vapor deposition (MOCVD), molecular beam epitaxy (MBE), and PLD [69]. Difficulties involving preserving the stoichiometry of the grown film, as well as the advantages of the PLD method make it the preferred choice for studying growth mechanisms of these films. Bismuth telluride thin films were first deposited using PLD by Dauscher et al. in 1996 [13]. Despite the advantages and flexibility of this method, there are certain conditions that must be met to preserve the structure and stoichiometry of bismuth telluride during PLD growth. The two most critical parameters for stoichiometric transfer of the target material are the deposition pressure and the substrate temperature. Achieving stoichiometric transfer of bismuth telluride is difficult due to differences in the vapor pressure between bismuth and tellurium. Since tellurium is very volatile, much more so than bismuth, a careful balance must be made between the deposition pressure and the substrate temperature. If the substrate temperature is too high, then re-evaporation of the tellurium can occur in the grown film, leading to a bismuth-rich film. However, if the substrate temperature is not high enough, the film will not form the more stable Bi_2Te_3 phase, and individual Bi and Te domains can be present [65]. Furthermore, having a deposition pressure that is too low will cause re-evaporation of the more volatile tellurium atoms, resulting in a bismuth-rich film [67].

Novel work done by Bailini et al. [65] provided a baseline of ideal growth conditions for the stoichiometric transfer of bismuth telluride. The ideal temperature

range was found to be between 250°C and 350°C, and the ideal deposition pressure was found to be between 0.075 torr and 1.5 torr [65]. Additionally, within the range of ideal growth conditions, several trends were observed regarding the particular growth of bismuth telluride films. For example, as the laser fluence on the target increases (with all else remaining constant) the tellurium content in the film decreases. This can be explained by a sputtering of the Te atoms, which are more volatile than the Bi atoms, by the highly energetic species impacting the substrate as a result of the increased laser fluence. The tellurium content also decreases with decreasing pressure, due to the high volatility of tellurium. The domain size of the films also decreases with decreasing pressure in the range of 1.5 torr down to 0.075 torr. Moving on to substrate temperature, it was found that if the temperature increases above 350°C, the tellurium content in the film decreases, again due to the high volatility of tellurium. When the temperature is above 250°C, the formation of the more stable Bi_2Te_3 phase is favored, leading to better stoichiometry in the films. Films grown at room temperature are not fully crystallized, and while they may contain some stoichiometric Bi_2Te_3, there are also Bi and Te domains present in the film. Finally, it was found that the substrate material only affects film morphology, and the stoichiometry of films grown on different types of substrate was unaffected [65].

Using too large a laser fluence can negatively impact the growth of bismuth telluride. For a laser fluence much larger than 1.2 J/cm^2, the lighter and more volatile tellurium atoms in the deposited film can be sputtered away by the highly energetic plume species [65]. The type of substrate can also affect the film morphology, but it does not seem to affect the film stoichiometry or crystallinity. The orientation of the grown

film can be affected by van der Waals epitaxy, where film growth is initiated by weak forces on the saturated substrate surface molecules. This occurs with substrates such as mica and creates an orientation tendency that can be used to control film morphology or affect transport properties of the film [65] [70].

The morphology of the bismuth telluride films grown via PLD can be modified by changing the deposition pressure. It was found that for low ambient gas pressures (0.075 torr), films are more compact and horizontally oriented with some irregularities throughout the surface. However, when the deposition pressure increases to 1.5 torr, the films consist of less dense, 3-dimensional nanoparticle agglomerates or columnar structures [70]. In addition, the type of ambient gas can also have an effect on the grown films. In general, argon is the most common ambient gas used when growing bismuth telluride thin films via PLD. Although the effect is much less pronounced, by switching from argon to helium as the ambient gas, the morphology of the grown film becomes less dense and connected, looking more like a random agglomeration of nano-platelets than a continuous, nanostructured film [70].

Room temperature growth with post annealing processing can also lead to stoichiometric bismuth telluride films due to the enhanced crystallization at higher temperatures [63]. To achieve crystallization of bismuth telluride films, an annealing temperature above 200°C must be used. This will lead to significant changes in the surface structure, and a transition from an amorphous film to one with polycrystalline phases. For an annealing temperature near 300°C, the main growth directions are (015) and (006), which correlates to the hexagonal structure of Bi_2Te_3. As the annealing temperature increases up to 400°C, the grain size also increases, eventually leading to a

smearing of the grains and a nanorod structure growth perpendicular to the surface along the (006) axis [64]. Bismuth telluride films grown without post-annealing show preferential growth directions along the (015) and (1010) planes [13]. The application of post-annealing has also been shown to increase the electrical transport properties of the grown films by reducing point defects and increasing the mobility of the charge carriers [67].

Tablex below shows a summary of different bismuth telluride films grown via PLD. Included in the first three columns are some properties of bulk Bi2Te3, bulk bismuth, and bulk tellurium. The remainder of the table provides some of the growing conditions and film properties of different thin film bismuth telluride or bismuth telluride-based materials.

Table 2-2: Electrical properties of Bi_2Te_3 films (top) and bulk Bi_2Te_3 (bottom)

Material	Temperature (°C)	Pressure (torr)	Resistivity (mΩ cm)	Seebeck (μV/K)	Source
Bi_2Te_3	250-350	0.075-1.5 argon			Bailini [65] (Parametric)
Bi_2Te_3	300 (anneal)	$2x10^{-6}$	3-4		Faraji [64]
Bi_2Te_3	190	0.15	1.5		Obara [71]
Bi_2Te_3	20	$2x10^{-2}$	1.0	-(25-65)	Yu [63]
Bi_2Te_3	250-350	0.075-1.5 argon	1.4-1.5	-(175-250)	Li Bassi [70]
Doped Bi_2Te_3	350	10^{-7}	1-10	-(50-75)	Makala [67]
Bi_2Te_3	20	$3.75x10^{-5}$	0.2-0.5	-(20-80)	Zeipl [58]
Bulk Material	**Thermal Conductivity**	**Power Factor**	**Resistivity (mΩ cm)**	**Seebeck (μV/K)**	**Source**
Bulk Bi_2Te_3	1 W/m K	20-45 $\mu W/cm\ K^2$	1.0	-240 (single crystal)	Li Bassi [70]
Bulk Bi			0.13	-70 (poly-crystalline)	Li Bassi [70]
Bulk Te			10		Li Bassi [70]

Characterization of bismuth telluride films is carried out after the growth is complete. This consists of both morphological and electrical characterization. Surface morphology and crystal structure are probed using SEM and XRD, respectively. Electrical characterization consists of the determination of the electrical resistivity and Seebeck coefficient of grown films. When growing bismuth telluride thin films, it is always reported to be n-type [58] [70]. As a result, the Seebeck coefficient should always be negative, an indication that the majority charge carriers consist of electrons. Bismuth telluride can be doped with antimony ($Bi_{0.5}Sb_{1.5}Te_3$) to become p-type, or with selenium ($Bi_2Te_{2.7}Se_{0.3}$) to become n-type [67].

Examining the growth mechanisms of nanostructured bismuth telluride can improve understanding of how grains at the nanoscale affect bulk material properties, as well as improve the functionality of thermoelectric devices. Once this is understood, a correlation between the growth parameters and the resulting transport properties of the grown materials can be made, which would allow for the tunable growth of thermoelectric materials for specific applications with optimized properties.

3 Experimental setup

The vacuum chamber used for this work consists of a stainless steel vessel with multiple ports and flanges for the hardware necessary to properly manipulate the equipment, perform different experiments, and monitor conditions inside the chamber. Modifications were made to an initial chamber that consisted of the cylindrical vessel with only some of the required flanges to seal the chamber and none of the electrical fittings. To make the chamber ready for experimentation, all of the necessary seals, flanges, and feedthroughs were added. There are nine total flanges on the vacuum chamber, each of which are now equipped with the appropriate seal or fitting to accommodate high vacuum and any feedthrough or connection to within the chamber. Figure 3–1 shows a schematic of the vacuum chamber with the flanges shown and numbered. Flange 1 is a standard Kwik-Flange ISO (KF) flange that is used for a pressure gauge. Flange 2 is another standard KF flange that is capped for potential use in the future. Flange 3, underneath the chamber, is a ConFlat flange that is used for pumping ambient or annealing gas into the chamber. Attached to the flange is a series of valves used for controlling the input of up to three different gasses (typically H_2, Ar, or N_2) into the chamber. Flange 4 is a valve for connecting the inlet of the roughing vacuum pump. This flange is the same as valve 1 in Figure 3–4. Flange 5 is a large flange ISO component that is custom made to interface the inlet of the turbo-molecular vacuum pump to the vacuum chamber, with a manual control valve. This flange is the same as valve 3 in Figure 3–4. Flange 6 and 7 are the substrate and target flanges, respectively. These items will be explained in more detail below. Flange 8 is where the laser entrance window is located, and will hereby be referred to as the front of the vacuum chamber.

Finally, flange 9 is a viewing port window, and will hereby be referred to as the rear of the chamber.

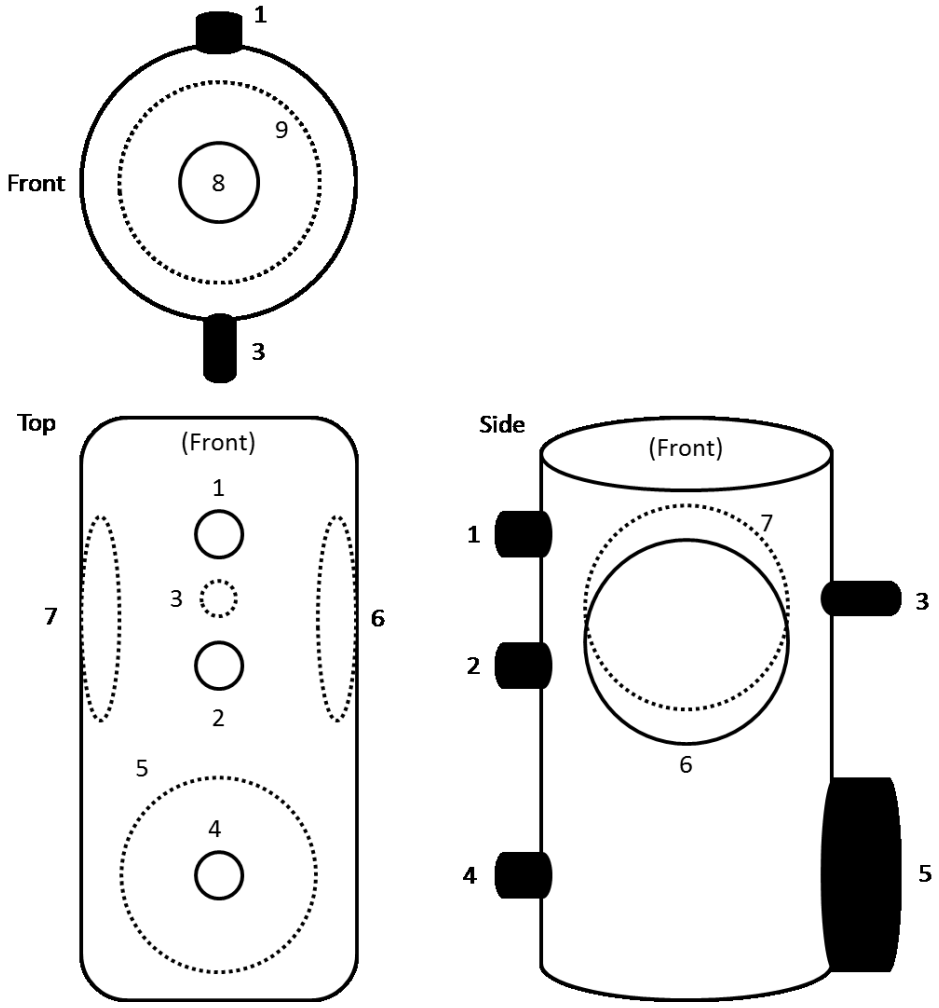

Figure 3–1: Schematic of the PLD (vacuum) chamber with the different ports and flanges labeled

The substrate flange (flange 6) is responsible for accommodating the substrate holder, heating the substrate, and monitoring the temperature of the substrate. It consists of a thermocouple feedthrough to measure the temperature of the heating element inside the vacuum chamber, and a power feedthrough to supply current to the coiled resistance heater housed within the ceramic plate that also acts as a substrate holder. The target

flange (flange 7) is responsible for accommodating the target holder and the target shield. This is done with two rotary feedthroughs, which allow the target holder to rotate and the target shield to be positioned in and out of the ablation plume.

Figure 3–2 shows the exterior of the PLD chamber, and Figure 3–3 shows a schematic of the entire experimental setup. The laser beam enters the front of the vacuum chamber through a broadband, uncoated UV-fused silica window (ThorLabs, WG42012). A glass viewing port at the rear of the chamber allows for continuous observation of the PLD process in real time. A webcam is set up at the viewing port, which allows pictures and videos to be taken during experiments. This viewing port is also where the fiber optics were mounted to perform optical emission spectroscopy. Two different vacuum pumps are connected to the chamber in order to create a vacuum for deposition. The roughing pump (Edwards, E2M-12, rotary pump) is used for initial pumping, typically from atmospheric pressure down to about 10^{-2} torr. The turbo-molecular pump (Pfeifer, TMH-260PC), which is cooled via a Neslab water chiller (Endocal RTE-5DD), is then used to reach ultimate vacuum pressure down to 10^{-6} torr. The turbo-molecular pump requires the use of a roughing pump, since it is not designed to work at atmospheric pressure. For this reason, the two vacuum pumps are connected in series, with the exhaust of the turbo pump leading to the intake of the roughing pump, with valves to control which pump is exposed to the chamber at a given time. Figure 3–4 shows the schematic of the vacuum chamber pumps and gauges. For initial pumping, valve 1 is opened, while valves 2 and 3 are closed. Once the pressure in the chamber reaches 10^{-2} torr, valve 2 is opened, and the turbo pump and chiller are turned on to warm up and reach full speed. Once the turbo pump is ready, valve 1 is closed, and valve 3 is

opened. This procedure exposes the turbo pump to the chamber, and closes off the roughing pump inlet to prevent an open loop, which could cause the turbo pump to pull oil from the roughing pump into the chamber, potentially contaminating the vacuum chamber and turbo pump with motor oil. The exhaust of the two vacuum pumps is directed away from the chamber into the building exhaust system.

The pressure of the system is monitored by two different pressure gauges. The first gauge is attached directly to the vacuum chamber (flange 1) and can monitor pressure from atmospheric down to 10^{-8} torr. This is the micro-ion gauge (Granville-Phillips, 390411-O-YK-T), which monitors the pressure in the vacuum chamber. The second gauge is a mini-convectron gauge (Granville-Phillips, 275-923-EU), which is attached to the foreline of the roughing pump. This gauge monitors the pressure at the roughing pump inlet (between valve 1 and the roughing pump) from atmospheric to 10^{-2} torr. This is vital for determining when it is safe to turn on the turbo pump, as to prevent any damage from trying to use the turbo pump at atmospheric pressure.

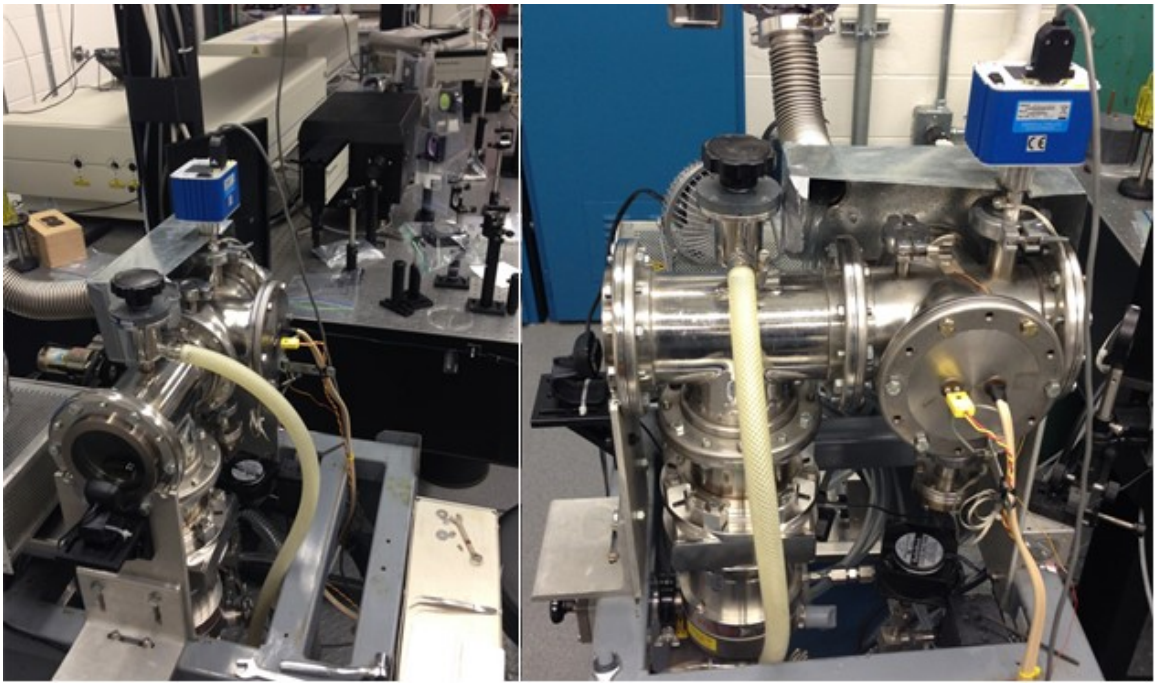

Figure 3–2: PLD chamber and attached hardware.

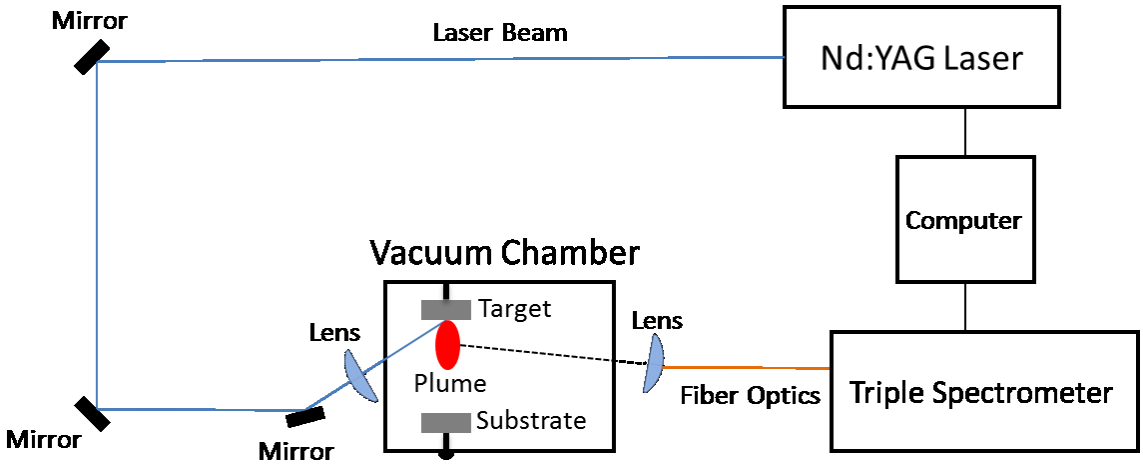

Figure 3–3: Schematic of the experimental setup.

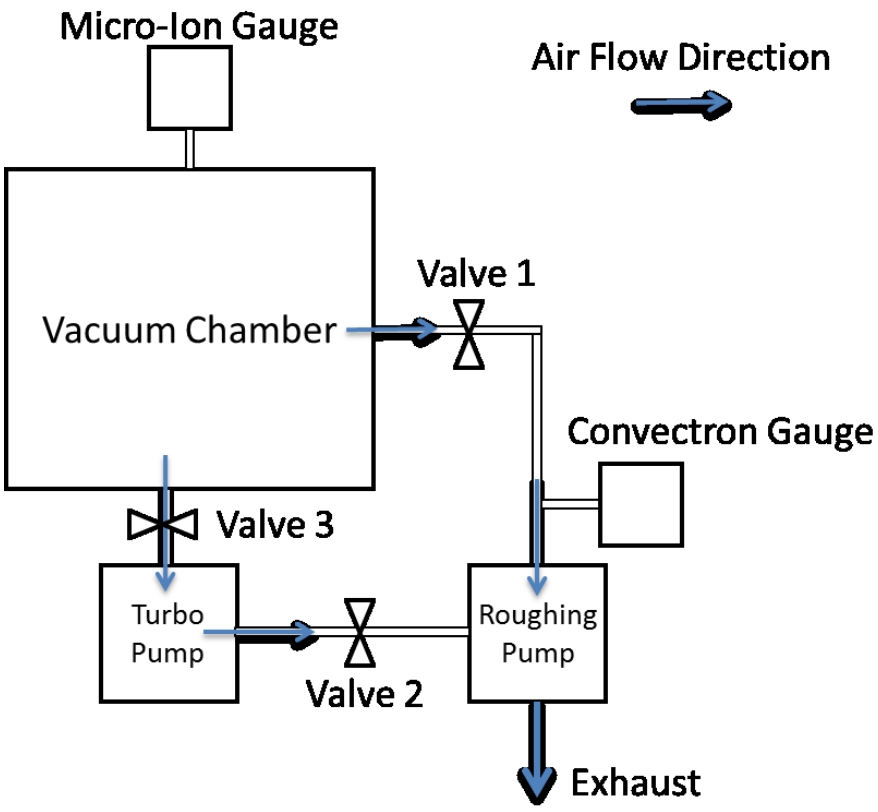

Figure 3–4: Schematic of vacuum chamber pumps and gauges.

The electrical panel mounted to the side of the vacuum chamber is responsible for supplying all of the necessary power and safety to the electronics that comprise the experimental setup, as seen in Figure 3–5. The power supply (Siemens 6EP1 333-2BA00), which is the gray box located in the center of the panel, converts the 120 volt AC from the wall outlet to a 24 volt DC, 5 ampere supply. This is used to power the target motor, the two temperature controllers, and the two pressure gauges. Above the power supply is the solid state relay (Omega SSR240AC45), which is used to control the current flowing through the resistance heater. The SSR and the interior thermocouple is controlled and monitored by the substrate temperature controller (Omega CN9111A), located near the top of the electrical panel. The second temperature controller

(Eurotherm 818P) monitors the temperature on the exterior wall of the vacuum chamber, measured using a standard Omega K-type thermocouple. The motor (Pittman GM9413-4) is operated using a prefabricated circuit board, which has a variable speed control dial to allow for precise rotation speed of the target. The motor is coupled to the target manipulator shaft through a rotary belt (Gates Truflex 0140).

There are two cooling fans to help cool the exterior of the vacuum chamber. The first (PMX HVRA-4D) is a 4" fan that can be mounted on top of the vacuum chamber to blow over the target and substrate region. The second (RadioShack 273-242) is a 3" fan mounted below the chamber. Together they form a cross breeze to remove excess heat from the exterior of the vacuum chamber and keep the vacuum chamber cool enough to prevent any damage to the electronics or to the O-rings sealing the flanges of the chamber.

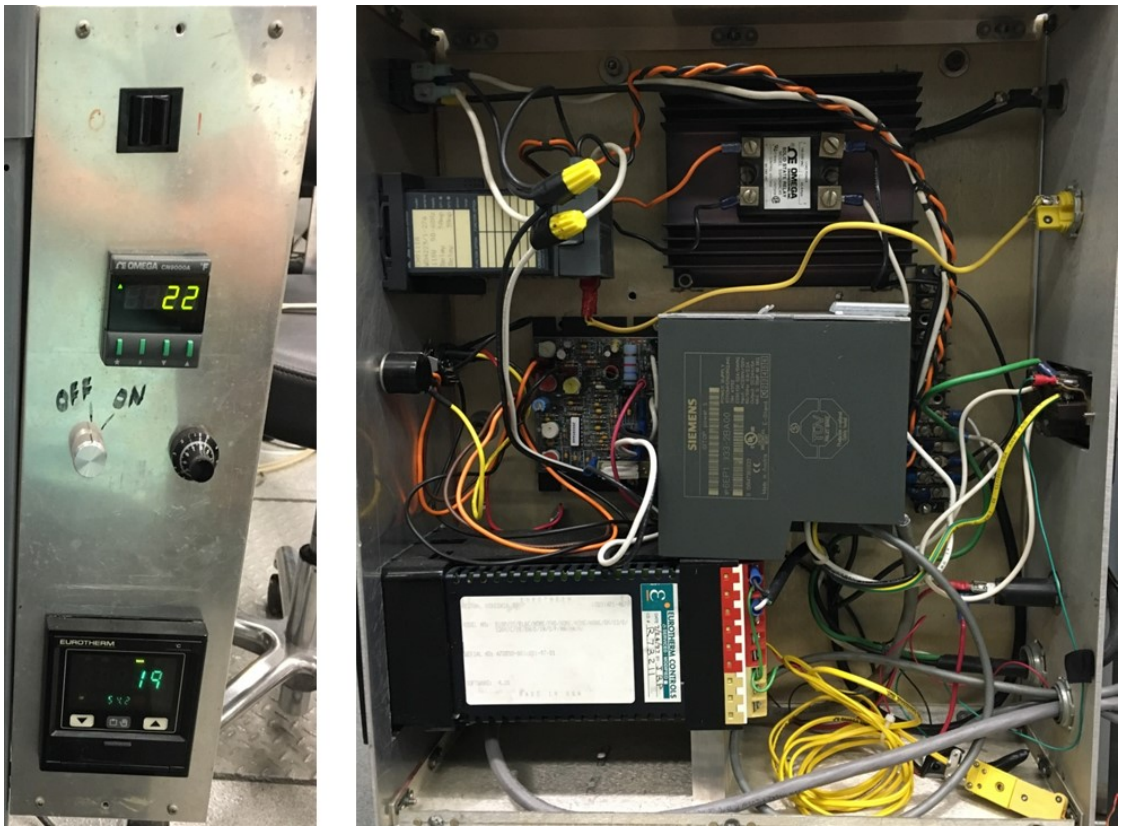

Figure 3–5: Front (left) and interior (right) of the electrical panel for the vacuum chamber setup.

The laser used for ablation is a Quanta Ray PRO-250 pulsed Nd:YAG Q-switched laser with a fundamental frequency of 1064 nanometers. The frequency doubled (532 nm) and frequency quadrupled (266 nm) outputs of the laser, using two separate harmonic generators, are used in this study The laser repetition rate is 10 Hz and pulse width is 8-12 nanoseconds for the fundamental frequency (1064 nm). The pulse width for 532 (266) nm is 1-2 (3-4) ns less than the fundamental pulse width. The energy of the fundamental frequency is rated at 1500 mJ/pulse. The 532 nm laser energy is rated at 800 mJ/pulse, and the 266 nm laser energy is rated at 150 mJ/pulse. Typical laser fluence (optical energy delivered per unit area) values used in the experiments range from 0.5 to 5 J/cm^2, which is achieved by using fused silica neutral density filters and by adjusting the spot size of the laser beam on the target. The laser spot size is independently controlled by translation of a plano-convex UV-fused silica focusing lens (f = 200 mm) positioned outside of the vacuum chamber. The laser power is measured using an Ophir power meter (Nova Display, 1Z01500). Due to the Gaussian nature of the Nd:YAG laser beam profile, an iris diaphragm (ThorLabs, ID25) is used to block the outer edges of the laser spot, ensuring a more uniform ablation area on the target surface.

Substrates used for these experiments consist of various materials, including silicon wafers, copper foil, nickel foil, glass, and several others. The different substrate materials are summarized in Table 3-1. Both target and substrate materials are always cleaned before being introduced into the vacuum chamber. Typical cleaning procedure includes ultrasonic cleaning (Fisherbrand, FB11201) in acetone for five minutes, followed by rinsing in deionized water. The samples are then sonicated in isopropanol for five minutes, rinsed in deionized water, and dried to remove any grease or residual

particulates from the surface. The substrates are then adhered to the substrate holder via a conductive silver paste (SPI High Purity Silver Paint, SPI-05002-AB and SPI Flash Dry Silver Paint, 04999-AB). The substrate holder also serves as the heating element, with a resistance heater coiled within the ceramic plate. The heating element is controlled by the substrate temperature controller. The temperature of the substrate holder is measured by an Omega K-type thermocouple located underneath the surface of the substrate holder in the middle of the coiled heater wire. The temperature measured by this thermocouple is accurate within a 5% margin of error to the temperature of the substrate on the surface of the heater. There is also an external thermocouple used to measure the temperature on the outside of the vacuum chamber. The target material, after being cleaned in the ultrasonic cleaner, is loaded into the target holder within the vacuum chamber. This holder keeps the target in place, while also rotating it, ensuring a uniform ablation track and preventing large pits from being etched out of the target surface from static laser irradiation. The target and substrate are approximately 4.5 centimeters apart and are oriented so that the surfaces are parallel to one another. The targets consist of various high purity solid discs that are one inch in diameter and ¼" or 1/8" in thickness. The target and substrate material specifications are outlined below in Table 3-1.

Table 3-1: Substrate and target material specifications (* denotes type of doping in silicon substrate)

Material	Purity	Thickness	Manufacturer	Part Number
Copper Foil	99.9%	0.675 mm	Alfa Aesar	40374
Copper Foil	99.8%	0.025 mm	Alfa Aesar	46365
Puratronic Copper Foil	99.9999%	0.1 mm	Alfa Aesar	42973
Puratronic Copper Foil	99.9999%	0.25 mm	Alfa Aesar	42974
Nickel Foil	99%	0.025 mm	Alfa Aesar	12722

Silicon Wafer (1 0 0)	*N-Phosphorus	381 microns + native oxide	El-Cat	30
Silicon Wafer (1 0 0)	*P-Boron	500 microns + 300 nm oxide	University Wafer	43
Graphite Target	99.999%	0.250 in	Kurt J. Lesker	EJT C 501A4
Pyrolytic Graphite Target (HOPG)	99.999%	0.250 in	Kurt J. Lesker	EJT PYRO 501A4
Bismuth Telluride Target	99.99%	0.125 in	American Elements	BI-TE-04M-D.1125
Iron Target	99.95%	0.125 in	Kurt J. Lesker	EJT FE XX351A2
Copper Target	99.999%	0.250 in	Kurt J. Lesker	EJT CU XX501A4
Nickel Target	99.99%	0.125 in	Kurt J. Lesker	EJT NI XX401A2
Zinc Target	99.993-99.995%	0.250 in	Kurt J. Lesker	EJT ZN XX451A4

Once the target and substrate are loaded into the vacuum chamber, the chamber must be pumped down to remove any impurities. The pumping steps have already been described in detail above. Once the final deposition pressure is obtained, an optional nitrogen purge and/or hydrogen reduction reaction can be performed, depending on the specific deposition parameters for a given experiment. For instance, when using copper substrates, the native oxide layer can be removed via a hydrogen reduction reaction. To do this, the vacuum chamber is backfilled with hydrogen and heated to chemically remove the native oxide layer and expose a pure copper surface. This hydrogen reduction is typically done at elevated temperatures (up to 700°C) and at pressures from 50-200 torr. Once the hydrogen reduction is completed, the chamber is purged with inert gas and evacuated to remove any residual hydrogen or water vapor. Once the chamber achieves high vacuum, the substrate is heated to its final deposition temperature, and the chamber is either continually pumped or backfilled with the appropriate background gas to a specific pressure. The target is then cleaned via laser ablation while rotating on its

axis. By irradiating the target with the laser for 1-2 minutes prior to deposition, the surface is cleaned of any impurities or contaminates. During this time, a shield is placed in-between the target and the substrate to prevent any deposition onto the substrate from occurring. Once this target annealing is completed, the shield is removed and deposition experiments may begin.

During film growth, in-situ optical emission spectroscopy is used to analyze the laser-produced plasma and determine what species are being ablated from the target surface, as well as how those species (or particles) evolve as they move from the target to the substrate for deposition and film nucleation. The spectroscopy setup consists of a Canon receiving lens (f-number = 1.4) on a linear stage coupled with a fiber optic cable (Thorlabs FT600EMT) to a triple spectrometer (Princeton Instruments TriVista) with a 200 micrometer entrance slit and an 1800 groove per millimeter holographic grating, mounted with an ICCD camera (Princeton Instruments PIMAX 3). The triple spectrometer operates in single mode, utilizing only the first spectrometer. Spectral calibration is confirmed using a low pressure discharge mercury-argon lamp (Ocean Optics HG-1) with a well-defined peak, and intensity calibrations are carried out through the spectral range using a NIST calibrated tungsten lamp (Ocean Optics LS-1-CAL). A three-dimensional linear stage setup allows precise focus of the plasma plume, as well as a continuous spatial analysis along the plume axis (perpendicular to the target surface) up to a range of one inch from the target surface. The relative timing of the laser Q-switch, laser pulse, and camera gating are monitored with a 1.5 GHz digital oscilloscope (Agilent Infiniium 54845A) and controlled by a computer. The software used to control the ICCD

camera is called WinSpec 32, and the software for fitting emission spectrum across the full spectral range is called S&I Triple Raman System 555AS.

Once the films are grown, several different methods are used to analyze and characterize the samples. Sample morphology and thickness are analyzed using a Zeiss Sigma 8100 field emission scanning electron microscope (FESEM) equipped with energy dispersive spectroscopy (EDS) for chemical and stoichiometric analysis. Crystallinity is analyzed using a PANalytical X'Pert PRO X-ray diffraction (XRD) machine, using Cu K-alpha radiation with a Pixel1D detector. The type of bonding in the films is analyzed using a Renishaw 1000 inVia Raman spectrometer system. The nanostructure of the samples and diffraction patterns are analyzed using a JEOL 2010F transmission electron microscopy (TEM). Electrical characterization is carried out using the Van der Pauw 4-point probe method, which uses a Keithley 2400 SourceMeter to apply a current through two probes, while measuring the voltage through the other two probes located on the edges of the sample. The Seebeck coefficient is also determined by measuring the change in voltage across a sample when a temperature gradient is applied.

4 Graphene Growth and Characterization

Nanostructured few-layer graphene films are grown using pulsed laser deposition in an attempt to study the basic growth mechanisms of graphene and other two dimensional structures. By controlling various experimental parameters, different aspects of the growth mechanism could be individually examined in a parametric, fundamental study.

4.1 Raman Spectroscopy

Raman scattering describes the inelastic scattering of a photon incident on a molecule or atom. Most photons scatter elastically, at the same frequency as the incoming photon, which is known as Rayleigh scattering. However, when elastic (Raman) scattering occurs, the frequency of the scattered photon can be either higher or lower than the incoming photon frequency. Stokes scattering occurs when the frequency of the scattered photon is lower than the initial frequency, and Anti-Stokes scattering occurs when the frequency of the scattered photon is higher than the initial frequency. This change in frequency of the scattered photons is what Raman spectroscopy measures.

Raman spectroscopy has become the standard for reliable and non-destructive analysis of many materials, in particular graphene and carbon-based materials [72]. Raman spectroscopy can be used to characterize samples using an Argon ion laser (514 nm, 50 mW) focused to a spot of about 10 micrometers on the sample surface. Here, measurements are performed in a backscattering geometry at room temperature using a Renishaw inVia Raman microscope. Visible Raman spectroscopy is used because of the higher absorption cross-section of carbon sp^2 bonds compared to that for sp^3 bonds in visible wavelength excitation [18]. Raman spectroscopy of graphene typically consists of

three main peaks, as shown in Figure 4–1. The first peak occurs at around 1350 cm^{-1} and is known as the disorder or D peak. This peak originates from small crystal size and unorganized domains and is due to zone-boundary phonons. The intensity of the D peak is associated with non-sp^2 bonding, and it is not present in defect-free graphite since the phonons do not satisfy the Raman fundamental selection rule [72]. The next peak in the Raman spectrum of graphene is the G peak, which occurs at about 1590 cm^{-1}. The G peak originates from sp^2 bonded carbon atoms and is due to the doubly degenerate zone center E_{2g} mode from in-plane vibrations [72]. It indicates the formation of aromatic rings from crystalline graphite [73]. The final peak is the 2D, or G' peak, which occurs at around 2700 cm^{-1} and is a characteristic feature of graphene. This second order peak appears because of zone-boundary phonons and is due to a two-phonon double resonance Raman scattering process [74]. The 2D peak links the phonon wave vectors to the electronic band structure [49]. For bi-layer graphene, the 2D peak splits into four different components due to interlayer coupling of the graphene planes [73].

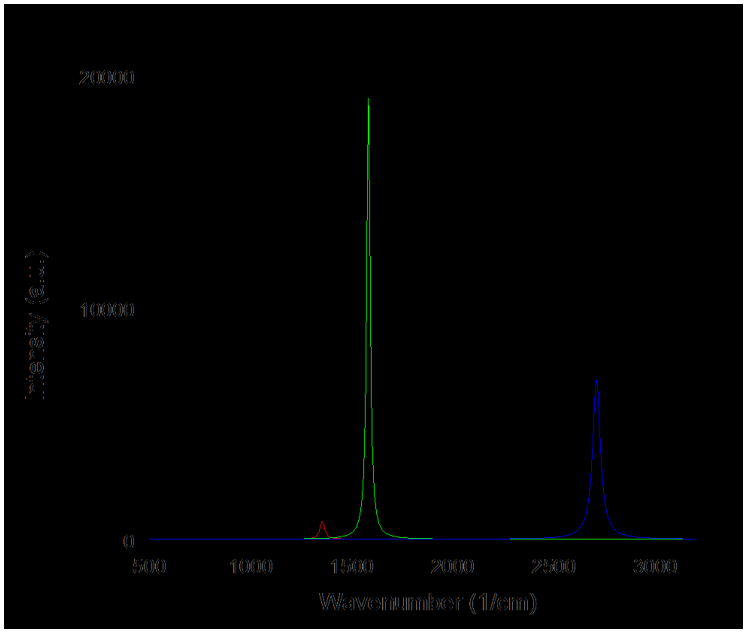

Figure 4–1: Raman analysis of HOPG target

$$\frac{I(D)}{I(G)} = 0.04; \quad \frac{I(2D)}{I(G)} = 0.36$$

By comparing the relative heights of the 2D and G peaks it is possible to estimate the number of layers of graphene in a given sample. This method has been used to effectively count the number of layers of graphene in a quick and non-destructive manner [72]. Figure 4–2 shows the comparison of Raman spectra of graphene films of varying thicknesses, taken from Reference [33]. As the number of graphene layers decrease in a sample, the intensity of the 2D peak increases until the 2D peak is approximately twice the intensity of the G peak for a single layer of graphene. As the number of layers increase, the intensity of the 2D peak decreases, relative to the G peak, until the spectra is identical to that of bulk graphite. This occurs at approximately 5 or more layers of graphene, at which point the thin graphitic film is indistinguishable from a bulk graphite sample using Raman spectroscopy.

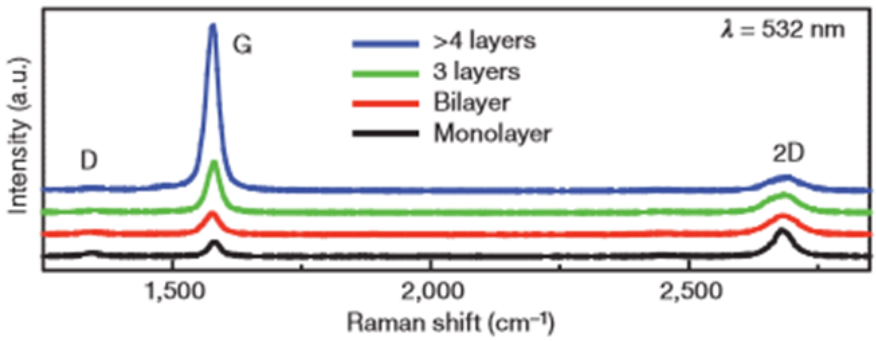

Figure 4–2: Raman spectra of varying thicknesses of FLG film (reproduced with caption from [33])

In addition to counting the number of graphene layers in a sample, Raman spectroscopy can be used to determine the crystallite size of the domains of nanographite

films by examining the ratio of the intensities of the D and G peaks. This is done using the TK relation [75]:

$$\frac{I_D}{I_G} = \frac{C(\lambda)}{L_a}$$

where I_D is the intensity of the D peak, I_G is the intensity of the G peak, $C(\lambda)$ is a constant based on the laser excitation energy, and L_a is the crystallite size. Using an Argon ion laser as the excitation source, the constant C(514 nm) = 4.4 nanometers [76]. Using this equation, the crystallite size (grain size) for the highly ordered pyrolytic graphite (HOPG) target, as determined by Raman spectroscopy, is about 108 nanometers. However, the TK equation tends to underestimate the grain size due to the dominant effect of smaller crystallites compared to larger crystallites [77]. Recently, it was found that the ratio of I_D/I_G can be interpreted as integrated areas instead of peak intensities and used to quantify nanographite crystallite size via the following general equation [78]:

$$L_a(nm) = \frac{560}{E_{laser}^4}\left(\frac{I_D}{I_G}\right)^{-1} = (2.4\ x\ 10^{-10})\lambda_{laser}^4\left(\frac{I_D}{I_G}\right)^{-1}$$

where E_{laser} is the excitation laser energy used in the Raman spectroscopy, and I_D and I_G are the integrated areas of the D and G peak, respectively. This method is useful for determining the extent of nanostructuring in a graphene film.

4.2 Laser Excitation Effects

Figure 4–3 shows the Raman spectra of carbon films grown on n-Si substrates using both 266 nm and 532 nm laser irradiation. The spectra show films grown at increasing temperature, from room temperature up to 900°C. At room temperature (25°C), there is a single, broad peak centered around 1535 cm^{-1}. This is indicative of an amorphous carbon structure with mostly disordered sp^2 bonding [73]. As the substrate

temperature increases, the single broad peak separates into the D and G peaks of graphitic carbon at 1350 and 1590 cm^{-1}, respectively. This separation of peaks indicates the formation of aromatic rings and the growth of nanocrystalline graphite as the temperature increases, which is induced by thermal relaxation of sp^3 to sp^2 bonds [79]. Figure 4–4, which consists of carbon films grown on copper foil substrates instead of silicon wafer substrates, displays very similar trends to that of Figure 4–3, and shows that the substrate material does not have as large an effect on the crystalline structure as does the substrate deposition temperature. When comparing Figure 4–3 and Figure 4–4, it is evident that the growth mechanism is similar for the two different substrate materials.

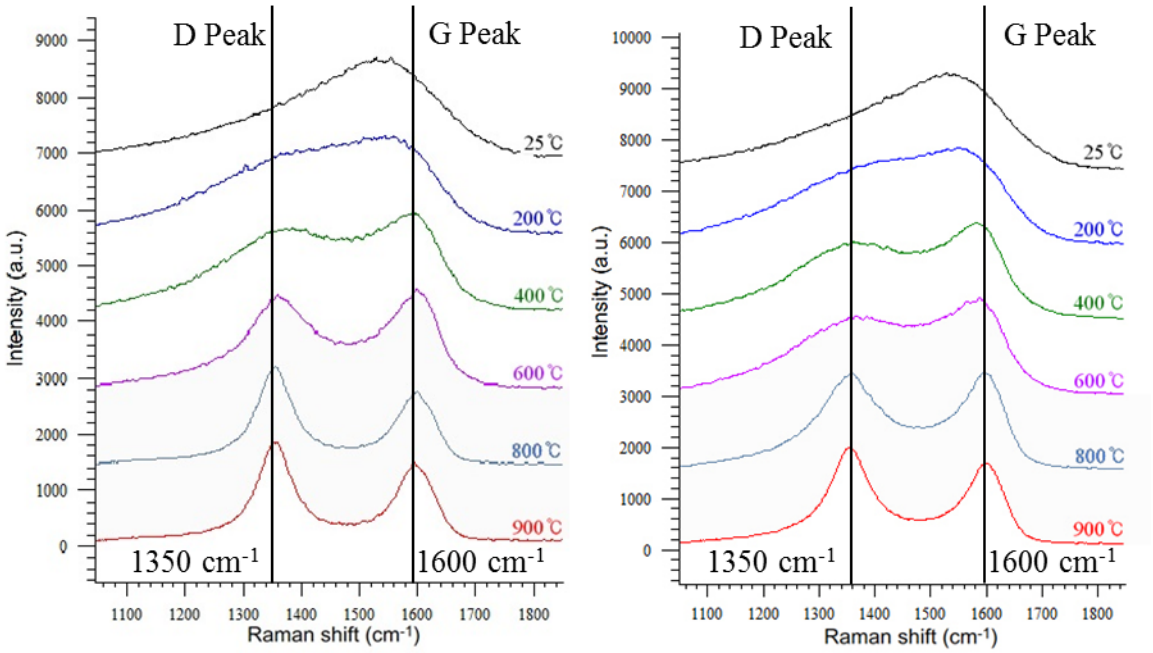

Figure 4–3: Raman spectra of carbon films grown on silicon wafer substrates at different temperatures using 266 nm wavelength (left) and 532 nm wavelength (right)

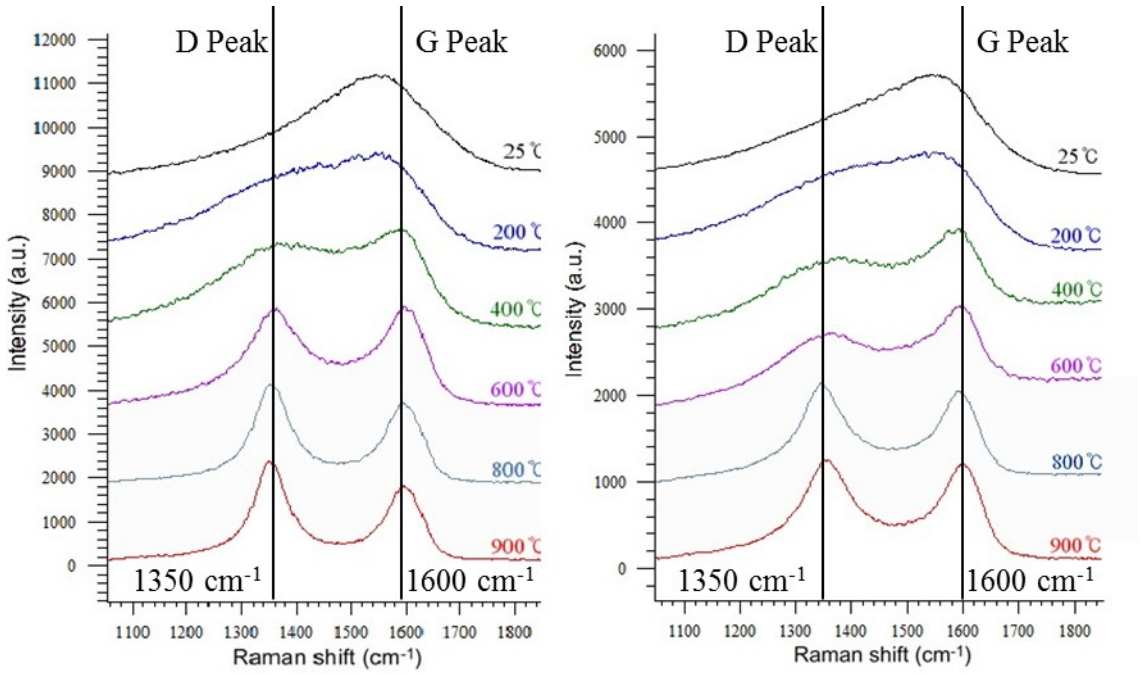

Figure 4–4: Raman spectra of carbon films grown on copper foil substrates at different temperatures using 266 nm wavelength (left) and 532 nm wavelength (right)

From Figure 4–3 and Figure 4–4, it is also evident that the growth mechanism is similar for the different laser excitation energies tested, independent of substrate. However, there are two noticeable differences in the D peaks of the spectra for the different laser wavelengths. The first difference occurs at 600°C, where the films grown using 266 nm laser irradiation show a more prominent D peak than those grown using 532 nm laser irradiation. The second occurs at 900°C, where the D peak is larger in comparison to the G peak for films grown using 266 nm laser irradiation. These differences in the films grown using the 266 nm laser may be attributed to the formation of smaller domain sizes as the film approaches the nanocrystalline form of graphite faster than that for the 532 nm films. The 532 nm wavelength has a laser energy of 2.33 eV, which is lower than the carbon-carbon bond energy in graphite (3.7 eV). As a result, the

bonds in the target graphitic lattice cannot be broken simply by absorption, and material removal instead relies on different types of defects and imperfections to ablate carbon clusters with linear or ring structures from the target surface. However, at 266 nm, the energy of the laser beam is 4.66 eV, which is enough to photochemically break the carbon-carbon bonds, resulting in smaller carbon species being ablated from the carbon target. This is important for low temperature growth, where the substrate temperature is not high enough to allow readily for the rearrangement of carbon atoms on the substrate surface. It is not until around 900°C (as seen in Figure 4–3 and Figure 4–4) that the substrate temperature is high enough to provide the mobility for the carbon atoms to completely undergo graphitization and form the sp^2 bonded hexagonal lattice of graphene. With a high enough laser power and small enough wavelength, the carbon species can be controlled to be predominantly C_1^+ and C_3^+ ions [17]. The films produced by these smaller species lead to smaller nanocrystalline domains with a larger D peak in the films grown using a 266 nm laser compared to films grown using a 532 nm laser.

Figure 4–5 shows the Raman spectra of FLG samples grown on copper substrates at 900°C using a laser fluence of 4 J/cm^2 at different laser wavelengths. It is evident that the FLG films grown using different laser wavelengths are similar in structure. The only significant difference is the 2D/G ratio, which reveals that the film grown using 532 nm (right) has slightly more layers of graphene than the film grown using 266 nm (left). With all other parameters being equal (pressure, laser energy, temperature), this shows that the 532 nm laser irradiation tends to ablate more material than does the 266 nm laser irradiation. This outcome agrees with previous results in which the estimated ablation volume per pulse for higher wavelength lasers was larger than that for lower wavelength

lasers [18]. In addition, when using the 266 nm laser, the plasma plume will absorb more energy than when using the 532 nm laser, so less energy will reach the target surface. This effect coincides with the experimental observations of obtaining thinner films when using lower wavelengths. Additionally, another peak can be seen in these spectra around 2900 cm^{-1}, which is a combination of the D and G peaks and is called the S3 peak [37].

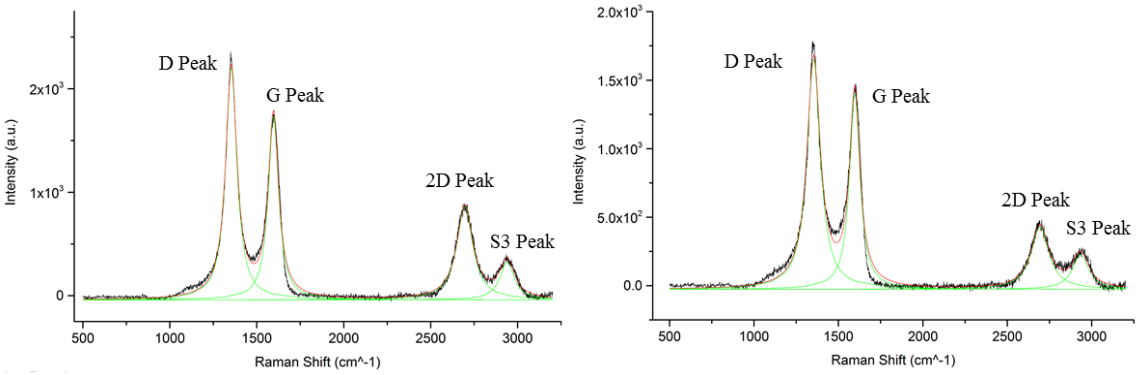

Figure 4–5: FLG film grown on copper substrate using 266 nm laser (left) and 532 nm laser (right)

Peak Ratios:

Left: $\frac{I(D)}{I(G)} = 1.26;\ \ \frac{I(2D)}{I(G)} = 0.51$ Right: $\frac{I(D)}{I(G)} = 1.18;\ \ \frac{I(2D)}{I(G)} = 0.32$

The total laser irradiation exposure time directly affects the amount of target material that is ablated, which corresponds to the amount of deposited material on the substrate surface. To verify this, the laser ablation duration was investigated for two different substrates to investigate if there was an optimal deposition time for graphene nanostructures. The deposition duration ranged from 30 seconds up to eight minutes, and the results are summarized below. The figures shown only go up to three minutes because any deposition durations longer than three minutes looked similar and followed the trend of decreasing both D/G and 2D/G ratios. For deposition durations of less than

one minute, the results became inconsistent. This result is due to not enough carbon species being ablated from the target to form a full monolayer on the substrate. To ensure full coverage on the substrate, more than one monolayer of carbon species must impinge upon the substrate surface. As a result, this method may not be ideal for depositing a single layer of any material. However, as mentioned previously, once enough material is ablated from the target and reaches the substrate, the growth is extremely uniform. The optimal deposition time for graphene nanostructures on both silicon and copper substrates is found to be approximately two minutes, for the conditions studied.

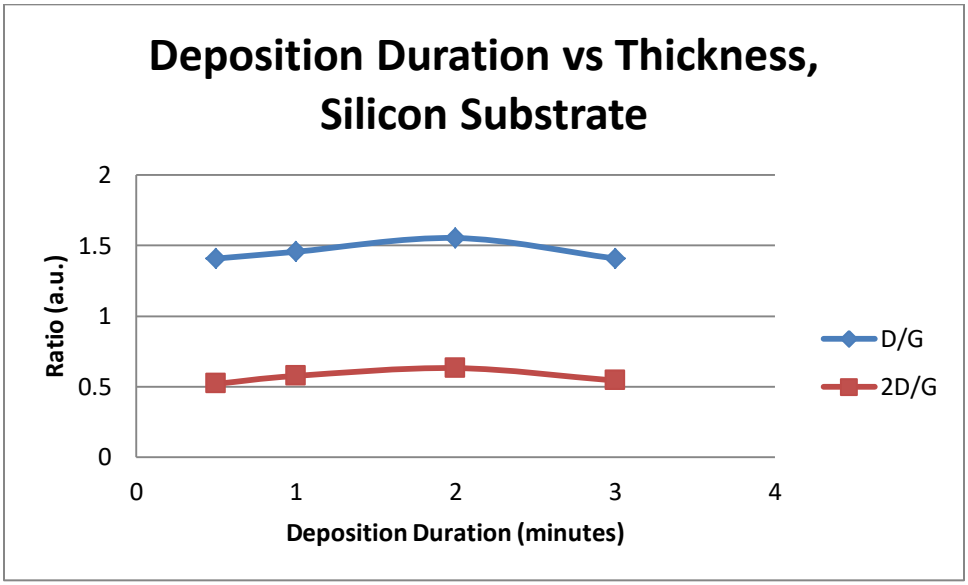

Figure 4–6: Deposition duration vs graphene layer thickness for silicon substrates

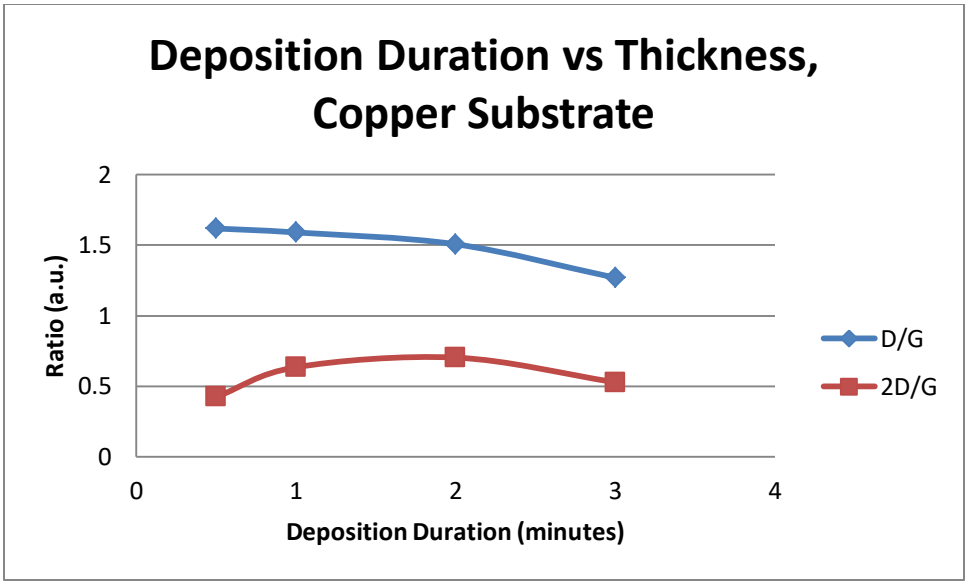

Figure 4–7: Deposition duration vs graphene layer thickness for copper substrates

4.3 Substrate Effects

4.3.1 Mechanical Polishing

The effect of the substrate on the growth of carbon films is examined to determine if any type of pre-processing can affect the graphene films, or if certain substrates tend to produce different results. Table 4-1 shows the effects of mechanical polishing the copper substrates prior to deposition of graphene films. This is done to see if the microstructure of the substrate has a significant effect on the domain and disorder of the resulting carbon films. Polishing is carried out in multiple steps, gradually decreasing the size of the sandpaper grit. The first step used a large grit, typically P120, which corresponds to a surface feature size of about 125 microns. This was followed by a gradual decrease in the coarseness of the sandpaper until grit 1200 was reached, which corresponds to a surface feature size of about 15 microns. Once this size was attained, the surface had a mirror-like finish, and the surface inconsistencies were significantly less pronounced.

The final step involved the use of a liquid solution containing 3-5 micron sized diamond particulates. Once these polishing steps were completed, the substrates were cleaned ultrasonically via the standard method outlined above.

Table 4-1: Ratios of the different Raman peaks of FLG films grown on different substrates using different carbon sources for ablation

Trial	Target	Substrate	D/G Ratio	2D/G Ratio
15	HOPG	Silicon	1.43	0.45
18	HOPG	Virgin Cu	1.51	0.63
18	HOPG	Polished Cu	1.29	0.49
19	Graphite	Virgin Cu	1.60	0.65
19	Graphite	Polished Cu	1.36	0.58
26	HOPG	Virgin 6N Cu, 0.25”	1.31	0.67
26	HOPG	Polished 6N Cu, 0.25”	1.24	0.58
27	HOPG	Virgin 6N Cu, 0.1”	1.19	0.47
27	HOPG	Polished 6N Cu, 0.1”	1.09	0.40
28	HOPG	Flame Annealed Cu	2.09	0.41

From these results, it is evident that both the D/G ratio and the 2D/G ratio decrease for the polished samples. The D/G ratio shows a decrease of about 15% for the standard samples and about 7% for the ultra-high purity samples. The 2D/G ratio shows a decrease of about 16% for the standard samples and about 15% for the ultra-high purity samples. This shows that the microstructure can in fact have an impact on the disorder and domain size of the carbon films, as well as the number of layers of the film. In general, as the microstructure of the substrate becomes more uniform, the grown graphene film has a smaller D peak, which is associated with less disorder and a larger grain size. This is true for all of the copper samples that were tested. Additionally, the 2D/G ratio also decreases for the polished samples. This corresponds to an increase in the number of layers of graphene being deposited. The polished copper substrates have better surface smoothness compared to that for the unpolished samples, leading to a more

uniform growth of carbon with less surface features and micron-sized flaws. However, the films accumulated slightly more layers, as opposed to filling in micron-sized imperfections and defects in the featured copper substrates, which have larger surface areas. Figure 4–8 shows SEM images of few-layer graphene films on different substrates showing the physical differences in microstructure of the various substrates used and how the mechanical polishing affected the surface structure.

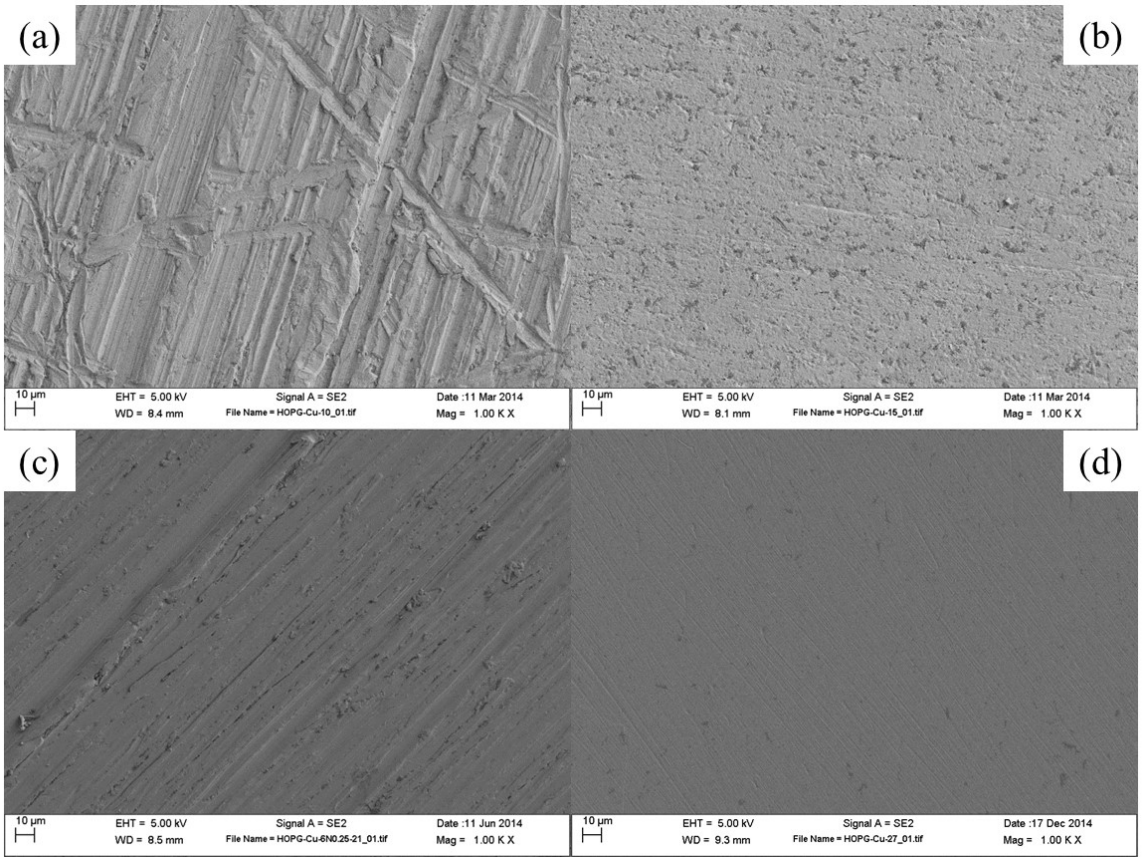

Figure 4–8: FESEM images of FLG on (a) unpolished copper sheet, (b) polished copper sheet, (c) unpolished high purity copper foil and (d) polished high purity copper foil

Figure 4–9 displays the D/G and 2D/G ratios from Table 4-1 graphically to emphasize the effects of mechanically polishing the copper substrates prior to depositing the graphene films. The trends are very consistent, showing a decrease in both the D/G

and 2D/G ratios for polished substrates, regardless of the target or substrate used. The top plot is the D/G ratios, while the bottom plot is the 2D/G ratios. The trials in the legend of Figure 4–9 correspond to their respective growth conditions outlined in Table 4-1 above. This result shows the importance of substrate choice when depositing films grown via PLD. Other surface modification methods have been explored to examine their effect on the growth of nanostructured materials. These other surface modification, which are not included in the scope of this work, include methods such as chemical etching and bonding, heat treatments, and film coatings.

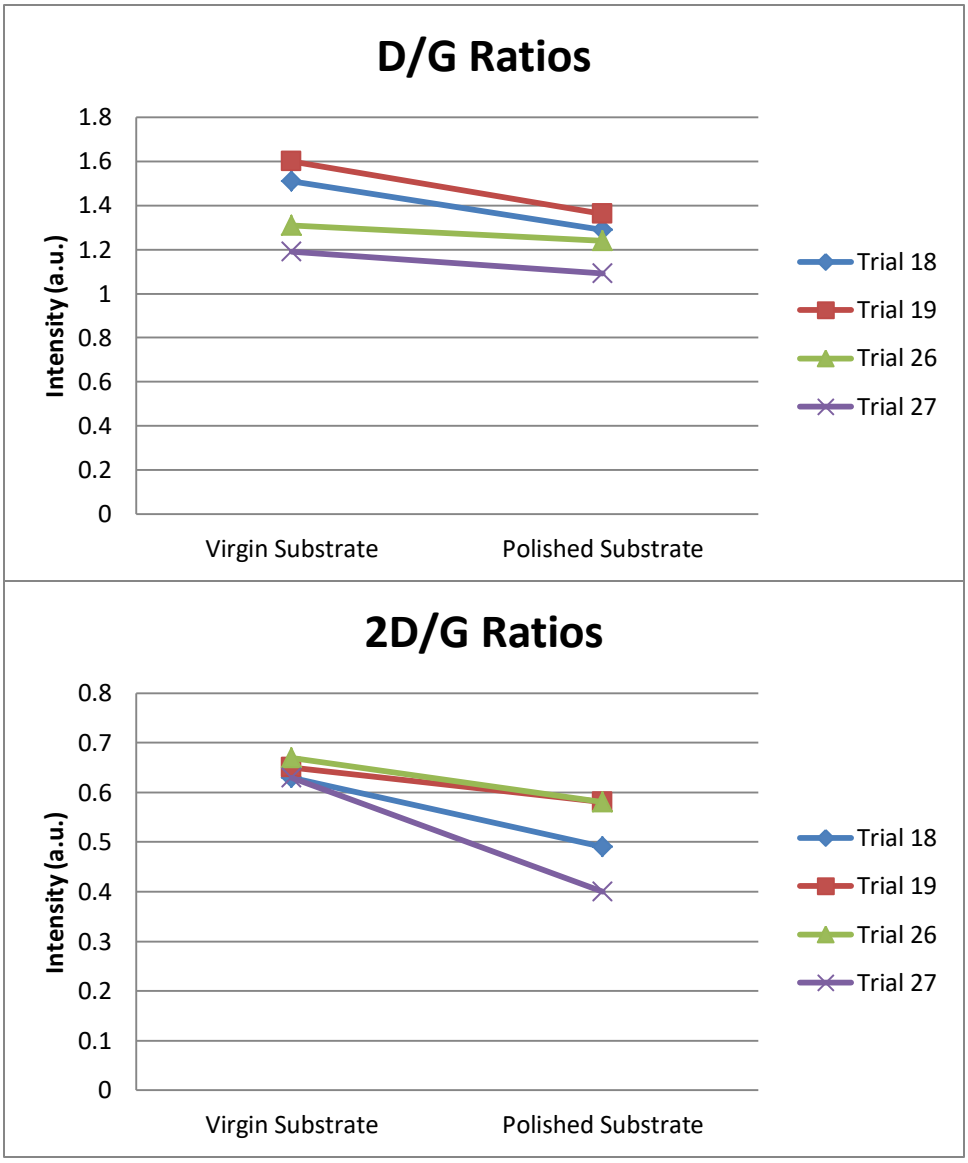

Figure 4–9: Polishing effects on Raman peak ratios of FLG films grown on different substrates from different sources; the legend refers to the growth conditions of different experimental trials outline in Table 4-1

4.3.2 Substrate Material

Further work on how the substrate affects the films are required. Substrates such as other transition metals, thin films of copper deposited by electron beam evaporation, and liquid substrates are currently being explored. Copper films are deposited on silicon

substrates in an attempt to create an atomically smooth, extremely uniform copper substrate for subsequent graphene growth. Initially, thin copper films were deposited on silicon wafers using PLD. However, due to the extremely high electrical and thermal conductivity of copper, the surfaces of the films were covered in spherical particulates as large as several microns in diameter. Using PLD to deposit metals, or any material with a very large thermal conductivity, is a difficult to control process because of the presence of particulates in the deposited films resulting from excessive laser energy absorption by the target surface. While reducing the laser power significantly reduces the amount of particulates, there is no way to completely remove them from the substrate surface. As a result, copper with an atomically smooth surface could not be produced through the conventional PLD method.

Flame annealed copper substrates are also used in an attempt to get a more uniform, atomically smooth surface for graphene growth. Standard copper substrates are annealed at high temperature, just under the melting point of copper (1085°C) using a modified inverse diffusion flame (m-IDF) burner. The m-IDF burner setup is described elsewhere (for in-depth details, see [80]). These films show similar Raman results of previously grown films with regard to the 2D/G ratio, but show a significantly larger D/G ratio. This is typically caused by smaller grain sizes and more disorder in the grown film. While this result is not exactly was expected, it is thought to have occurred due to annealing effects on the copper substrate and the interaction with the flame itself. Such high temperature, volatile annealing can cause more complicated effects on the copper surface, which in turn can affect the growth of graphene films. For example, there could be impurities on the copper substrate from incomplete combustion reactions within the

flame, or there can be a larger or more complicated oxide layer formed on the copper substrate. Further study is required to investigate the mechanisms of carbon growth on flame annealed copper substrates.

In order to get an atomically smooth copper surface, electron beam evaporation is tested as a new technique for fabricating appropriate copper substrates. Electron beam evaporation is another physical vapor deposition method used for depositing thin films onto specific substrates. However, instead of using a laser as the excitation source as in PLD, a beam of electrons, typically supplied via a charged tungsten filament under high vacuum, is used to vaporize the target material. Then, similar to PLD, the vaporized species transfer to the substrate through line of sight, creating a thin film dependent on the ablation duration of the electron beam. The system used for this process is a Varian E-beam System.

For the electron beam evaporator, a graphite crucible (International Advanced Materials, 15C-502-03) is used to hold the target material, which consisted of high purity (99.999%) copper pellets (International Advanced Materials, 130745). The crucible is used to increase heat transfer and uniformly melt and evaporate the target material. The substrates are loaded into the chamber, which is pumped down to at least 10^{-5} torr to allow for the unhindered flow of electrons from the gun to the target. Once this is done, the electron beam is focused onto the copper pellets within the graphite crucible, and the power is slowly ramped up until the copper starts to melt and evaporate. The deposition rates are typically around 10 angstroms per second at 5% power output, and the film thickness is monitored in-situ.

Once the copper films are deposited onto the silicon substrates using electron beam evaporation, the surfaces are examined using standard SEM investigation. It is confirmed that the films are extremely smooth, but atomic force microscopy (AFM) is required to confirm an atomically smooth surface and visualize any imperfections at the atomic scale. These thin copper films are then used as substrates for graphene growth to assess if using an atomically smooth copper surface would result in more uniform graphene growth. However, when reaching the ultimate deposition temperature of 900°C, the copper films began dewetting on the silicon wafer surface and eventually peeling off completely. This is evident through both physical observation and SEM investigation, as shown below in Figure 4–10. A hydrogen anneal is performed on the copper films in an attempt to relieve some of the surface stresses resulting from lattice mismatch between copper and silicon. However, this high temperature annealing (700-900°C) resulted in a widespread dewetting of the copper film on the silicon substrate, hindering any uniform graphene growth on the surface.

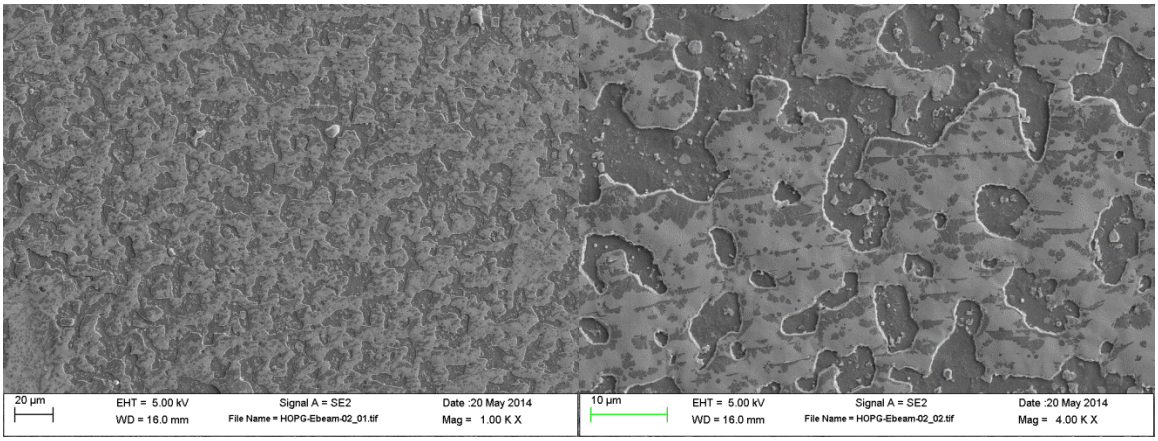

Figure 4–10: SEM images of copper films deposited on silicon wafers via electron beam evaporation, with subsequent graphene growth on top

Graphene films are also grown on nickel substrates to examine how different substrate materials affect graphene growth. When graphene is grown on nickel, the mechanism is different than most surfaces like copper. As mentioned previously, copper has a very low carbon solubility, leading to very little carbon penetrating into the bulk copper during PLD deposition. However, when depositing on a nickel substrate, the carbon atoms can penetrate into the bulk of the nickel due to the moderate carbon solubility of nickel. This is applicable for high temperatures, typically in the 500-1000°C range [10]. Once the nickel substrate starts to cool, these carbon atoms precipitate to the surface of the nickel, leading to the formation of graphene layers. While this mechanism is well known, it is difficult to reproduce without extremely precise temperature control, since the proper cooling rate is essential for graphene growth [10]. While uniform graphene films on nickel are not grown here using PLD, there are some very interesting surface and grain features of carbon species grown on nickel substrates that are observed in the SEM, as seen below in Figure 4–11.

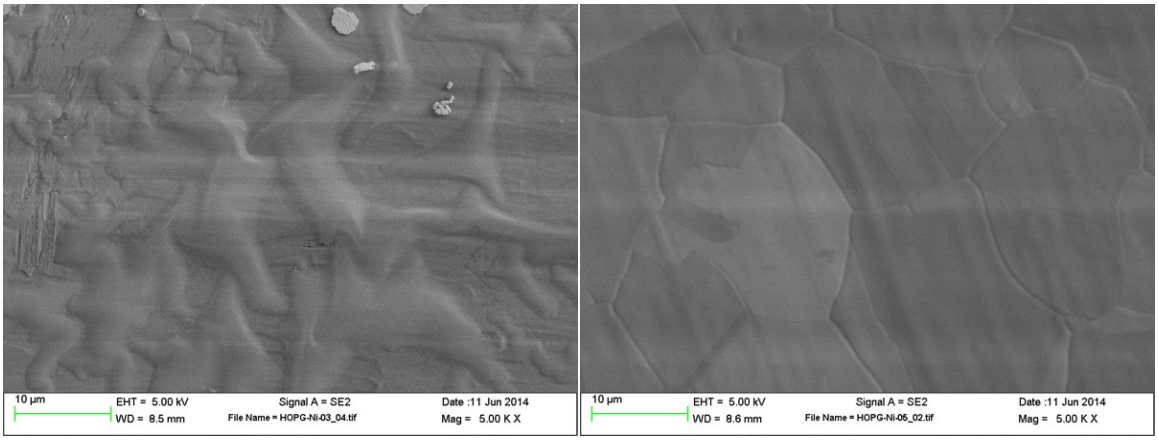

Figure 4–11: Graphene growth on nickel films

Raman spectra of different films grown on nickel substrates are shown below. Figure 4–12 shows Sample 3, which consists of a film grown at 600°C using 266 nm at

5.8 J/cm^2. The spectrum shows a film that consists of partially amorphous carbon with no distinguishable 2D peak. This shows a film that is not entirely made up of graphene, but has some of the sp^2 lattice in an amorphous network.

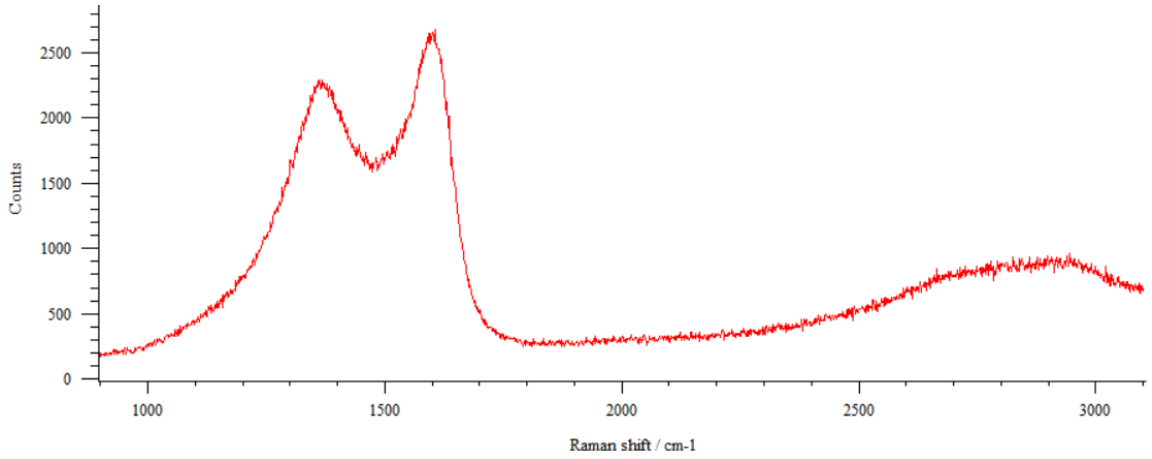

Figure 4–12: Raman Spectrum of Carbon Film on Nickel Substrate, Sample 3

Figure 4–13 shows the Raman spectra of a FLG film grown on a nickel substrate. The film varies in both thickness and structure, as shown by the different Raman peak ratios taken at different areas of the film surface. This may be from local variations of the cooling rate of the substrate, which would lead to local variations of carbon content and structure at specific locations. Thu, graphene growth on nickel is inconsistent without the proper control of cooling rates.

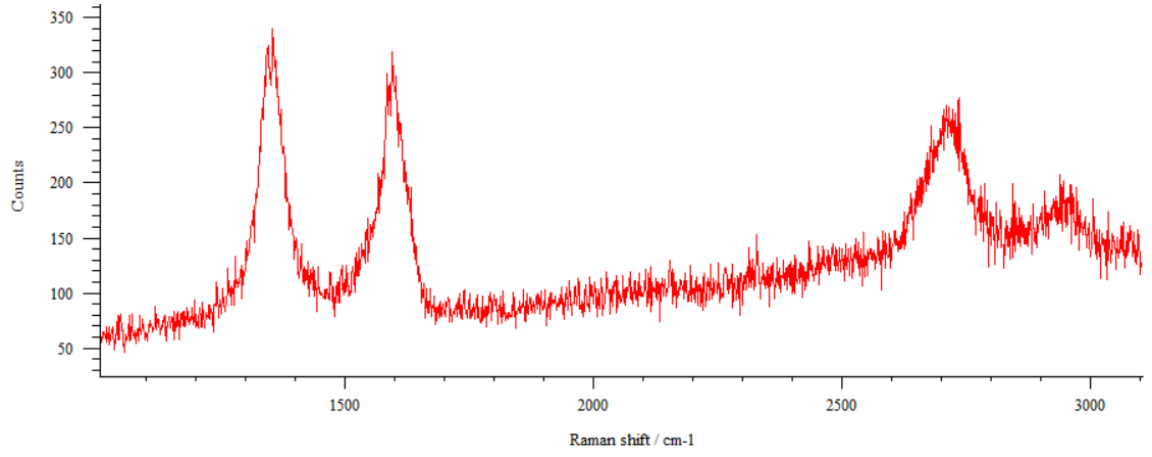

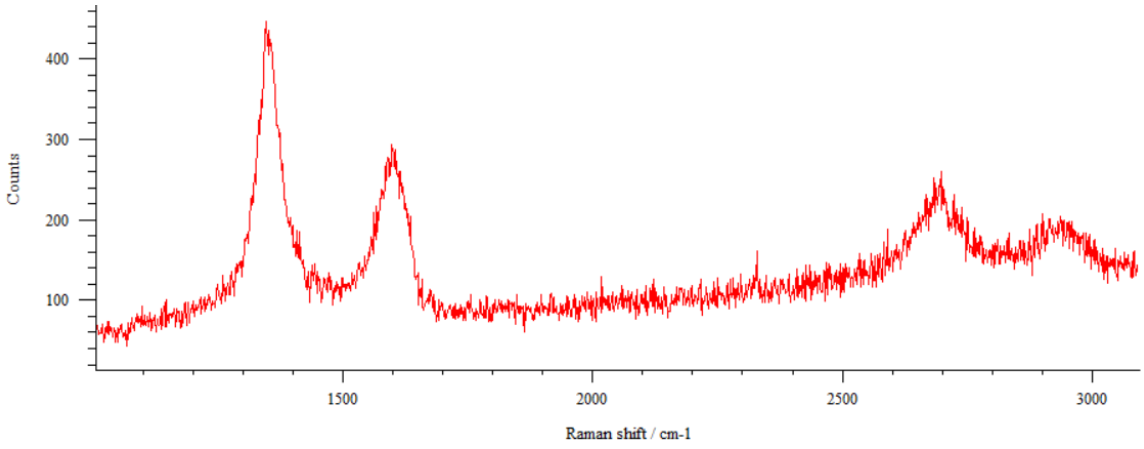

Figure 4–13: Raman Spectra of FLG Film on Nickel Substrate, Sample 4

Another approach to examine how the substrate affects graphene film growth is to try a liquid substrate. It is theorized that by using a liquid substrate with low carbon solubility, the process could be easily scalable, where the fabrication and transfer of the graphene film could be accomplished in a manner similar to the float glass manufacturing process with tin as the float bath. Moreover, the stringent requirements of a high substrate temperature may be circumvented. Having a liquid substrate could supply the mobility necessary for carbon atoms to rearrange in the hexagonal lattice that forms graphene at lower temperatures than that if using a standard, solid substrate. This is tested by using a silver tin solder alloy (Alfa Aesar, 41032, 3.5% Ag, 96.5% Sn weight percent), with a melting point of 221°C (430°F). This particular material was chosen due to the low melting temperature, ease to work with, and safety of materials. A rosin additive (Alfa Aesar, 36734) is also used to help the solder bond with different substrate materials. When applied to a silicon wafer substrate, this solder balled up on the surface and would not wet to cover the entire surface. However, when applied to a copper substrate, the solder wetted the surface and formed a thin layer of solder. The solder-

coated copper substrate was then loaded into the vacuum chamber to attempt a low temperature, liquid substrate graphene growth. However, the results of this experiment are inconclusive, and Raman analysis was unable to be performed accurately on the grown samples. When the substrates were heated to the solder melting temperature, the solder balled up at the bottom of the substrate, and the top of the substrate was heavily featured and only partially covered in solder. This made examination extremely difficult, and it is unlikely that graphene was grown directly on the solder.

4.4 Target and Pressure Effects

The type of carbon source used for ablation is also explored to determine if and how it affects the resulting graphene films. Using two different carbon sources (HOPG and graphite), it is determined that the source of carbon has little effect on the quality and domain size of graphene films synthesized by PLD at high temperature and low pressure. Table 4-1 shows how the different carbon sources affect the resulting carbon films grown at 900°C using 266 nm laser wavelength at 4.4 J/cm^2 for 2 minutes. From these results, it appears that when a compressed graphite target is used as the source material, the D/G and 2D/G ratios are slightly larger than when an HOPG target is used as the source material. This could mean that samples grown from an HOPG target are slightly less disordered and have more layers than samples grown from a compressed graphite target. Besides these slight differences in ratios, the source of carbon has little effect on the resulting carbon films. However, it has been shown that when working in a low pressure argon atmosphere (about 1.0 torr) at room temperature, the source of carbon is a critical parameter, and graphene films are unable to be made with a compressed graphite target as opposed to a pyrolytic graphite target [81]. This method of graphene growth is

proposed to be more of an exfoliation technique, as opposed to the bottom-up growth process that constitutes PLD, mostly due to the pressure at which the growth occurs. This highlights the significance of the deposition pressure when synthesizing graphene via laser ablation.

Laser exfoliation was demonstrated by Qian et al. to grow free standing graphene at room temperature (20°C) and in a low pressure argon environment (1.0 torr) [81]. Using only 1-2 pulses of laser irradiation (Nd:YAG, 532 nm), small flakes (several microns) of pristine graphene are exfoliated from a target and deposited onto a substrate. Depending on the power of the impinging laser, different results were obtained. No material was found on the substrate below a laser fluence of 0.8 J/cm^2, which coincides with the ablation threshold of graphite [47]. Once the threshold is met, the graphite is thermally decomposed into small clusters and deposited as amorphous carbon. Between 1.0 and 10.0 J/cm^2, few-layer graphene is detected on the substrate, implying that larger clusters and sheet fragments are ablated from the target, as opposed to small clusters and individual carbon species. Using this laser exfoliation method, the type of target used is critical to what is deposited on the substrate. Amorphous carbon was the only material found when using a compressed graphite tablet as the target. On the other hand, using an HOPG target yielded graphene clusters on the substrate. This is due to the structure of HOPG, and reinforces the growth mechanism of laser exfoliation as opposed to complete ablation and self-assembly on the substrate surface. Laser exfoliation requires an HOPG target, a laser with photon energy lower than the C-C bond energy (3.7 eV) and an appropriate ablation depth to properly deposit few-layer graphene [81]. The energy of the in-plane covalent bonds in HOPG is 5.4 eV, and the energy of the van der Waals

bonds between layers is 0.06 eV [48]. As a result, using a 2.3 eV laser will not break the in-plane C-C bonds, but it will break apart the loosely bound layers of graphene, leading to exfoliation of intact clusters of graphene.

Figure 4–14 below shows the results obtained from Qian et al. [81] of few-layer graphene grown by laser exfoliation at room temperature and low pressure. The SEM and Raman data show a small region, about 2 microns across, of very high quality few-layer graphene. There is some folding up of the graphene layer, which suggests some instability in the transfer of material or adhesion to the substrate.

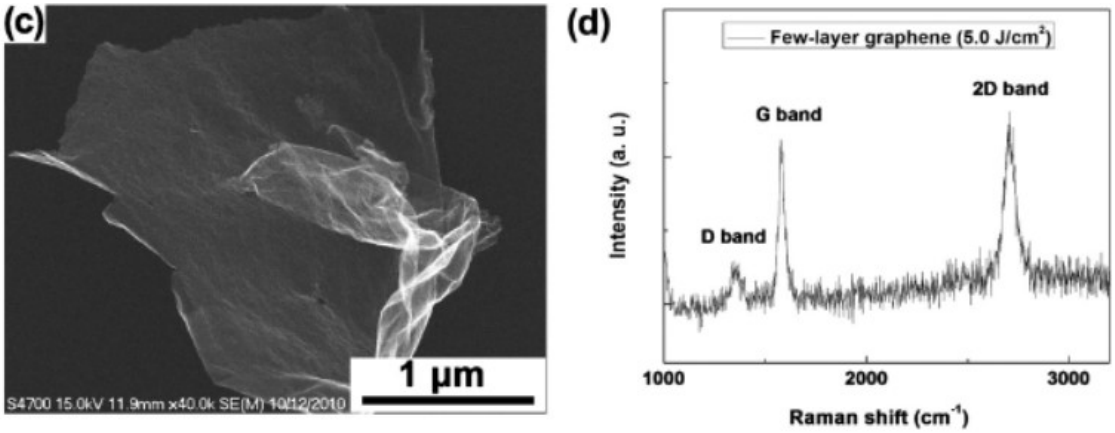

Figure 4–14: FLG grown by laser exfoliation (reproduced from [81])

This result is replicated, with near identical growth conditions, to explore the method of laser exfoliation. Figure 4–15 shows the Raman spectrum of a FLG spot on a silicon substrate after one second of laser ablation performed at room temperature and in 1 torr of argon. The majority of the substrate is bare silicon, but there are a few small areas of FLG particulates, about 10-15 microns in size. The experimental conditions are outlined as Sample 10 in Table 4-2. By comparing Figure 4–14 and Figure 4–15, the obvious difference is the magnitude of the D peak. This indicates that the grain size of the graphene particulate is larger, and the disorder is higher than that in the work done by

Qian [81]. The different in D peak intensity could be a result of differences in the carbon target, slight differences in the laser energy used, or even differences in the exact laser spot size on the target. These differences in experimental conditions could lead to very different growth conditions, which highlights the versatility of the PLD method, but it is also what makes replicating an exact result extremely difficult.

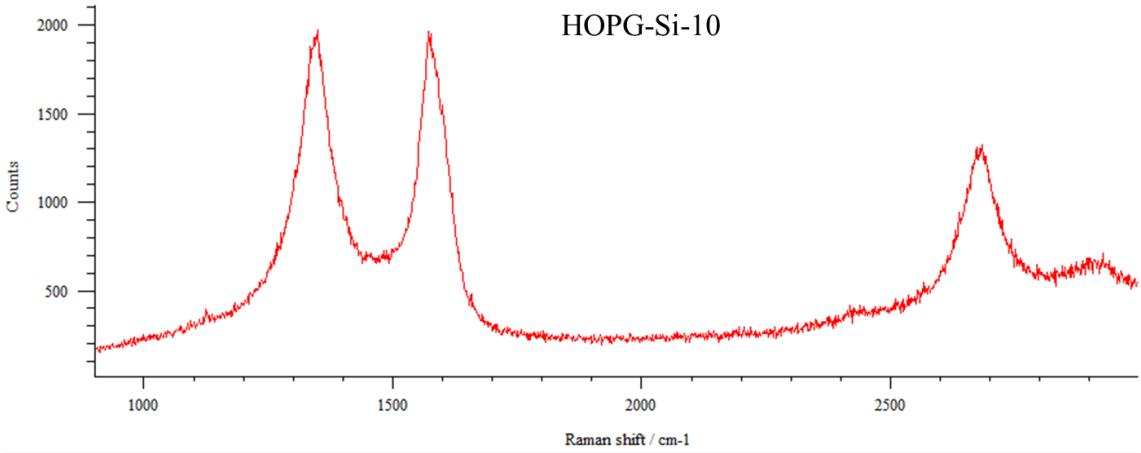

Figure 4–15: Raman spectrum of FLG sample deposited on a silicon substrate after 10 laser pulses

Carbon films have been grown in an attempt to bridge the gap between laser ablation and laser exfoliation. Table 4-2 and Figure 4–16 summarize the results, which show that the source of carbon species being ablated by the laser is crucial for graphene growth at low pressure. Films are grown in 1.0 torr of argon at high and low temperatures using a 532 nm laser wavelength to explore the mechanism of non-vacuum, low pressure growth. At room temperature (20°C) there are large particulates (2-15 microns) with large D peaks that sparsely cover the substrate. On the other hand, at high temperature (900°C) there is widespread coverage of amorphous carbon on the substrate, as shown in Figure 4–17. The high temperature films include particulates of extremely high quality FLG with a very small D peak, even from a graphite target as the ablation

source. This shows a combination of laser ablation and laser exfoliation that is dependent on the deposition pressure and temperature, but not on the carbon source. This contradicts the result of Qian [81] that laser exfoliation of high quality FLG can only be done with an HOPG target.

Table 4-2: Carbon nanostructures grown on a silicon wafer using 532 nm laser irradiation in 1 torr argon

Sample	Target	Temperature (°C)	Deposition Time	D/G Ratio	2D/G Ratio
10	HOPG	20	1 second	0.98	0.49
11	HOPG	20	5 minutes	1.54	0.41
12	HOPG	900	5 minutes	0.15	0.51
13	Graphite	20	5 minutes	0.95	0.12
14	Graphite	900	5 minutes	0.14	0.55

Figure 4–16 summarizes some of the results from the low pressure investigation. Sample 11 uses an HOPG target at room temperature, and the resulting Raman spectrum is of a carbon particulate with a large D peak and a low 2D/G peak ratio, while the majority of the substrate is bare silicon. Sample 12 uses an HOPG target at 900C. Compared to Sample 11, the D peak is significantly lower, and the 2D/G ratio is slightly higher. This sample has an amorphous carbon layer covering the entire silicon substrate, with small particulates of very high quality FLG. Sample 13 and Sample 14 mirror Sample 11 and Sample 12, except using a graphite target instead of an HOPG target. The results are almost identical, with the room temperature samples sparsely covered by carbon particulates with high disorder and low 2D/G ratios, and high temperature (900°C) samples covered by an amorphous carbon film with small particulates of high quality FLG.

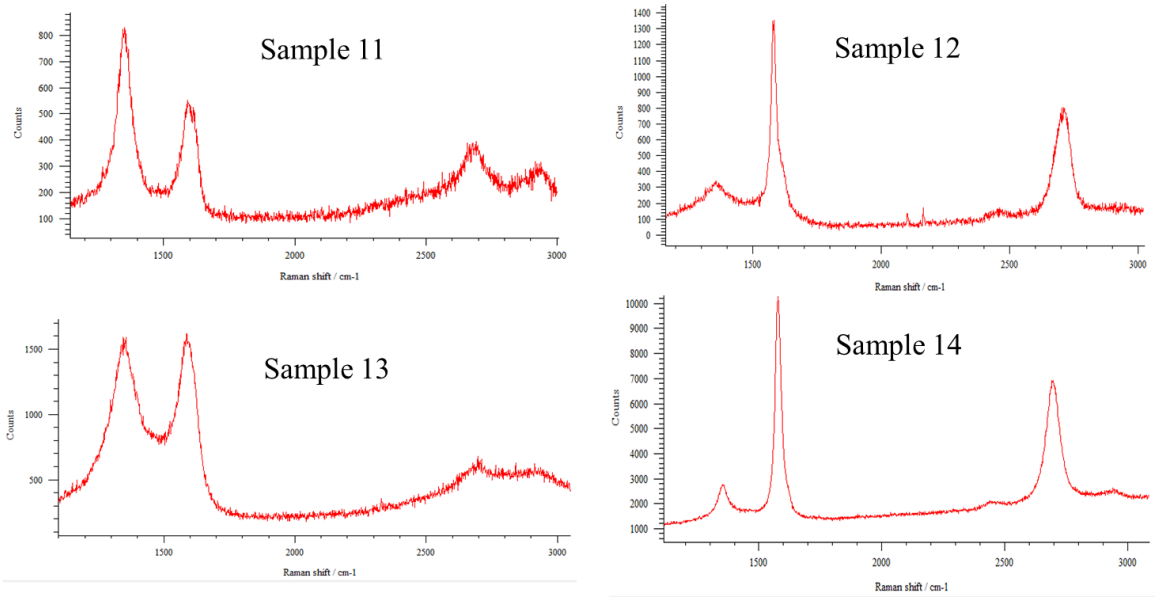

Figure 4–16: Summary of Table 4-2, showing the Raman spectrum of carbon films grown at (Left) low temperature (20°C) and (Right) high temperature (900°C) using (Top) an HOPG target and (Bottom) a graphite target

Figure 4–17 below shows the amorphous carbon film covering the bulk of the silicon substrates in the high temperature (900°C) growth outlined above for Sample 12 and Sample 14. Sample 12 uses an HOPG target, while Sample 14 uses a graphite target. The 2D peak is barely evident, and the D and G peaks have not completely decoupled from a single, amorphous peak.

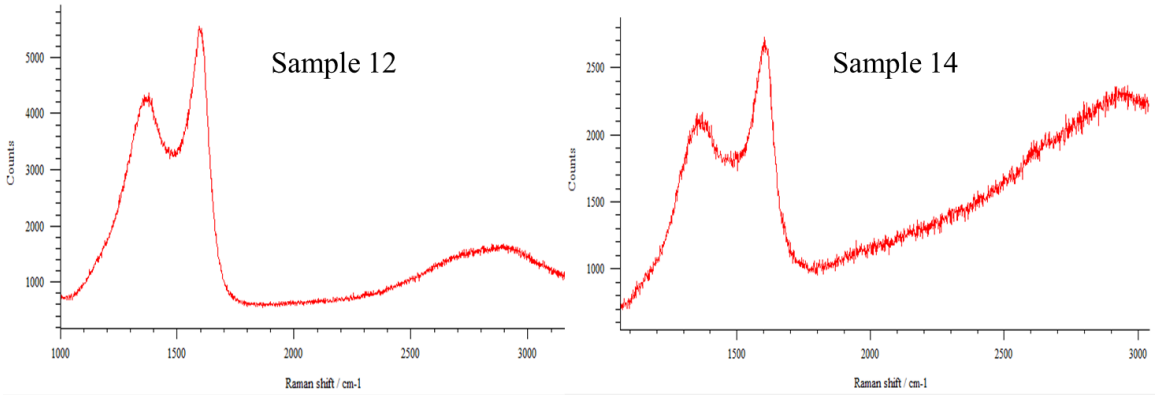

Figure 4–17: Raman spectrum of amorphous films grown at 900°C and low pressure using HOPG target (left) and graphite target (right)

By controlling the deposition pressure at which graphene growth occurs, it is possible to isolate the main factors involved with low pressure graphene growth. When incrementally increasing the deposition pressure from high vacuum (10^{-3} to 10^{-7} torr) to low vacuum (or low pressure, 0.01 to 10 torr), it is shown that as the pressure increases, the D/G ratio actually decreases. However, the 2D peak is very weak and barely distinguishable when films are grown in any background pressure above 10^{-2} torr. This indicates that the films are less structured than graphene and probably consist of a nanostructured graphitic film without long range order or layered sheets like in graphene and HOPG. As a result, it is not feasible to reliably grow graphene films via PLD at low pressure, regardless of the target composition or temperature. Instead, the growth is more of an exfoliation technique, where intact flakes of high quality graphene are ejected from the target and deposited directly onto the substrate. This can be done at room temperature, but when done at elevated temperature (900°C), the resulting flakes are typically higher in quality than those deposited at room temperature. In addition, Figure 4–17 shows that films grown at 900°C consist of an amorphous carbon film covering the substrate, with small particulates of high quality graphene. The films shown in Table 4-3 lack well-defined 2D peaks, but still include graphitic bonding, as shown by the large G peaks. These films are graphitic in nature, with a large amount of sp^2 bonding, but they are not in the ordered, two-dimensional form of graphene. Instead, they are closer to a three-dimensional graphite structure, with grains on the nanoscale, but very little short-range order.

Table 4-3: Carbon nanostructures grown using 266 nm laser irradiation at 4-5 J/cm^2 at varying pressures of nitrogen and hydrogen

Target	Substrate	Pressure (torr)	D/G Ratio	2D/G Ratio

HOPG	Cu-25	10^{-5}	1.6	0.43
HOPG	Cu Foil	0.05 N_2	1.23	0.28
HOPG	Cu Foil	0.1 N_2	1.09	0.27
HOPG	Cu Foil	1.0 N_2	0.99	0.2
HOPG	Si-25	10^{-5}	1.34	0.24
HOPG	Silicon	0.03 N_2	1.44	0.16
HOPG	Silicon	0.1 N_2	1.27	0.22
HOPG	Silicon	1.0 N_2	1.16	0.19
HOPG	Cu Foil	0.1 H_2	0.83	0.19
HOPG	Cu Foil	1.0 H_2	0.7	0.16

Low pressure graphene growth via PLD is unable to be achieved due to several factors. The dominant factor is the energy loss of the ablated carbon species because of collisions with the background gas. This reduces the energy of the carbon species, making it thermodynamically unfavorable to form the hexagonal sp^2 lattice that makes up graphene [82]. In addition, the presence of a background gas increases the amount of gas phase condensation, which creates larger surface features and prevents the formation of a smooth surface. Figure 4–18 summarizes the pressure effects on the peak ratios of few layer graphene films grown on copper substrates, showing the decreasing trend of both ratios as the pressure increases using both nitrogen and hydrogen as the background gas.

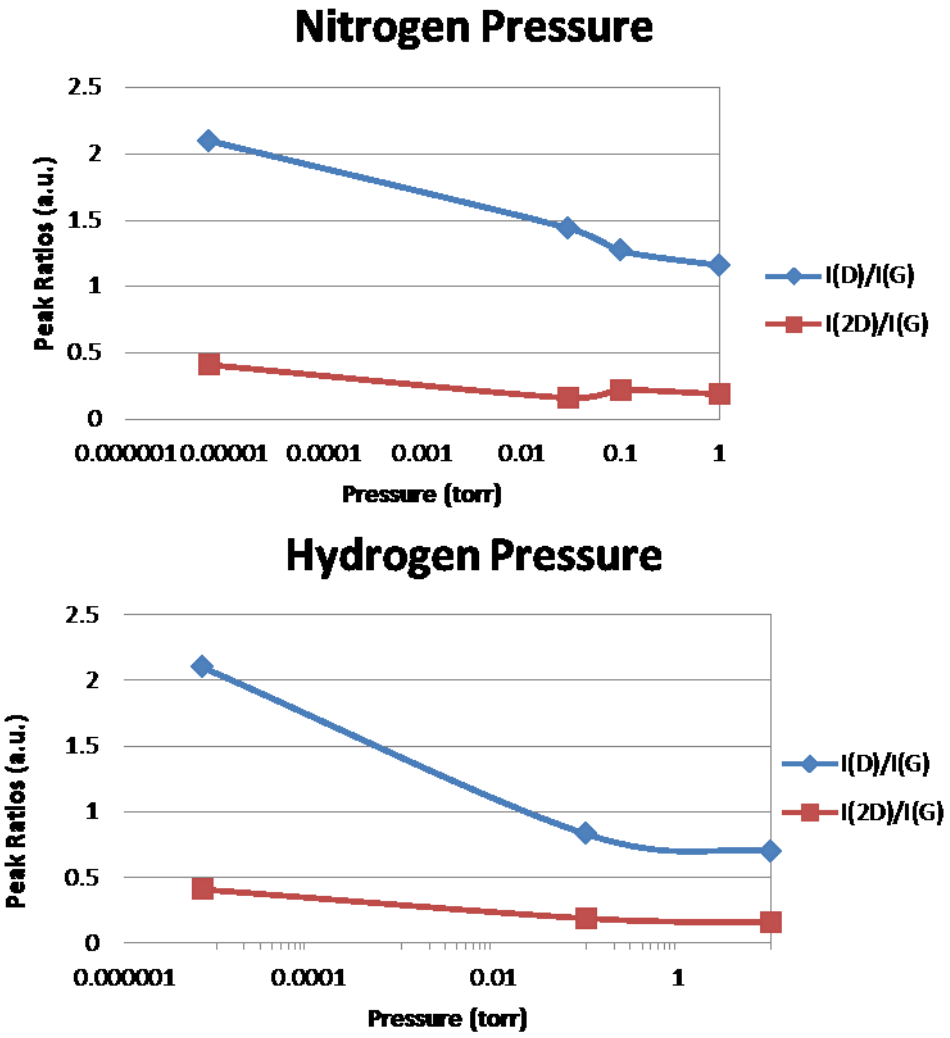

Figure 4–18: Peak Ratios as a Function of Deposition Pressure for Nitrogen Atmosphere (Top) and Hydrogen Atmosphere (Bottom).

4.5 Ablation Plume Analysis

In order to analyze how the ablated material affects film growth, in-situ optical emission spectroscopy is performed on the laser-produced plasma plume. From the resulting spectra, the type of species being ablated can be assessed, and the temperature of the plasma can be calculated. The electron temperature (T) is determined from the

relative intensities of two or more spectral lines of successive ionization stages [83], and can be obtained by a linear fitting of the following equation:

$$ln\left(\frac{I\lambda}{Ag}\right) = -\frac{E_j}{kT} + ln\left(\frac{hcN_0}{4\pi Z}\right)$$

where I is the emission intensity, A is the transition probability (Einstein A coefficient) from the upper state to the lower state with an energy difference of hv, g is the statistical weight of the upper state (j), E_j is the energy of the upper state, and k is the Boltzmann constant. The second natural logarithm term is a constant, so it can be neglected during the linear fitting.

To find the electron temperature (T), a full optical emission spectrum of the laser produced plasma is needed, with the appropriate spectral and intensity calibration factors taken into account. The main peaks in the spectrum are identified using the NIST Atomic Spectra Database Lines Form [84] and fitted using a Lorentzian fit. Once the peaks are identified, the emission intensity (I) is determined by the area of the fitted peak. Then, by plotting E_j vs. $ln(I\lambda/Ag)$ and applying a linear fit to the data, the resulting slope of the fit would yield minus $1/kT$. The values of these parameters are found in the NIST Atomic Spectra Database. Finally, by rearranging and converting units, the electron temperature (T) is determined. The entire process is outlined for the first dataset, showing each individual step leading to the determination of the electron temperature. It should be noted that the temperature resulting from the Boltzmann equation is known as the excitation temperature, and at local thermal equilibrium (LTE), this temperature corresponds to the electron kinetic temperature [85].

Figure 4–19 below is a typical plasma emission spectrum from an HOPG target through a broad wavelength range, showing strong emission lines from C, C^+, and C_2

swan bands. To determine the electron temperature of the C+ ions, the four main peaks identified by the NIST Atomic Spectra Database are at 426.7 nm, 589 nm, 658 nm, and 723 nm. According to the database, several of these peaks are actually a combination of 2 or more peaks located almost on top of one another. In these cases, the emission intensity of the peak (I) is weighted by the ratio of the areas of the fitted peaks in the spectrum. This is found by setting the left side of the electron temperature equation equal to zero, using the constants defined by the NIST Atomic Spectra Database, and solving for I. Table 4-4, shown below, summarizes the peaks for the characteristic case shown in Figure 4–19, with the constants necessary for temperature calculations given by the NIST database (A, g, E_j).

Table 4-4: Peak analysis and constants used for calculating the electron temperature of C+ ions in the laser-produced plasma plume

λ (nm)	A	g (2J+1)	E_j (eV)	I (Area)	ln(Iλ/Ag)
426.7	2.23e8	6	20.95064	0.957362	-15.0019
426.726	2.38e8	8	20.95064	1.362262	-15.0019
426.726	1.59e7	6	20.95064	0.068256	-15.0019
588.977	3.15e7	4	20.15048	2.844046	-11.2282
589.159	3.49e7	2	20.14965	1.575024	-11.2282
657.805	3.67e7	4	16.33312	9.4095	-10.074
658.288	3.66e7	2	16.33174	4.68686	-10.0743
723.132	3.49e7	4	18.04581	2.53551	-11.2403
723.642	4.18e7	6	18.04599	5.04929	-11.1366

Below are the different analyses for the laser-produced plasma temperatures for various experiments, showing the full spectrum of the plasma as well as the linear fitting of the electron temperature equation, with the resulting temperature values summarized in Table 4-5. The full spectrum peak analysis for the plasma plume is attained by using the embedded spectrometer's software "Step & Glue" function, which increased the limited

spectral range of the spectrometer (~40 nanometers) over the required range by seamlessly combining multiple analyses into one continuous spectrum. All of the in-situ spectroscopy results are taken at 0.4 inches from the target surface at a delay of 400 nanoseconds after each laser pulse.

Figure 4–19 shows the laser produced plasma of Trial 33 (HOPG target, 10^{-6} torr, 910°C, 266 nm, 4.9 J/cm^2. The extrapolated temperature of the C+ ions using 9 data points is 12,697 K, with an R^2 value of 0.64.

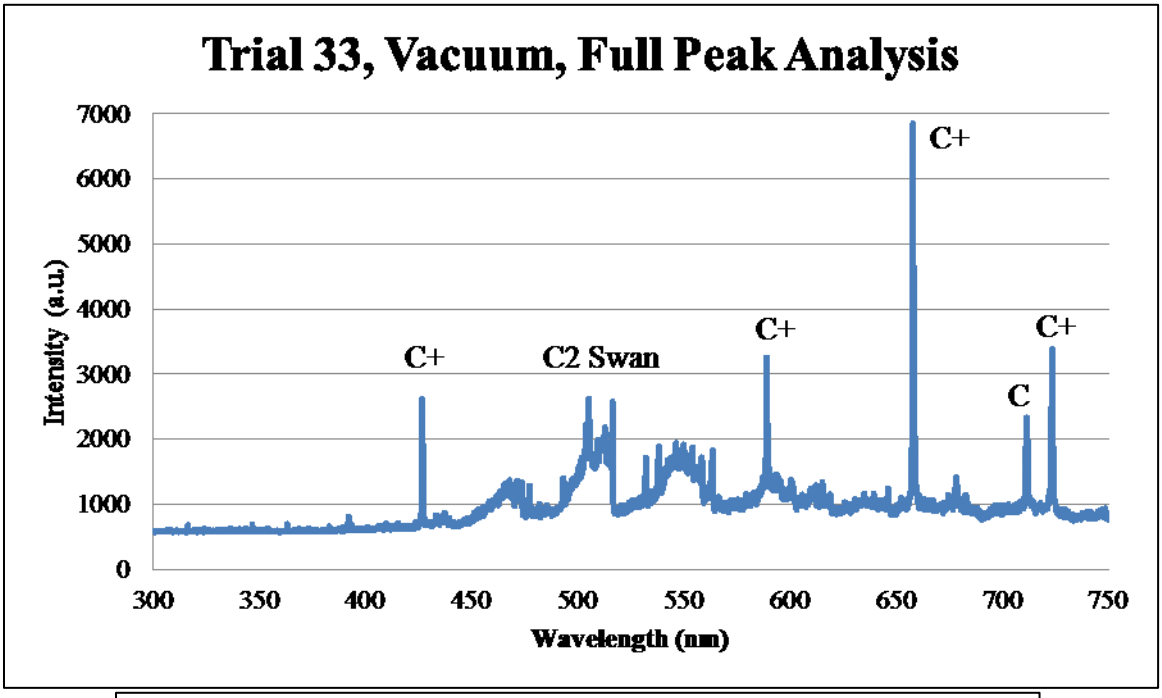

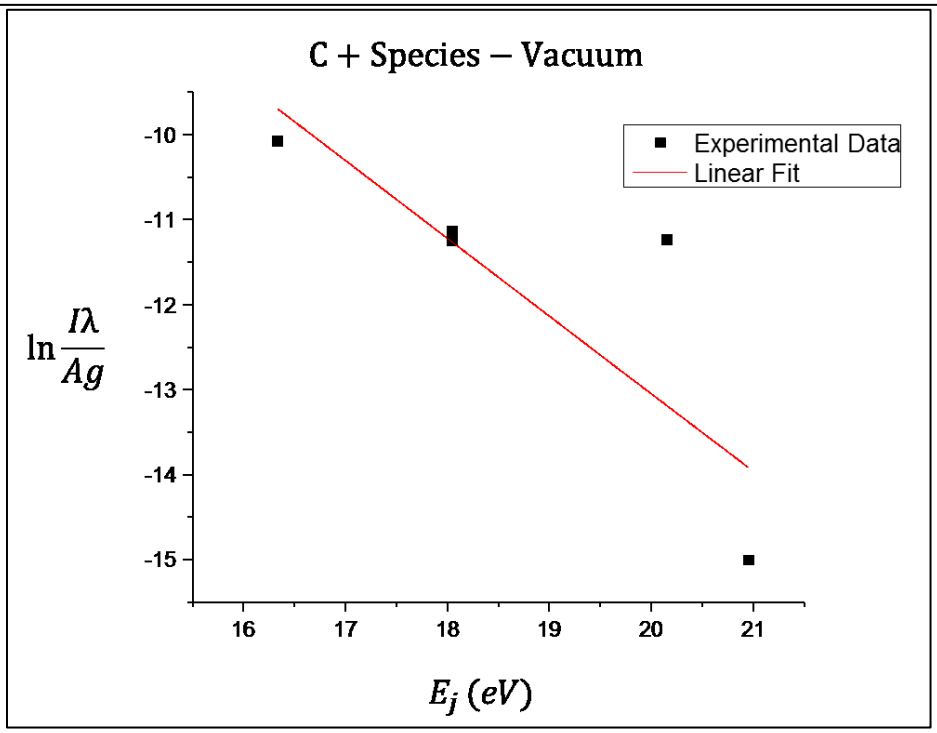

Figure 4–19: (Top) Full spectrum of laser produced plasma of HOPG target showing prominent carbon peaks; (Bottom) C+ plasma temperature linear fit

Figure 4–20 shows the laser produced plasma of Trial 34 (HOPG target, 10^{-6} torr, 910°C, 266 nm, 4.75 J/cm^2). The extrapolated temperature of the C+ ions using 9 data points is 11,859 K, with an R^2 value of 0.74.

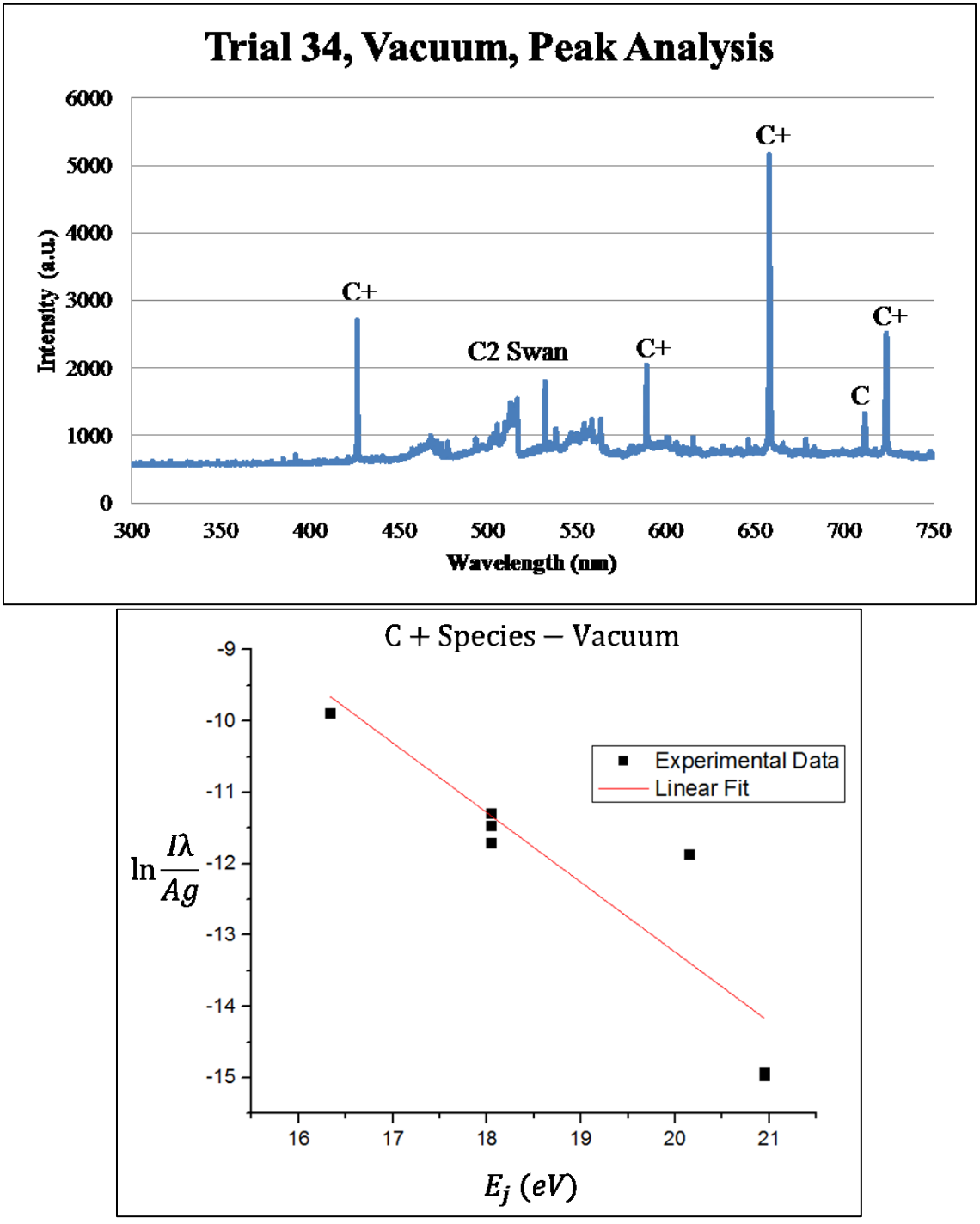

Figure 4–20: (Top) Full spectrum of laser produced plasma of HOPG target showing prominent carbon peaks; (Bottom) C+ plasma temperature linear fit

Figure 4–21 shows the laser produced plasma of Trial 34 (HOPG target, 0.1 torr H_2, 910°C, 266 nm, 4.75 J/cm^2). The extrapolated temperature of the C+ ions using 7 data points is 10,319 K, with an R^2 value of 0.97.

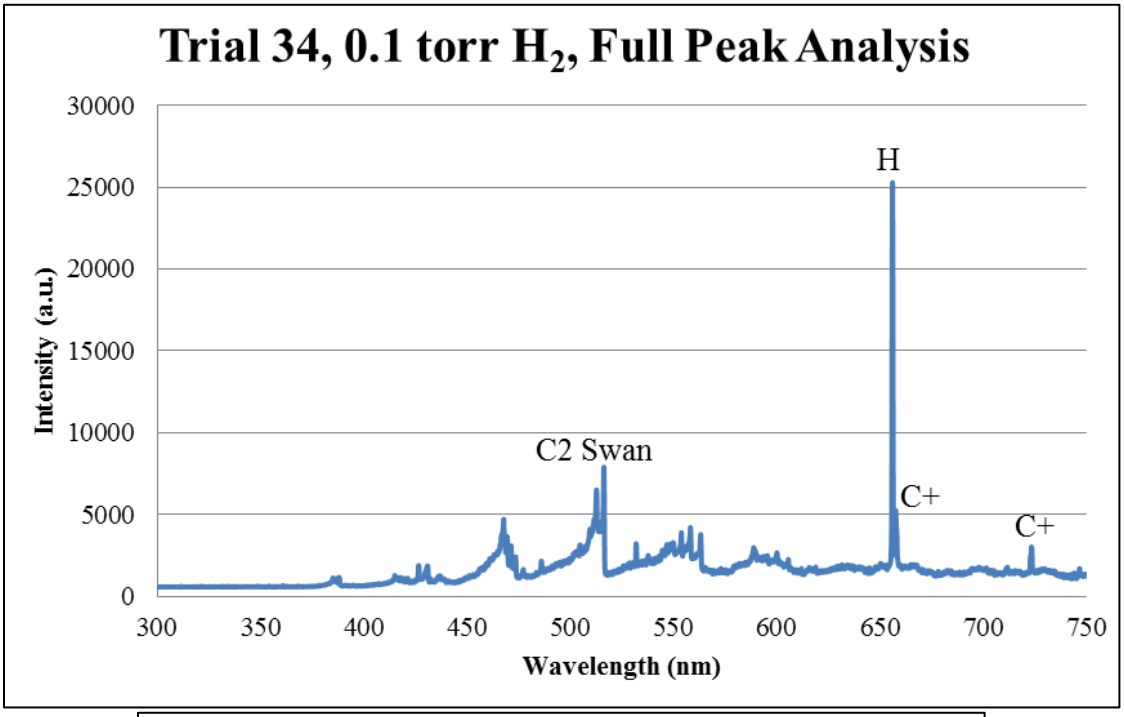

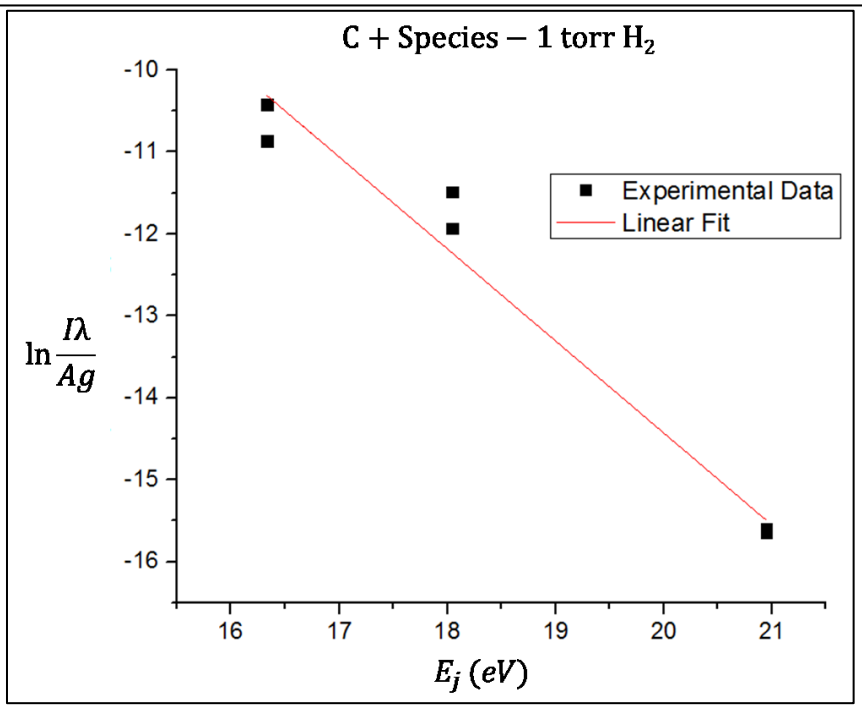

Figure 4–21: (Top) Full spectrum of laser produced plasma of HOPG target showing prominent carbon peaks; (Bottom) C+ plasma temperature linear fit

Figure 4–22 shows the laser produced plasma of Trial 35 (HOPG target, 10^{-6} torr, 910°C, 266 nm, 4.5 J/cm^2). The extrapolated temperature of the C+ ions using 9 data points is 13,539 K, with an R^2 value of 0.71.

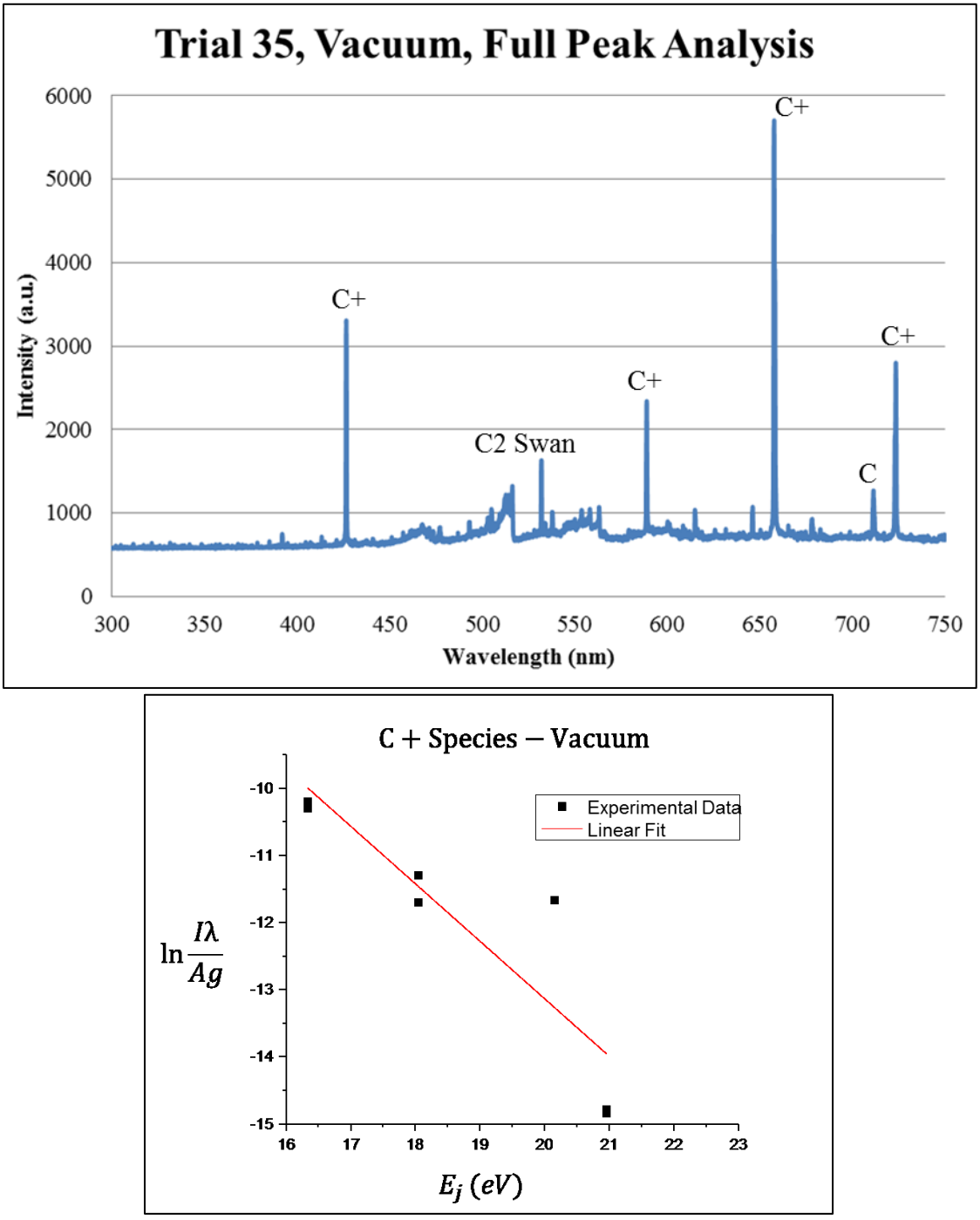

Figure 4–22: (Top) Full spectrum of laser produced plasma of HOPG target showing prominent carbon peaks; (Bottom) C+ plasma temperature linear fit

Figure 4–23 shows the laser produced plasma of Trial 35 (HOPG target, 10 torr H_2, 910°C, 266 nm, 4.5 J/cm^2). The extrapolated temperature of the C+ ions using 8 data points is 10,907 K, with an R^2 value of 0.67.

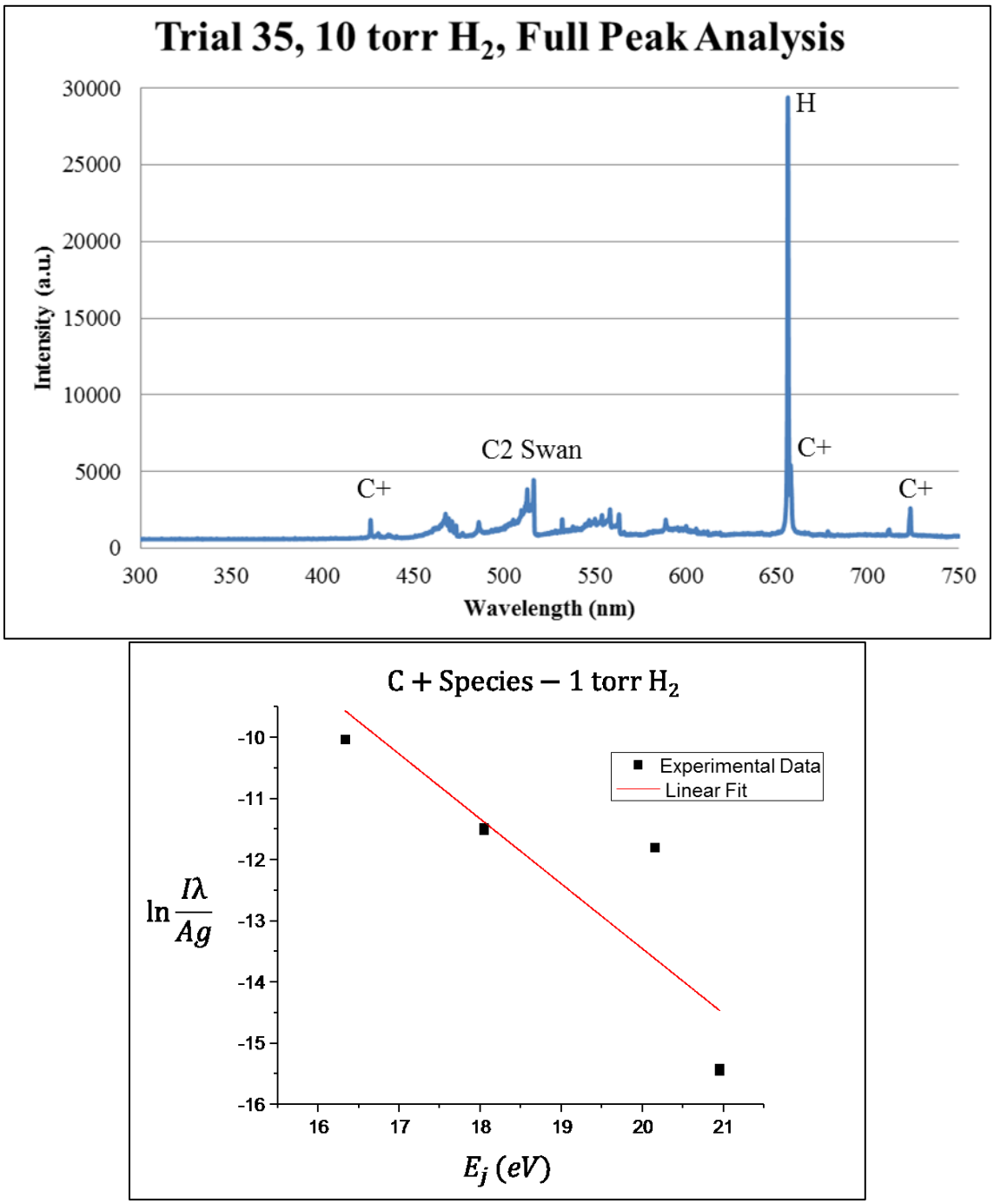

Figure 4–23: (Top) Full spectrum of laser produced plasma of HOPG target showing prominent carbon peaks; (Bottom) C+ plasma temperature fitting

Figure 4–24 shows the laser produced plasma of Trial 36 (HOPG target, 10^{-6} torr, 910°C, 266 nm, 4.2 J/cm^2). The extrapolated temperature of the C+ ions using 7 data points is 14,937 K, with an R^2 value of 0.54.

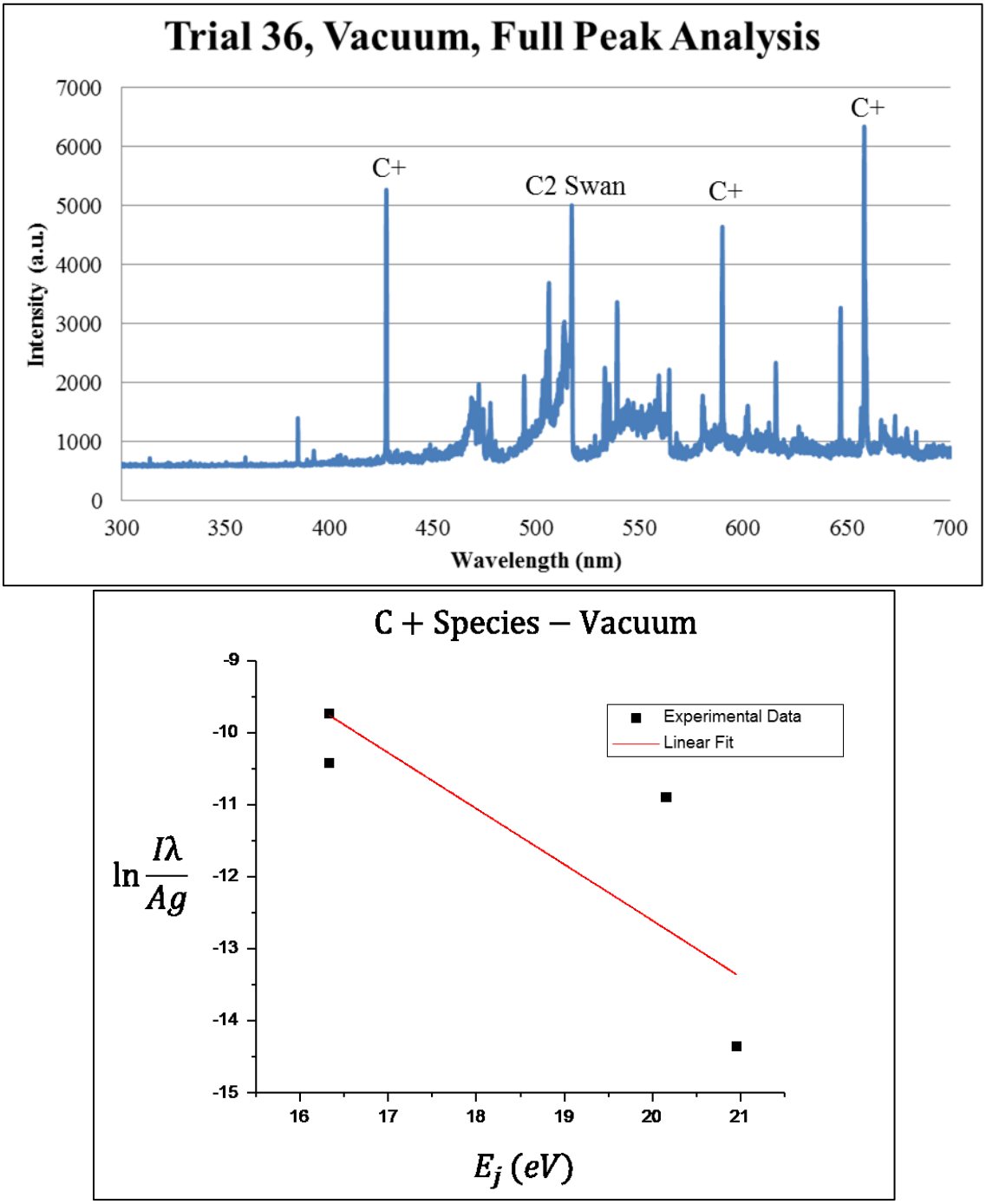

Figure 4–24: (Top) Full spectrum of laser produced plasma of HOPG target showing prominent carbon peaks; (Bottom) C+ plasma temperature linear fit

The previous plots (Figure 4–19 through Figure 4–24) show the linear fits of the electron temperature equation, which is used to calculate the plasma temperature of the laser ablated carbon plume. From these result, the calculated temperature of C+ ions in the plasma plume is approximately 12,000 Kelvin. Furthermore, the C+ ion temperature was calculated while in the presence of a hydrogen ambient gas (1 torr), leading to an ion temperature of about 10,000 Kelvin. This 2,000 Kelvin reduction in temperature coincides with other results in which laser ablation in the presence of a background gas leads to increased collisions between the gas and the ablated ions, effectively reducing the energy, and thus temperature, of the ablated species [82].

Table 4-5 shows a summary of the plasma temperature calculations for the difference samples examined. The neutral carbon atoms (C) have very poor coefficients of determination (R^2 value), meaning the fit is not very accurate. This can be due to the fact that the lines were misinterpreted from other atomic emission lines, or that the temperature of the species themselves is not very consistent. The plasma temperature calculation of the hydrogen atoms only consist of two points, so no R^2 value could be computed, leading to a value with no measure of accuracy. However, for the C+ ions, the values were consistent, leading to more accurate temperature calculations that are consistent with previous calculations [86].

Table 4-5: Summary of Plasma Temperature Calculations

Trial	Pressure (torr)	Species	Temperature (K)	R^2 Value
04/30/2015	10^{-6}	C+	12697	0.6404
04/30/2015	10^{-6}	C	37745	-0.05484
05/06/2015	10^{-6}	C+	11859	0.73641
05/06/2015	0.1 H_2	C+	10319	0.965
05/07/2015	10^{-6}	C+	13539	0.70727
05/07/2015	10 H_2	C	3396	0.11735

05/07/2015	10 H_2	C+	10907	0.66616
05/07/2015	10 H_2	H	4505	N/A (2 points)
08/26/2015	10^{-5}	C+	14937	0.5416
08/26/2015	10^{-5}	C	213050	-0.16627

Transmission electron microscopy is used to confirm the layers of graphene on the nanometer scale. Figure 4–25 below shows the TEM image of a FLG sample grown at 900°C and 10^{-5} torr using a 266 nm wavelength laser at a fluence of 4.5 J/cm^2. The sample is grown directly on a copper TEM grid. The TEM images show very small grain sizes that overlap and intertwine with each other, which is indicative of a high amount of disorder in the film. This supports the results of the Raman data of a large D/G peak ratio and shows how the grains are arranged at the nanoscale.

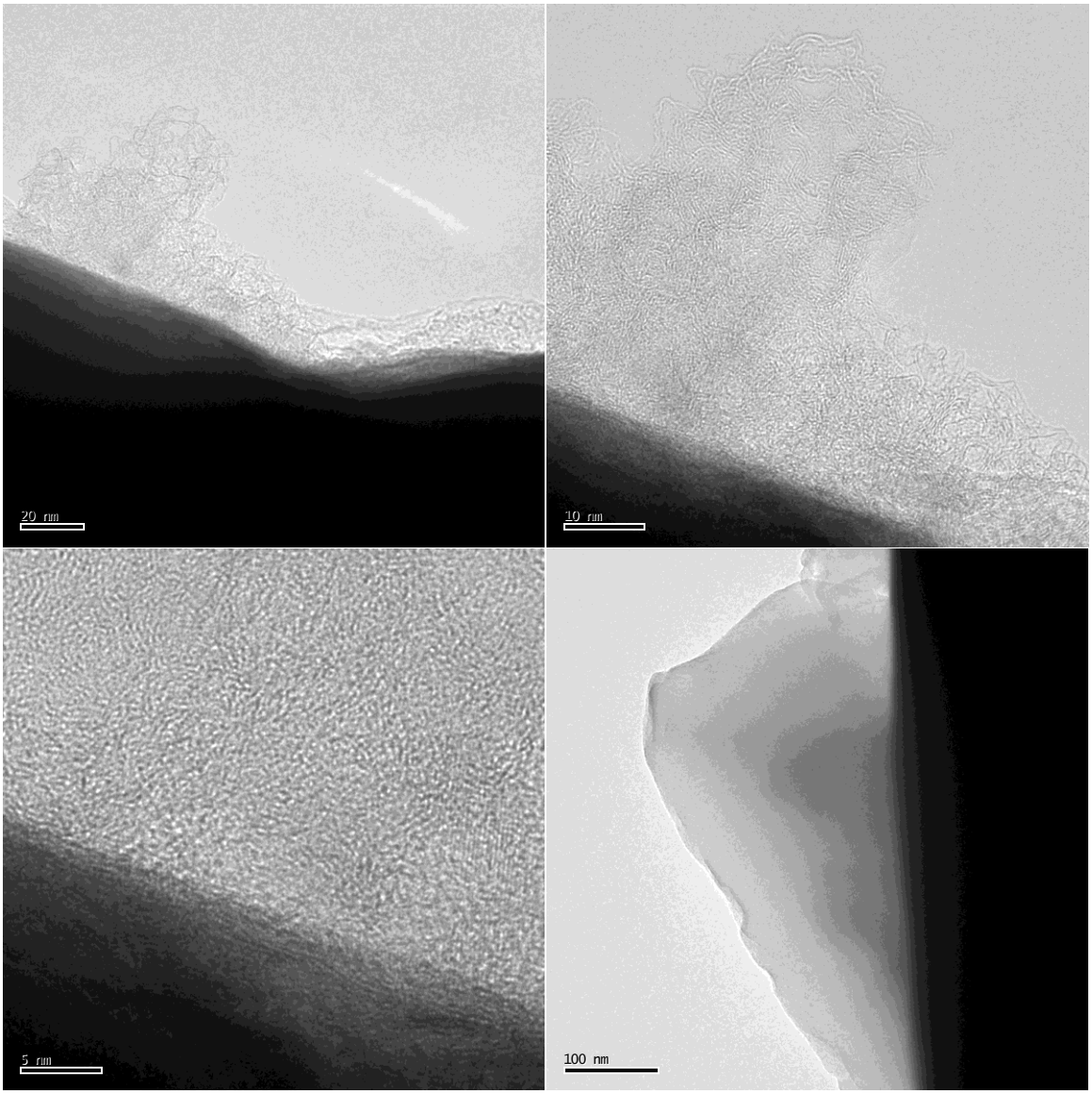

Figure 4–25: TEM Image of FLG Film on Copper TEM Grid

This sample is also examined using SEM to see larger features and overall surface morphology. Figure 4–26 shows low and high magnification of a few-layer graphene sample grown on a copper TEM grid as the substrate. The low magnification image (left) shows the surfaces of the TEM grid with varying degrees of material deposited on top of it. The TEM grid is mounted on a piece of copper. The high magnification image (right)

shows a FLG film with good surface coverage, and very large grains. These grains vary in size and shape, but are typically around 10 microns across.

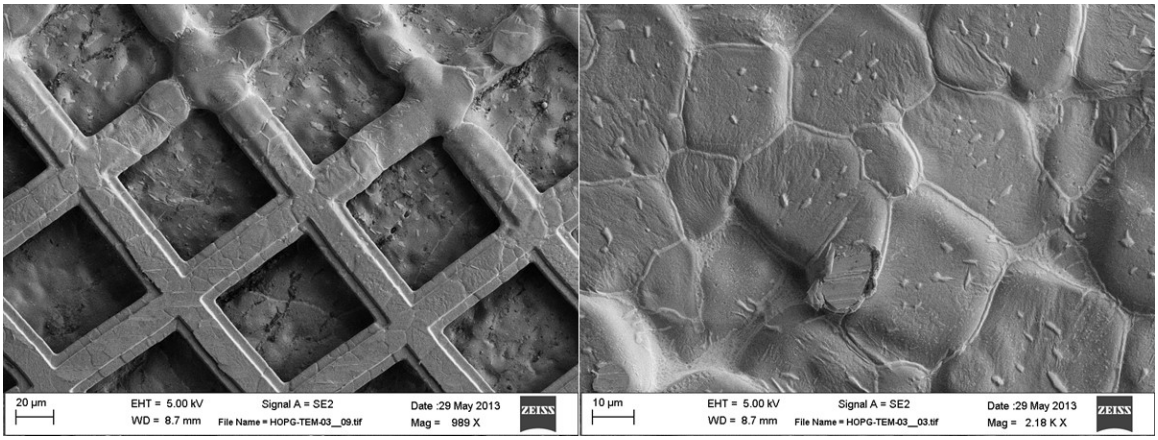

Figure 4–26: SEM analysis of FLG grown on a copper TEM grid under low (left) and high (right) magnification

4.6 Carbon Seeding for Flame Synthesis of Graphene on Arbitrary Substrates

Carbon nanomaterials are grown using a scalable flame synthesis method based on an open-atmosphere multi-element inverse-diffusion flame (m-IDF) burner. This method is scalable, so it has the potential to scale up production and be capable of large quantities of high quality graphene and other carbon nanostructures. Figure 4–27 shows a schematic of the experimental setup

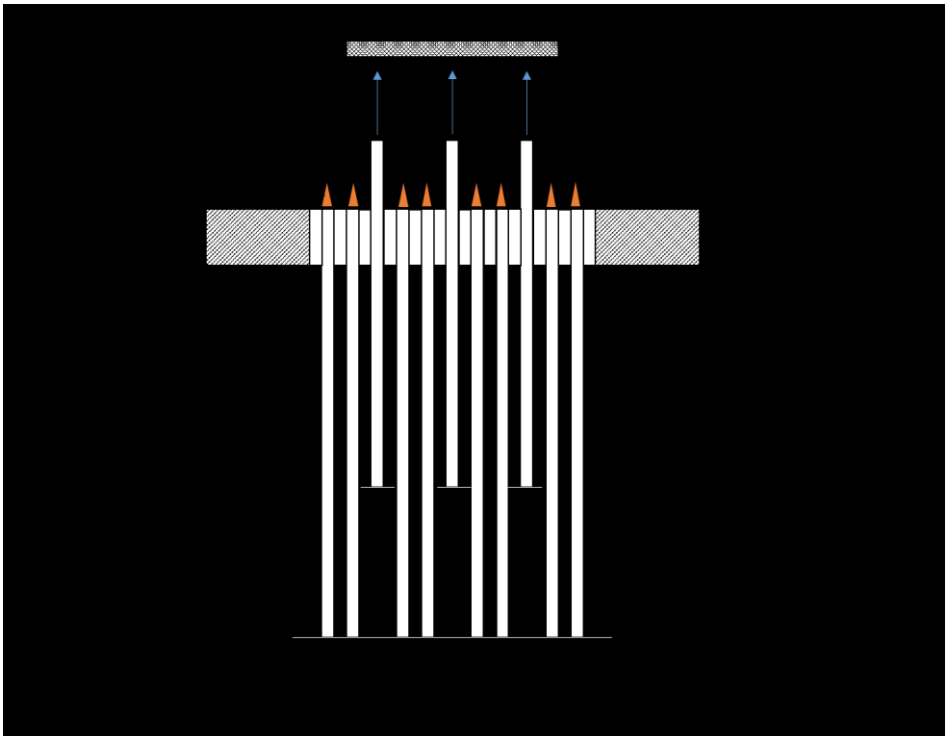

Figure 4–27: Schematic diagram of a modified m-IDF setup modified with uniform-distributed precurson tubes elevated above the burner surface at a fixed height (reproduced with caption from [80])

Using PLD, few layer graphene is grown on Si/SiO_2 wafers at 900°C. These samples are then loaded into the m-IDF setup for hydrogen annealing and additional growth. However, the FLG is completely etched away from the Si/SiO_2 wafer during the hydrogen anneal. This is most likely due to the highly defected nature of the FLG film. This results in weak carbon-carbon bonds, a large number of dangling bonds on the surface of the film, and strong interactions with the hydrogen atoms at high temperature. When methane is added to the hydrogen flow (conditions for graphene growth on copper substrates using m-IDF setup), the graphene film is retained on the substrate, but no changes are evident in the Raman spectrum. From these results, it is evident that this combination of methods does not work for highly defected graphene samples, and no

improvements are made to the FLG films. However, using a pristine graphene sample may allow for the growth or modification of graphene using the m-IDF synthesis method.

In addition, small islands of carbon are seeded onto silicon wafers via PLD in an attempt to grow graphene via flame synthesis (m-IDF method) directly on silicon wafers. Flame synthesis can only be used to grow graphene on copper (and other transition metals) substrates. By combining these techniques, it may be possible to grow graphene and other carbon nanostructures on arbitrary substrates via flame synthesis. Several samples were grown using PLD with very low carbon atom coverage, i.e. very low deposition time. While these samples were not suitable for subsequent flame synthesis growth of graphene, the idea is still a promising one, and further analysis is warranted.

5 Bismuth Telluride Growth and Characterization

Nanostructured bismuth telluride films have been grown on silicon and copper substrates via pulsed laser deposition. This growth mechanism is highly dependent on several experimental parameters, such as substrate temperature and laser power. By adjusting the substrate temperature, deposition pressure, and laser parameters, a range of morphologies have been grown from thin films to nanorods to hexagonal nanoplatelets. We also explore how the substrate material affects the as-grown film characteristics, as well as how the wavelength and energy of the incident laser beam affects the growth mechanism of the ablated material. The growth conditions can then be directly linked to structural and transport properties of the bismuth telluride films, correlating the thermoelectric properties of the films to the structure and morphology of those films on the nanoscale and how the films are grown. The deposited samples are characterized using micro-Raman spectroscopy, scanning electron microscopy, energy dispersive X-Ray spectroscopy, and X-Ray diffraction.

5.1 Laser Parameter Effects

Bismuth telluride films were initially grown in two different regimes, a high laser fluence regime and a low laser fluence regime, to determine how the incoming energy of the laser beam affects the growth of the films. The high fluence regime consists of a laser fluence greater than 20 J/cm^2 on the target surface, while the low fluence regime consists of a laser fluence less than 5 J/cm^2 on the target surface. The films grown using the high laser fluence (Trials 1-5, Table 5-1) are inconsistent and made up of agglomerates of nanoplatelets with low coverage and low crystallinity. In addition, the stoichiometry of the films varied significantly and without much order or reproducibility. The high laser

fluence causes extremely energetic evaporants to eject from the target surface, which leads to the creation of films with incorrect stoichiometry and inconsistent morphologies. Regardless of other experimental parameters, Bi_2Te_3 films could not be made. This is consistent with previous results of an ideal laser fluence close to 1.0 J/cm^2 for stoichiometric bismuth telluride growth [65].

On the other hand, the low laser fluence regime (all subsequent trials starting with Trial 6) produced much more consistent films in terms of stoichiometry, crystallinity, and substrate coverage. In general, the stoichiometry was within 6% of the proper Bi_2Te_3 chemical composition (40% atomic bismuth, 60% atomic tellurium). Slight changes to the laser energy has very little effect on the grown films when working in the optimal range of 1-5 J/cm^2, so further investigation focuses on how other parameters affect bismuth telluride film growth.

Most of the samples in this work are grown using 266 nm laser irradiation on the target. However, to examine how the laser wavelength may affect film growth, 532 nm laser irradiation is also used to ablate the target material. Films grown using the 532 nm laser wavelength typically have very good stoichiometry and are very crystalline in structure. These films also exhibit larger grain sizes when compared to other films grown in this study, with one of the samples actually consisting of nanoparticles as opposed to a uniform film while still having 100% surface coverage. This unique sample (see Sample 8 below in Figure 5–19) is the only sample to have grown entirely of nanoparticles with diameters ranging from 200 to 400 nanometers. Another interesting feature of this sample is the difference in shape of the nanoparticles depending on the substrate used. This will be discussed further in the following section (Section 5.2). In addition, Sample

12 has very prominent, mostly hexagonal-shaped nanoplatelets randomly oriented within and protruding from the film surface. This sample, which was grown using 532 nm laser irradiation, has a unique surface structure and pristine stoichiometric transfer of bismuth telluride. Since most of the previous work involving bismuth telluride growth via PLD uses excimer lasers (193 nm, 248 nm, and 308 nm are the most common excimer lasers), these growth conditions and resulting samples are unique. Thus, it leads to some interesting questions regarding the role of the laser wavelength in the ablation and subsequent growth of bismuth telluride thin films and nanostructured materials.

5.2 Substrate and Pressure Effects on Surface Features

The low laser fluence trials are consistent enough to start looking at how other parameters affect the film growth, starting with substrate temperature, substrate material, and deposition pressure. These parameters are found to be crucial in determining the nanostructure and the crystallinity of the resulting films. At higher temperatures (300°C) and lower pressures (0.035 torr), there is a slight excess of bismuth, confirming the higher volatility of tellurium and the difficulty in achieving consistent stoichiometric transfer of bismuth telluride [13]. Of the first five samples grown (high laser fluence regime), four of the samples were deposited at temperatures of at least 300°C. This may also explain the inconsistent results, since this is the top end of the optimal range for bismuth telluride growth [65]. Furthermore, this may also be the reason for the poor sample coverage on the substrate. Temperatures in this range could be ejecting the already energetic incoming material from the substrate surface, leading to sparsely covered substrates and extremely low depositions rates, as see in Trials 1-5 of this study.

When the deposition pressure drops below 0.1 torr, film growth becomes less consistent. For example, Trials 9 and 11 use a deposition pressure of 0.035 torr of argon, and the resulting films have different chemical compositions based on the material of the substrate used. On a copper substrate, the bismuth concentration is lower than on a silicon substrate, leading to a slight excess of tellurium. This discrepancy directly contradicts previous research, which claimed that the material of the substrate is only expected to affect the morphology of the film, not the stoichiometry or crystalline structure [65]. Thus, how the substrate material affects film growth requires further analysis. The different trials and their experimental parameters are summarized below in Table 5-1.

Table 5-1: Summary of Bismuth Telluride Films Grown via PLD

Trial	Temp. (°C)	Pressure (torr)	Fluence (J/cm^2)	Laser λ (nm)	Surface Morphology	Stoichiometry (EDS)
1	300	1.0 Ar	33	266	Nanoplatelets	30% Bi
2	190	0.15Ar	22	266	Nanoplatelets	40% Bi
3	300	1.0 Ar	82	266	Nanoplatelets	35% Bi
4	325	1.0 Ar	67	266	Nanoparticles, Nanorods	-
5	300	0.1 Ar	49	266	Nanoplatelets	49% Bi
6	300	0.1 Ar	2.0	266	Film, Nanoplatelet	45% Bi
7	200	0.1 Ar	2.7	266	Film	37% Bi
8	200	0.1 Ar	2.5	532	Nanoparticles	40-42% Bi
9	200	0.035 Ar	2.7	266	Film, Nanoparticles	Si: 44% Bi Cu: 34% Bi
10	250	0.1 Ar	3.2	266	Film, Nanoplatelets	34-36% Bi
11	200	0.035 Ar	3.4	266	Film, Nanoplatelets	Si: 45% Bi Cu: 37% Bi
12	200	0.1 Ar	3.9	532	Film, Nanoplatelets	36% Bi
13	200	1.0 Ar	3.8	266	Sparse coverage, Delaminated	37% Bi
14	200	1.0 N_2	4.5	266	Film, Spheres	37% Bi
15	200	1.0 Ar	3.9	266	Film, wavy	38% Bi

16	200	0.1 Ar	5.0	532	Film, protrusions	36% Bi
17	200	0.1 Ar	4.6	532	Film, protrusions	38% Bi
18	300	0.03 Ar	3.4	266	Film	24% Bi
19	250	1.0 Ar	2.9	266	Nanoplatelets, Not a film	36% Bi
20	200-300	0.1 Ar	3.4	266	Film, protrusions	49% Bi

5.2.1 Electron Microscopy Analysis of Surface Features

The surface morphology of the initial bismuth telluride films generally consists of an agglomeration of nanoplatelets, a collection of nanoparticles, or more of a film-like surface. These surface features are examined in depth using electron microscopy. Figure 5–1 shows the low coverage nanoplatelets that dominate the surface morphology in the high laser fluence regime. Figure 5–1 (a) and (b) are samples made up of agglomerates of nanoplatelets that show inconsistent stoichiometry, coverage, and crystallinity. The deposition time should be long enough to cover the entire substrate, but the non-ideal growth conditions prevent that from occurring. These conditions are also responsible for the interesting appearance of the nanoplatelets, which seem to be very thin in the direction perpendicular to the substrate surface, but have varying lateral dimensions and geometrical shapes. The samples shown in Figure 5–1 (c) and (d) shows some interesting features that are not present in any of the other samples. The sample grown on a silicon substrate (Figure 5–1(c)) shows three-dimensional hexagonal nanoparticles and a small number of nanorods. These hexagonal nanoparticles seem to be larger in the direction perpendicular to the substrate surface, giving them more of a three-dimensional look, as opposed to the more flat appearance shown in Figure 5–1 (a) and (b). On the other hand, Figure 5–1(d), which is grown on a copper substrate, shows clusters of nanorods growing

along the grooves in the micron-sized features of the copper surface. These types of features are unique and have not been replicated in the other films grown during the scope of this work.

Figure 5–1 (e) and (f) show films in the low laser fluence regime that includes both a low coverage area as well as a high coverage area. Figure 5–1 (e) shows a region of low coverage that looks similar to films grown in the high laser fluence regime with patches of nanoplatelets, while Figure 5–1 (f) shows a region of good coverage yet unorganized domains of nanoplatelets. Although this sample is in the more ideal low laser fluence regime, the temperature is still slightly high. This may give rise to the discrepancy in surface morphology, showing both film-like and nanoparticulate behavior on the substrate surface. Having two distinct regions of differing surface morphology in the same sample is another unique occurrence in this work and has not been replicated.

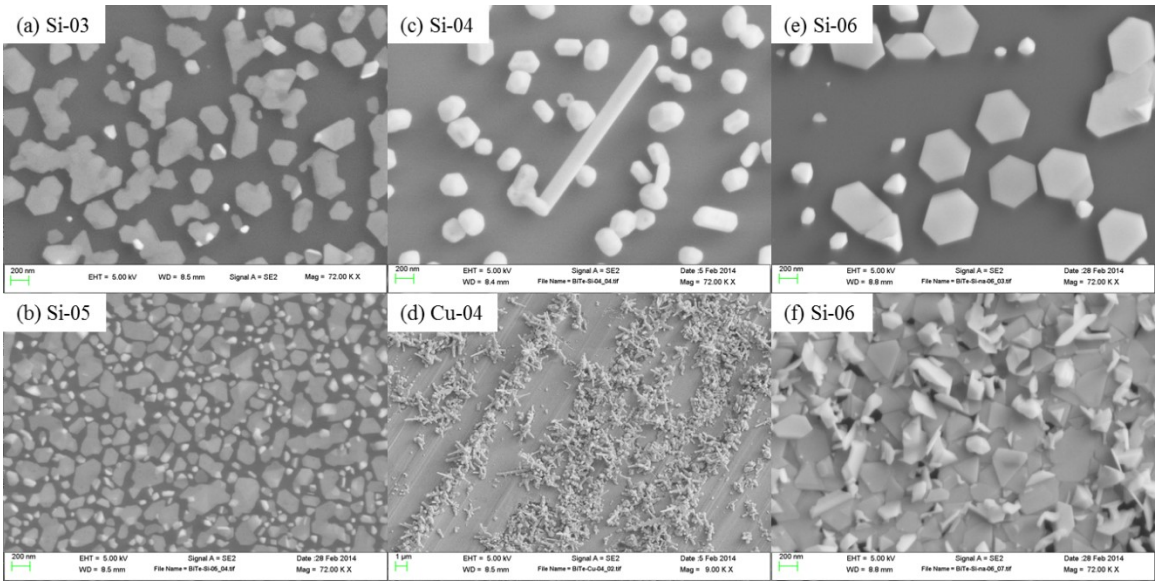

Figure 5–1: FESEM images of the surface morphology of different bismuth telluride films

For the low laser fluence regime, film coverage and crystallinity were in general much better than films grown in the high laser fluence regime, i.e. films were continuous and more crystalline in nature. Figure 5–2 (a), (b), and (d) show nanoparticles that are typically 50-400 nanometers in size, and are either rounded (Figure 5–2 (a) and (d)) or hexagonal-like (Figure 5–2 (b)) in structure. Sample 8 (see Figure 5–19) is the only sample made entirely of nanoparticles with the correct chemical composition. This sample is extremely interesting in morphology, especially considering the differences that can be seen by using different growth substrates. As mentioned previously, most of the previous work done on the PLD growth of bismuth telluride is done with excimer lasers. Thus, samples grown using 532 nm laser irradiation such as Sample 8, are difficult to classify, but extremely interesting and promising in terms of exploring new morphologies and nanostructured properties. Sample 9 (copper substrate) is also made up of nanoparticles, but the size of the nanoparticles are much smaller than Sample 8, and the stoichiometry is slightly rich in tellurium. The extremely small nanoparticles that make up the sample may be a result of a change in the growth regime of film-like structures versus structures made up of agglomerates of nanoparticles. The deposition pressure of Sample 9 is lower than the optimal range of growth parameters (0.035 torr, argon gas), which may be the reason for nanoparticle growth, incongruent chemical composition, and the deposition and/or evaporation of chemical species at the substrate surface.

On the other hand, the film-like surfaces (Figure 5–2 (c), (e), and (f)) are generally very flat with some protruding nanometer-sized hexagonal platelets (Figure 5–2 (e)) or mismatched planes (Figure 5–2 (f)). These different morphologies are a result of both the deposition parameters and the substrates used. Ideal growth conditions, outlined

above in Section 2.3.4, typically yield smooth, continuous bismuth telluride films with consistent surface morphology, stoichiometry, and crystallinity. From these ideal parameters, individual variables are examined to see how they affect film growth and material properties. When films are grown at pressures less than 0.1 torr (background gas is assumed to be argon, unless otherwise specified), the film morphology starts to differentiate based on the substrate used for growth. For example, Sample 9 and Sample 11 have two different surface morphologies based on if the bismuth telluride film was grown on copper or silicon. This is in agreement with previous work stating that the substrate material only affects film morphology [70].

In general, as the pressure increases, the films become less smooth and compact and more like an agglomeration of nanoparticles. This is most likely due to increased gas phase condensation that occurs at higher pressure. Higher pressure means an increase in the total number of atoms in the deposition chamber and an increased chance of collisions between ablated species and the background gas. This is in agreement with some previous work done by Li Bassi *et al.* in exploring the role of substrate material and deposition pressure of bismuth telluride film growth [70]

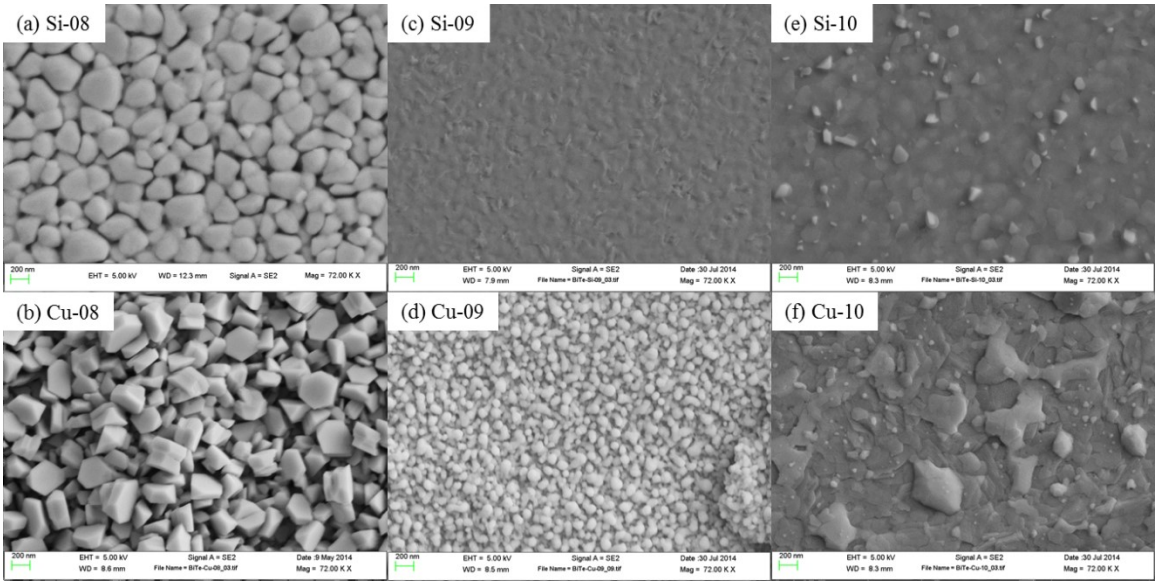

Figure 5–2: FESEM images of the surface morphology of different bismuth telluride films

Cross sectional SEM analysis was used to confirm the growth and thickness of bismuth telluride films. Figure 5–3 shows the cross sectional view of a bismuth telluride film grown directly on a silicon wafer using a 532 nm laser at 3.9 J/cm^2, 200°C, and 0.1 torr argon (Sample 12). The top left portion of the material is the underlying silicon wafer. The middle section of the material is the silicon dioxide layer on top of the silicon wafer. From the SEM image, the oxide layer is approximately one micron thick, which is much larger than the expected thickness of about 300 nm. This discrepancy is most likely an error in the EDS analysis of the sample cross section. The outer layer of the sample is the bismuth telluride film, which is approximately 200 nm thick. In addition, this cross-sectional analysis reveals a bismuth telluride film growth rate of approximately 20 nm per minute using 532 nm laser irradiation.

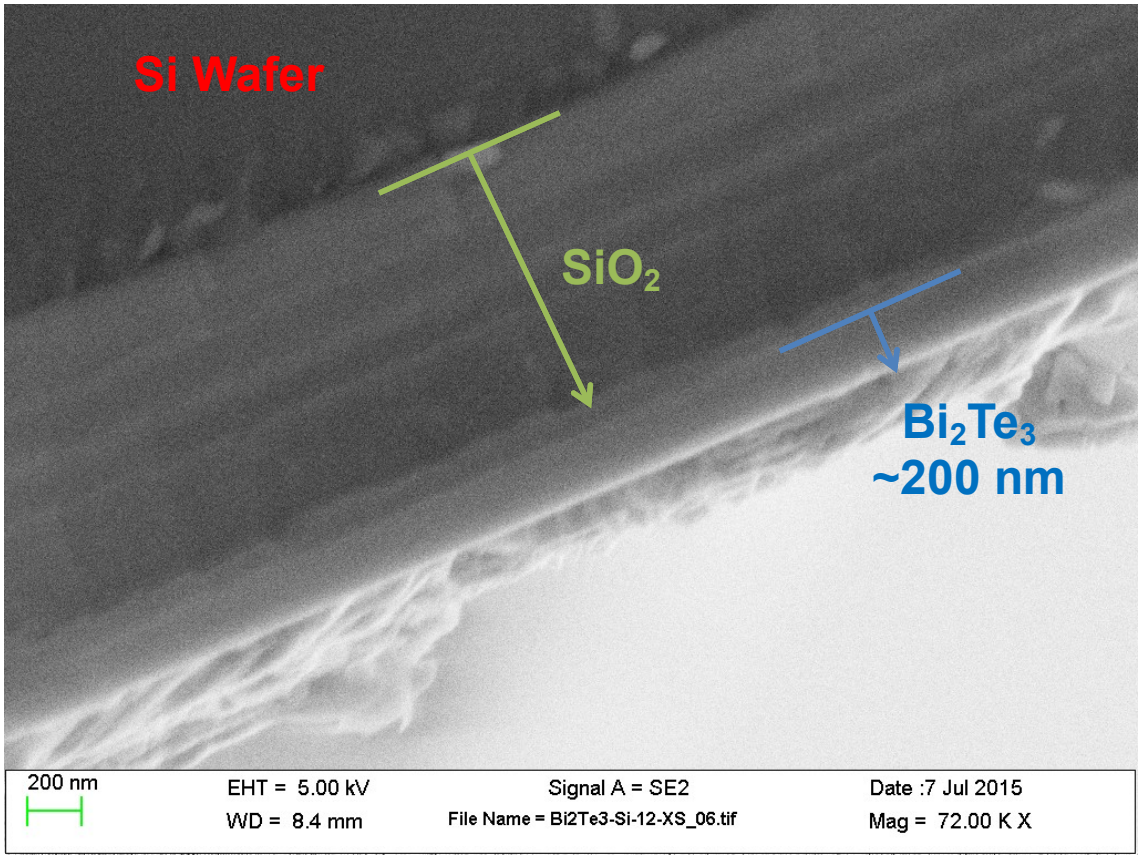

Figure 5–3: Cross-sectional SEM image of Bi_2Te_3 film grown on Si/SiO_2 wafer, showing the film thickness

Figure 5–4 shows another cross-sectional SEM image of a bismuth telluride sample grown on a silicon substrate using a 266 nm laser at 4.5 J/cm^2, 200°C, and 1 torr of nitrogen gas. This result clearly shows the 300 nm oxide layer on top of the silicon wafer, with the sphere-like particulates of bismuth telluride on the surface ranging in height from 100 nm to 150 nm (see Figure 5–25). Lateral sizes of the particulates are typically 150 nm to 300 nm in diameter, revealing that these particulates are partially compressed perpendicular to the substrate surface. Additionally, this cross-sectional analysis reveals a bismuth telluride film growth rate of approximately 10-15 nm per minute using 266 nm laser irradiation. This is consistent with previous results in which less material is ablated when using higher energy (lower wavelength) lasers [8].

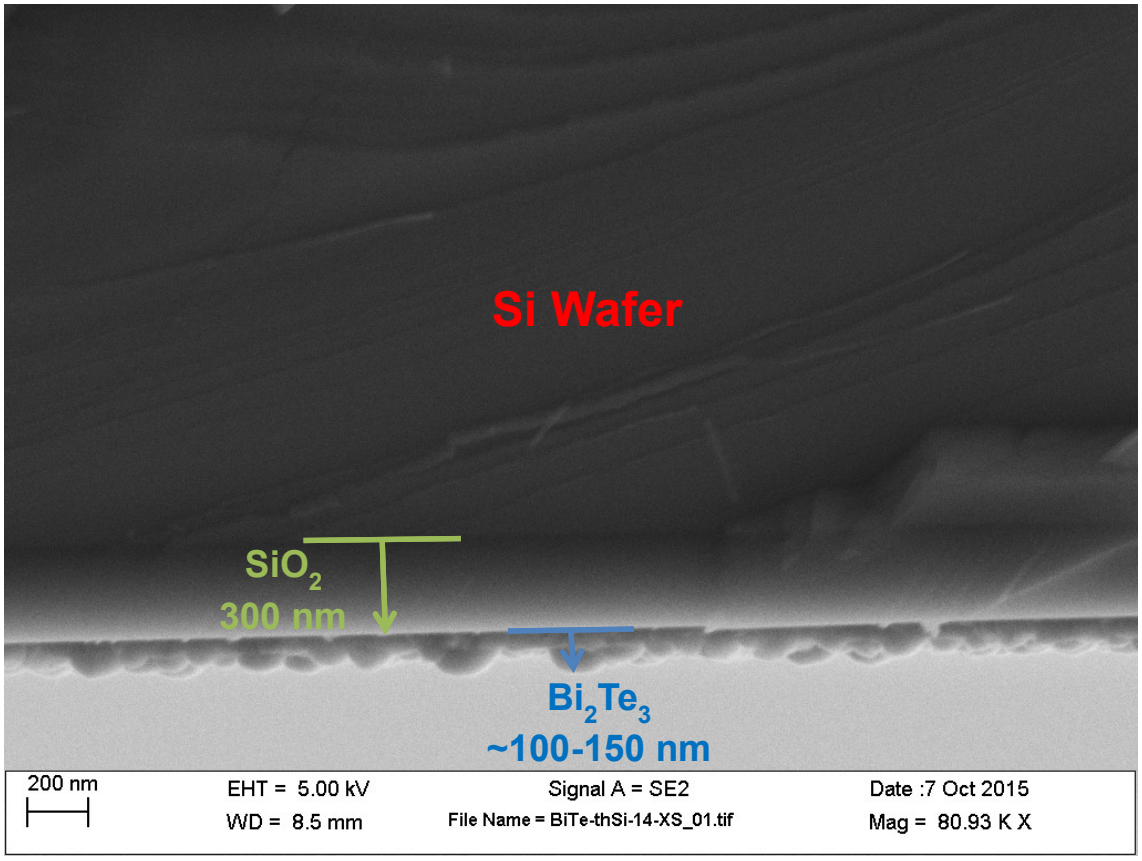

Figure 5–4: Cross-sectional SEM image of Bi_2Te_3 film on Si/SiO_2 substrate using 266 nm laser in 1 torr nitrogen

Finally, Figure 5–5 shows the cross-sectional SEM image of a bismuth telluride sample grown on a silicon substrate using a 266 nm laser at 3.9 J/cm^2 at 200°C and 1 torr of argon gas. Argon gas typically yielded more consistent, film-like bismuth telluride samples, as opposed to using nitrogen. For this sample, the silicon oxide layer is slightly less than the pre-deposition oxide layer of 300 nm. This is probably due to the hydrogen reduction reaction that is performed prior to deposition of the bismuth telluride film. This is done to remove any residual moisture or impurities and reveal a smooth surface for subsequent film growth. As a result, some of the thermal oxide layer on the silicon wafer is removed as well, leading to a slightly thinner oxide layer of approximately 210

nm. The thickness of the bismuth telluride film is approximately 280 nm, which equates the growth rate to about 28 nm per minute.

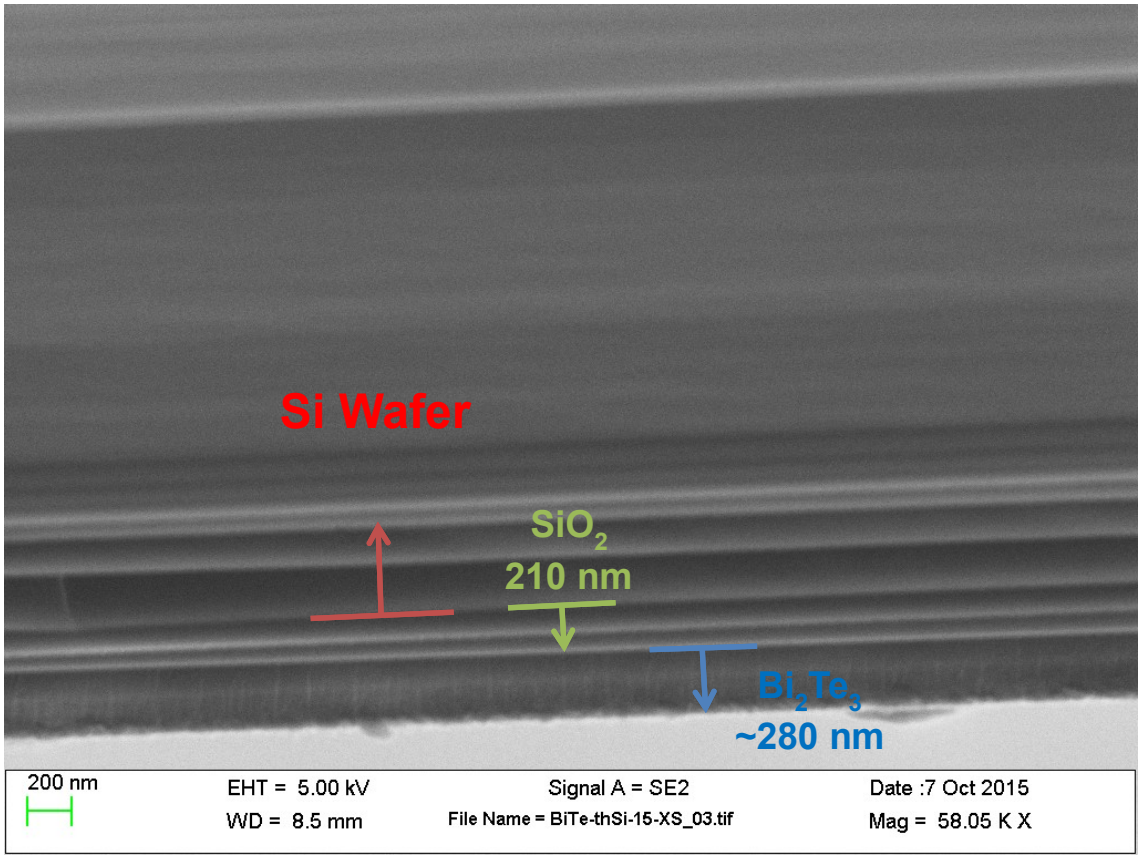

Figure 5–5: Cross-sectional SEM image of Bi_2Te_3 film on Si/SiO_2 substrate using 266 nm laser in 1 torr argon

The following is the SEM surface analysis of the bismuth telluride films grown during the scope of this work. For each figure, the left side shows a lower magnification (~9000x) and the right side shows a higher magnification (~72000x).

Figure 5–6 shows Sample 1, grown in the high laser fluence regime. Sample 1 shows good coverage of the silicon substrate, but not a smooth, continuous film of bismuth telluride. Instead, the sample consists of an agglomeration of two-dimensional nanoplatelets, typically 50 to 600 nanometers in lateral size. There is much less material

on the substrate than is expected, which is most likely a result of the high laser fluence and high temperature used during growth. Using EDS, the stoichiometry is determined to be about 30% bismuth and 70% tellurium, which is rich in tellurium. At these very energetic conditions there should be a deficiency in tellurium due to a re-evaporation of the more volatile tellurium atoms [65]. This is consistent with the unpredictable results obtained from high laser fluence and high temperature conditions of the early trials.

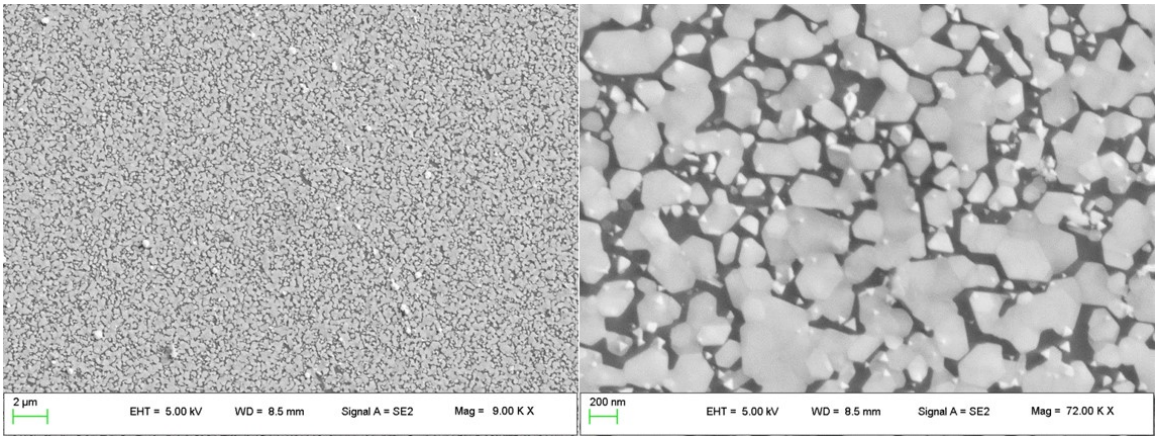

Figure 5–6: Sample 1, silicon substrate, 300°C, 1 torr Ar, 266 nm, 33 J/cm^2

Figure 5–7 shows Sample 2, grown in the high laser fluence regime, showing good coverage of the silicon substrate, but similar to Sample 1, not a smooth, continuous film of bismuth telluride. Instead, the sample consists of an agglomeration of small two-dimensional nanoplatelets, typically 25 to 100 nanometers in size. Using EDS, the stoichiometry is determined to be about 29% bismuth and 70% tellurium. These results are similar to Sample 1.

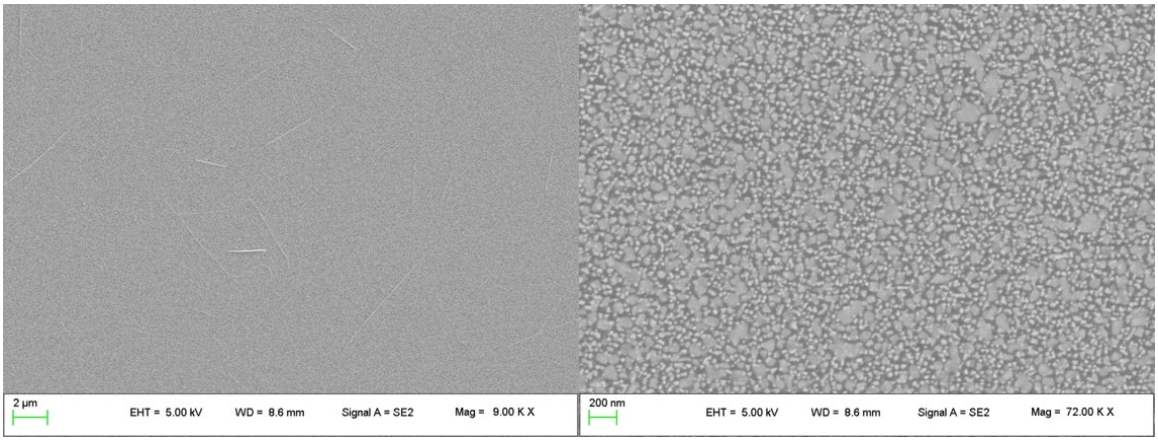

Figure 5–7: Sample 2, silicon substrate, 190°C, 0.15 torr Ar, 266 nm, 22 J/cm^2 – 29% Bi, 71% Te

Sample 2 is annealed after the growth of the bismuth telluride material to see how it affects the film, which is done at 350°C in vacuum for two hours. The sample is analyzed in the SEM, shown below in Figure 5–8. There is nothing left on the silicon substrate after the annealing process. This is probably due to the weak bonding of the bismuth telluride to the substrate since it is not a continuous film. The small islands of material are not as stable as a film, so the annealing process effectively evaporates all of the deposited material from the silicon substrate.

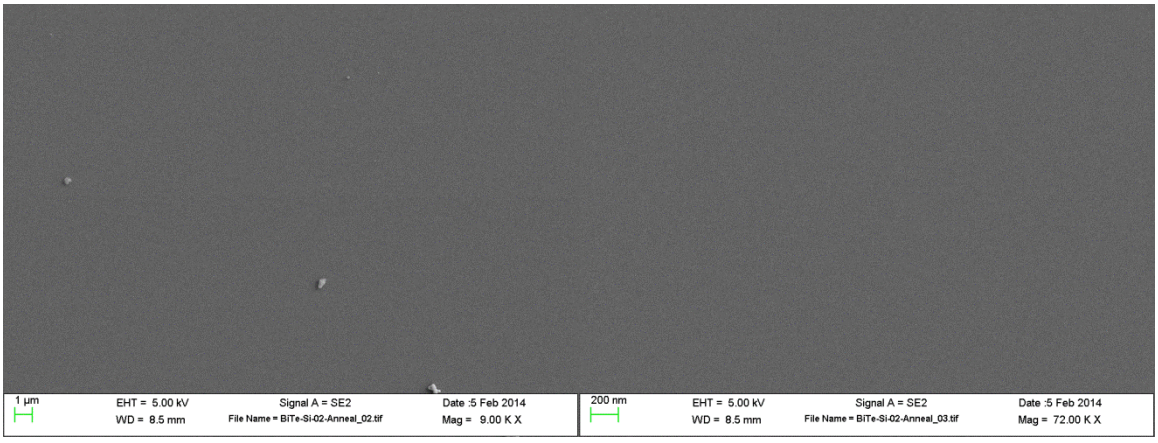

Figure 5–8: Sample 2 post-annealing

Sample 3, shown below in Figure 5–9, is similar to the previous samples in growth conditions and results, showing a low coverage agglomeration of two-dimensional nanoplatelets grown in the high laser fluence regime. The lateral size of these particles is typically 100 to 400 nanometers. Using EDS, the stoichiometry is determined to be about 35% bismuth and 65% tellurium. This is closer to the chemical composition of Bi_2Te_3, but still slightly off, most likely due to the unfavorable growth conditions.

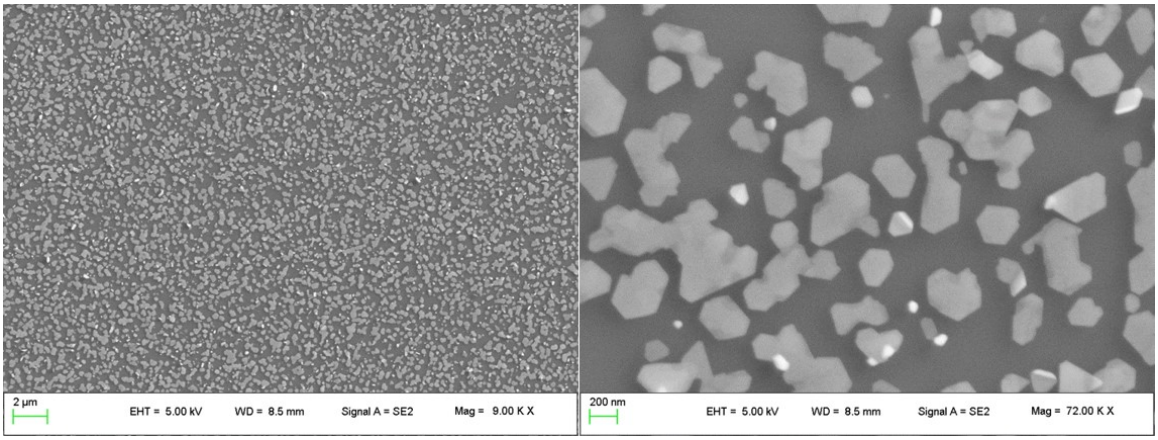

Figure 5–9: Sample 3, silicon substrate, 300°C, 1 torr Ar, 266 nm, 82 J/cm^2

Sample 3 is also annealed after the growth of the bismuth telluride material to see how it affects the film, which is done at 350°C in vacuum for two hours. The sample is analyzed in the SEM, shown below in Figure 5–10. Again, there is nothing left on the silicon substrate after the annealing process. This is due to the weak bonding of the bismuth telluride to the substrate since it is not a continuous film. The small islands of material are not as stable as a film, so the annealing process effectively evaporates all of the deposited material from the silicon substrate.

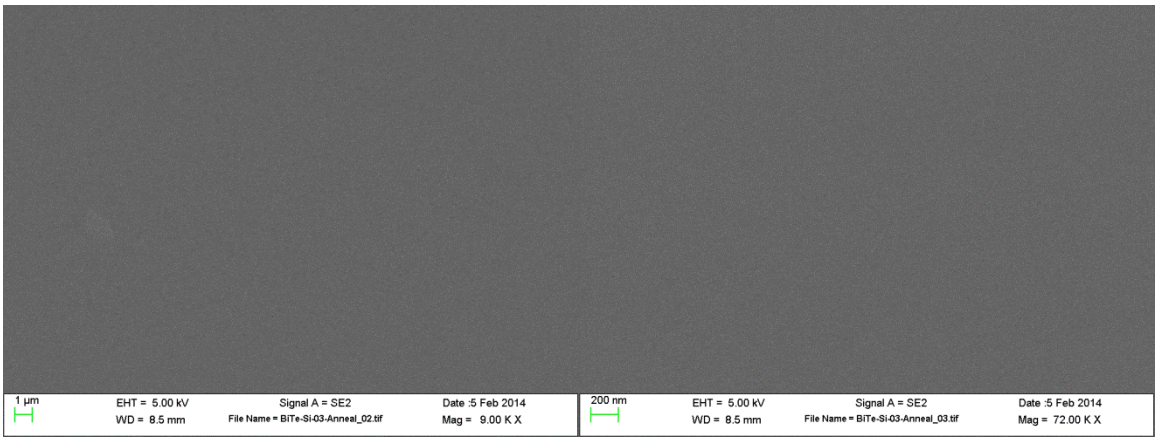

Figure 5–10: Sample 3 Post-Annealing

Sample 3 is also grown on a copper substrate, shown below in Figure 5–11. The material deposited on the copper substrate is slightly different than that deposited on the silicon substrate. The particles are smaller, typically under 200 nanometers, and the coverage looks slightly better. This is an interesting result because it opens the door to being able to control the nanostructure of a material based on the material of the substrate. Using EDS, the stoichiometry is determined to be about 46% bismuth and 54% tellurium. While this composition is still slightly off from pure Bi_2Te_3, it is deficient in tellurium, which is what is expected from the highly energetic growth conditions [65].

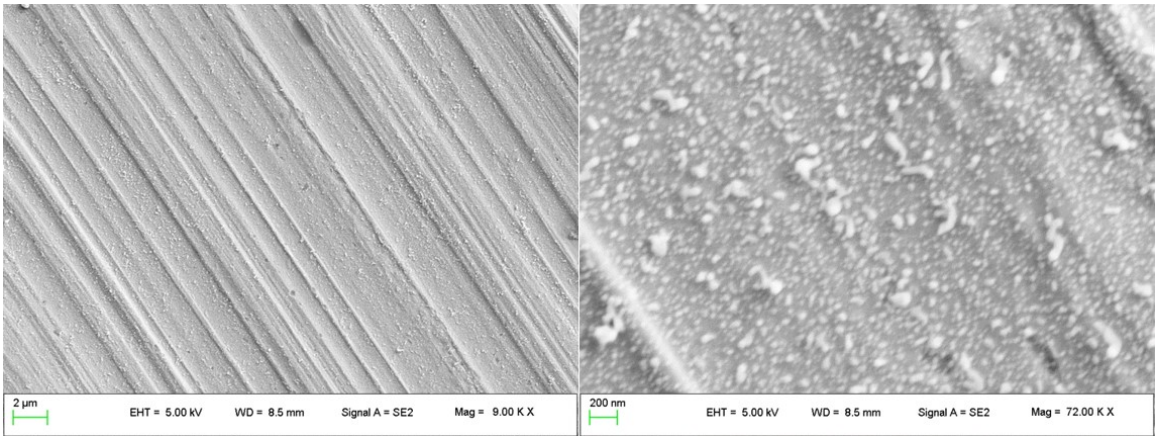

Figure 5–11: Sample 3, copper substrate, 300°C, 1 torr Ar, 266 nm, 82 J/cm^2

Figure 5–12 below shows Sample 4, grown on a silicon substrate (top) and a copper substrate (bottom). These samples show more of a three-dimensional nanoparticle with hexagonal shape, as opposed to the more two-dimensional shapes seen previously. In addition, there are a few nanorod or nanowire structures on the silicon substrate that are not seen in any other samples. However, the substrate coverage is very poor. The substrate coverage issue is similar to the previous samples, which is a result of high laser fluence and high temperature. Sample 4 was grown at a slightly higher temperature of 325°C, which is the main difference in growth conditions. The surface morphology on the copper substrate is also very unique, consisting of clusters of these nanorods, which were rare on the silicon substrate, but very prevalent on the copper substrate. The clustering of the nanorods on the copper surface grooves is another interesting result that is not replicated. The coverage is still fairly poor, but the clusters show that all that may be needed for the growth of nanostructures is some sort of surface imperfection or feature. As a result, the difference between growing smooth films versus nanoparticles or nanorods may be predominantly the surface morphology of the substrate. The stoichiometry of this sample is undetermined, as EDS is unable to be performed.

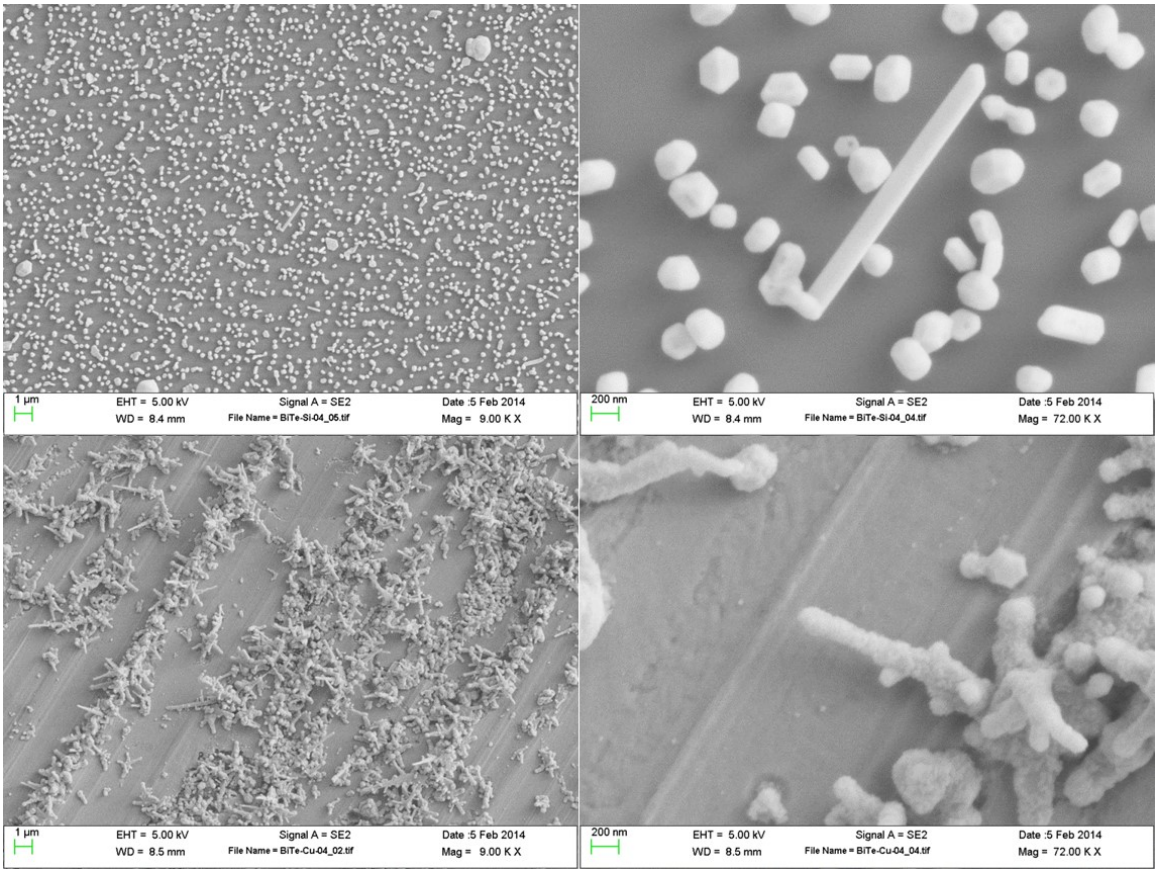

Figure 5–12: Sample 4, silicon substrate (top) and copper substrate (bottom), 325°C, 1 torr Ar, 266 nm, 67 J/cm^2 – No XRD

Figure 5–13 below shows Sample 5, grown on a silicon substrate (top) and a copper substrate (bottom). This sample shows the two-dimensional nanoplatelets seen previously, with lateral sizes ranging from 100 to 300 nanometers. The substrate coverage is slightly better, but still consists of an agglomeration of nanoparticles as opposed to a uniform film. Using EDS, the stoichiometry is determined to be about 49% bismuth and 51% tellurium for the silicon substrate, with certain large particulates composed of about 58% bismuth and 42% tellurium. This is a very tellurium-deficient sample, which is consistent with highly energetic growth conditions [65]. The

stoichiometry of the sample grown on the copper substrate is undetermined, as EDS is unable to be performed.

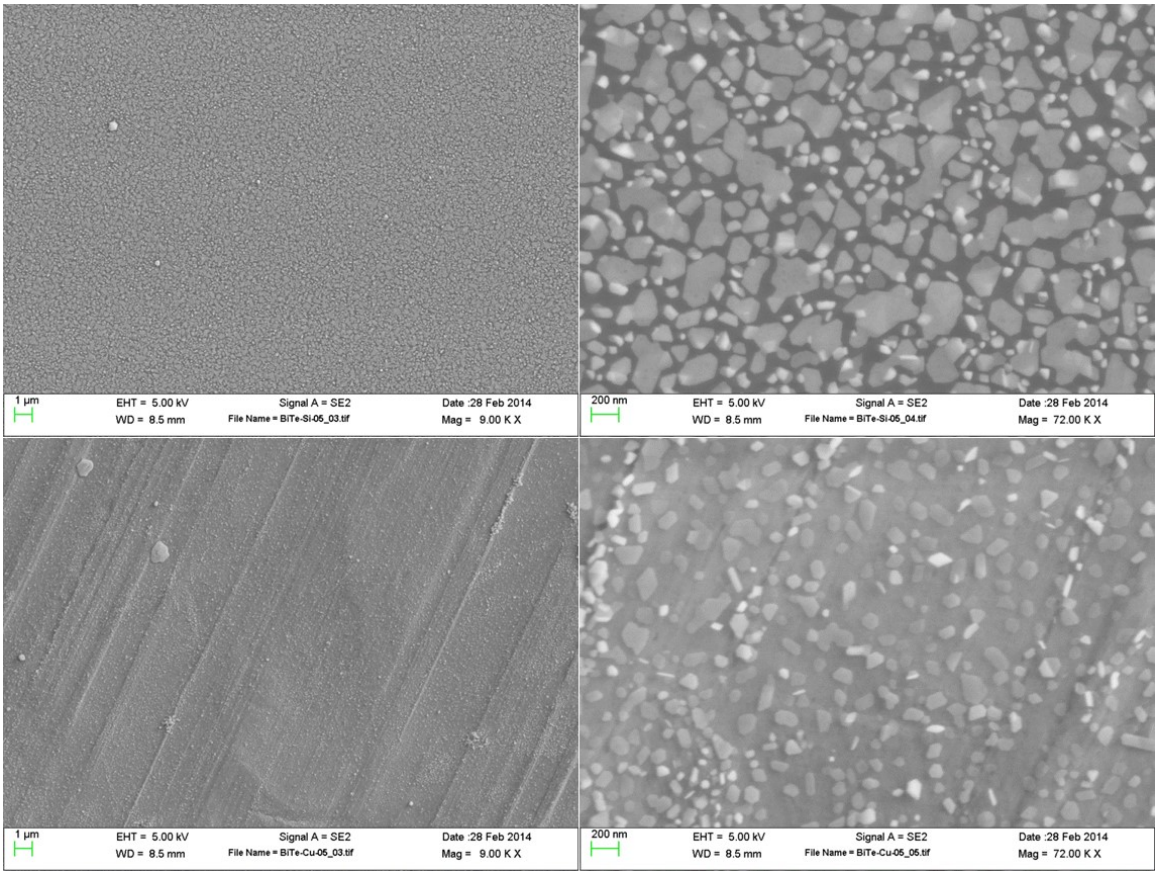

Figure 5–13: Sample 5, silicon substrate (top) and copper substrate (bottom), 300°C, 0.1 torr Ar, 266 nm, 49 J/cm^2

Figure 5–14 below shows a low-magnification image of Sample 6, grown on a native oxide silicon substrate. This sample is grown in the low laser fluence regime, but still at the elevated temperature of 300°C. There are two different distinct areas of the film, one with high contrast and one with low contrast, each with different surface morphology and coverage. These experimental conditions seem to be a transition area between optimal and sub-optimal conditions, with some areas of good coverage, and some areas of poor coverage.

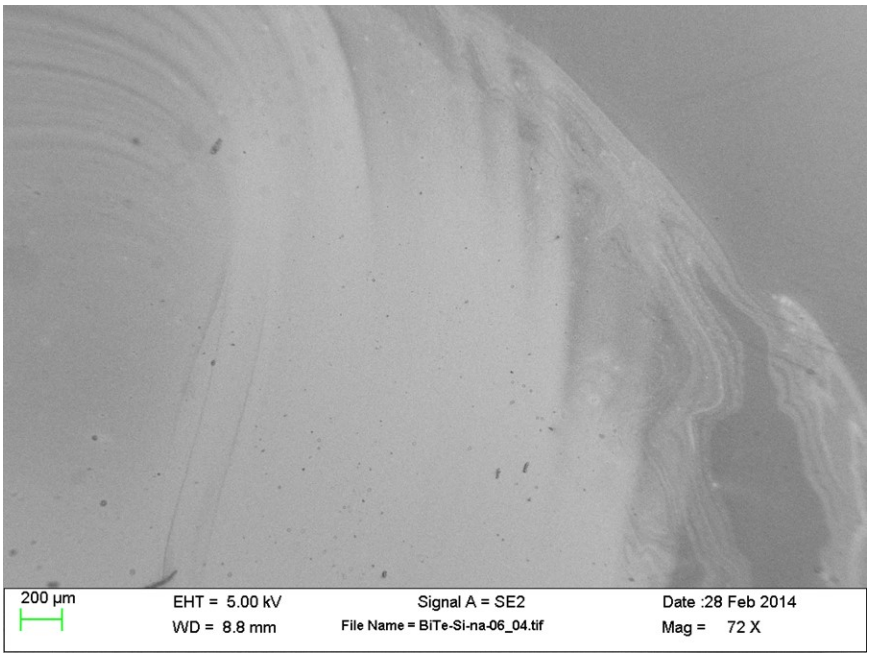

Figure 5–14: Sample 6, native oxide silicon substrate, 300°C, 0.1 torr Ar, 266 nm, 2.0 J/cm^2

Figure 5–15 below shows the magnified SEM images of the two regions of Sample 6 (native oxide silicon). The low contrast (dark) area has very sparse coverage of mostly two-dimensional hexagonal nanoplatelets. This island-growth region is similar to previous results in the high laser fluence regime with poor coverage of the substrate. The high contrast (light) area has complete coverage of the substrate surface and also consists of a film of two-dimensional hexagonal nanoplatelets. This region is much more densely packed and has a more random orientation of the nanoplatelets, as opposed to being flat on the surface like the previous samples. This discrepancy in the light and dark regions of Sample 6 may be a transition region from sub-optimal growth conditions to more optimal growth conditions, with better film coverage and stoichiometry of samples. Using EDS, the stoichiometry is determined to be about 45% bismuth and 55% tellurium

for both regions of the sample. This shows that the two regions are similar in chemical composition, but different in surface morphology only.

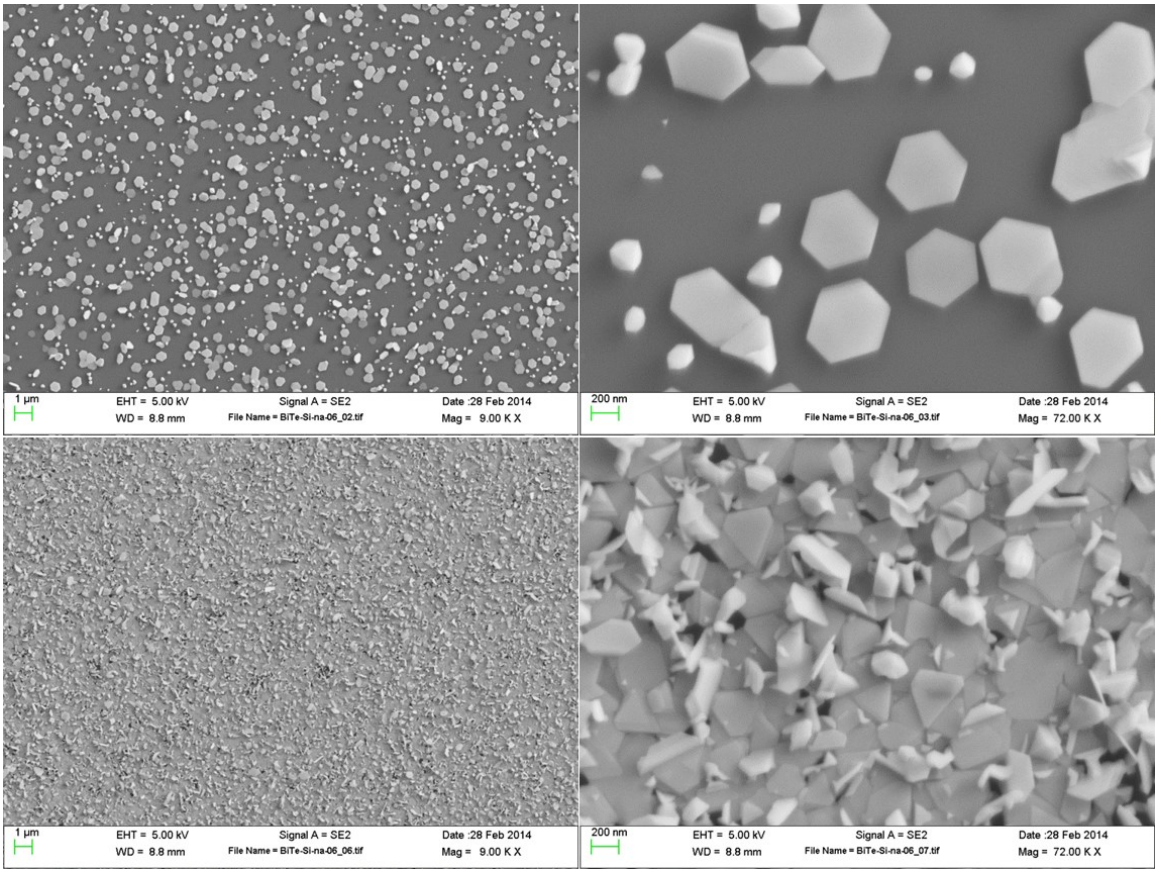

Figure 5–15: Sample 6, native oxide silicon substrate, dark region (top) and light region (bottom), 300°C, 0.1 torr Ar, 266 nm, 2.0 J/cm^2

Figure 5–16 below shows a low-magnification image of Sample 6, grown on a thermal oxide silicon substrate. This sample is grown in the low laser fluence regime, but still at the elevated temperature of 300°C. Similar to the native oxide silicon substrate, there are two different distinct areas of the film, one with high contrast and one with low contrast, each with different surface morphology and coverage. These experimental conditions seem to be a transition area between optimal and sub-optimal conditions, with

some areas of good coverage, and some areas of poor coverage. The high contrast area is much smaller than in the native oxide silicon substrate, but is still present.

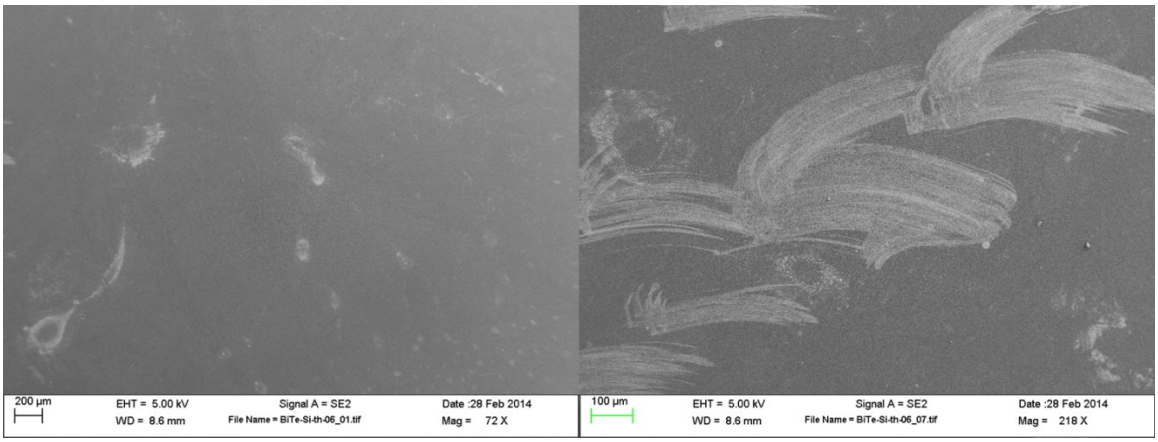

Figure 5–16: Sample 6, thermal oxide silicon substrate, 300°C, 0.1 torr Ar, 266 nm, 2.0 J/cm^2

Figure 5–17 below shows the magnified SEM images of the two regions of Sample 6 (thermal oxide silicon). The low contrast (dark) area has sparse coverage of smaller three-dimensional nanoparticles and larger two-dimensional hexagonal nanoplatelets. The smaller nanoparticles are typically 200 nanometers or less in size, with hexagonal or cubic shapes. The larger nanoplatelets are typically 200 to 300 nanometers in lateral size, and are mostly flat against the substrate surface, but occasionally have a random orientation. This island-growth region is similar to previous results in the high laser fluence regime with poor coverage of the substrate. The high contrast (light) area has much better coverage of the substrate surface and consists of an agglomeration of two-dimensional hexagonal nanoplatelets. This region is much more densely packed and has a more random orientation of the nanoplatelets, as opposed to being flat on the surface like the previous samples. This discrepancy in the light and dark

regions of Sample 6 may be a transition region from sub-optimal growth conditions to more optimal growth conditions, with better film coverage and stoichiometry of samples. The stoichiometry of the dark region is undetermined, as EDS is unable to be performed on the sparsely covered substrate. However, the stoichiometry of the light region is determined to be about 45% bismuth and 55% tellurium. This is identical to the stoichiometry of Sample 6 grown on the native oxide silicon substrate, which shows that the two substrates have similar growth conditions.

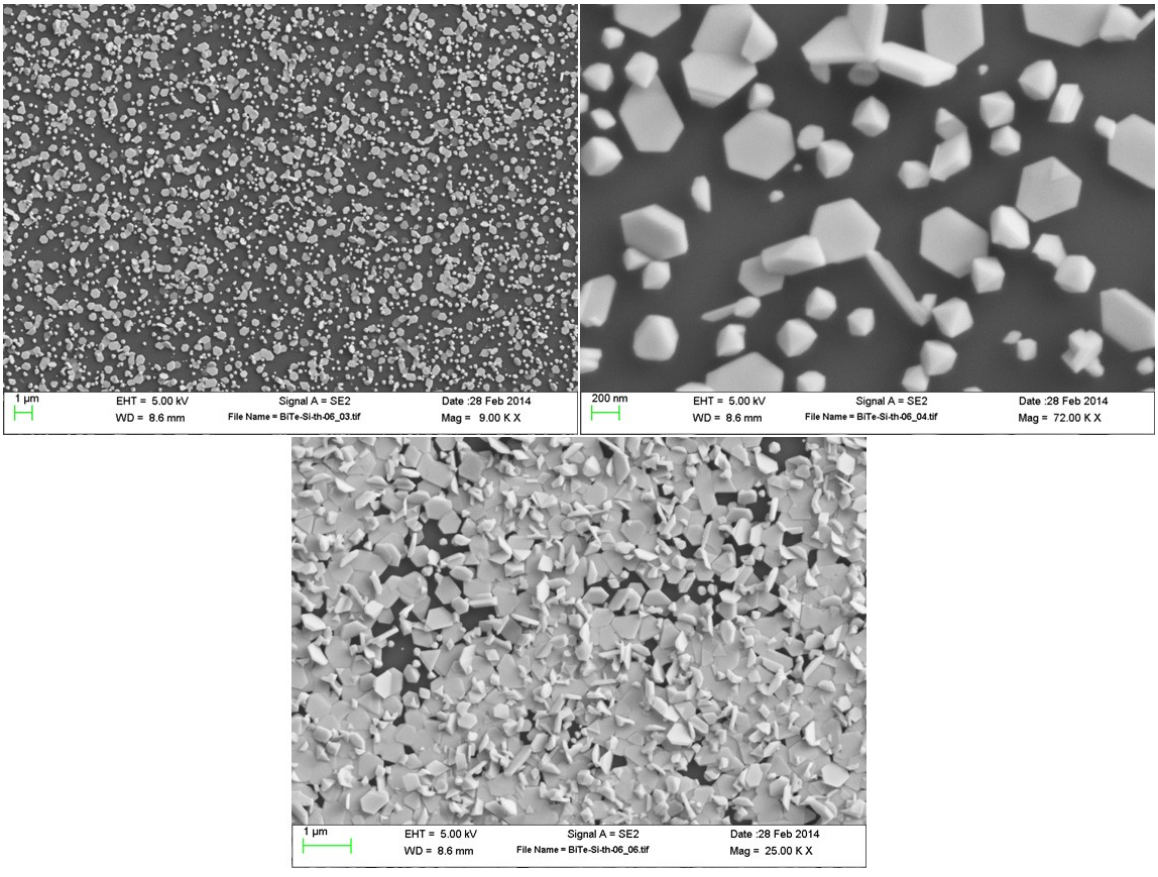

Figure 5–17: Sample 6, thermal oxide silicon substrate, dark region (top) and light region (bottom), 300°C, 0.1 torr Ar, 266 nm, 2.0 J/cm^2

Figure 5–18 below shows Sample 7, grown on a silicon substrate (top) and a copper substrate (bottom). This sample shows very good coverage of the substrate, in

addition to nanostructures on and protruding from the surface. The surface is similar on the copper substrate, with the exception being the number of nanostructures on the surface. For both substrates, the surface is a combination of a uniform film and an agglomeration of nanostructures, but they both have distinct structures on the surface in addition to a film of bismuth telluride covering the entire substrate surface. Using EDS, the stoichiometry is determined to be about 37% bismuth and 63% tellurium for the silicon substrate, and 39% bismuth and 61% tellurium for the copper substrate. These two substrates show very similar features in terms of morphology and chemistry.

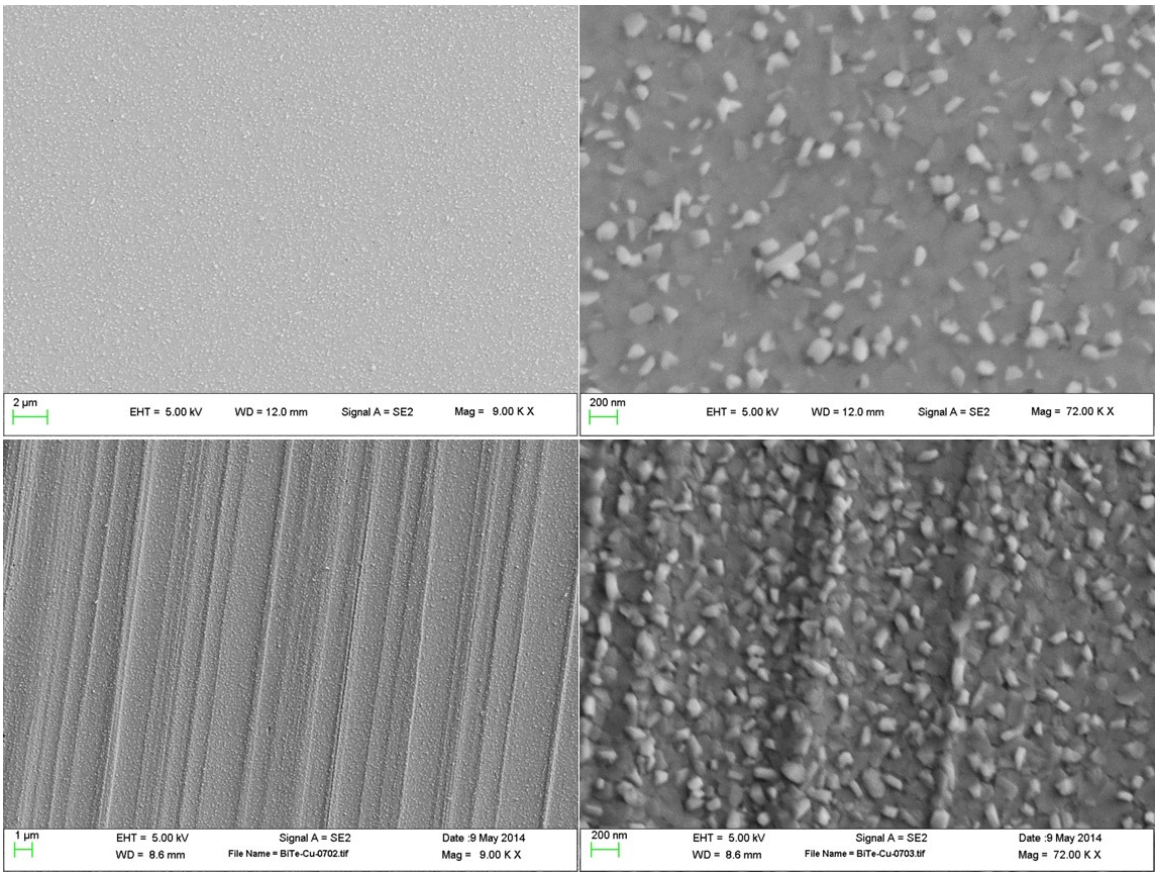

Figure 5–18: Sample 7, silicon substrate (top) and copper substrate (bottom), 200°C, 0.1 torr Ar, 266 nm, 2.7 J/cm^2

Figure 5–19 below shows Sample 8, grown on a silicon substrate (top) and a copper substrate (bottom). This sample shows very good coverage of the substrate, with the film consisting of different sizes of nanoparticles. For the silicon substrate, the nanoparticles are typically 200 to 400 nanometers in size, and are rounded in shape. For the copper substrate, the nanoparticles are typically 200 to 300 nanometers in size, and are hexagonal in shape. Using EDS, the stoichiometry is determined to be about 42% bismuth and 58% tellurium for the silicon substrate, and 40% bismuth and 60% tellurium for the copper substrate. These two substrates show very similar features in terms of morphology and chemistry, with the main difference being the shape of the nanoparticles. This morphology of a film of densely packed nanoparticles is unique, and it has not been replicated by future experiments. The main difference with Sample 8 is the use of 532 nm laser irradiation, as opposed to the 266 nm laser irradiation that is used for most other samples. As discussed previously, the laser wavelength may be the reason for this unique surface morphology. The 532 nm laser wavelength is lower in energy (2.33 eV versus 4.66 eV of a 266 nm laser), so the particles being ablated from the target surface are larger than when using a 266 nm laser. These larger particles may begin to coalesce via gas phase condensation en route to the substrate surface, leading to already-formed nanoparticles arriving at the substrate surface. This may be the reason why the surface of the sample is made up of nanoparticles as opposed to a smooth film. The combination of low pressure growth conditions (0.1 to 1.0 torr) and lower laser energy has a noticeable effect on the growth of bismuth telluride nanostructures.

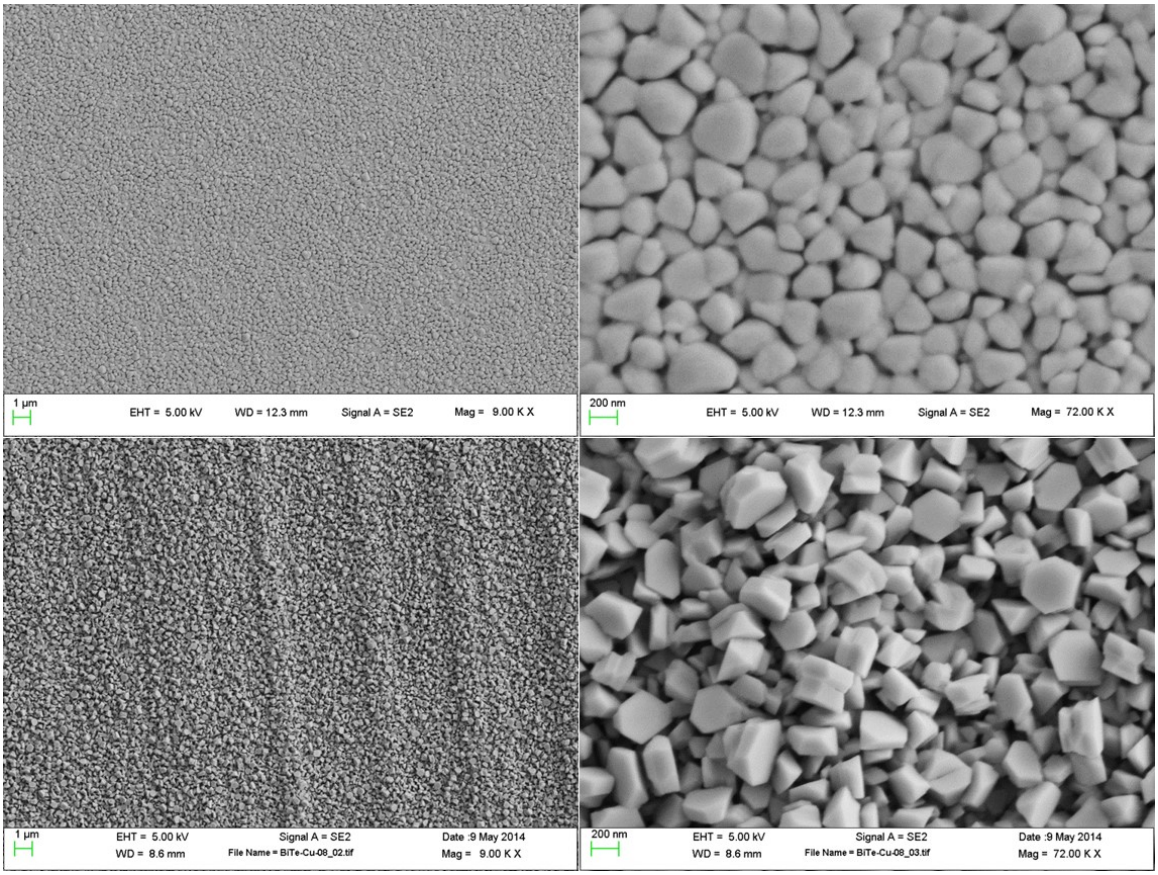

Figure 5–19: Sample 8, silicon substrate (top) and copper substrate (bottom), 200°C, 0.1 torr Ar, 532 nm, 2.55 J/cm^2

Figure 5–20 below shows Sample 9, grown on a silicon substrate (top) and a copper substrate (bottom). This sample shows good coverage of the substrate, with a very smooth film on the silicon substrate. However, the surface on the copper substrate is made up of very small, sphere-like nanoparticles. Using EDS, the stoichiometry is determined to be about 58% bismuth and 42% tellurium for the silicon substrate, and 45% bismuth and 55% tellurium for the copper substrate. Both substrates have deficiencies in tellurium, which may be a result of the lower pressure at which deposition occurs (0.035 torr). This coincides with the fact that tellurium is more volatile, and re-evaporation occurs from the substrate surface because of the sub-optimal pressure. The morphology

of the copper substrate is unique, and differs significantly from the morphology of the silicon substrate. As mentioned previously, the morphology of different substrates is more prone to discrepancies if the pressure is lower than the optimal range of 0.1-1.0 torr. Sample 9 reinforces this idea with the obvious differences in surface morphology between the material grown on the silicon and copper substrates.

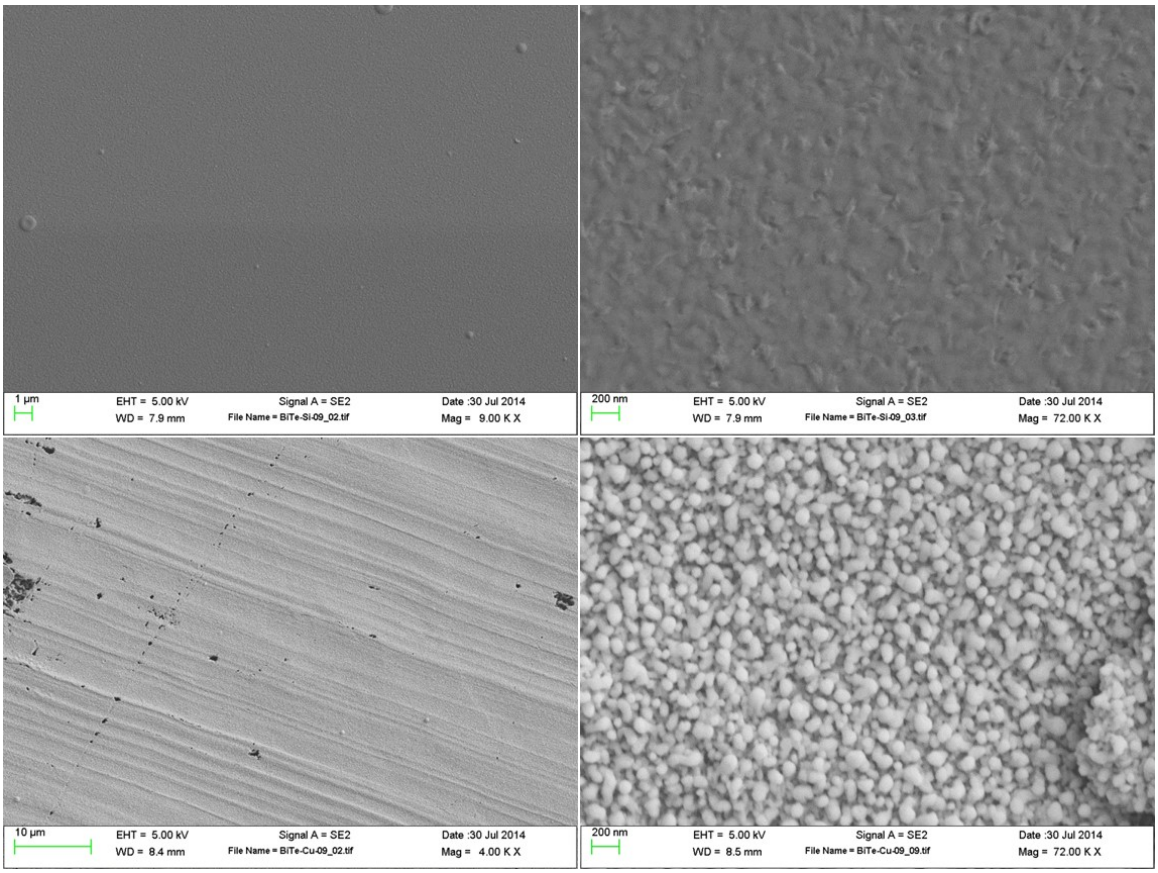

Figure 5–20: Sample 9, silicon substrate (top) and copper substrate (bottom), 200°C, 0.035 torr Ar, 266 nm, 2.7 J/cm^2

Figure 5–21 below shows Sample 10, grown on a silicon substrate (top) and a copper substrate (bottom). This sample shows very good coverage of the substrate, in addition to nanostructures on and protruding from the surface. On the other hand, the surface on the copper substrate is much more textured, showing overlapping layers of

stratified material. It is mostly film-like, with the grains intertwined, almost looking like they are melted together. The surface morphology of the silicon substrate is similar to other samples, but the surface of the copper substrate is very unique. This may be due to the slightly elevated deposition temperature of the sample (250°C). Using EDS, the stoichiometry is determined to be about 36% bismuth and 64% tellurium for the silicon substrate, and 33% bismuth and 67% tellurium for the copper substrate. These samples are slightly rich in tellurium, which is not what is expected from the high temperature growth conditions.

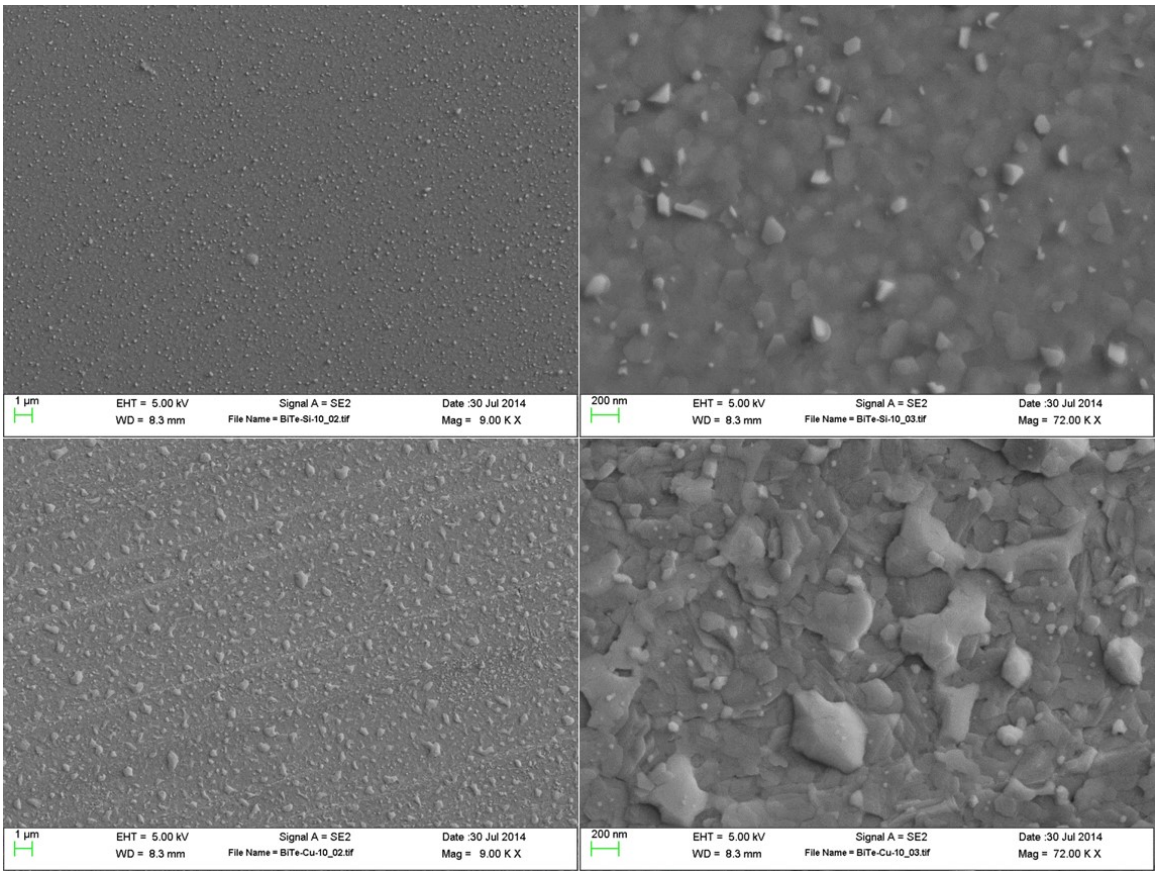

Figure 5–21: Sample 10, silicon substrate (top) and copper substrate (bottom), 250°C, 0.1 torr Ar, 266 nm, 3.25 J/cm^2

Figure 5–22 below shows Sample 11, grown on a silicon substrate (top) and a copper substrate (bottom). This sample shows good coverage of the substrate, with a very smooth film on the silicon substrate. However, the surface on the copper substrate is made up of a densely packed film of small nanoplatelets on the order of 50 nanometers, with many larger nanoparticles of about 200 nanometers embedded in the surface. Using EDS, the stoichiometry is determined to be about 44% bismuth and 56% tellurium for the silicon substrate, and 36% bismuth and 64% tellurium for the copper substrate. Both substrates are close to stoichiometric Bi_2Te_3, but they are very different from each other. The morphology of the copper substrate is unique, and differs significantly from the morphology of the silicon substrate. This sample is grown at a lower deposition pressure (0.035 torr) than other samples, which explains the reason for the differences in surface morphology and chemical composition when depositing on different substrate materials.

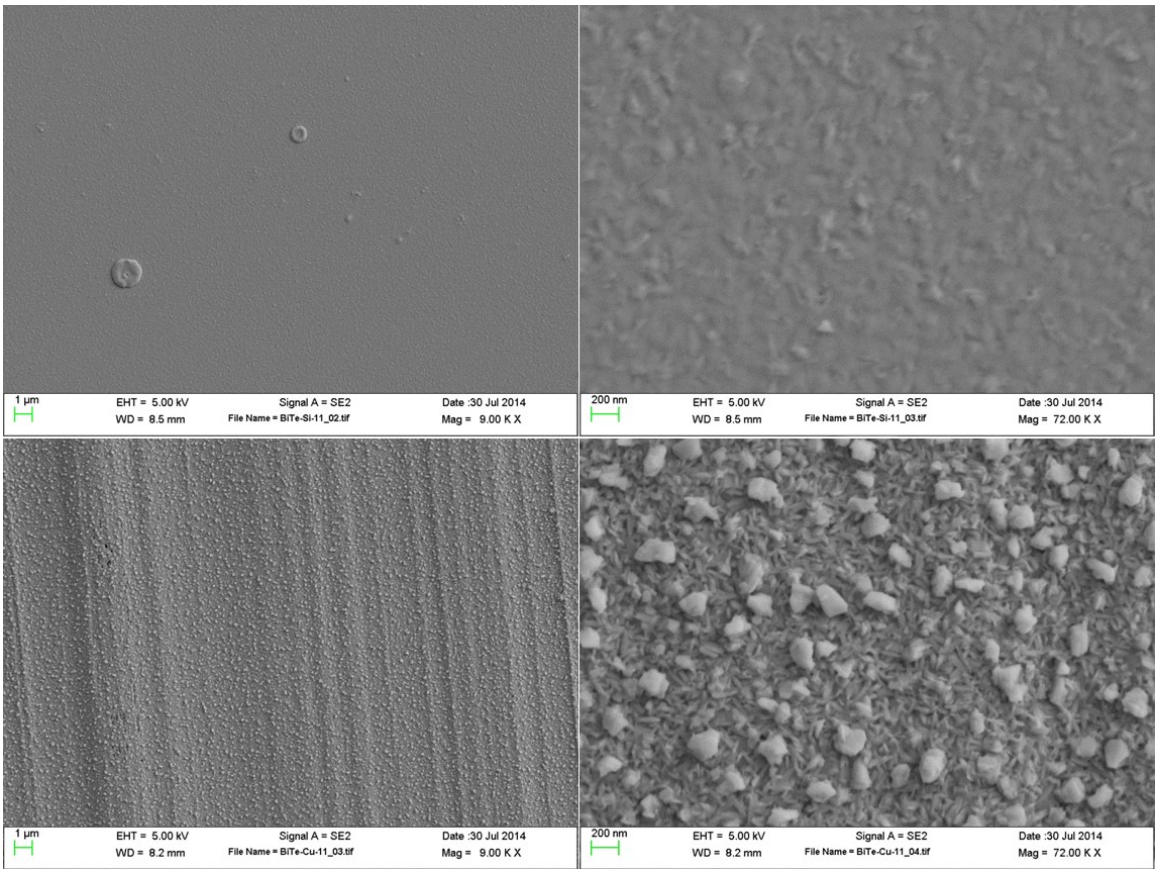

Figure 5–22: Sample 11, silicon substrate (top) and copper substrate (bottom), 200°C, 0.035 torr Ar, 266 nm, 3.4 J/cm^2

Figure 5–23 below shows Sample 12, grown on a silicon substrate (top) and a copper substrate (bottom). This sample shows good coverage of the substrate, with a film of bismuth telluride covered by hexagonal shaped nanoplatelets on the silicon substrate. The surface of the copper substrate is almost identical to that of the silicon substrate. Using EDS, the stoichiometry is determined to be about 36% bismuth and 64% tellurium for both the silicon substrate and the copper substrate. Both substrates are close to stoichiometric Bi_2Te_3. This sample is grown using 532 nm laser irradiation, which explains the reason for the differences in surface morphology and chemical composition when depositing on different substrate materials.

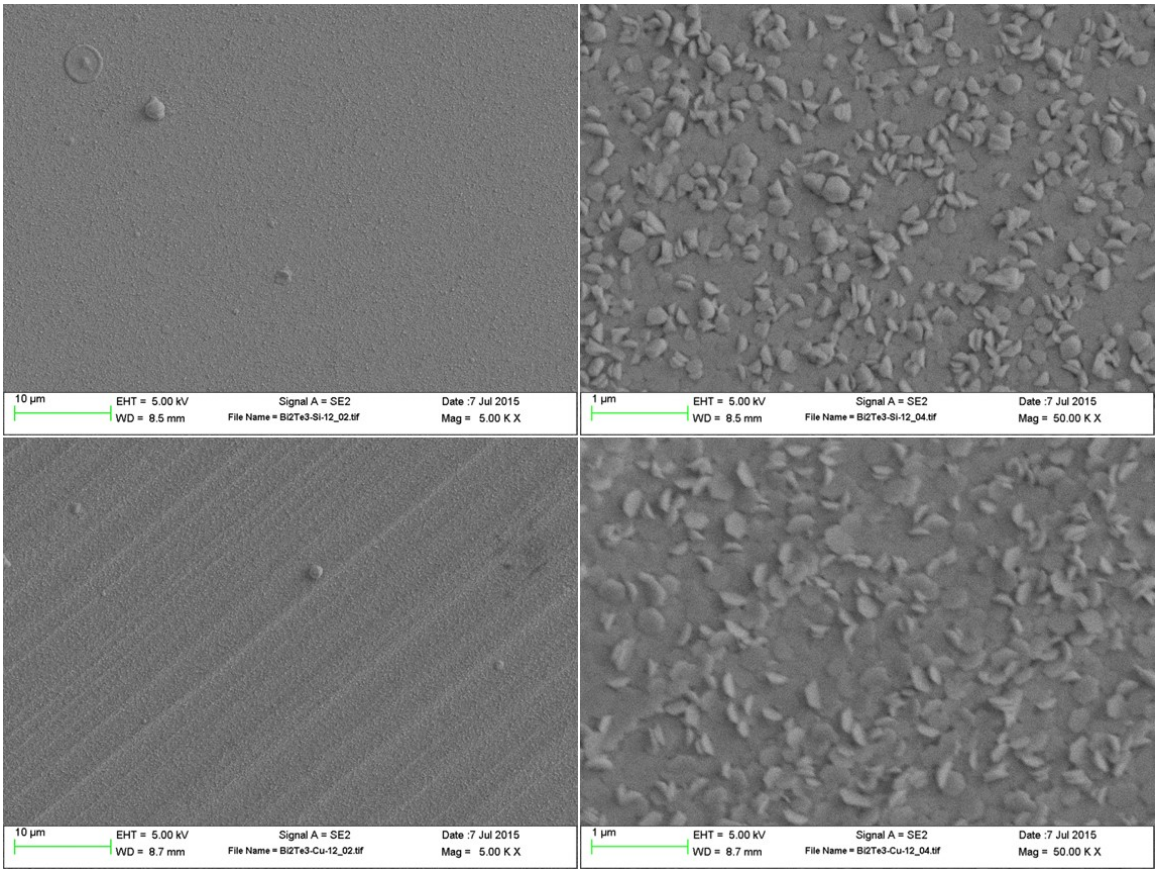

Figure 5–23: Sample 12, silicon substrate (top) and copper substrate (bottom), 200°C, 0.1 torr Ar, 532 nm, 3.9 J/cm^2

Figure 5–24 below shows Sample 13, grown on a silicon substrate (top) and a copper substrate (bottom). This sample was exposed to acetone when being removed from the deposition chamber, which caused the film on the silicon substrate to delaminate and peel off. The surface of the copper substrate is sparsely covered by nanoparticles of about 100 nanometers or less. Using EDS, the stoichiometry is determined to be about 37% bismuth and 63% tellurium for what remains of the rolled up bismuth telluride film on the silicon substrate, with most of the substrate consisting of only silicon. The chemical composition on the copper substrate is 29% bismuth and 71% tellurium, which

may be contaminated by the acetone exposure. These experimental conditions are replicated in Sample 15, shown below.

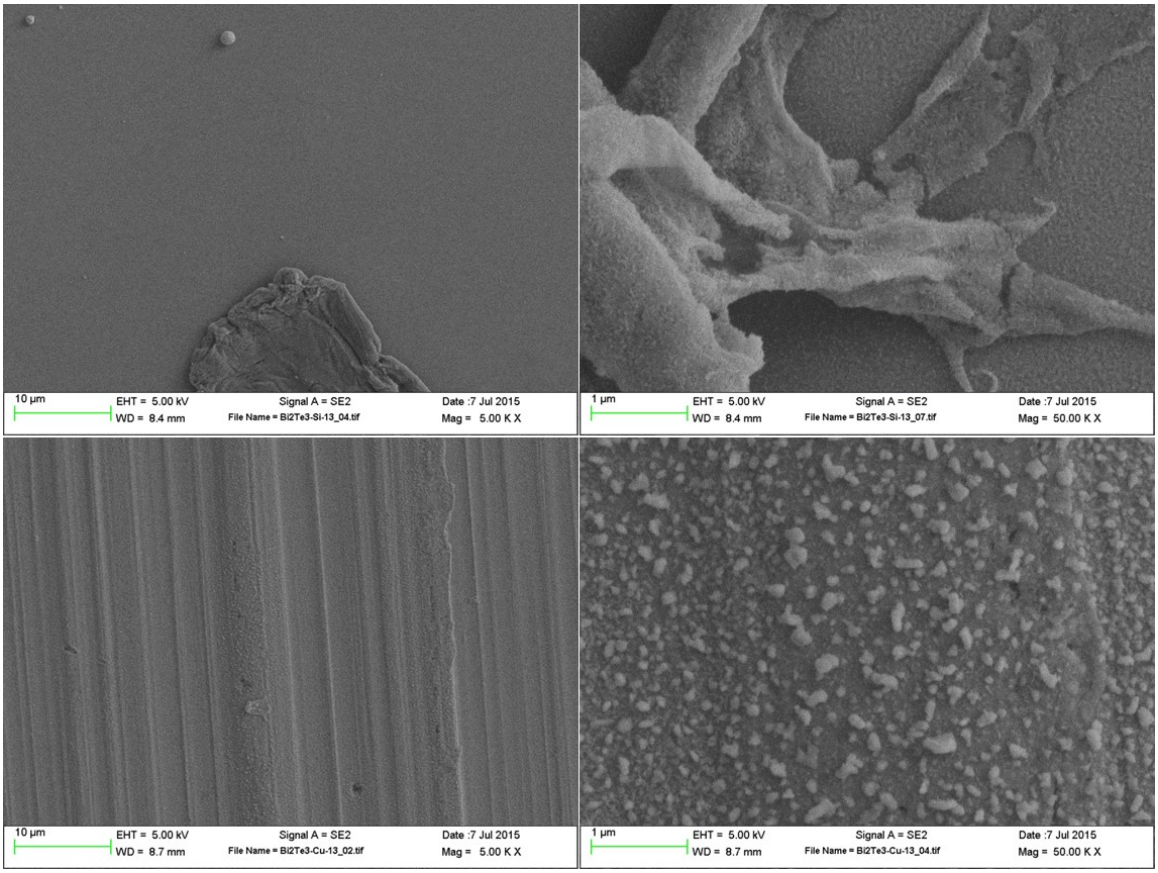

Figure 5–24: Sample 13, silicon substrate (top) and copper substrate (bottom), 200°C, 1 torr Ar, 266 nm, 3.8 J/cm^2

Figure 5–25 below shows Sample 14, grown on a native oxide silicon substrate (top), a thermal oxide silicon substrate (middle), and a copper substrate (bottom). This sample shows good coverage of the substrate, with a film of bismuth telluride covered by spherical nanoparticles 100 to 200 nanometers in diameter on the silicon substrates. The surface of the copper substrate is similar, but with less defined spherical nanoparticles. Using EDS, the stoichiometry is determined to be about 37% bismuth and 63% tellurium for both silicon substrates, and 38% bismuth and 62% tellurium for the copper substrate.

This sample is grown using a background gas of nitrogen instead of argon, which may explain the reason for the unique surface morphology, which is not replicated in any further experiments. Nitrogen is lighter than argon in terms of weight, but it is also diatomic, which causes it to interact with the ablated species differently than argon atoms. The collision cross section of N_2 is larger than for Ar (0.43 nm^2 for N_2 vs 0.36 nm^2 for Ar) [87], which causes the ablated species to interact more frequently with the N_2, causing further gas-phase condensation, and creating these spherical nanoparticles before reaching the surface of the substrate. Once these particles reach the substrate surface, they deposit on the surface as spherical particles. The underlying film of bismuth telluride is most likely a result of the energetic particles repeatedly colliding with the surface and transporting enough mobility on the surface to coalesce into a film. This explains why only the very top surface layer remains in the form of spherical nanoparticles as opposed to a uniform film.

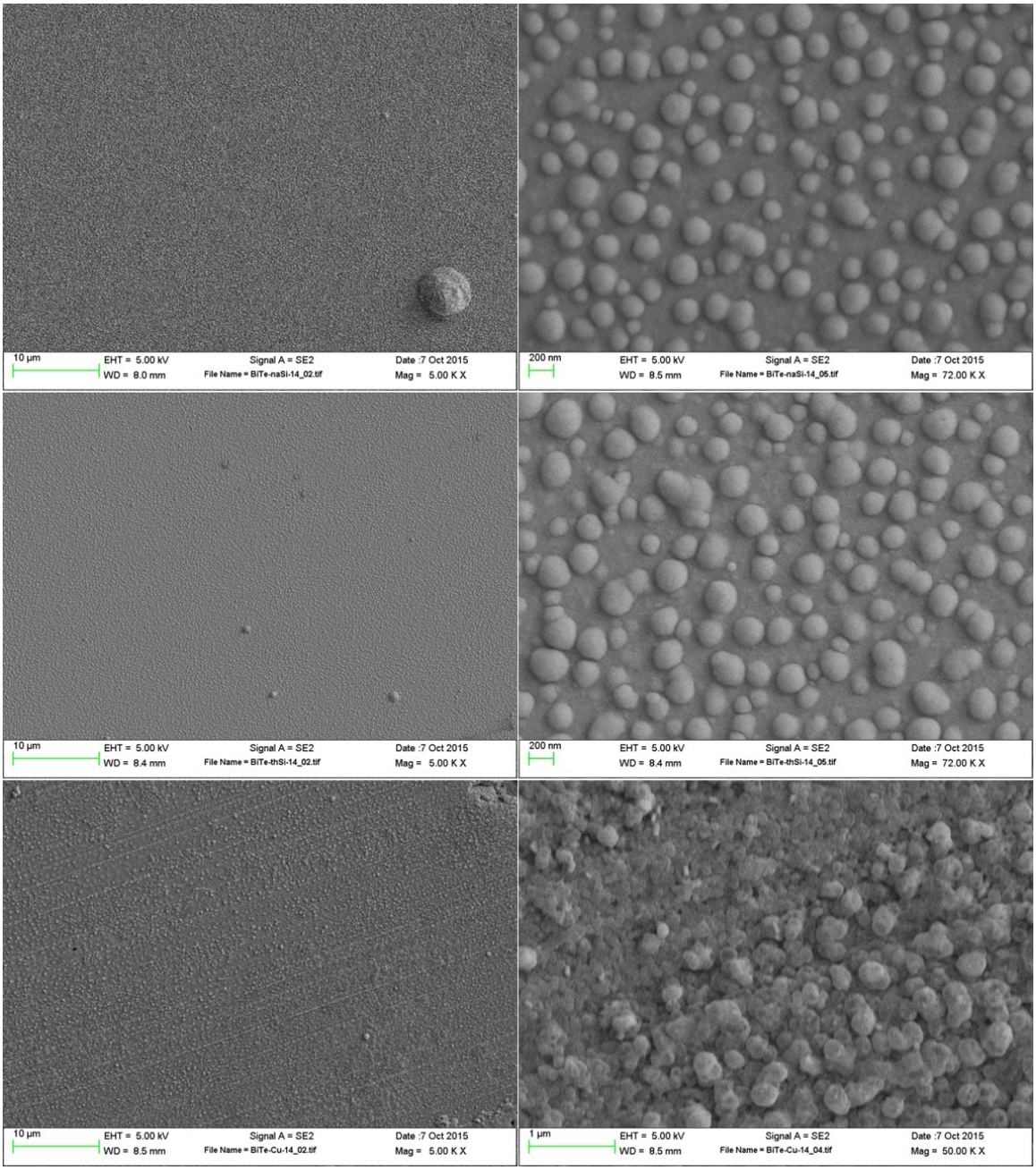

Figure 5–25: Sample 14, native oxide silicon substrate (top), thermal oxide silicon substrate (middle), and copper substrate (bottom), 200°C, 1.0 torr N_2, 266 nm, 4.5 J/cm^2

Figure 5–26 below shows Sample 15, grown on a native oxide silicon substrate (top), a thermal oxide silicon substrate (middle), and a copper substrate (bottom). This sample shows good coverage of the substrate, with a very smooth film of bismuth

telluride covering the different substrates. Using EDS, the stoichiometry is determined to be about 38% bismuth and 62% tellurium for the native oxide silicon substrate, 40% bismuth and 60% tellurium for the thermal oxide silicon substrate, and 34% bismuth and 66% tellurium for the copper substrate. The silicon substrates are close to stoichiometric Bi_2Te_3, while the copper substrate is slightly rich in tellurium. This sample is a reproduction of the conditions of Sample 13, which was contaminated by acetone.

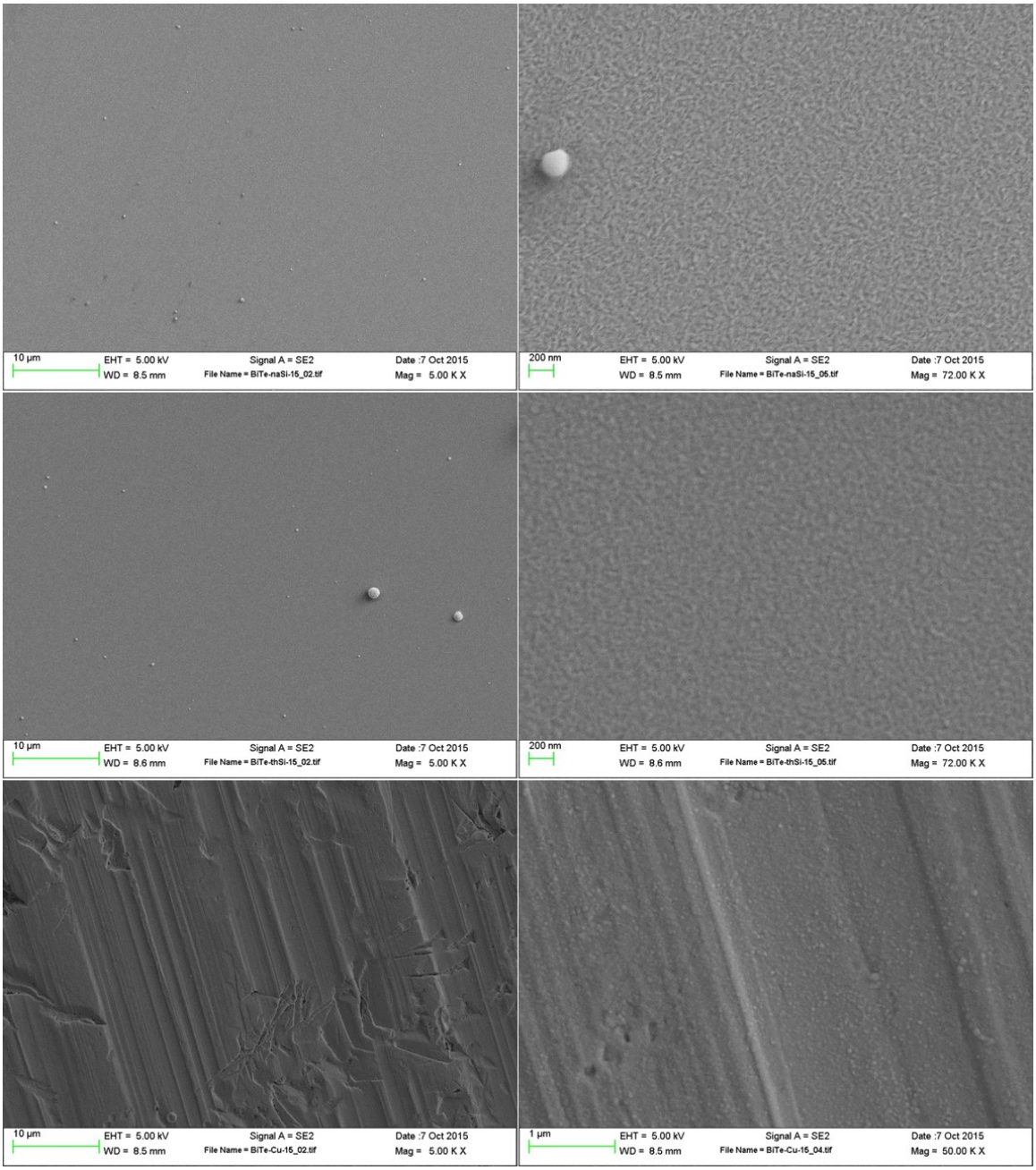

Figure 5–26: Sample 15, native oxide silicon substrate (top), thermal oxide silicon substrate (middle), and copper substrate (bottom), 200°C, 1.0 torr Ar, 266 nm, 3.9 J/cm^2

Figure 5–27 below shows Sample 16, grown on a native oxide silicon substrate (top), a thermal oxide silicon substrate (middle), and a copper substrate (bottom). This sample shows good coverage of the substrate, with a uniform film of bismuth telluride

covering the different substrates. The silicon substrates show surface features and small grain boundaries on the order of about 50 to 100 nanometers, while the copper substrate show similar film structure, but with larger particles on the surface, typically in the range of 100 to 200 nanometers. Using EDS, the stoichiometry is determined to be about 36% bismuth and 64% tellurium for the native oxide silicon substrate, 37% bismuth and 63% tellurium for the thermal oxide silicon substrate, and 40% bismuth and 60% tellurium for the copper substrate. All three substrates are close to stoichiometric Bi_2Te_3. This sample is grown using 532 nm laser irradiation, which may be the reason for the larger grain sizes in the sample deposited on the copper substrate. Due to a filter breaking during the deposition, there are some larger particulates spread out on the surface of the substrate, which are visible in the low-magnification images of the samples. This is due to a brief period of time when the laser fluence was much higher than intended, due to a crack in the neutral density filter, leading to larger particulates of material being ablated from the target surface. Sample 17 replicates this experiment to ensure than this had no other negative effects on the growth of the bismuth telluride films.

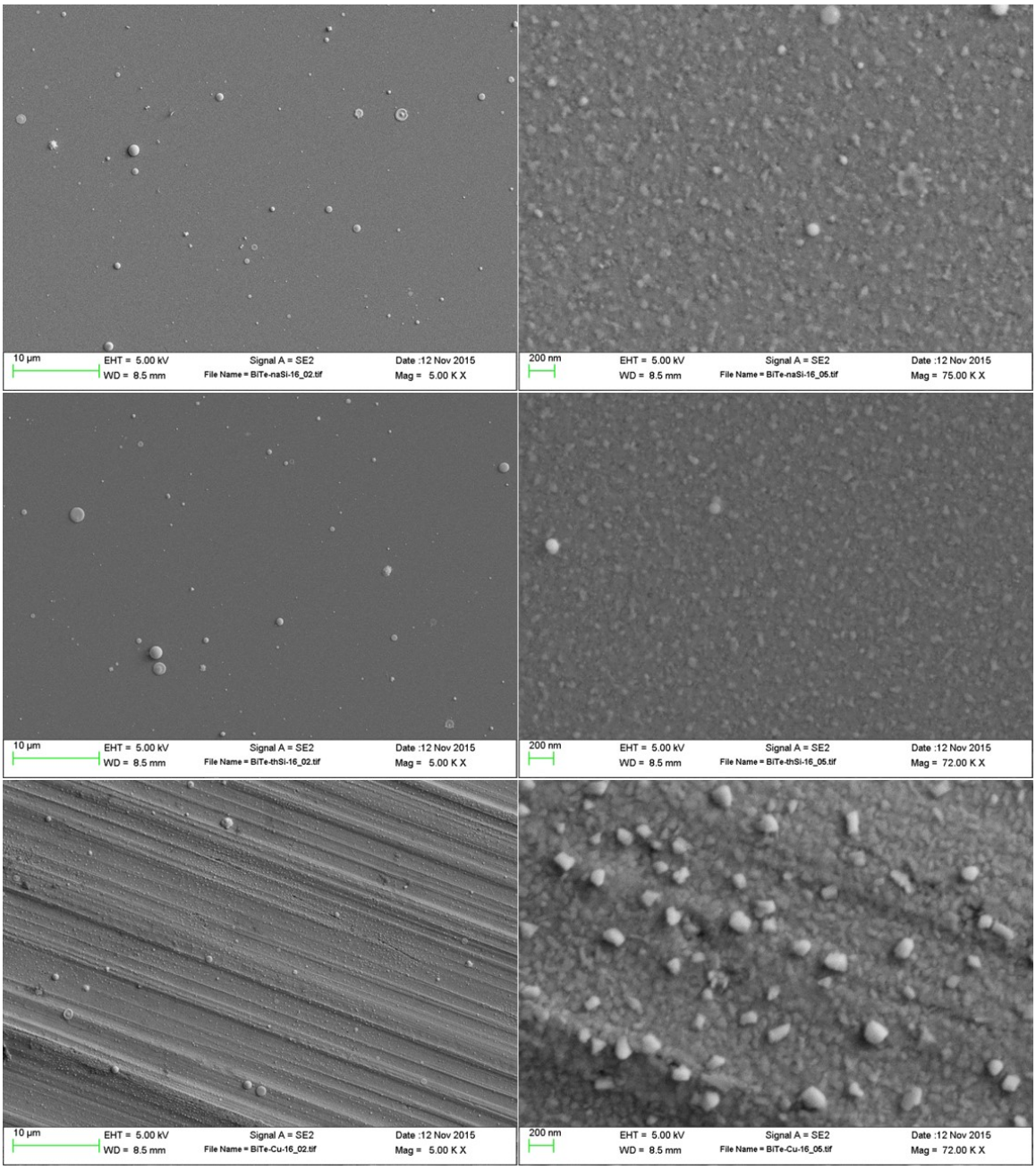

Figure 5–27: Sample 16, native oxide silicon substrate (top), thermal oxide silicon substrate (middle), and copper substrate (bottom), 200°C, 0.1 torr Ar, 532 nm, 5.0 J/cm^2

Figure 5–28 below shows Sample 17, grown on a native oxide silicon substrate (top), a thermal oxide silicon substrate (middle), and a copper substrate (bottom). This sample replicates the conditions from Sample 16 to verify the results. Upon inspection,

Sample 17 is very similar to Sample 16, with the exception of a lack of large particulates. This is exactly what is expected, since the laser fluence was kept to the proper level, and no large particulates were ablated from the target surface. Sample 17 shows good coverage of the substrate, with a uniform film of bismuth telluride covering the different substrates. The silicon substrates show surface features and small grain boundaries on the order of about 50 to 100 nanometers, while the copper substrate show similar film structure, but with slightly larger particles on the surface, typically in the range of 100 to 200 nanometers. Using EDS, the stoichiometry is determined to be about 38% bismuth and 62% tellurium for the native oxide silicon substrate, 37% bismuth and 63% tellurium for the thermal oxide silicon substrate, and 40% bismuth and 60% tellurium for the copper substrate. All three substrates are close to stoichiometric Bi_2Te_3. This sample is grown using 532 nm laser irradiation, which may be the reason for the slightly larger grain sizes in the sample deposited on the copper substrate.

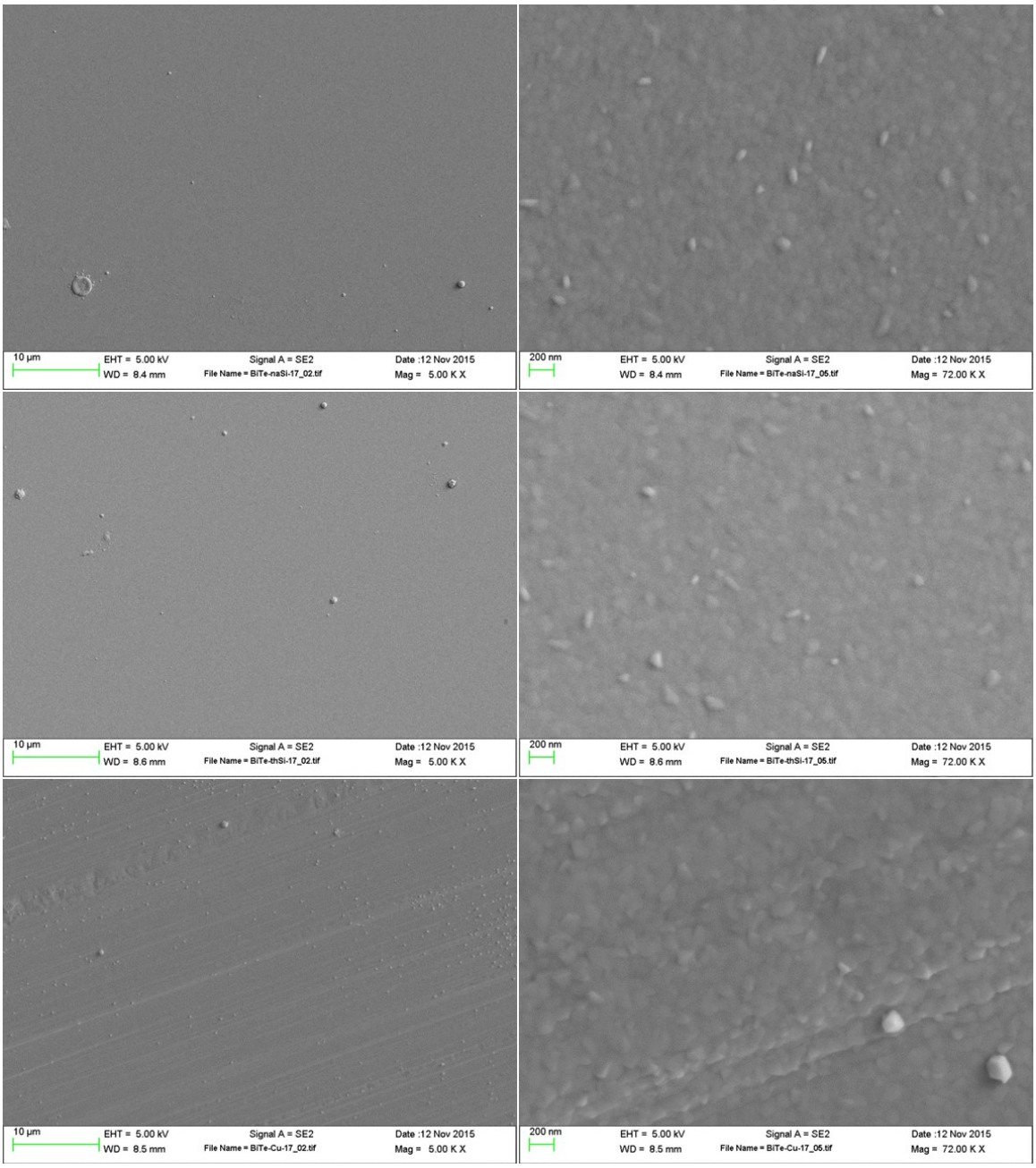

Figure 5–28: Sample 17, native oxide silicon substrate (top), thermal oxide silicon substrate (middle), and copper substrate (bottom), 200°C, 0.1 torr Ar, 532 nm, 4.6 J/cm^2

Figure 5–29 below shows Sample 18, grown on a native oxide silicon substrate (top), a thermal oxide silicon substrate (middle), and a copper substrate (bottom). This sample is very inconsistent depending on the substrate material, and the films that are

grown are not the correct stoichiometry. The native oxide silicon substrate has a smooth film with very small grain size, while the thermal oxide silicon substrate has no detectable film at all on the surface. The copper substrate consists of a film covered in particulates up to 100 nanometers in size. Using EDS, the stoichiometry is determined to be about 24% bismuth and 76% tellurium for the native oxide silicon substrate, and 13% bismuth and 87% tellurium for the copper substrate. For the thermal oxide silicon substrate, there are some large particulates with a stoichiometry of about 48% bismuth and 52% tellurium. For the two samples with films, the chemical composition is extremely rich in tellurium. This is interesting because the growth conditions are high temperature (300°C) and low pressure (0.03 torr), which should result in films that are tellurium deficient. Instead, the films are either completely missing, or rich in bismuth. This may be due to the combination of a high deposition temperature, which increases the amount of re-evaporation present at the substrate surface, and a low deposition pressure, which reduces the interaction of the ablated species with the ambient gas, leaving the species with too much energy when they impinge upon the substrate surface. This does not exactly explain the large bismuth deficiency, or the fact that the thermal oxide silicon substrate has no film on the surface at all, but they results were not replicated in other experiments, so further investigation would have to be done to determine if this is an anomalous experiment or if there is some other mechanism at work.

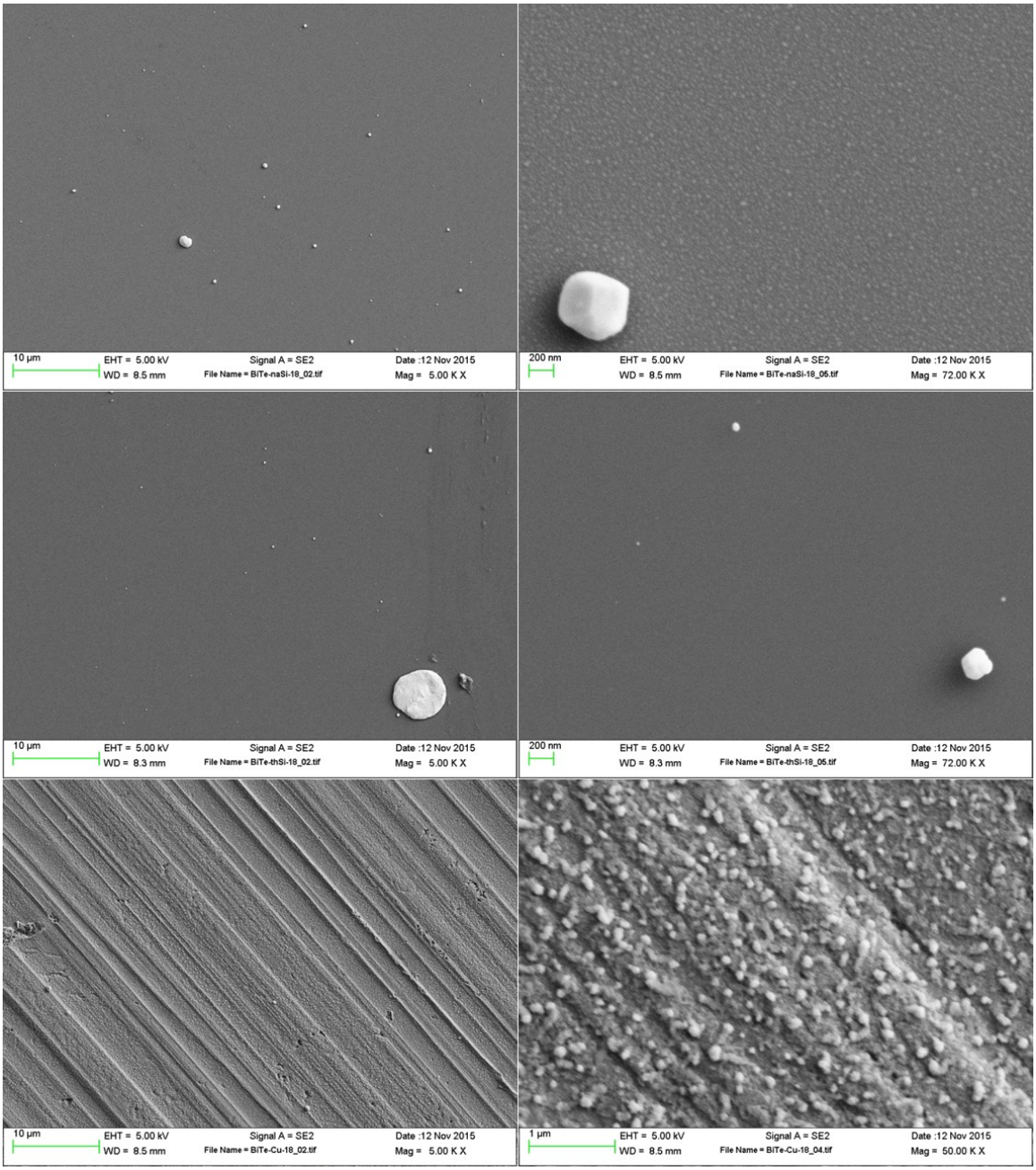

Figure 5–29: Sample 18, native oxide silicon substrate (top), thermal oxide silicon substrate (middle), and copper substrate (bottom), 300°C, 0.03 torr Ar, 266 nm, 3.4 J/cm^2

Figure 5–30 below shows Sample 19, grown on a native oxide silicon substrate (top), a thermal oxide silicon substrate (middle), and a copper substrate (bottom). This sample shows poor substrate surface coverage, with very small nanoparticles partially

covering the substrates. The silicon substrates show surface features and small grain boundaries on the order of about 100 nanometers and less, while the copper substrate shows more of a film-like surface with slightly larger particulates, typically 50 to 200 nanometers. Using EDS, the stoichiometry is determined to be about 36% bismuth and 64% tellurium for the native oxide silicon substrate, 37% bismuth and 63% tellurium for the thermal oxide silicon substrate, and 41% bismuth and 59% tellurium for the copper substrate. All three substrates are close to stoichiometric Bi_2Te_3. This sample is grown using a slightly elevated temperature (250°C) and 1 torr of argon, which may explain the low coverage and surface morphology of the sample, since the re-evaporation rate of material on the substrate is higher for increased temperature.

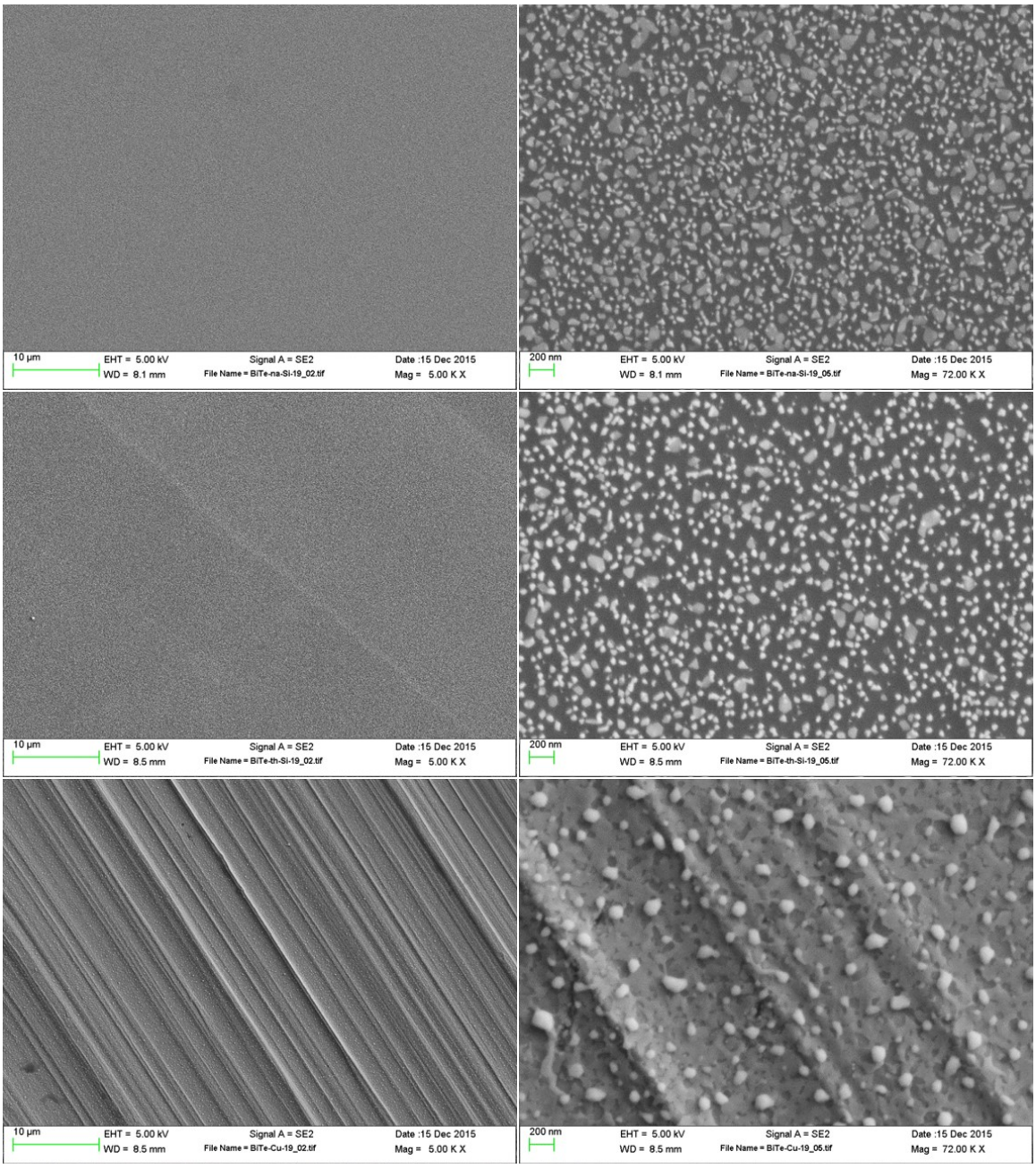

Figure 5–30: Sample 19, native oxide silicon substrate (top), thermal oxide silicon substrate (middle), and copper substrate (bottom), 250°C, 1.0 torr Ar, 266 nm, 2.9 J/cm^2

Figure 5–31 below shows Sample 20, grown on a native oxide silicon substrate (top), a thermal oxide silicon substrate (middle), and a copper substrate (bottom). This sample shows good coverage over the different substrates. The silicon substrates show

surface features and small grain boundaries on the order of 100 nanometers. On the other hand, the copper substrate consists of nanoparticles, typically 50 to 200 nanometers in size, covering almost the entire substrate surface. Using EDS, the stoichiometry is determined to be about 49% bismuth and 51% tellurium for both silicon substrates, and 42% bismuth and 58% tellurium for the copper substrate. . It is believed that due to the volatility of tellurium, the deposition temperature has an upper limit at which the tellurium species evaporate faster than they can be replaced by incoming species, leading to the deficiency of tellurium in films grown at deposition temperatures over 200°C. This is tested by growing this sample using a range of temperatures. Deposition begins at a substrate temperature of 200°C; the temperature of the substrate is then increased to 300°C during deposition, followed by letting the substrate cool back down to 200°C, all while deposition is occurring. From these results, it is clear that for the silicon substrate, the sample is still deficient in tellurium. However, the stoichiometry of the copper substrate is very close to Bi_2Te_3, and the surface morphology shows an interesting mix of an underlying film with small nanoparticles on top of the film.

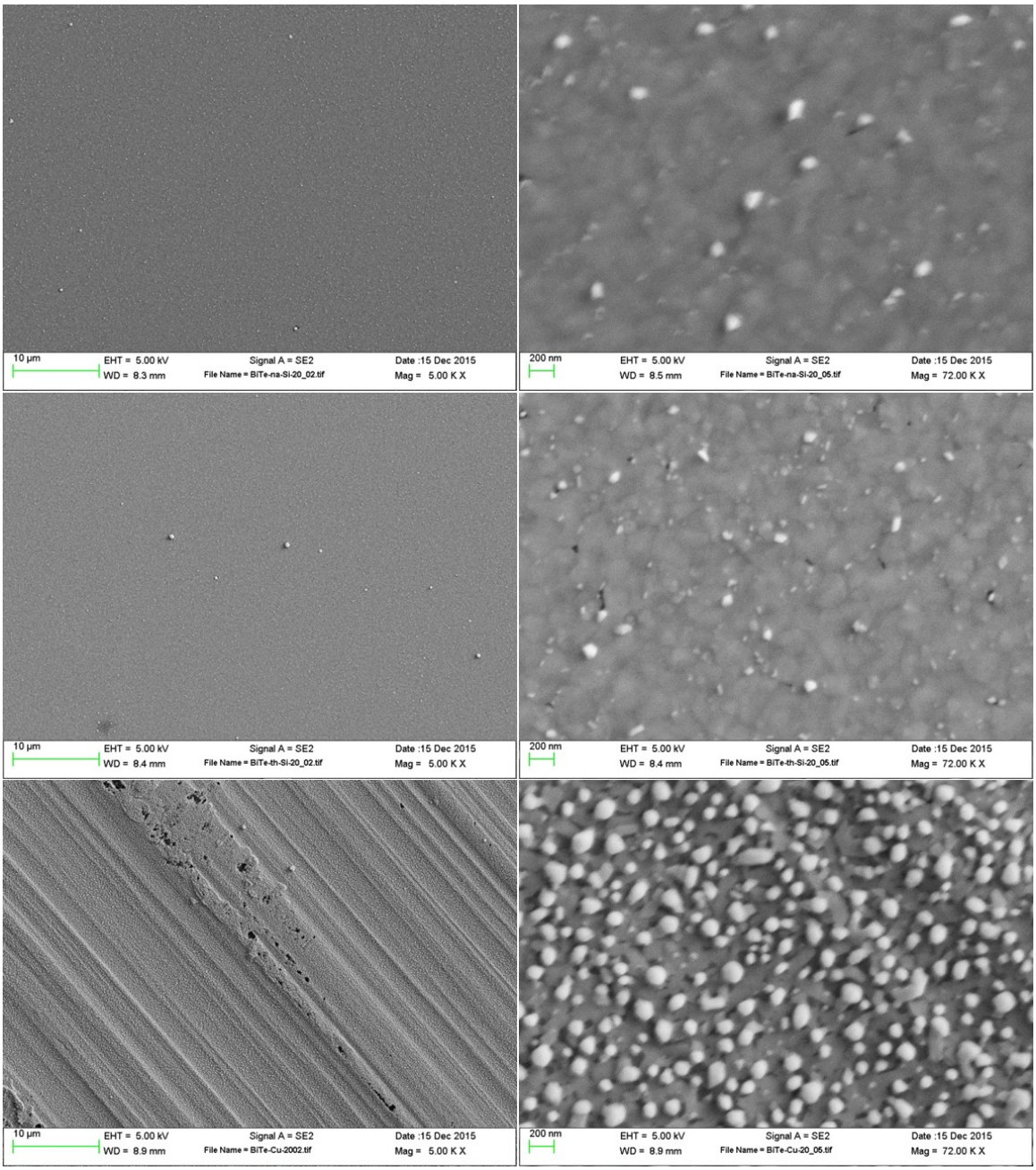

Figure 5–31: Sample 20, native oxide silicon substrate (top), thermal oxide silicon substrate (middle), and copper substrate (bottom), 200-300°C, 0.1 torr Ar, 266 nm, 3.4 J/cm^2

5.2.2 Stoichiometric Analysis

Bismuth telluride films examined using the SEM are also analyzed using EDS to determine the film stoichiometry and chemical composition. While SEM consists of backscattered electron images that display compositional contrast resulting from elements of different atomic numbers, EDS can identify particular elements and their relative abundance in samples. This allows for the determination of relative values such as atomic percent and weight ratios. As a result, EDS is extremely useful for determining the chemical composition of grown bismuth telluride films and confirming the stoichiometric transfer and deposition of the PLD method.

From a specific SEM backscattered image, an X-ray spectrum is created by directing a beam of X-rays onto the sample surface. The energy of these X-rays is determined from the specific elements that will be identified. Larger elements require higher energy X-rays to get an accurate representation of their chemical composition within the sample. Due to the high energy required for bismuth and tellurium (> 10 keV), the penetration depth of the X-rays is large, resulting in a large interference from the underlying substrate. As a result, particular elements must be isolated to accurately determine the chemical composition of the surface film itself. The software used for collection and analysis of the EDS data is called INCA. A typical EDS spectrum is shown below in Figure 5–32:

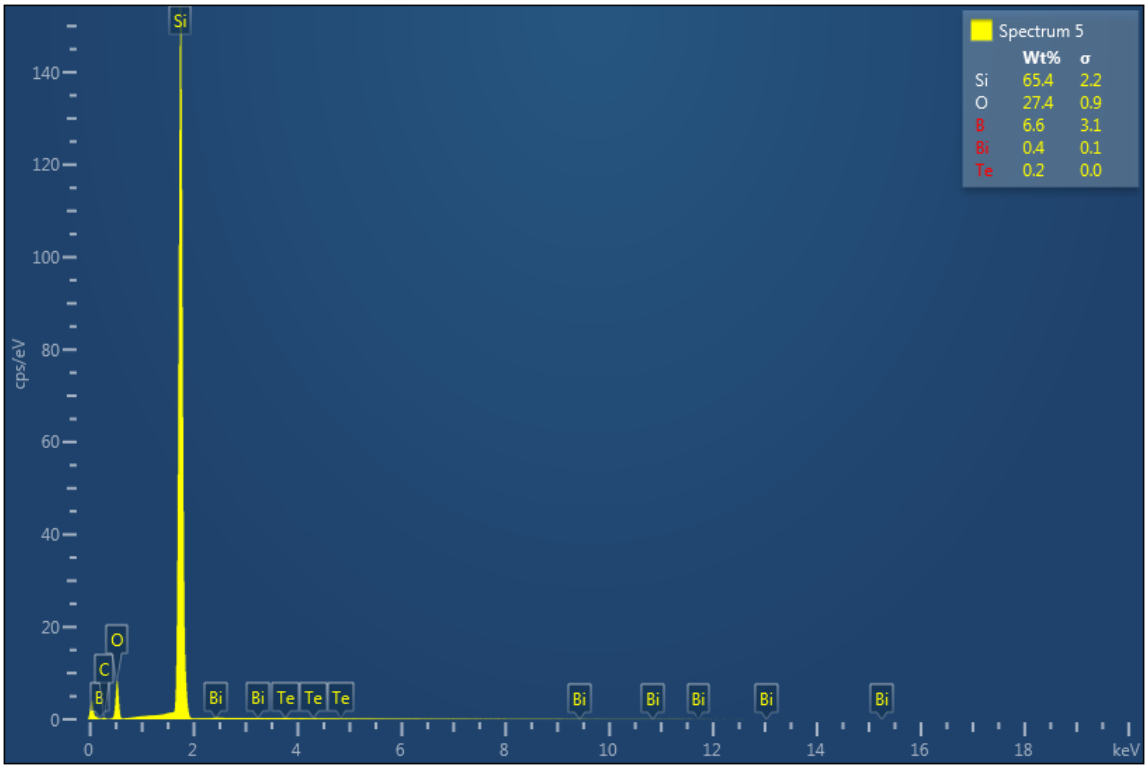

Figure 5–32: EDS Spectrum of Bismuth Telluride Film on Silicon Wafer

The spectrum is dominated by the underlying Si/SiO_2 wafer substrate, so to get an accurate chemical composition, elemental bismuth and tellurium are isolated using the software, and a chemical composition is extracted. We know the films are extremely pure due to the process of PLD, so this technique minimizes the error in excluding the known substrate materials and other miscellaneous elements.

5.3 Electrical Characterization of Films

Electrical characterization of the bismuth telluride films is carried out using the Van der Pauw method, consisting of a 4-point probe setup, to measure the film resistivity. A current is applied through two of the probes, while the voltage difference across the other two probes is measured. This is done using a Keithley 2400 SourceMeter. The probe tips, typically made of copper due to good electrical and thermal conductivity, are

positioned on the perimeter of the sample using four independent three-dimensional micro-positioner translation stages (Quater XYZ 300 TR). Current-voltage (I-V) curves are then obtained, and the sheet resistance is determined from the slope of those curves. Using these values, as well as the thickness of the films (determined by cross-sectional SEM analysis), the resistivity can be determined numerically using the following formulation:

$$exp\left(-\pi\frac{R_{AB-CD}*d}{\rho}\right)+exp\left(-\pi\frac{R_{BC-DA}*d}{\rho}\right)=1$$

where d is the film thickness, ρ is the film resistivity, and $R_{AB\text{-}CD}$ and $R_{BC\text{-}DA}$ are the sheet resistance values found by fitting the slope of the I-V curves for the two different Van der Pauw orientations. A schematic of the Van der Pauw method, and the two different orientations used for taking measurements, is shown below in Figure 5–33.

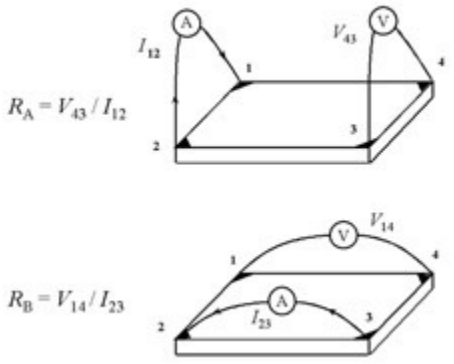

Figure 5–33: Schematic of a Van der Pauw Configuration Setup (reproduced with caption from [88])

The experimental setup of the Van der Pauw method is shown below in Figure 5–34. The image on the left shows the entire experimental apparatus; the image on the top right shows the base plate where the sample is held and the probe tips make contact with

the surface; and the bottom left image shows a magnified view of the sample area and probe tips.

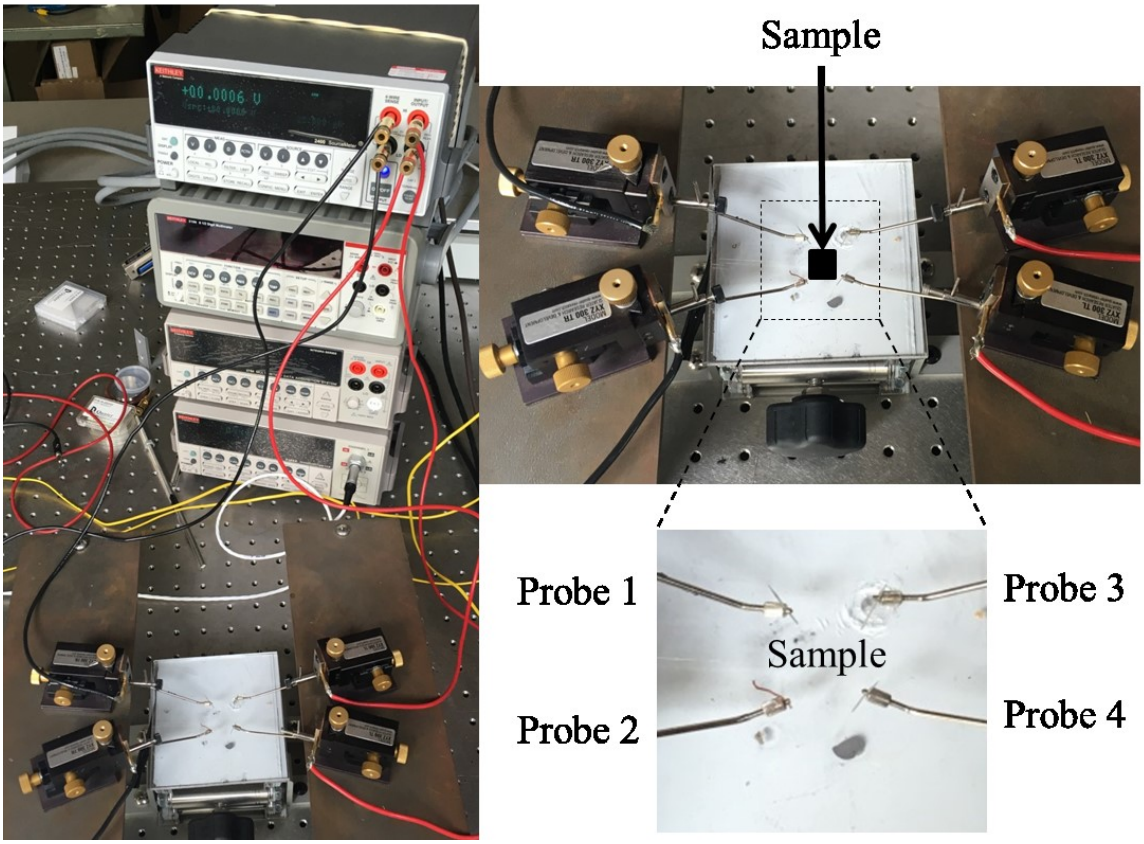

Figure 5–34: Experimental Setup of the Van der Pauw Equipment

The Seebeck coefficient of the bismuth telluride films is measured by applying a temperature difference across the film and measuring the resulting voltage induced over the sample. The temperature gradient is applied using an Acopian Power Supply (Model Y0135LXB530-C1EM3) and the voltage is measured using a Keithley Nanovoltmeter (Model 2182A). The sample is positioned over a physical gap to help thermally isolate a "hot" side and a "cold" side of the sample. The temperature is measured by two different thermocouples, one on each side of the gap. Two micro-positioner translation stages

(Quater XYZ 300 TR) align probe tips on each side of the gap to measure the voltage potential between the hot and cold sides. The measured voltage versus the change in temperature is then plotted, and a linear fit is used to determine the slope of the line. This slope gives the Seebeck coefficient, measured in microvolts per Kelvin (μV / K). Figure 5–35 shows the experimental setup of the Seebeck coefficient measurement apparatus. The top left image is the entire assembly; the bottom left image is a magnified view of where the sample is located with a white probe tip (Probe) and silver thermocouple (TC) on each side of the gap; and the right image shows the heating element feeding into one side of the gap to supply the temperature difference.

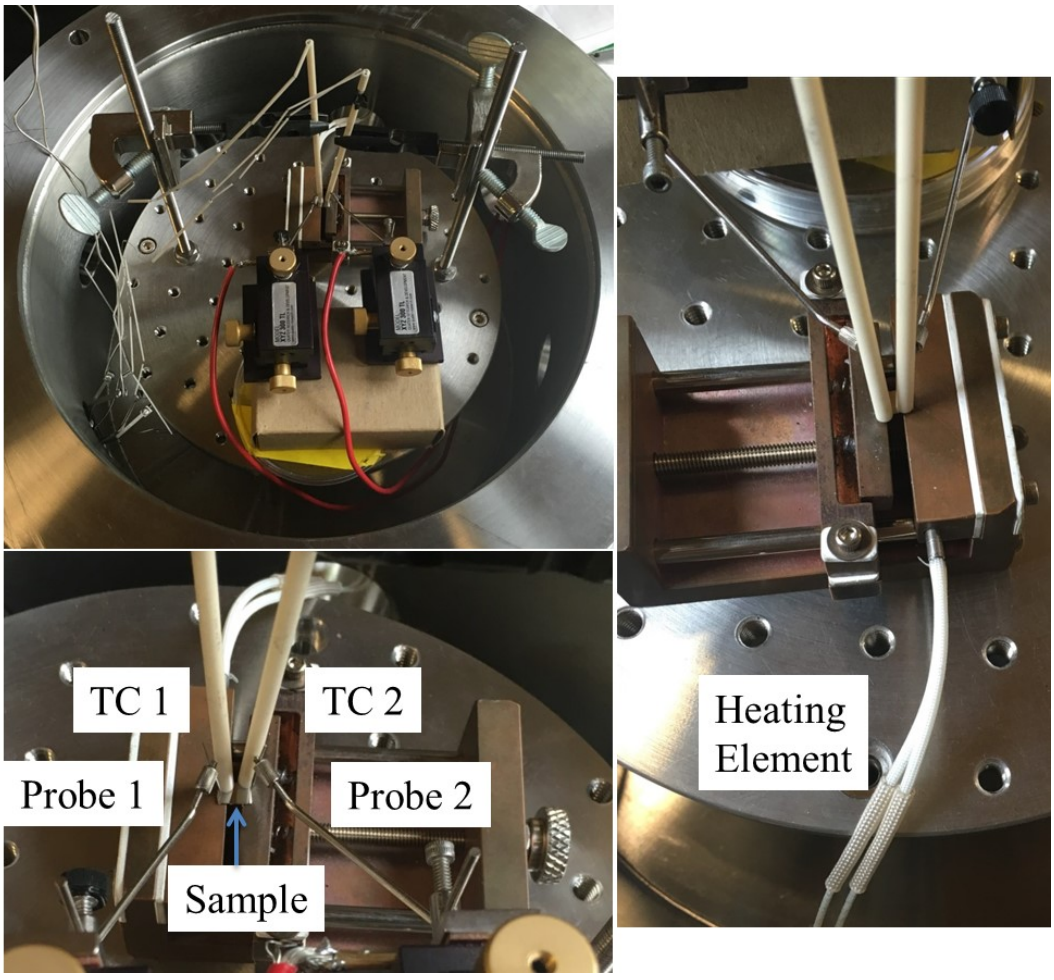

Figure 5–35: Experimental Setup of Seebeck Coefficient Measurement Apparatus

Figure 5–36 shows the voltmeter and power supply equipment used for Seebeck coefficient measurements.

Figure 5–36: Nanovoltmeter (top) and Power Supply (bottom) used for Seebeck Coefficient Measurements

Table 5-2 below summarizes the resistivity and Seebeck coefficient of the different bismuth telluride film samples. Seebeck coefficient measurements are only taken for a few of the samples, based on expected performance and resistivity results. Future work should examine each of the samples for electrical properties.

Table 5-2: Van der Pauw and Seebeck Coefficient Results for Bi_2Te_3 Films

Sample	Temperature (°C)	Pressure (torr)	Thickness (nm)	Resistivity (mΩ cm)	Seebeck (μV/K)
na-Si-8	200	0.1 Ar	450	24.8	43
na-Si-9	200	0.035 Ar	200	60.1	

na-Si-10	250	0.1 Ar	200	191.2	
na-Si-11	200	0.035 Ar	200	64.7	
na-Si-12	200	0.1 Ar	300	28.3	-103
na-Si-13	200	1.0 Ar	200	-	
na-Si-14	200	1 N_2	200	224.4	
th-Si-14	200	1 N_2	200	568.7	
na-Si-15	200	1 Ar	200	4224.4	
na-Si-16	200	0.1 Ar	30	-	
th-Si-16	200	0.1 Ar	30	173.9	
na-Si-17	200	0.1 Ar	30	6	31
na-Si-18	300	0.03 Ar	60	216.5	327
na-Si-19	250	1 Ar	100	Non Conductive	
na-Si-20	200-300	0.1 Ar	180	112.2	-28

From this data, it is evident that the films with the lowest electrical resistivity (highest electrical conductivity) are those with the most prominent surface features. This coincides with the samples grown using 532 nm laser irradiation, as well as samples grown at slightly lower pressures (less than 0.1 torr). Furthermore, samples with the largest Seebeck coefficient correspond to samples with low electrical resistivity. The sample with the highest potential thermoelectric figure of merit is Sample 12, which is one of the samples grown using 532 nm laser irradiation. Sample 18 has a very large Seebeck coefficient, but the film composition is not stoichiometric Bi_2Te_3, so there may be other factors involved.

In his study, Li Bassi shows that the more compact films give better values for electrical resistivity and power factor than the films composed of nanostructures [70]. While this work does not measure the density of the samples, it was determined that the best films in terms of electrical resistivity and power factor were those that were densely packed nanoparticles, or continuous films with abundant surface features on the nanoscale. This is in agreement with the work done in reference [70].

The following data shows the I-V curves of the different bismuth telluride film samples, which are used to calculate the resistivity of the films. Samples 1 through 7 were either non-conductive, or the film did not have enough coverage over the substrate to pick up a signal from the Van der Pauw experimental setup.

Figure 5–37 below shows the I-V curve for the Bi_2Te_3 material used as the ablation target. The two-point resistance, measured using a digital multimeter (Fluke-179 Series), is about 0.6 ohms. The film resistivity is calculated to be 8263 milliohm-centimeters from the Van der Pauw method.

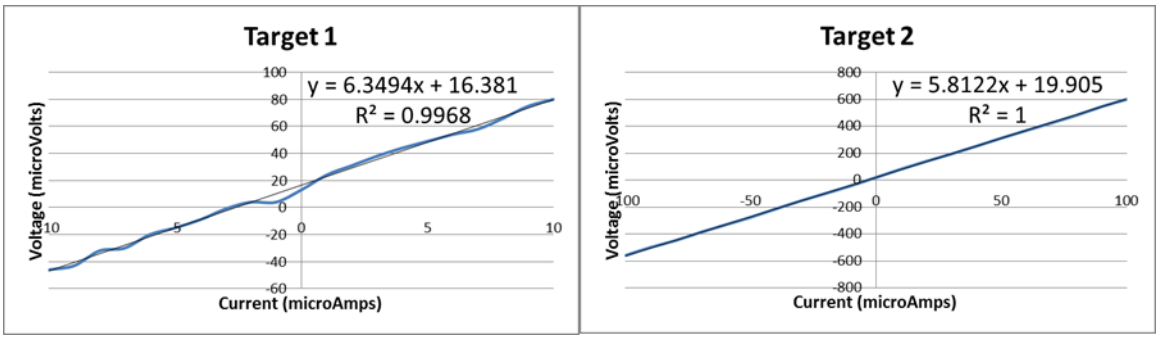

Figure 5–37: Bi_2Te_3 Target I-V curve; 8263 mΩ cm

Figure 5–38 below shows the I-V curve for Sample 8 (native oxide silicon substrate). The two-point resistance, measured using a digital multimeter, is about 100 ohms. The film resistivity is calculated to be between 16.5 and 24.8 milliohm-centimeters (based on the film thickness) from the Van der Pauw method.

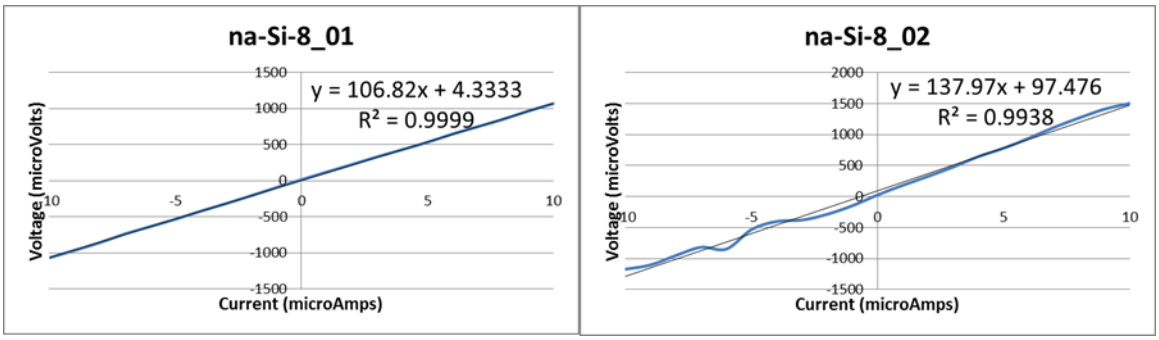

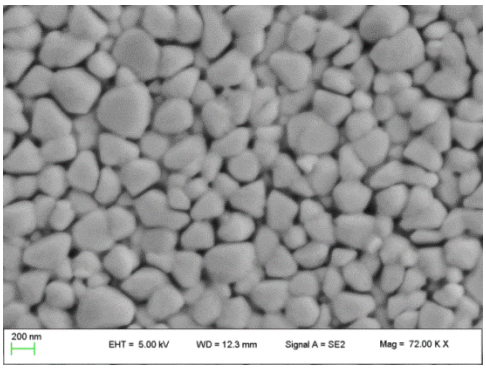

Figure 5–38: Sample 8, native oxide silicon substrate, 16.5 mΩ cm (300 nm thick) to 24.8 mΩ cm (450 nm thick)

Figure 5–39 below shows the I-V curve for Sample 9 (native oxide silicon substrate). The two-point resistance, measured using a digital multimeter, is about 600 ohms. The film resistivity is calculated to be 60.1 milliohm-centimeters from the Van der Pauw method.

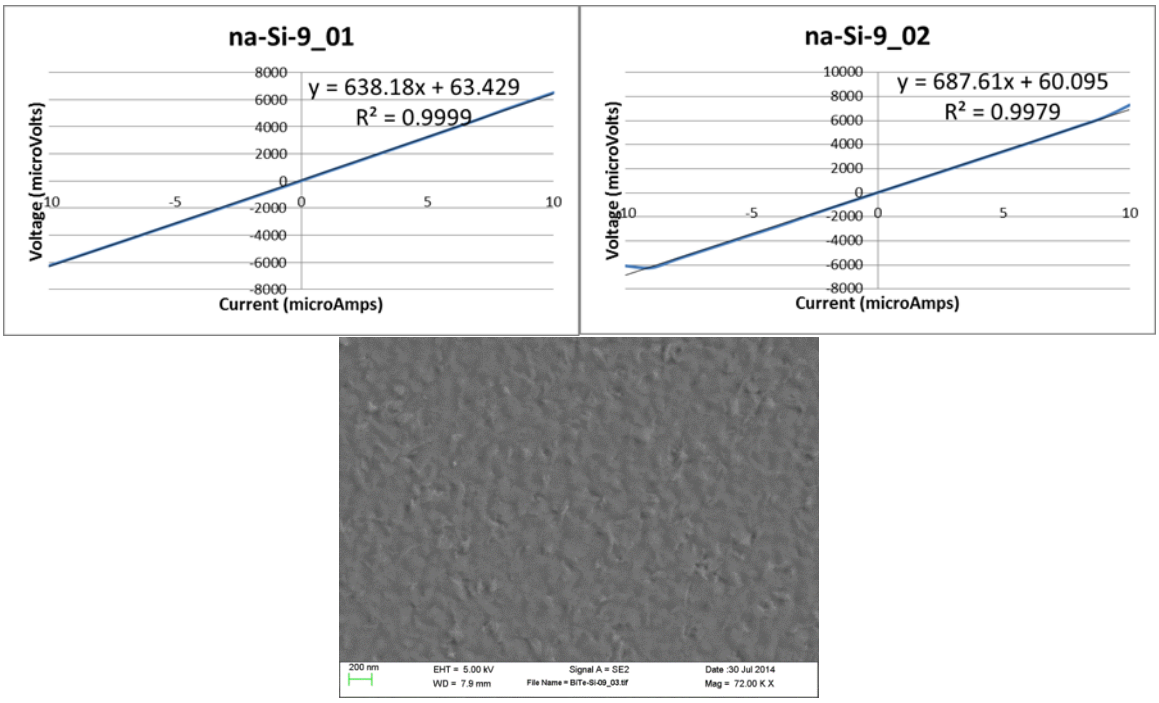

Figure 5–39: Sample 9, native oxide silicon substrate, 60.1 mΩ cm

Figure 5–40 below shows the I-V curve for Sample 10 (native oxide silicon substrate). The two-point resistance, measured using a digital multimeter, is about 1500 ohms. The film resistivity is calculated to be 191.2 milliohm-centimeters from the Van der Pauw method.

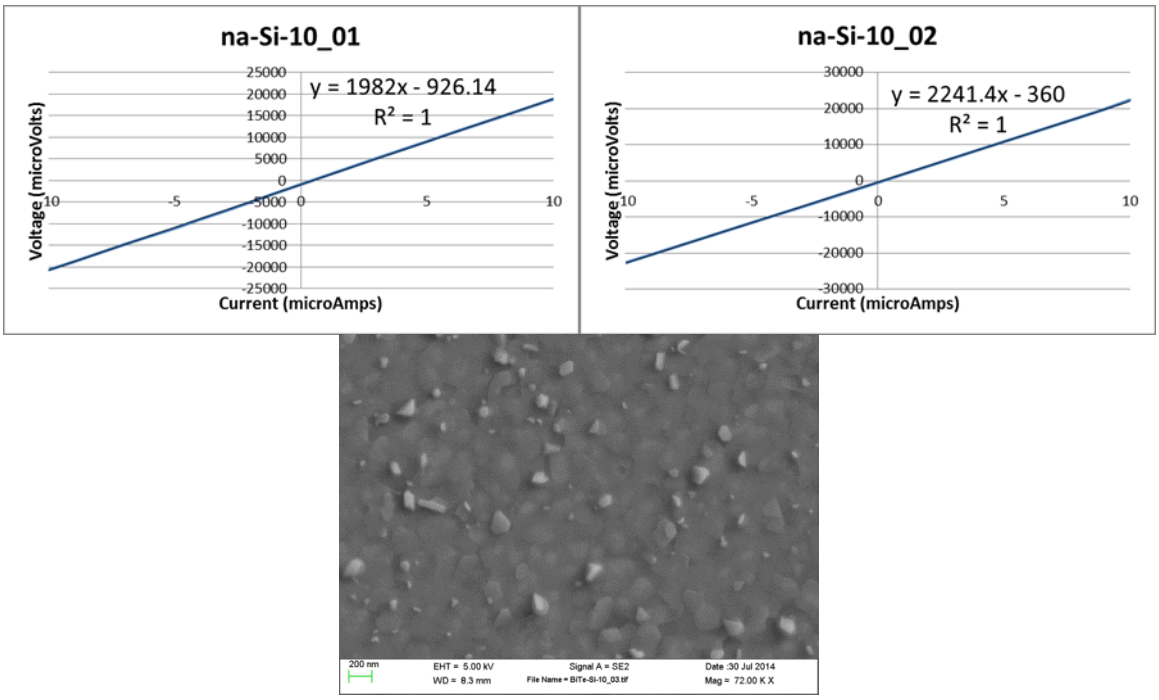

Figure 5–40: Sample 10, native oxide silicon substrate, 191.2 mΩ cm

Figure 5–41 below shows the I-V curve for Sample 11 (native oxide silicon substrate). The two-point resistance, measured using a digital multimeter, is about 600 ohms. The film resistivity is calculated to be 64.7 milliohm-centimeters from the Van der Pauw method.

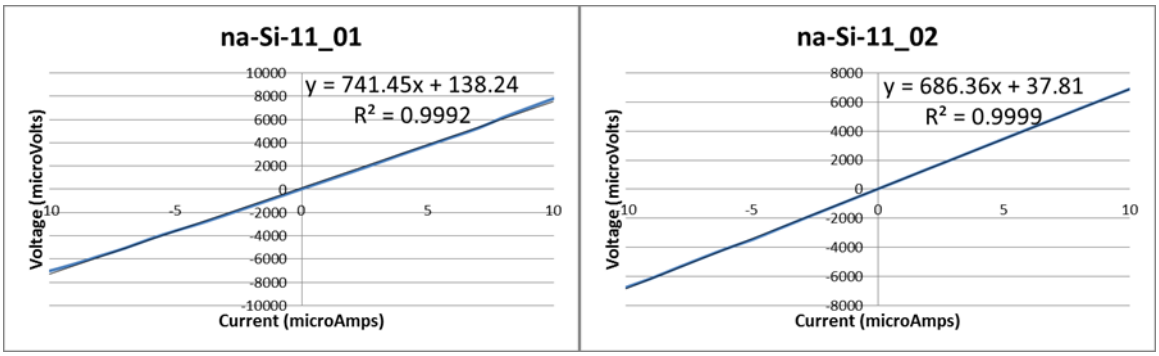

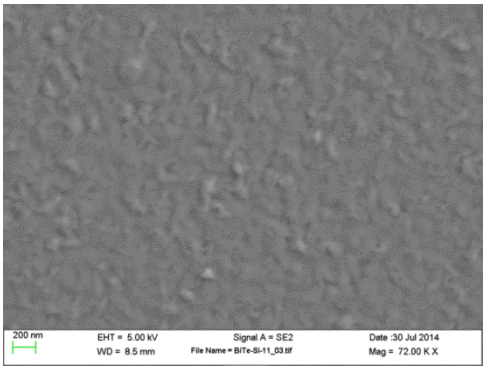

Figure 5–41: Sample 11, native oxide silicon substrate, 64.7 mΩ cm

Figure 5–42 below shows the I-V curve for Sample 12 (native oxide silicon substrate). The two-point resistance, measured using a digital multimeter, is about 250 ohms. The film resistivity is calculated to be between 18.9 and 28.3 milliohm-centimeters (based on the film thickness) from the Van der Pauw method.

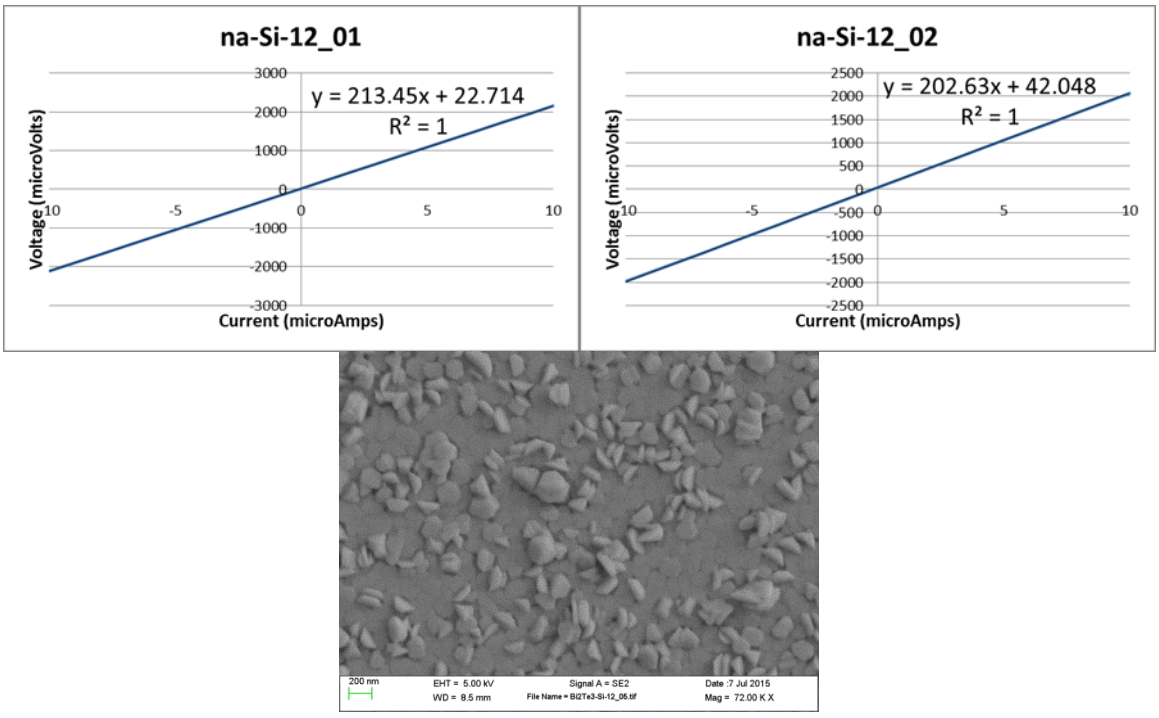

Figure 5–42: Sample 12: native oxide silicon substrate, 18.9 mΩ cm (200 nm thick) to 28.3 mΩ cm (300 nm thick)

Sample 13 is unable to be tested with the Van der Pauw method because of the acetone delamination that occurred in removing the sample from the deposition chamber, which resulted in a loss of almost the entire bismuth telluride film.

Figure 5–43 below shows the I-V curve for Sample 14 (native oxide silicon substrate). The two-point resistance, measured using a digital multimeter, is about 2500 ohms. The film resistivity is calculated to be 224.4 milliohm-centimeters from the Van der Pauw method.

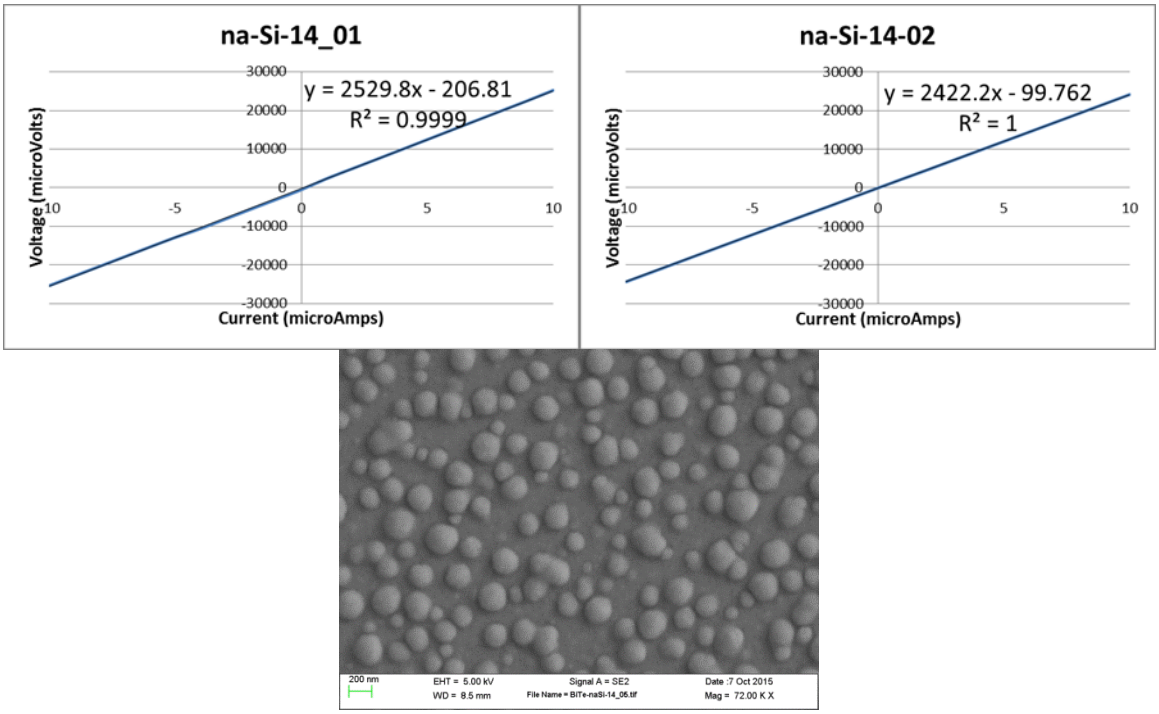

Figure 5–43: Sample 14, native oxide silicon substrate, 224.4 mΩ cm

Figure 5–44 below shows the I-V curve for Sample 14 (thermal oxide silicon substrate). The two-point resistance, measured using a digital multimeter, is about 4500 ohms. The film resistivity is calculated to be 568.7 milliohm-centimeters from the Van der Pauw method.

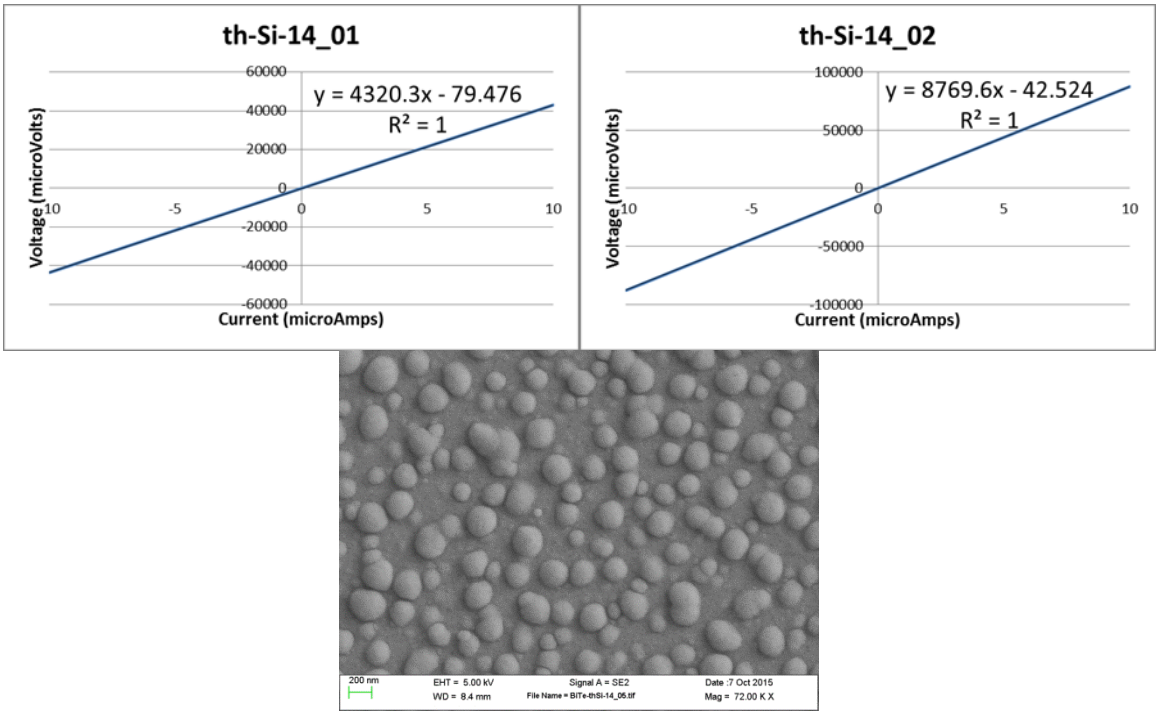

Figure 5–44: Sample 14, thermal oxide silicon substrate, 568.7 mΩ cm

Figure 5–45 below shows the I-V curve for Sample 15 (native oxide silicon substrate). The two-point resistance, measured using a digital multimeter, is about 50,000 ohms. The film resistivity is calculated to be 4224 milliohm-centimeters from the Van der Pauw method.

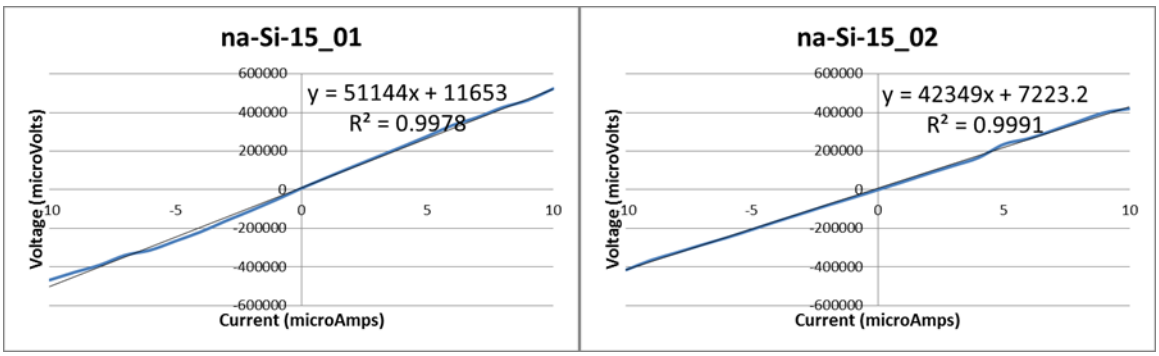

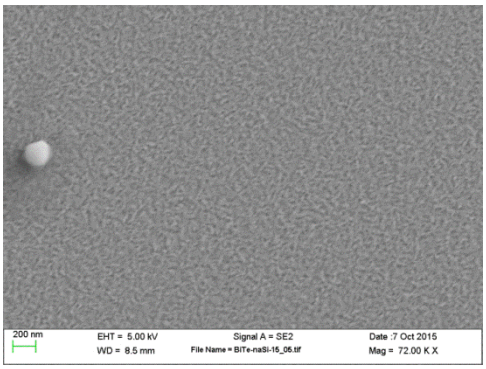

Figure 5–45: Sample 15, native oxide silicon substrate, 4.2244 Ω cm

Sample 16 (native oxide silicon substrate) could not be measured in the Van der Pauw setup due to a bad connection between the electrical pins and the sample. The two-point resistance, measured using a digital multimeter, is about 5700 ohms.

Figure 5–46 below shows the I-V curve for Sample 16 (thermal oxide silicon substrate). The two-point resistance, measured using a digital multimeter, is about 15,000 ohms. The film resistivity is calculated to be 173.9 milliohm-centimeters from the Van der Pauw method.

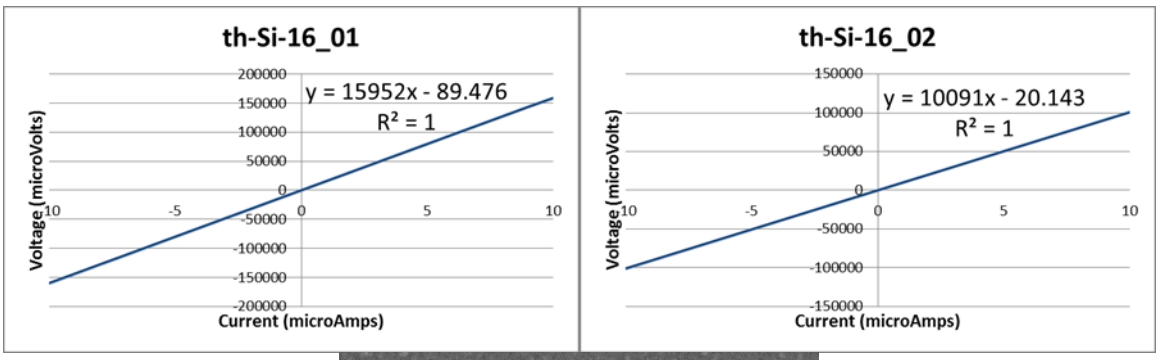

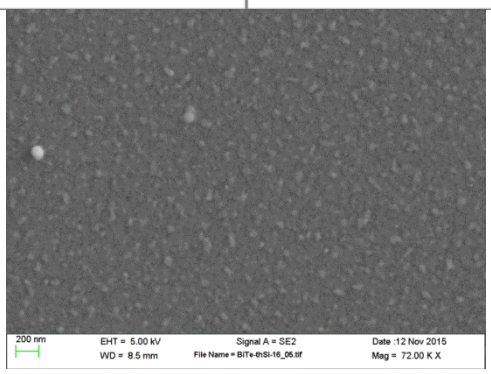

Figure 5–46: Sample 16, thermal oxide silicon substrate, 173.9 mΩ cm

Figure 5–47 below shows the I-V curve for Sample 17 (native oxide silicon substrate). The two-point resistance, measured using a digital multimeter, is about 400 ohms. The film resistivity is calculated to be 6.0 milliohm-centimeters from the Van der Pauw method.

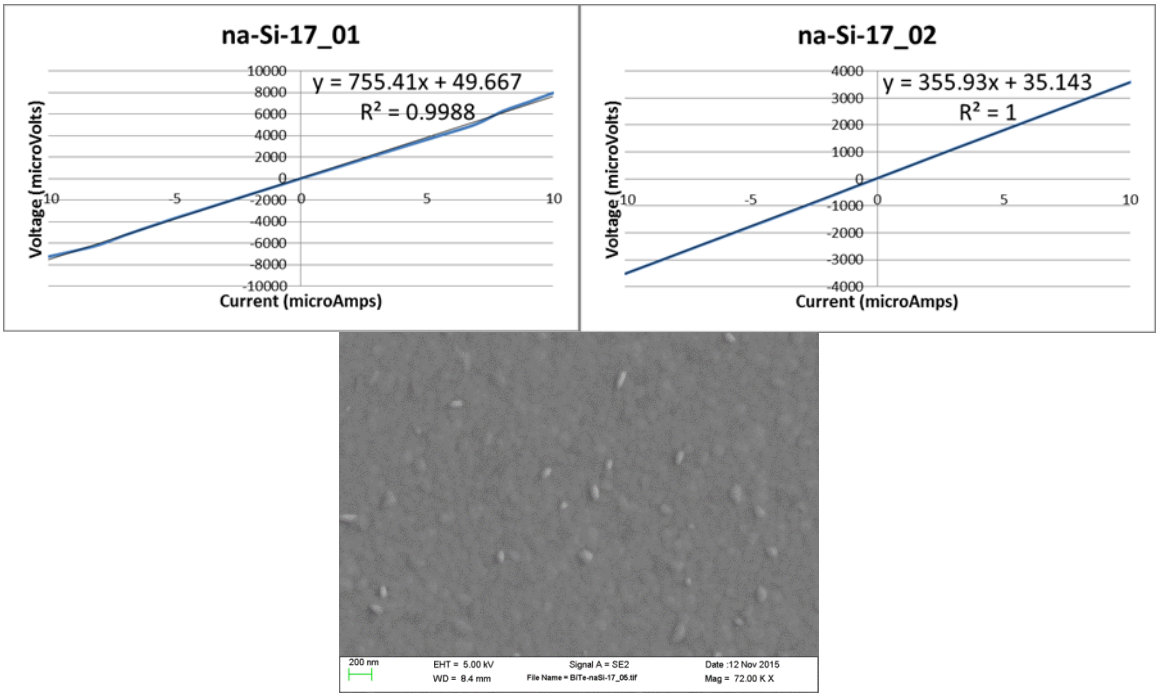

Figure 5–47: Sample 17, native oxide silicon substrate, 6.0 mΩ cm

Figure 5–48 below shows the I-V curve for Sample 18 (native oxide silicon substrate). The two-point resistance, measured using a digital multimeter, is about 9400 ohms. The film resistivity is calculated to be 216.5 milliohm-centimeters from the Van der Pauw method.

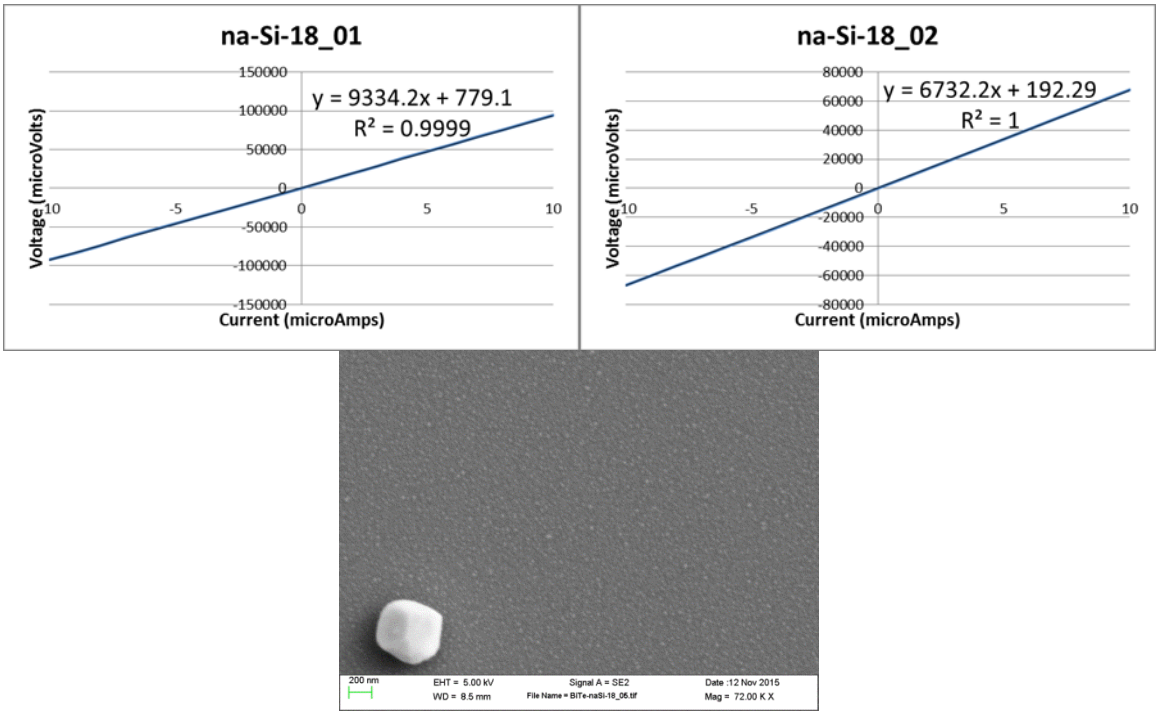

Figure 5–48: Sample 18, native oxide silicon substrate, 216.5 mΩ cm

Sample 19 (native oxide silicon substrate) could not be measured in the Van der Pauw setup due to the sample being non-conductive. This may be a result of the incomplete coverage of bismuth telluride on the substrate surface. The two-point resistance, measured using a digital multimeter, is over 10 mega-ohms.

Figure 5–49 below shows the I-V curve for Sample 20 (native oxide silicon substrate). The two-point resistance, measured using a digital multimeter, is about 600 ohms. The film resistivity is calculated to be 112.2 milliohm-centimeters from the Van der Pauw method.

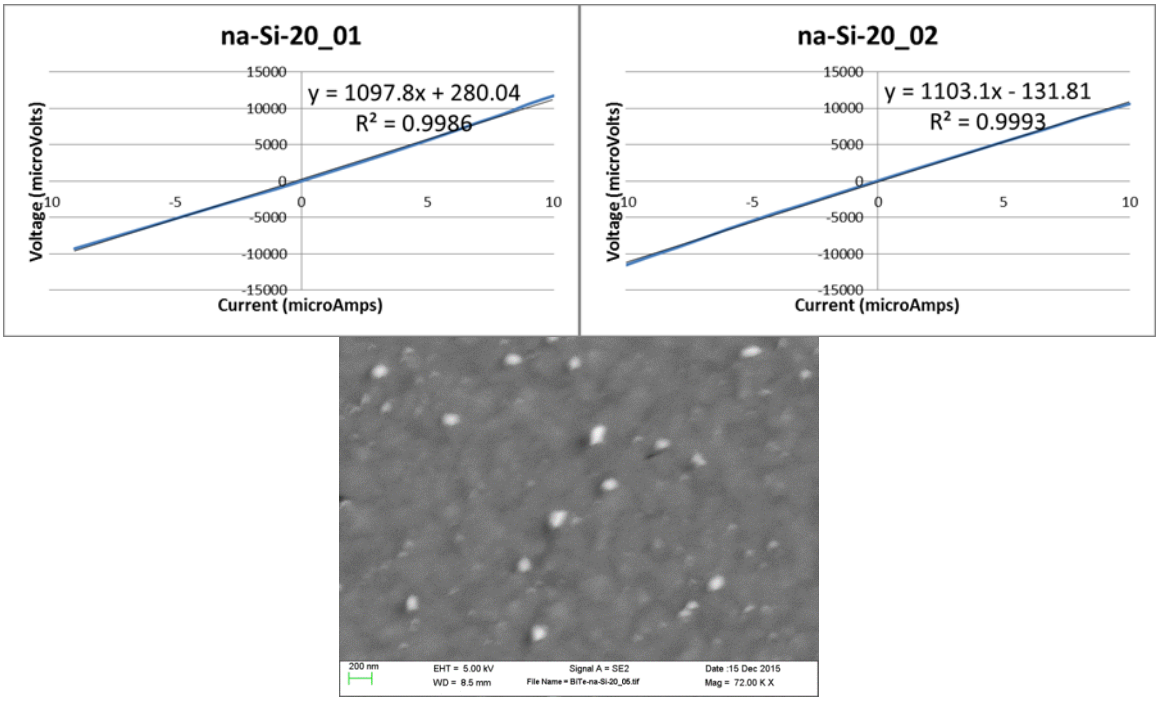

Figure 5–49: Sample 20, native oxide silicon substrate, 112.2 mΩ cm

5.4 Film Crystallography

To determine the crystallinity of the bismuth telluride samples, X-ray diffraction (XRD) is performed. This method uses monochromatic X-rays to determine the spacing of planes in a crystal lattice. Using Bragg's Law ($n\lambda = 2d \sin\theta$), constructive interference occurs at specific angles. All of the lattice diffraction directions can then be determined by scanning the sample through a range of angles (2θ). The diffraction peaks of the sample are then converted to the *d*-spacing, which is unique for a given material. Figure 5–50 shows the XRD spectrum of the solid bismuth telluride sample used for ablation (top), as well as a powder sample (bottom) with the prominent peaks labeled with their respective crystalline orientation. The powder sample was obtained by grinding off some of the solid ablation target. This is done to compare the XRD results

for both the powder sample and the solid sample to ensure consistency. The software used for analysis and peak fitting of the XRD data is called JADE.

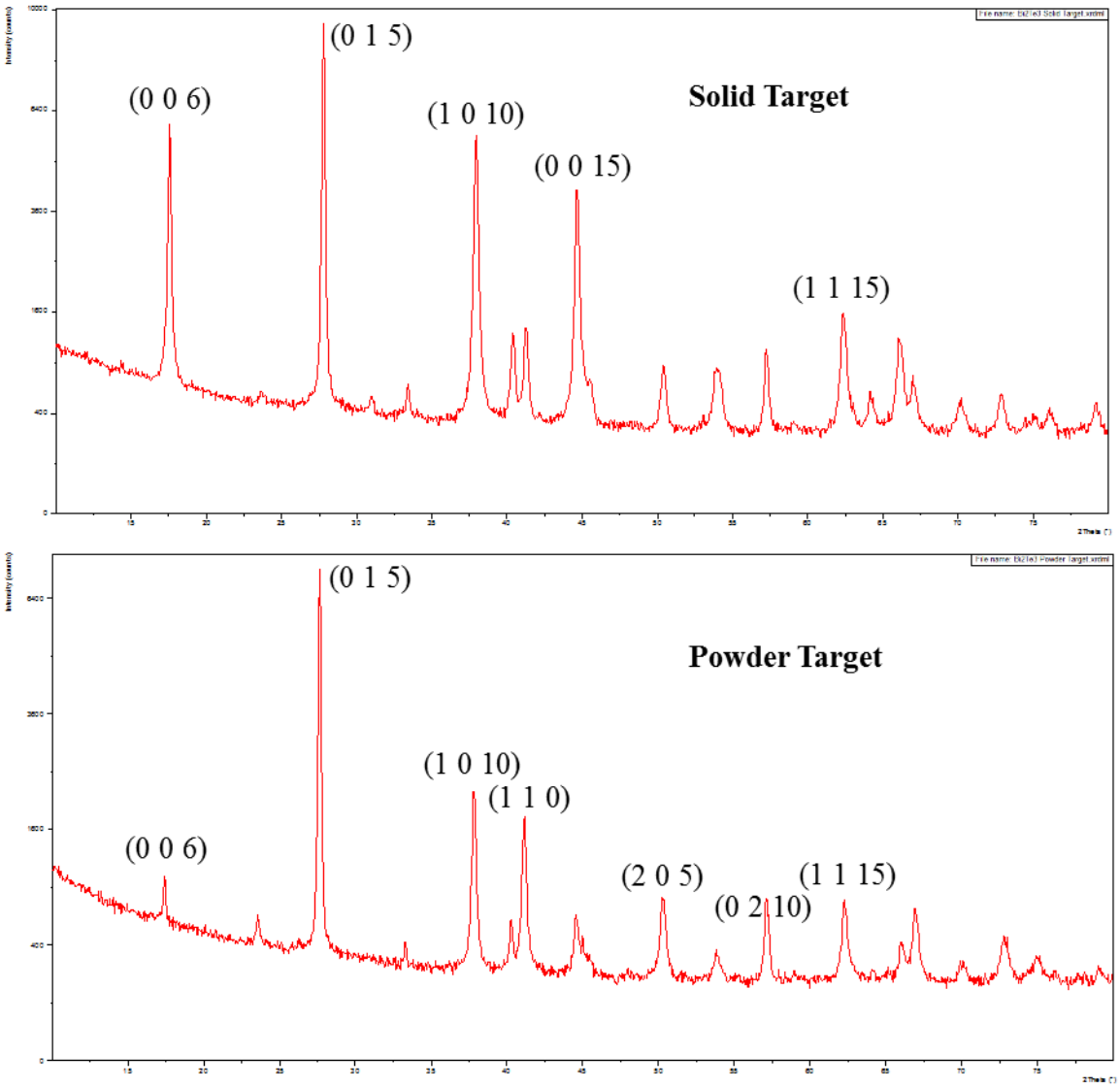

Figure 5–50: Solid target (top) and powder target (bottom) of bismuth telluride

Table 5-3 shows the full list of peaks visible in the XRD spectrum of the solid bismuth telluride target, including the respective *d* spacing and full-width half maximum (FWHM) for each peak.

Table 5-3: Visible XRD peaks of solid bismuth telluride target

Peak (2θ)	Intensity (a.u.)	FWHM	Orientation	*d* spacing (nm)
17.565°	5065 [3]	0.235	(0 0 6)	0.50767
27.79°	8778.3 [1]	0.221	(0 1 5)	0.32253
33.413°	294.5	0.221	(0 1 8)	0.26903
37.949°	5242.8 [2]	0.328	(1 0 10)	0.23772
40.399°	830.4	0.263	(0 1 11)	0.22383
41.266°	898.2	0.289	(1 1 0)	0.21950
44.667°	3836.6 [4]	0.334	(0 0 15)	0.20307
45.517°	~718	--	(1 0 13)	0.19947
50.404°	576.4	0.392	(2 0 5)	0.18146
54.005°	567.1	0.654	(1 0 16)	0.17023
57.257°	777.9	0.311	(0 2 10)	0.16127
62.385°	1260.9	0.422	(1 1 15)	0.14906
66.131°	768.1	0.402	(0 1 20)	0.14138
72.888°	309.9	0.469	(2 1 20)	0.12996

Substrates commonly used have the following XRD lines:

Copper Foil: 43.6°, 50.6° (smaller peaks include 45.5°, 55.0°, and 74.3°)

Silicon wafer: 69.4°

Table 5-4 below is a summary of the XRD data taken during the scope of this work.

Table 5-4: Summary of XRD peaks

Sample	Substrate Material	XRD Peaks (°) (Orientation)				
1	Silicon	17.7 (0 0 6)	44.8 (0 0 15)			
2	Silicon	17.7 (0 0 6)	27.7 (0 1 5)	44.7 (0 0 15)		
3	Silicon	N/A				
3	Copper	N/A				
4	Silicon	18.9 (0 0 6)	27.7 (0 1 5)	45.5 (1 0 13)		
4	Copper	38.2 (1 0 10)				
5	Silicon	18.4 (0 0 6)	27.9 (0 1 5)	33.2 (0 1 8)	45.5 (1 0 13)	
6	Silicon	18.6 (0 0 6)	27.8 (0 1 5)	45.5 (1 0 13)		
7	Silicon	17.8	28.0	44.8		

		(0 0 6)	(0 1 5)	(0 0 15)		
7	Copper	N/A				
8	Silicon	17.7 (0 0 6)	27.9 (0 1 5)	44.8 (0 0 15)	54.3 (1 0 16)	
8	Copper	17.6 (0 0 6)	27.8 (0 1 5)	37.9 (1 0 10)	41.3 (1 1 0)	44.7 (0 0 15)
9		N/A				
10		N/A				
11		N/A				
12	Silicon	17.7 (0 0 6)	27.8 (0 1 5)	44.8 (0 0 15)	54.0 (1 0 16)	
12	Copper	17.4 (0 0 6)	27.7 (0 1 5)	44.5 (0 0 15)		
13	Silicon	N/A				
13	Copper	N/A				
14	Native Silicon	17.6 (0 0 6)	33.2 (0 1 8)	44.7 (0 0 15)		
14	Thermal Silicon	N/A				
14	Copper	N/A				
15		N/A				
16	Silicon	17.6 (0 0 6)	44.7 (0 0 15)			
16	Copper	N/A				
17	Silicon	17.7 (0 0 6)	44.9 (0 0 15)			
17	Copper	17.7 (0 0 6)	44.8 (0 0 15)			
18		N/A				
19		N/A				
20		N/A				

From this XRD peak data, it is evident that the majority of the time, bismuth telluride crystallinity is inconsistent from one substrate to the next, even within the same experiment. Samples grown on silicon substrates have an orientation tendency along the (0 0 6) and (0 1 5) planes. On the other hand, samples grown on copper substrates have less consistency in their growth orientation. Samples grown on copper substrates show very little crystallinity, or for certain samples (Sample 8, Sample 12, Sample 17), they are very similar to the crystallinity of the silicon substrate. These films are the samples

grown using 532 nm laser irradiation, which is a strong indicator that samples grown on copper substrates using 532 nm irradiation show better crystallinity than samples grown on copper substrates using 266 nm irradiation. Furthermore, the better the crystallinity of the bismuth telluride films, the better the electrical conductivity of those films. While this experimental setup only allowed for the electrical characterization of bismuth telluride samples grown on silicon substrates, the trends are expected to be similar for bismuth telluride samples grown on copper substrates.

Using XRD analysis of bismuth telluride films grown via PLD, Dauscher [13] concluded that preferential growth is in the (0 1 5) and (1 0 10) planes. In addition, after annealing these samples, the orientation changed to (0 0 6), which suggests that films with a higher degree of crystallinity have preferential growth in the (0 0 6) plane. This is similar to results presented in this work, in which crystalline samples show preferential growth along the (0 1 5) and (0 0 6) planes.

Figure 5–51 shows the XRD spectrum of a bismuth telluride film grown via PLD. The top spectrum is the bismuth telluride film grown on a silicon wafer. There is significant peak matching with the solid bismuth telluride target used as the ablation source, shown in the bottom spectrum. The main peaks are labelled, with the first three resulting from different orientations of stoichiometric Bi_2Te_3, the next two resulting from residual atomic bismuth and tellurium, and the last one from the underlying silicon wafer.

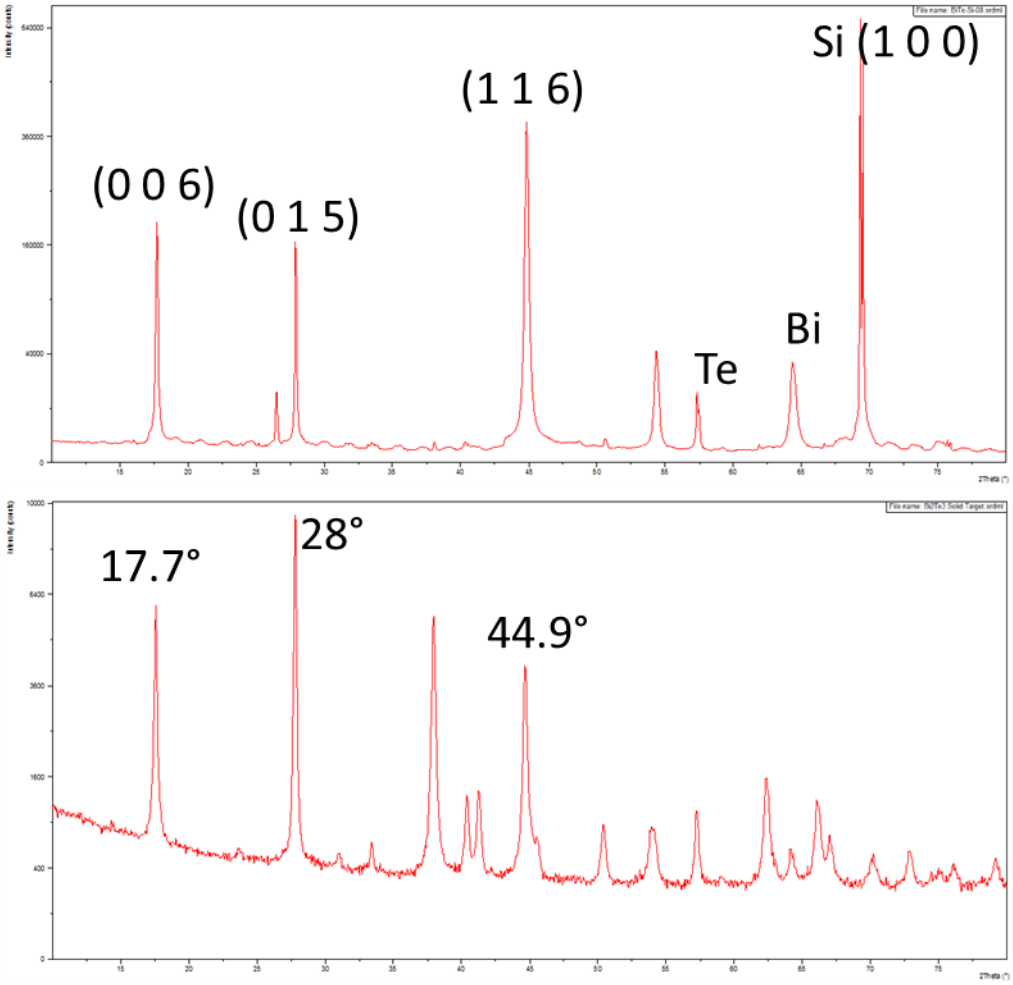

Figure 5–51: XRD results of a bismuth telluride film grown on a silicon wafer (top) compared to the solid bismuth telluride target used for ablation (bottom)

Annealing the grown films helps to reduce thermal stresses and point defects and increase the mobility of the surface atoms to increase homogeneity [67]. This process would increase the overall crystallinity of the samples and improve the electrical properties of the films. Some of the early samples grown using high laser fluence are annealed to verify the annealing effects. However, instead of improving the quality of the films, the deposited material completely evaporated from the substrate during annealing. This is probably the result of nanostructured materials having a lower melting temperature than their respective bulk material, since these early samples consisted

primarily of nanostructures instead of continuous films. It could also have been from improper annealing properties. If the annealing temperature is too high, it would account for the evaporation of the material. Also, if the annealing process should be done in an ambient atmosphere instead of in vacuum, this could explain the evaporation of the material from the substrate. Since annealing is only performed on the early, high laser fluence samples, future tests on annealing films will be conducted to validate the annealing process on nanostructured materials.

5.5 Further Characterization

Raman spectroscopy can also be used to characterize bismuth telluride materials. The vibrational mode, around 130 cm^{-1}, is the Raman-active A_{1g}^{1} mode, which indicates a stretching mode along the c-axis within the Bi-Te quintuple layers. The peak around 115 cm^{-1} corresponds to the A_{1u} mode, which is attributed to the out-of-plane vibration. The peak around 90 cm^{-1} corresponds to the Raman-active E_g^{2} in-plane vibration mode [63]. There are four Raman active modes in Bi_2Te_3: E_g^{1} at 36.5 cm^{-1}, A_{1g}^{1} at 62 cm^{-1}, E_g^{2} at 102.3 cm^{-1}, and A_{1g}^{2} at 134.0 cm^{-1} [65]. Using Raman spectroscopy to characterize bismuth telluride is very difficult in practice due to the low wavenumber of the Raman active peaks. It is difficult to resolve these peaks and separate them from the much larger Rayleigh scattering peak.

The triple spectrometer used for in-situ analysis can also be used for Raman analysis of Bi_2Te_3 samples since its resolution can be within 5 wavenumbers (cm^{-1}) of the Rayleigh line. However, this spectrometer could not be calibrated for solid samples, and no Raman results could be obtained. Future work could focus on getting this spectrometer calibrated to perform Raman analysis of solid samples at very low

wavenumbers, which would allow Bi_2Te_3 samples to be further characterized, both in-situ and ex-situ.

Characteristic Raman spectroscopy is shown below if Figure 5–52.

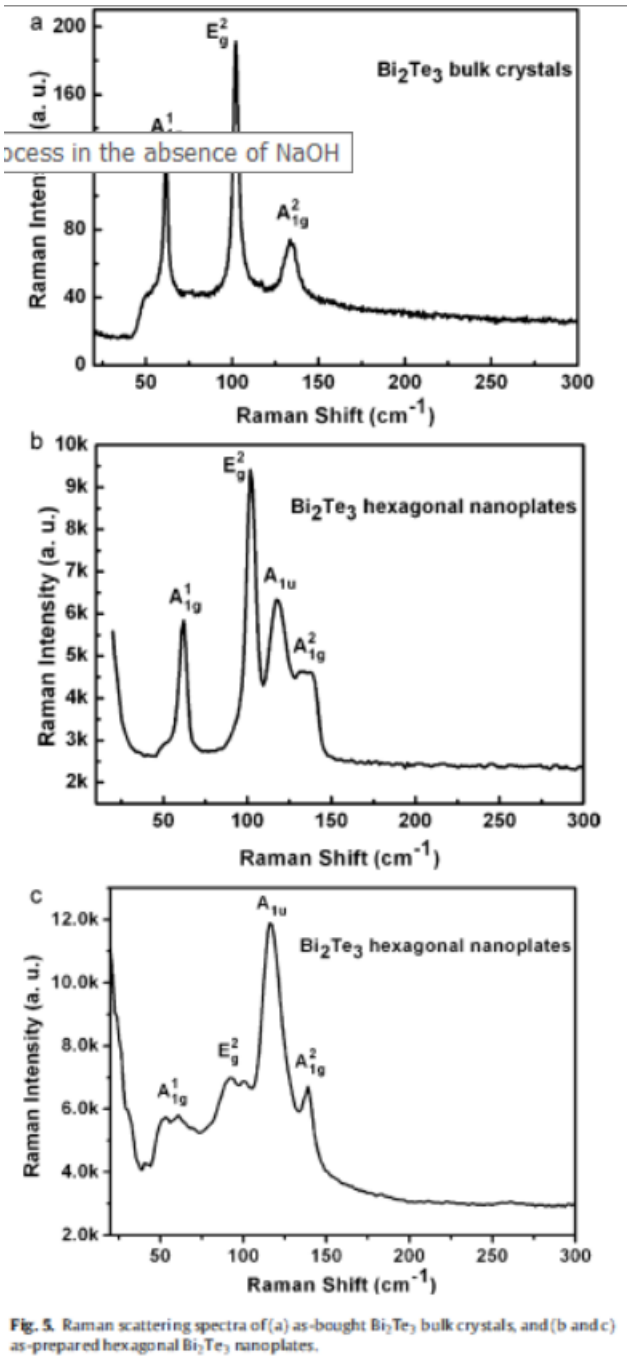

Fig. 5. Raman scattering spectra of (a) as-bought Bi_2Te_3 bulk crystals, and (b and c) as-prepared hexagonal Bi_2Te_3 nanoplates.

Figure 5–52: Raman scattering spectra of (a) bulk Bi2Te3 crystal and (b) and (c) grown Bi_2Te_3 hexagonal nanoplatelets (reproduced with caption from [89])

In-situ plume spectroscopy is also used for the bismuth telluride films to determine the species present during laser ablation of the bismuth telluride target. Figure 5–53, shown below, is a characteristic spectrum of the plume species in the bismuth telluride laser produced plasma plume.

Similar to the plume analysis of the carbon work above, the plasma plume generated from laser ablation of the bismuth telluride target can be analyzed. However, because of a lack of data from the NIST database on atomic bismuth and tellurium (http://physics.nist.gov/PhysRefData/ASD/lines_form.html), full analysis of the plume species and electron temperature could not be performed.

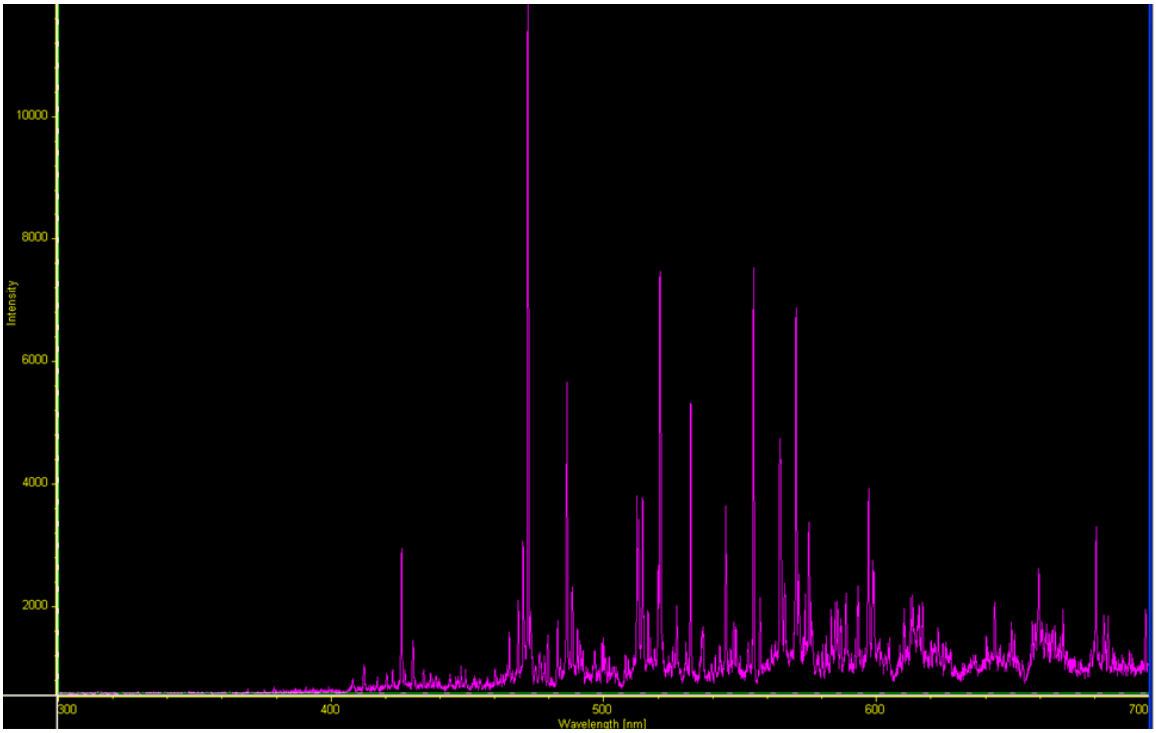

Figure 5–53: Spectrum of bismuth telluride plasma plume – 266nm, 1 torr Ar

6 Advanced Heterostruture Growth and Characterization

Complex heterostructures are grown to explore the unique properties of several different materials within the same structure. Despite being present since the 1960s, using intentionally tailored heterostructures to achieve very specific applications became widespread when the Nobel Prize in physics was awarded to Z. Alferov and H. Kroemer "for developing semiconductor heterostructures used in high-speed- and opto-electronics" in 2000 [90]. Since then, applications have ranged from semiconductor lasers and transistors to photocatalysis and energy generation. In particular, due to the seemingly limitless combination of materials and structures, the potential for complex heterostructured materials is enormous. This work focuses on graphene and bismuth telluride nanostructures, and how these two materials could interact with other materials and with each other within a complex heterostructure.

6.1 Bi_2Te_3/Graphene Heterojunctions

Thermoelectric materials are coupled with graphene in an attempt to create a more efficient thermoelectric device. Recent graphene-based heterojunction devices have shown very promising properties and behaviors for applications in photovoltaics, electron transport, and light absorption [91]. Starting with a copper substrate, 1-3 layers of graphene is grown, followed by 5-10 layers of bismuth telluride. These structures can be standalone structures, or they could be sandwiched together with the copper substrates acting as book ends. For this process, graphene can be grown via PLD or via flame synthesis, each with their own benefits. While the graphene grown via flame synthesis is extremely pristine with a very low D peak, graphene grown via PLD could be better for these heterostructures due to the high concentration of defects on the surface. These

defects on the surface means better bonding from dangling bonds, and a smaller intrinsic grain size.

To test this idea, bismuth telluride films are grown on copper substrates with a thin layer of graphene already deposited on top of the copper. This is done under standard bismuth telluride growth conditions, described previously. Sample 1 consists of a 30 second growth of bismuth telluride on a graphene/copper substrate grown via flame synthesis. This is done at a substrate temperature of 200°C, a deposition pressure of 0.1 torr of argon, and 266 nm laser irradiation at 3.25 J/cm^2. However, no detectable Bi_2Te_3 film is detected on the graphene/copper surface. Raman spectroscopy, SEM, and EDS are all employed to try to detect these thin film heterostructures, but no efficient method of detecting what exactly is grown on the substrate could be developed. Figure 6–1 below shows the SEM results of the Bi_2Te_3/graphene/copper substrate. No bismuth or tellurium of any kind is detected on the substrate after growth with the exception of a few very small particulates, seen as the high contrast spots in Figure 6–1. These particulates consist of approximately 60% Bi, 40% Te, and the vast majority of the substrate consist of the underlying carbon/copper material. The optimal growth conditions for this type of substrate is not the same as previously determined, since not only is there no film growth, but the particulates that are deposited are very bismuth-rich.

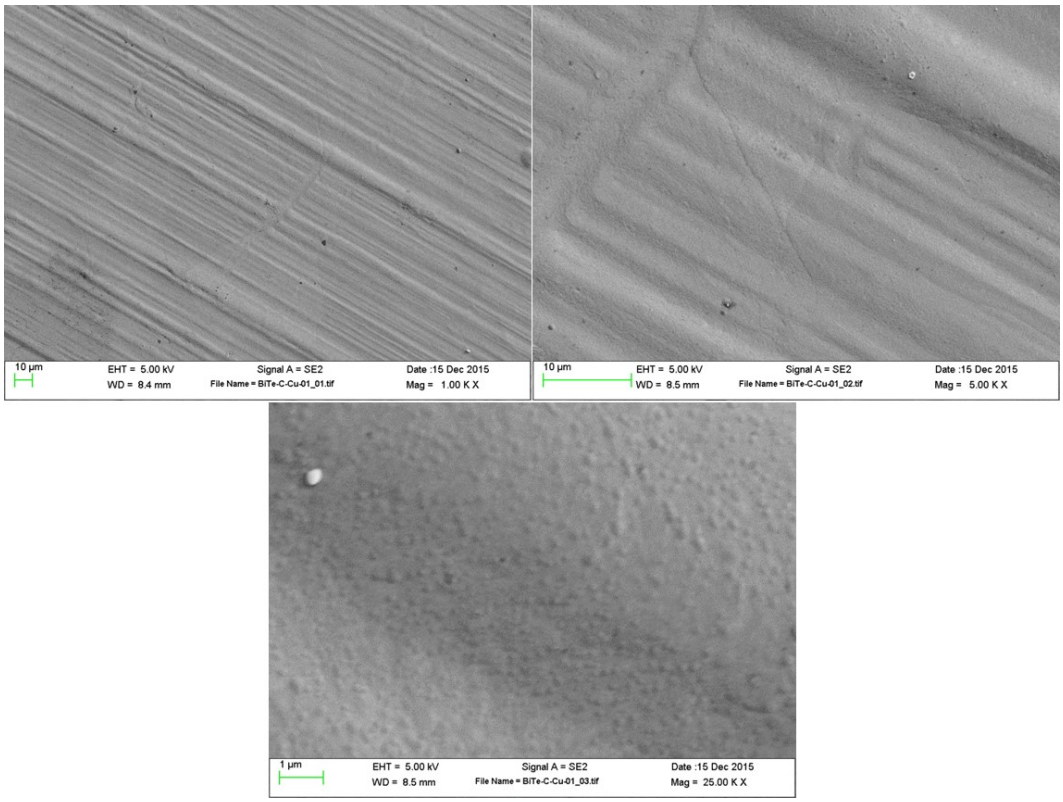

Figure 6–1: Sample 1, Bi_2Te_3/graphene/copper heterostructure

Sample 2 consists of a graphene/copper substrate similar to that in Sample 1 grown using flame synthesis, in addition to a graphene/copper substrate grown using PLD. A 90 second bismuth telluride PLD growth is carried out in an attempt to get better coverage of the thermoelectric material directly on the graphene layer. This is done at a substrate temperature of 200°C, a deposition pressure of 0.1 torr of argon, and 266 nm laser irradiation at 3.25 J/cm^2. The graphene/copper structure grown via flame synthesis is shown below in Figure 6–2, and the graphene/copper structure grown via PLD is shown below in Figure 6–3. Once again, the sample shows no signs of any bismuth or tellurium on the surface after the growth occurs. There are some particulates, similar to those in Sample 1, which consist of approximately 63% bismuth, 37% tellurium. Again,

the growth conditions have to be modified, since there is no film growth, and the particulates that are on the substrate are very bismuth-rich.

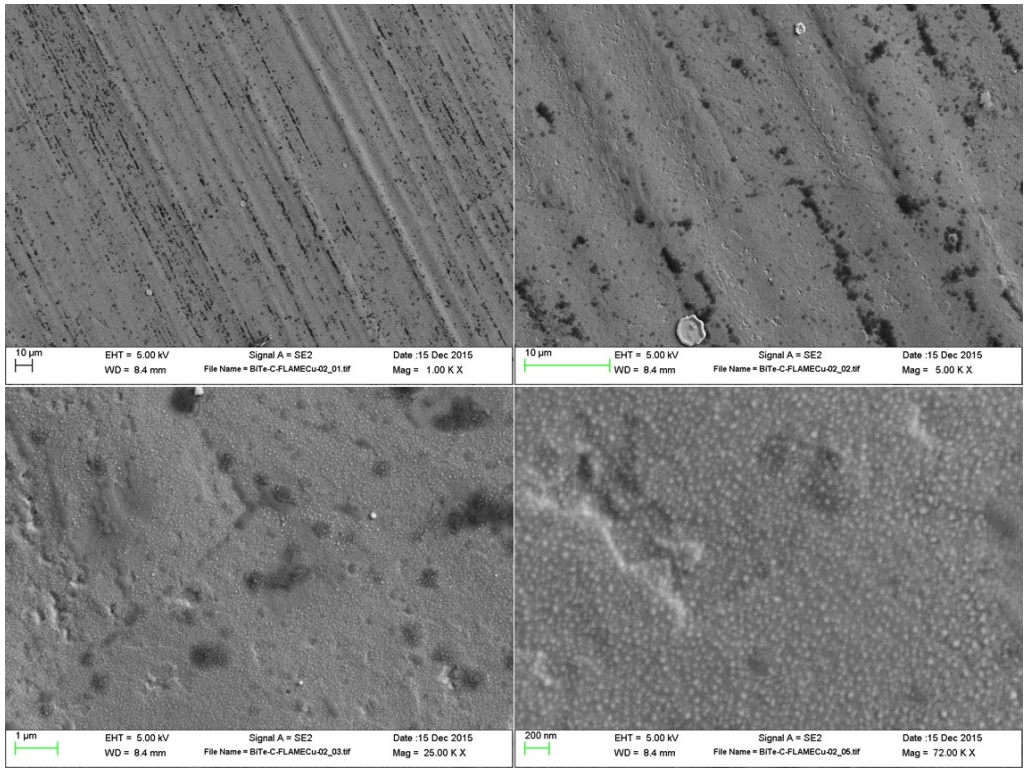

Figure 6–2: Sample 2, Bi_2Te_3/graphene/copper heterostructure, flame synthesis substrate

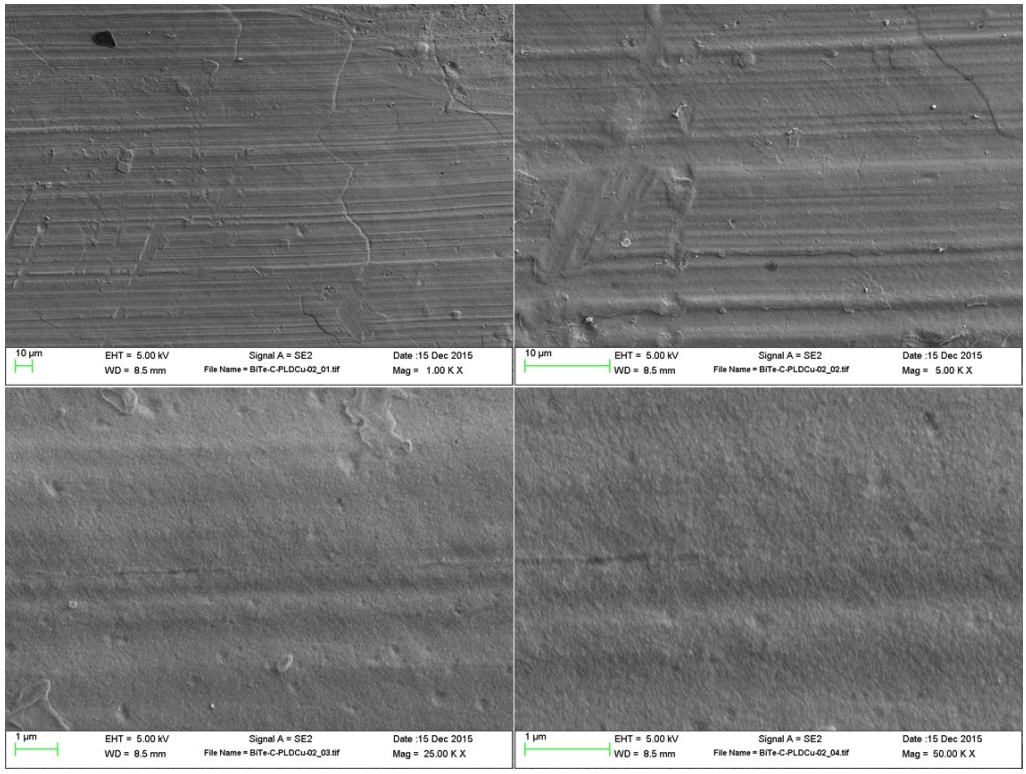

Figure 6–3: Sample 2, Bi_2Te_3/graphene/copper heterostructure, PLD substrate

Longer growth times of the bismuth telluride must be attempted for the successful growth of a Bi_2Te_3 film directly onto a graphene/copper heterostructure substrate.

6.2 Thermoelectric Heterostructure

The recent advances in the thermoelectric figure of merit due to nanoscale phenomena has been explored and demonstrated shortly after its prediction in 2007 [6]. These advancements of thermoelectric materials have taken several routes towards increasing the figure of merit. One such route involves a heterostructured thermoelectric device that can operate at much higher efficiencies than previous thermoelectric devices. By combining several materials in advanced nanostructures, increased thermoelectric performance can be achieved. While there are limitations to this method, Dr. Liu has proposed a way of improving the power factor of thermoelectric materials by several

orders of magnitude by laminating good conductors and good thermoelectric materials [92]. This heterostructured material would consist of, for example, a thin layer of bismuth telluride sandwiched between thick copper layers of the proper proportion. The percent volume of the thermoelectric material compared to the thermally and electrically conducting material (metal, typically copper) would be about 0.25%. According to Dr. Liu's theory, the maximum power factor of the heterostructure can be 100 times greater than the constituent semiconductor (Bi_2Te_3). A schematic of the proposed heterostructure is shown in Figure 6–4 below.

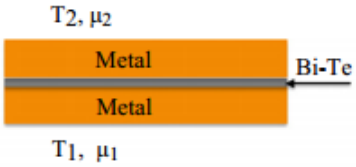

Figure 6–4: Schematic view of proposed thermoelectric heterostructure (reproduced from [92])

A theoretical breakdown of the economic feasibility of large-scale power plants based on thermoelectric effects in ocean or geothermal generators has been performed, and the result is a potential source of energy that rivals the cost of current solar energy in the United States. In addition, this sandwich structure is convenient for mass production and electrical connections, since the metal can also serve as electrodes [92].

From the previously discussed electrical results of bismuth telluride films grown directly on copper substrates, the electrical resistivity and Seebeck coefficient values are very promising. Another layer of copper would then be deposited on the bismuth telluride/copper films to complete the sandwich structure. This can be done by electron beam evaporation, as discussed previously, or by other methods such as sputtering.

These structures have not yet been completed, but the theoretical studies have been done, and partial experimental verification has been carried out through the scope of this work.

7 Future Work

This chapter outlines some of the future work that can be explored as a result of questions raised throughout the scope of this work.

7.1 Fundamental Growth Mechanisms

From these results and the work done previously in the field, it is clear that the mechanism for nanomaterial growth via pulsed laser deposition is still not completely understood. The results from the various graphene growth experiments point to two different growth regimes being present depending on the deposition parameters being utilized. The first is the classical idea of laser ablation, in which the target material is vaporized and partially ionized, and the outward flux of material consists of atoms, ions, and particles with sizes that depend on the laser excitation energy and wavelength. This regime has been extensively studied, but no current models exist that can fully explain or predict the phenomenon. Furthermore, when done in a background gas, this technique incorporates gas phase condensation into the classical PLD growth model, making it even more complex. When performing PLD in some type of inert or reactive environment, the ablated species have a medium to interact with and exchange energy, allowing for more versatility in the energy of the ablated species and types of films that can be grown.

On the other hand, the second mechanism of film growth is a laser exfoliation method that may or may not include gas phase condensation to produce films as well as nanoparticles and nanostructures. For this regime, instead of completely vaporizing a target material, flakes are exfoliated from a target and deposited, largely intact, onto a substrate. Interaction of these flakes with the background gas has not been explored, but it may contribute to the larger structures that are deposited on the substrate by laser

exfoliation. This has also been seen in the deposition of polymer chains via matrix-assisted pulsed laser evaporation, or MAPLE [93].

The continuation of this study aims to develop a model that sufficiently describes these different growth mechanisms. To that end, a simple kinetic model must be developed to begin to work out the complicated mechanisms involved in the PLD process. If an accurate model is developed, it could lead to significant improvements in the understanding of the method, as well as additional applications in new fields of study that were previously unknown or inaccessible. Ultimately, a computational model for simulating laser ablation of a target material, as well as film nucleation and growth on a substrate material, would be paramount to determining what is possible with pulsed laser deposition as a method. A comprehensive model would allow for analytical studies to be performed to predict optimal growth parameters for each individual material system

7.2 Pressure Effects o Graphene Films

Pressure effects on graphene films were outlined above, but further work on how the laser wavelength affects graphene growth at low vacuum is necessary. The laser exfoliation regime is still relatively new and not fully explored. Using a very high energy laser (266 nm) to exfoliate a graphite or HOPG target could potentially lead to interesting graphitic films or nanoparticles, since the laser energy is high enough to break the C-C bonds of the target material. This method must be studied further, including parametric studies of how the laser wavelength affects low vacuum laser ablation and exfoliation, as well as how the carbon source affects the ablated species and the resulting carbon samples.

7.3 Substrate Effects on Graphene Films

For a given type of substrate, the microstructure was found to have an impact on the graphene films grown via PLD (See Table 4-1). By polishing a copper substrate, graphene films showed less disorder and larger grain sizes than those grown on an unpolished copper substrate. Using this result, other substrate pre-treatments (i.e. polishing, laser etching, preferential coatings, etc.) can be analyzed to see how they affect film growth. Post-treatment of graphene samples should also be examined. By annealing these films at high temperature after the deposition process, the graphene films can be modified or improved. The high temperature annealing process can smooth out grain boundaries on the surface and relax the growth-induced surface stresses. This could increase the quality of the graphene films and possibly reduce the amount of layers that accumulate on the substrate.

The type of substrate is critical for the growth of graphene via methods such as CVD [31] and flame synthesis [94]. However, PLD has much more flexibility in the choice of substrate. In addition to the common substrates used for graphene growth, such as copper and nickel, new substrates have been examined. Instead of growing graphene on transition metals and having to transfer it to an insulating substrate for electronic applications, graphene can be grown directly onto silicon wafer substrates. Future graphene experiments will explore other substrates to determine what materials graphene can be grown on via PLD, and how the type of substrate affects film quality and structure. In addition, the substrate temperature, which is critical to the growth of graphene, will be increased to see how it affects the films. New equipment allows the substrate temperature to go beyond the current maximum of 900°C, which could help to improve

the quality of the graphene films and enlarge the grain size when grown on a copper surface.

Similar to how float glass is made, growing graphene directly on a molten liquid substrate could lead to drastically reduced substrate temperature requirements, leading to cheaper production. Using a liquid substrate could provide enough mobility to the incoming carbon species to crystallize the carbon atoms into graphene sheets at reduced temperatures. The idea of graphene growth on a liquid substrate is very promising and could potentially revolutionize the production of graphene films on a large-scale manufacturing capacity.

7.4 Growth Conditions for Bismuth Telluride Films

Optimal growth conditions for nanostructured Bi_2Te_3 include a substrate temperature of around 200°C, a deposition pressure of 0.1-1.0 torr of argon, and a laser fluence of 2.0-5.0 J/cm^2. These values are in agreement with previous results [65]. There were some very interesting surface morphologies that were created throughout the course of this work. These surface morphologies should be replicated and examined thoroughly to determine if they possess any unique characteristics that would make them useful in electrical or thermoelectrical applications. Even though some of the samples with interesting morphologies had very low coverage, if they can be replicated, the material can be collected and pressed into dense samples for characterization.

7.5 Laser Parameters for Bismuth Telluride Films

From Table 5-1, it is evident that the films become more consistent once the laser fluence is reduced below 5 J/cm^2. As a result, the lower laser fluence regime is explored.

This lower laser fluence regime creates more consistent films of stoichiometric bismuth telluride. However, the high laser fluence regime is not fully explored. This regime produced some very interesting surface morphologies, and if it could be examined and made to be consistent, then some very promising structures may be produced and should be studied further. Furthermore, the films grown using 532 nm laser irradiation show the most promising films in terms of stoichiometry, crystallinity, and electrical properties. Further exploration into how the laser wavelength affects the material properties of the films is required. The laser wavelength can be varied between 1064 nm, 532 nm, 355 nm, and 266 nm in this setup to see how the different wavelengths affect film properties.

7.6 Bi_2Te_3/Graphene Heterojunction

While Bi_2Te_3/graphene heterojunction structures show a lot of potential, a better way to characterize the samples must be developed. Raman spectroscopy can determine the properties of the graphene layer, and the electrical characterization technique described previously can determine the electrical conductivity and Seebeck coefficient of the film. However, there is no way to tell if there is a bismuth telluride layer deposited on the graphene layer, and how thick it is. SEM can be used to explore the surface morphology, but films that thin are difficult to resolve. The samples that were grown showed very little Bi_2Te_3 on the surface of the graphene. This is surprising since the lattice structure is similar between Bi_2Te_3 and graphene, as they both form a hexagonal lattice. To move this work forward, this growth rate issue must be explored and the samples must be further characterized.

7.7 Thermoelectric Heterostructure

Creating a symmetrical heterostructure with Bi_2Te_3 sandwiched between layers of copper is not a trivial issue. Starting with a copper substrate, growing a thin layer of Bi_2Te_3 can be achieved, and sputtering or electron beam evaporation can be used to grow the top layer of copper. For this structure to work, precise control of these techniques must be achieved, and characterization and verification of the structure will be very difficult. SEM can be used to examine the surface morphology and stoichiometry of the Bi_2Te_3 layer prior to the top layer of copper being deposited, as outlined previously, and cross-sectional SEM can be used to verify the thickness of the thermoelectric layer once the entire structure is created. However, ensuring that the layers are electrically isolated may require some sort of cleaving or etching of the edges. The biggest hurdle will be characterizing the final heterostructure. The electrical characterization techniques described previously are for in-plane properties. However, this structure uses out-of-plane (perpendicular to the surface) geometry to operate. New characterization techniques would have to be developed to test the samples and determine the electrical properties. While this structure show promising applications and potential, the specific growth procedures and characterization techniques still need to be developed.

8 Bibliography

[1] K. S. Novoselov, "Electric Field Effect in Atomically Thin Carbon Films," *Science,* vol. 306, no. 5696, pp. 666-669, 2004.

[2] K. S. Novoselov, A. K. Geim, S. C. Morozov, D. Jiang, M. I. Katsnelson, I. V. Grigorieva, S. V. Dubonos and A. A. Firsov, "Two-dimensional gas of massless Dirac fermions in graphene," *Nature,* vol. 438, no. 7065, pp. 197-200, 2005.

[3] A. K. Geim and K. S. Novoselov, "The rise of graphene," *Nature Materials,* vol. 6, no. 3, pp. 183-191, 2007.

[4] C. Soldano, A. Mahmood and E. Dujardin, "Production, properties and potential of graphene," *Carbon,* no. 48, pp. 2127-2150, 2010.

[5] A. K. Geim, "Graphene: Status and Prospects," *Science,* vol. 324, no. 5934, pp. 1530-1534, 2009.

[6] M. S. Dresselhaus, G. Chen, M. Y. Tang, R. G. Yang, H. Lee, D. Z. Wang, Z. F. Ren, J. P. Fleurial and P. Gogna, "New directions for low-dimensional thermoelectric materials," *Advanced Materials,* vol. 19, no. 8, pp. 1043-1053, 2007.

[7] H. M. Smith and A. F. Turner, *Applied Optics,* vol. 4, pp. 147-148, 1965.

[8] D. B. Chrisey and G. K. Hubler, Pulsed Laser Deposition of Thin Films, New York: Wiley, 1994.

[9] D. Dijkkamp, T. Venkatesan, X. D. Wu, S. A. Shaheen, N. Jisrawi, Y. H. Minlee, W. L. Mclean and M. Croft, "Preparation of Y-Ba-Cu oxide superconductor thin films using pulsed laser evaporation from high Tc bulk material," *Applied Physics Letters,* vol. 51, no. 8, pp. 619-621, 1987.

[10] F. Bonaccorso, A. Lombardo, T. Hasan, Z. Sun, L. Colombo and A. C. Ferrari, "Production and processing of graphene and 2d crystals," *Materials Today,* vol. 15, no. 12, pp. 564-584, 2012.

[11] R. Eason, Pulsed Laser Deposition of Thin Films: Applications-Led Growth of Functional Materials, R. Eason, Ed., Hoboken: John Wiley & Sons, Inc., 2007, pp. 3-31.

[12] M. Lorenz and M. R. Rao, "25 years of pulsed laser deposition," *Journal of Physics D - Applied Physics,* vol. 47, no. 3, p. 030301, 2014.

[13] A. Dauscher, A. Thomy and H. Scherrer, "Pulsed laser deposition of Bi2Te3 thin films," *Thin Solid Films,* vol. 280, pp. 61-66, 1996.

[14] D. L. Pappas, K. L. Saenger, J. J. Cuomo and R. W. Dreyfus, "Characterization of laser vaporization plasmas generated for the deposition of diamond-like carbon," *Journal of Applied Physics,* vol. 72, no. 9, pp. 3966-3970, 1992.

[15] R. Zeipl, M. Pavelka, M. Jelinek, J. Chval, P. Lostak, K. Zdansky, J. Vanis, S. Karamazov, S. Vackova and J. Walachova, "Some properties of very thin Bi2Te3 layers prepared by laser ablation," *physica status solidi (c),* vol. 0, no. 3, pp. 867-871, 2003.

[16] A. A. Voevodin and M. S. Donley, "Preparation of amorphous diamond-like carbon by pulsed laser deposition: a critical review," *Surface & Coatings Technology,* vol. 82, no. 3, pp. 199-213, 1995.

[17] J. J. Gaumet, A. Wakisaka, Y. Shimizu and Y. Tamori, "Energetics for Carbon Clusters produced directly by Laser Vaporization of Graphite: Dependence on Laser Power and Wavelength," *Journal of the Chemical Society-Faraday Transactions,* vol. 89, no. 11, pp. 1667-1670, 1993.

[18] S. S. Yap, W. O. Siew, C. H. Nee and T. Y. Tou, "Parametric studies of diamon-like carbon by pulsed Nd:YAG laser deposition," *Diamond & Related Materials,* vol. 20, pp. 294-298, 2011.

[19] K. R. Chen, J. N. Leboeuf, R. F. Wood, D. B. Geohegan, J. M. Donato, C. L. Liu and A. A. Puretzky, "Mechanisms affecting kinetic energies of laser-ablated materials," *Journal of Vacuum Science & Technology A - Vacuum, Surfaces, and Films,* vol. 14, no. 3, pp. 1111-1114, 1996.

[20] R. W. Dreyfus, R. Kelly and R. E. Walkup, "Laser-induced Fluorescence Study of Laser Sputtering of Graphite," *Nuclear Instruments and Methods in Physics Research B23,* vol. 23, no. 4, pp. 557-561, 1987.

[21] J. A. Greer, "History and current status of commercial pulsed laser deposition equipment," *Journal of Physics D: Applied Physics,* vol. 47, p. 034005, 2014.

[22] M. I. Katsnelson, "Graphene: carbon in two dimensions," *Meterials Today,* vol. 10, no. 1-2, pp. 20-27, 2007.

[23] H. W. Kroto, J. R. Heath, S. C. O'Brien, R. F. Curl and R. E. Smalley, "C-60 - buckminsterfullerene," *Nature,* vol. 318, no. 6042, pp. 162-163, 1985.

[24] S. Iijima, "Helical microtubules of graphitic carbon," *Nature,* vol. 354, no. 6348, pp. 56-58, 1991.

[25] S. V. Morozov, K. S. Novoselov, M. I. Katsnelson, F. Schedin, D. C. Elias, J. A. Jaszczak and A. K. Geim, "Giant intrinsic carrier mobilities in graphene and its bilayer," *Physical Review Letters,* vol. 100, no. 1, p. 016602, 2008.

[26] C. Berger, Z. Song, T. Li, X. Li, A. Y. Ogbazghi, R. Feng, Z. Dai, A. N. Marchenkov, E. H. Conrad, P. N. First and W. A. de Heer, "Ultrathin Epitaxial Graphite: 2D Electron Gas Properties and a Route toward Graphene-based Nanoelectronics," *Journal of Physical Chemistry B,* vol. 108, no. 52, pp. 19912-19916, 2004.

[27] W. Lu, P. Soukiassian and J. Boeckl, "Graphene: Fundamentals and functionalities," *MRS Bulletin,* vol. 37, no. 12, pp. 1119-1124, 2012.

[28] C. Berger, Z. Song, X. Li, X. Wu, N. Brown, C. Naud, D. Mayou, T. Li, J. Hass, A. N. Marchenkov, E. H. Conrad, P. N. First and W. A. de Heer, "Electronic Confinement and Coherence in Patterned Epitaxial Graphene," *Science,* vol. 312, pp. 1191-1196, 2006.

[29] H. Huang, W. Chen, S. Chen and A. T. S. Wee, "Bottom-up Growth of Epitaxial Graphene on 6H-SiC(0001)," *ACS Nano,* vol. 2, no. 12, pp. 2513-2518, 2008.

[30] J. Wintterlin and M.-L. Bocquet, "Graphene on metal surfaces," *Surface Science,* vol. 603, pp. 1841-1852, 2009.

[31] P. W. Sutter, J.-I. Flege and E. A. Sutter, "Epitaxial graphene on ruthenium," *Nature Materials,* vol. 7, pp. 406-411, 2008.

[32] H. Ueta, M. Saida, C. Nakai, Y. Yamada, M. Sasaki and S. Yamamoto, "Highly oriented monolayer graphite formation on Pt(1 1 1) by a supersonic methane beam," *Surface Science,* vol. 560, pp. 183-190, 2004.

[33] K. S. Kim, Y. Zhao, H. Jang, S. Y. Lee, J. M. Kim, K. S. Kim, J.-H. Ahn, P. Kim, J.-Y. Choi and B. H. Hong, "Large-scale pattern growth of graphene films for stretchable transparent electrodes," *Nature,* vol. 457, no. 7230, pp. 706-710, 2009.

[34] A. Reina, X. Jia, J. Ho, D. Nezich, H. Son, V. Bulovic, M. S. Dresselhaus and J. Kong, "Large Area, Few-Layer Graphene Films on Arbitrary Substrates by Chemical Vapor Deposition," *Nano Letters,* vol. 9, no. 1, pp. 30-35, 2009.

[35] X. Li, W. Cai, J. An, S. Kim, J. Nah, D. Yang, R. Piner, A. Velamakanni, I. Jung, E. Tutuc, S. K. Banerjee, L. Colombo and R. S. Ruoff, "Large-Area Synthesis of High-Quality and Uniform Graphene Films on Copper Foils," *Science,* vol. 324, pp. 1312-1314, 2009.

[36] P. Avouris and C. Dimitrakopoulos, "Graphene: synthesis and applications," *Materials Today,* vol. 15, no. 3, pp. 86-97, 2012.

[37] V. C. Tung, M. J. Allen, Y. Yang and R. B. Kaner, "High-throughput solution processing of large-scale graphene," *Nature Nanotechnology,* vol. 4, pp. 25-29, 2009.

[38] S. Stankovich, D. A. Dikin, G. H. Dommett, K. M. Kohlhaas, E. J. Zimney, E. A. Stach, R. D. Piner, S. T. Nguyen and R. S. Ruoff, "Graphene-based composite materials," *Nature Letters,* vol. 442, pp. 282-286, 2006.

[39] E. Cappelli, S. Orlando, G. Mattei, C. Scilletta, F. Corticelli and P. Ascarelli, "Nano-structured oriented carbon films grown by PLD and CVD methods," *Applied Physics A-Materials Science & Processing,* vol. 79, no. 8, pp. 2063-2068, 2004.

[40] E. Cappelli, C. Scilletta, S. Orlando, R. Flammini, S. Iacobucci and P. Ascarelli, "Surface characterisation of nano-structured carbon films deposited by Nd:YAG pulsed laser deposition," *Thin Solid Films,* vol. 482, no. 1-2, pp. 305-310, 2005.

[41] E. Cappelli, S. Iacobucci, C. Scilletta, R. Flammini, S. Orlando, G. Mattei, P. Ascarelli, F. Borgatti, A. Giglia, N. Mahne and S. Nannarone, "Orientation tendency of PLD carbon films as a function of substrate temperature: A NEXAFS study," *Diamond and Related Materials,* vol. 14, no. 3-7, pp. 959-964, 2005.

[42] C. Scilletta, M. Servidori, S. Orlando, E. Cappelli, L. Barba and P. Ascarelli, "Influence of substrate temperature and atmosphere on nano-graphene formation and texturing of pulsed Nd:YAG laser-deposited carbon films," *Applied Surface Science,* vol. 252, pp. 4877-4881, 2006.

[43] E. Cappelli, S. Orlando, M. Servidori and C. Scilletta, "Nano-graphene structures deposited by N-IR pulsed laser ablation of graphite on Si," *Applied Surface Science,* vol. 254, no. 4, pp. 1273-1278, 2007.

[44] E. Cappelli, C. Scilletta, M. Servidori, V. Valentini and S. Orlando, "Morphology, structure and density evolution of carbon nano-structures deposited by N-IR pulsed laser ablation of graphite," *Diamond & Related Materials,* vol. 17, pp. 1476-1481,

2008.

[45] E. Cappelli, C. Scilletta, G. Mattei, V. Valentini, S. Orlando and M. Servidori, "Critical role of laser wavelength on carbon films grown by PLD of graphite," *Applied Physics A,* vol. 93, pp. 751-758, 2008.

[46] P. M. Ossi and A. Bailini, "Effect of ambient gas ionisation on the morphology of a pulsed laser deposited carbon film," *Carbon,* vol. 44, pp. 3049-3052, 2006.

[47] D. B. Chrisey, A. Pique, R. A. McGill, J. S. Horwitz, B. R. Ringeisen, D. M. Bubb and P. K. Wu, "Laser Deposition of Polymer and Biomaterial Films," *Chemical Reviews,* vol. 103, no. 2, pp. 553-576, 2003.

[48] M. Reininghaus, D. Wortmann, J. Flinger, O. Faley, R. Poprawe and C. Stampfer, "Laser induced non-thermal deposition of ultrathin graphite," *Applied Physics Letters,* vol. 100, p. 151606, 2012.

[49] H. Zhang and P. X. Feng, "Fabrication and characterization of few-layer graphene," *Carbon,* vol. 48, no. 2, pp. 359-364, 2010.

[50] A. T. Koh, Y. M. Foong and D. H. Chua, "Cooling rate and energy dependence of pulsed laser fabricated graphene on nickel at reduced temperature," *Applied Physics letters,* vol. 97, p. 114102, 2010.

[51] A. T. Koh, Y. M. Foong and D. H. Chua, "Comparison of the mechanism of low defect few-layer graphene fabricated on different metals by pulsed laser deposition," *Diamond & Related Materials,* vol. 25, pp. 98-102, 2012.

[52] K. Wang, G. Tai, K. H. Wong, S. P. Lau and W. Guo, "Ni induced few-layer graphene growth at low temperature by pulsed laser deposition," *AIP Advances,* vol. 1, p. 022141, 2011.

[53] T. M. Tritt, X. Tang, Q. Zhang and W. Xie, "Solar thermoelectrics: direct solar thermal energy conversion," in *Fundamentals of Materials for Energy and Environmental Sustainability*, New York, Cambridge University Press, 2012, pp. 289-294.

[54] V. Zlatic and A. C. Hewson, Properties and Applications of Thermoelectric Materials: The Search for New Materials for Thermoelectric Devices, Springer, 2008.

[55] C. Godart, A. P. Goncalves, E. B. Lopes and B. Villeroy, "Role of Structures on Thermal Conductivity in Thermoelectric Materials," in *Properties and Applications of Thermoelectric Materials*, Hvar, Croatia, 2009.

[56] M. G. Kanatzidis, "Nanostructured Thermoelectrics: The New Paradigm?," *Chemistry of Materials,* vol. 22, no. 3, pp. 648-659, 2010.

[57] B. G. Levi, "Simple compound manifests record-high thermoelectric performance," *Physics Today,* vol. 67, no. 6, pp. 14-16, 2014.

[58] R. Zeipl, J. Walachova, M. Pavelka, M. Jelinek, V. Studnicka and T. Kocourek, "Power factor of very thin thermoelectric layers of different thickness prepared by laser ablation," *Applied Physics A,* vol. 93, pp. 663-667, 2008.

[59] L. D. Hicks and M. S. Dresselhaus, "Effect of quantum-well structures on the thermoelectric figure of merit," *Physical Review B,* vol. 47, no. 19, pp. 12727-12731, 1993.

[60] M. G. Kanatzidis, "Advances in thermoelectrics: From single phases to hierarchical nanostructures and back," *MRS Bulletin,* vol. 40, pp. 687-694, 2015.

[61] Lawrence Livermore National Laboratory, "Estimated U.S. Energy Consumption in 2015: 97.5 Quads," LLNL, 2016.

[62] G. Mahan, B. Sales and J. Sharp, "Thermoelectric Materials: New Approaches to an Old Problem," *Physics Today,* vol. 50, no. 3, pp. 42-47, 1997.

[63] Z. Yu, X. Wang, Y. Du, S. Aminorroaya-Yamni, C. Zhang, K. Chuang and S. Li, "Fabrication and characterization of textured Bi2Te3 thermoelectric thin films prepared on glass substrates at room temperature using pulsed laser deposition," *Journal of Crystal Growth,* vol. 362, pp. 247-251, 2013.

[64] L. S. Faraji, R. P. Singh and M. Allahkarami, "Pulsed laser deposition of bismuth telluride thin film and annealing effects," *European Physical Journal Applied Physics,* vol. 46, p. 20501, 2009.

[65] A. Bailini, F. Donati, M. Zamboni, V. Russo, M. Passoni, C. S. Casari, A. Li Bassi and C. E. Bottani, "Pulsed laser deposition of Bi2Te3 thermoelectric films," *Applied Surface Science,* vol. 254, pp. 1249-1254, 2007.

[66] G. S. Nolas, J. Sharp and H. J. Goldsmid, Thermoelectrics - Basic Principles and New Materials Developments, New York: Springer, 2001.

[67] R. S. Makala, K. Jagannadham and B. C. Sales, "Pulsed laser deposition of Bi2Te3-based thermoelectric thin films," *Journal of Applied Physics,* vol. 94, no. 6, pp. 3907-3918, 2003.

[68] W. Kullmann, J. Geurts, W. Richter, N. Lehner, H. Rauh, U. Steigenberger, G. Eichhorn and R. Geick, "Effect of Hydrostatic and Uniaxial Pressure on Structural Properties and Raman Active Lattice Vibrations in Bi2Te3," *Physica Status Solidi (b),* vol. 125, no. 1, pp. 131-138, 1984.

[69] M. Takashiri, T. Shirakawa, K. Miyazaki and H. Tsukamoto, "Fabrication and characterization of bismuth-telluride-based alloy thin film thermoelectric generators by flash evaporation method," *Sensors and Actuators A,* vol. 138, pp. 329-334, 2007.

[70] A. Li Bassi, A. Bailini, C. S. Casari, F. Donati, A. Mantegazza, M. Passoni, V. Russo and C. E. Bottani, "Thermoelectric properties of Bi-Te films with controlled structure and morphology," *Journal of Applied Physics,* vol. 105, p. 124307, 2009.

[71] H. Obara, S. Higomo, M. Ohta, A. Yamamoto, K. Ueno and T. Iida, "Thermoelectric Properties of Bi2Te3-Based Thin Films with Fine Grains Fabicated by Pulsed Laser Deposition," *Japanese Journal of Applied Physics,* vol. 48, p. 085506, 2009.

[72] A. C. Ferrari, J. C. Meyer, V. Scardaci, C. Casiraghi, M. Lazzeri, F. Mauri, S. Piscanec, D. Jiang, K. S. Novoselov, S. Roth and A. K. Geim, "Raman Spectrum of Graphene and Graphene Layers," *Phsical Review Letters,* vol. 97, no. 18, p. 187401, 2006.

[73] A. C. Ferrari and J. Robertson, "Interpretation of Raman spectra of disordered and amorphous carbon," *Physical Review B,* vol. 61, no. 20, pp. 14095-14107, 2000.

[74] J. S. Park, A. Reina, R. Saito, J. Kong, G. Dresselhaus and M. S. Dresselhaus, "G' band Raman spectra of single, double and triple layer graphene," *Carbon,* vol. 47, no. 5, pp. 1303-1310, 2009.

[75] F. Tuinstra and J. Koenig, "Raman Spectrum of Graphite," *The Journal of Chemical Physics,* pp. 1126-1130, 1970.

[76] M. J. Matthews, M. A. Pimenta, M. S. Dresselhaus and M. Endo, "Origin of dispersive effects of the Raman D band in carbon materials," *Physical Review B,* vol. 59, no. 10, pp. 6586-6588, 1999.

[77] A. C. Ferrari, "Raman spectroscopy of graphene and graphite: Disorder, electron-phonon coupling, doping and nonadiabatic effects," *Solid State Communications,* vol. 143, no. 1-2, pp. 47-57, 2007.

[78] L. G. Cancado, K. Takai, T. Enoki, M. Endo, Y. A. Kim, H. Mizusaki, A. Jorio, L. N. Coelho, R. Magalhaes-Paniago and M. A. Pimenta, "General equation for the determination of the crystallite size La of nanographite by Raman spectroscopy," *Applied Physics Letters,* vol. 88, p. 163106, 2006.

[79] W. T. Mozet, S. D. Tse, B. H. Kear, M. Chhowalla and S.-W. Cheong, "Pulsed Laser Deposition of Carbon Nanomaterials," in *TechConnect World*, Washington, DC, 2014.

[80] H. Hong, "Unconfined Flame Synthesis of Carbon Nanomaterials and Nanostructures, and Investigation into the Fundamental Mechanisms and Applications," 2016.

[81] M. Qian, Y. S. Zhou, Y. Gao, J. B. Park, T. Feng, S. M. Huang, Z. Sun, L. Jiang and Y. F. Lu, "Formation of graphene sheets through laser exfoliation of highly ordered pyrolytic graphite," *Applied Physics Letters,* vol. 98, no. 17, p. 173108, 2011.

[82] Y. Yamagata, A. Sharma, J. Narayan, R. M. Mayo, J. W. Newman and K. Ebihara, "Optical emission study of ablation plasma plume in the preparation of diamond-like carbon films by KrF excimer laser," *Journal of Applied Physics,* vol. 86, no. 8, pp. 4154-4159, 1999.

[83] Z. Andreic, D. Gracin, V. Henc-Bartolic, H. J. Kunze, F. Ruhl and L. Aschke, "Dynamics of Laser-produced Carbon Plasma," *Physica Scripta,* vol. 53, no. 3, pp. 339-344, 1996.

[84] A. Kramida, Y. Ralchenko, J. Reader and NIST ASD Team, "NIST Atomic Spectra Database (ver. 5.3)," National Institute of Standards and Technology, Gaithersburg, 2015.

[85] C. Aragon and J. A. Aguilera, "Characterization of laser induced plasmas by optical emission spectroscopy: A review of experiments and methods," *Spectrochimica Acta Part B,* vol. 63, pp. 893-916, 2008.

[86] S. S. Harilal, C. V. Bindhu, R. C. Issac, V. Nampoori and C. Vallabhan, "Electron density and temperature measurements in a laser produced carbon plasma," *Journal of Applied Physics,* vol. 82, no. 5, pp. 2140-2146, 1997.

[87] "Collisional Cross Section," Chemistry LibreTexts.org, June 2016. [Online]. Available: http://chem.libretexts.org/Core/Physical_and_Theoretical_Chemistry/Kinetics/.

[88] W. Thurber, "The Hall Effect," National Institute of Standards and Technology (NIST), 25 August 2016. [Online]. Available: http://www.nist.gov/pml/div683/hall_effect.cfm. [Accessed 2016].

[89] Y. Liang, W. Wang, B. Zeng, G. Zhang, J. Huang, J. Li, T. Li, Y. Song and X. Zhang, "Raman scattering investigation of Bi2Te3 hexagonal nanoplates prepared by a solvothermal process in the absence of NaOH," *Journal of Alloys and Compounds,* vol. 509, pp. 5147-5151, 2011.

[90] "The Nobel Prize in Physics 2000," Nobel Media AB, [Online]. Available: https://www.nobelprize.org/nobel_prizes/physics/laureates/2000/. [Accessed 2016].

[91] C.-C. Chen, Z. Li, L. Shi and S. B. Cronin, "Thermoelectric transport across graphene/hexagonal boron nitride/graphene heterostructures," *Nano Research,* vol. 8, no. 2, pp. 666-672, 2015.

[92] L. Liu, "Feasibility of large-scale power plants based on thermoelectric effects," *New Journal of Physics,* vol. 16, p. 123019, 2014.

[93] A. Pique, R. A. McGill, D. B. Chrisey, D. Leonhardt, T. E. Mslna, B. J. Spargo, J. H. Callahan, R. W. Vachet, R. Chung and M. A. Bucaro, "Growth of organic thin films by the matrix assisted pulsed laser evaporation (MAPLE) technique," *Thin Solid Films,* vol. 355, pp. 536-541, 1999.

[94] N. K. Memon, S. D. Tse, J. F. Al-Sharab, H. Yamaguchi, A. B. Goncalves, B. H. Kear, Y. Jaluria, E. Y. Andrei and M. Chhowalla, "Flame synthesis of graphene films in open environment," *Carbon,* vol. 49, no. 15, pp. 5064-5070, 2011.

[95] L. G. Cancado, K. Takai, T. Enoki, M. Endo, Y. A. Kim, H. Mizusaki, N. L. Speziali, A. Jorio and M. A. Pimenta, "Measuring the degree of stacking order in graphite by Raman spectroscopy," *Carbon,* vol. 46, pp. 272-275, 2008.

[96] C. Scilletta, S. Orlando, M. Servidori, E. Cappelli, G. Conte and P. Ascarelli, "Role of growth temperature on nanostructure and field emission properties of PLD thin carbon films," *Applied Physics A,* vol. 93, pp. 783-787, 2008.

[97] X. Li, W. Cai, L. Colombo and R. S. Ruoff, "Evolution of Graphene Growth on Ni and Cu by Carbon Isotope Labeling," *Nano Letters,* vol. 9, no. 12, pp. 4268-4272, 2009.

[98] S. Sarath Kumar and H. Alshareef, "Ultraviolet laser deposition of graphene thin films without catalytic layers," *Applied Physics Letters,* vol. 102, p. 012110, 2013.